PREPARATION, CHARACTERIZATION AND APPLICATIONS OF CUSTOM DESIGNED NANOPARTICLES AND THEIR ORGANIZED ASSEMBLIES

A THESIS

SUBMITTED TO THE

UNIVERSITY OF PUNE

FOR THE DEGREE OF

DOCTOR OF PHILOSOPHY

IN

CHEMISTRY

BY

TRUPTI M. MADDANIMATH

PHYSICAL AND MATERIALS CHEMISTRY DIVISION

NATIONAL CHEMICAL LABORATORY

PUNE – 411 008

INDIA

JANUARY 2006

Dedicated To

My Parents…

DECLARATION

I hereby declare that the thesis entitled "**PREPARATION, CHARACTERIZATION AND APPLICATIONS OF CUSTOM DESIGNED NANOPARTICLES AND THEIR ORGANIZED ASSEMBLIES**" submitted for the degree of Doctor of Philosophy in Chemistry to the University of Pune has been carried out by me at Physical and Materials Chemistry Division, National Chemical Laboratory, Pune, 411008, India, under the supervision of Dr. K. Vijayamohanan. The work is original and has not been submitted in part or full by me for any degree or diploma to this or any other University.

Date: **TRUPTI M. MADDANIMATH**

Physical and Materials Chemistry Division
National Chemical Laboratory
Pune – 411 008

Dr. K. Vijayamohanan

Scientist

Physical and Materials
Chemistry Division
National Chemical Laboratory
Pune – 411008
INDIA

Tel: 91-020-25893300
Extn: 2270/2276
Res: 91-020-25893307
Fax: 91-020-25893044
Email: vk.pillai@ncl.res.in

CERTIFICATE

This is to certify that the work incorporated in the thesis "**PREPARATION, CHARACTERIZATION AND APPLICATIONS OF CUSTOM DESIGNED NANOPARTICLES AND THEIR ORGANIZED ASSEMBLIES**" submitted by **TRUPTI M. MADDANIMATH** was carried out by her under my supervision at Physical and Materials Chemistry Division, National Chemical Laboratory, Pune, 411008, India. All the materials from other sources have been duly acknowledged in the thesis.

Date :
Place : Pune

Dr. K. Vijayamohanan
(Research Guide)

ACKNOWLEDGEMENTS

The past five years at NCL have been an immensely rewarding educational and intellectual experience. Much of the credit for this must go to my adviser Dr. K. Vijayamohanan, without whose support this thesis would not have been possible. During these years I have known him as a sympathetic and principle-centered person. His integral view on research, profound knowledge and his mission for providing 'only high-quality work and not less', has made a deep impression on me. He is not only a great scientist with deep vision but also and most importantly a kind person. It gives me great pleasure to express my deep sense of gratitude and sincere thanks to him.

I express sincere thanks to Professor G. Ramanath for giving me a precious opportunity to work under his guidance in Rensselaer Polytechnic Institute, Troy, NY during my PhD as my advisor. His enthusiasm, professionalism and constant support were invaluable and went a long way towards the completion of this thesis. I would like to thank all his group members especially Darshan, and my friend Reena for the constant help during my stay in RPI.

I specially thank Dr. Mulla for the help extended to me when I approached him and the valuable discussions that I had with him during the course of my research. The cooperation and timely help received from him is greatly acknowledged. I also owe my deep regards to Dr. S. P. Vernekar who was always available when I needed his advises.

I thank Dr. P. Ratnaswamy and Dr. S. Sivaram, former and present Directors of NCL, Pune, for giving me the opportunity to work in this institute and making all the facilities available for my research work.

I thank Dr. S. K. Date and Dr. S. Pal, former and present Heads, Materials and Physical Chemistry Division for their constant assistance and encouragement. The cooperation I received from other faculty members Drs. Anil Kumar, P. A. Joy, Murali Sastry, P. Ghosh, V. Ravi, K. Shridhar of this department is gratefully acknowledged. The timely help from Mr. Punekar and Mr. Deepak Jori is greatly acknowledged.

I am very much thankful to Dr. S. R. Sainkar, Head of Center for Material Characterization for making available the Centre for Material Characterization facilities. I also thank Mrs. N. R. Pavaskar, Mrs. R. Pasricha and Dr. A. B. Mandale for the characterization of samples, which comprises a significant part of my research work.

I thank Dr. S. Sudrik and Sambhaji Chavan for synthesizing the organic molecules needed in my experimental work and also for many illuminating discussions. I take this opportunity to thank my former colleagues from our group Drs. Varsha, Aslam and Sushama for being always available when I needed their help; their stimulating suggestions helped me in the time of research.

Needless to say, that I am grateful to all of my colleagues Nirmal, Niranjan, Girish, Jadab, Bhalchandra, Mandar, Mahima, Mukta, and Gopi who have helped me in all possible ways and have been my extended family during the tenure of my work at NCL. I can never forget the help and support that I received from my labmate, my friend Deepali, especially during the last stages of my thesis completion.

A special mention of thanks to my friends in NCL, Rohini, Suvarna, Yogesh, Khalil and Sandeep for their continued support and cooperation during my stay. Their timely help and friendship shall always be remembered.

And a very special thanks goes to Anita. Anita is my cousin sister, my friend, my confidante, and my strongest supporter. She is never tired of listening to my ideas, complaints and in offering advice and much needed support all along the way.

My parents always gave me boundless love and encouragement to follow whatever path I chose. Their continual support gave me the strength, motivation, and willingness to continue my research. Heartfelt thanks goes to my mother for all her support over the years. My gratitude is beyond words. I am also very much grateful to my brother Praveen and sisters Jyoti and Swati for their constant inspiration and encouragement and always for believing in their little sister.

One person has contributed more than any other to me in finishing my Ph.D. with a smile on his face. Without his loving support and understanding I would never have completed my present work. I can never repay my husband Hemil, for the time that I spent in my study room over the past one year, but I wish to thank him for his patience, and constant support. Hemil, thank you for all you have done and thank you for all that you are.

Finally, I am thankful to library staff and administrative staff of NCL for cooperation and CSIR for financial support in the form Senior Research Fellowship.

Trupti M. Maddanimath

ABSTRACT

The current thesis addresses some of the major issues related to the synthesis and characterization of self-assembled monolayers (SAMs), monolayer protected metal nanoclusters (MPCs) as well as 1D nanostructures especially metallic nanowires and the motivation being both fundamental and technological applications in nanotechnology. The thesis has been divided into seven chapters. The **first chapter** represents a brief overview of basic aspects of self-assembled monolayers (SAMs), monolayer protected clusters (MPCs) and surface passivated one-dimensional metallic nanostructures and also discusses the experimental techniques used during the course of the present work. The **second chapter** primarily deals with a completely new template-less approach of assembling 2-D networks of nanowires at room temperature by the agitation of Au nanoparticles in toluene-aqueous mixtures. Subsequently, novel route for synthesizing custom designed superstructures of silver nanoparticles in one dimension using an organometallic chiral molecule as a source of silver have been discussed in **third chapter.** Further, **fourth chapter** a simple, one step synthesis of water-dispersible silver nanoparticles and networks of nanowires at room temperature has been demonstrated. **Chapter five** deals with the study of solvent mediated electron transfer behavior of silver nanoclusters. In **chapter six** some selected applications of self-assembled monolayers and monolayer-protected nanoclusters have been demonstraed. This chapter is divided into two subparts and the first part reveals the experimental proof of involvement of silver nanoparticles in the catalysis of α-diazoketones in the Wolff rearrangement while the second part discusses the proof-of-concept of using self assembled molecular nanocathodes of aromatic thiol molecules such as diphenyl disulfide (DDS) as active elements for rechargeable Li^+-ion batteries. Finally, **chapter seven** outlines a summary of all the major conclusions of the present study with respect to synthesis, characterization and electron transfer properties of monolayer protected metallic nanoclusters. The major theme of this study is to present novel protocol for the synthesis of monolayer protected clusters and one dimensional nanostructures and studying their properties especially electrochemical properties and exploring their applications.

Table of Contents

Chapter 1

Synthesis, Characterization, Properties and Applications of Monolayer Protected Metallic Nanoclusters *1-71*

1.1	Introduction	2
1.2	What is Nanoscience and Nanotechnology?	5
1.3	Why and How Properties Change in Reduced Dimensions?	7
1.4	Monolayer Protected Metallic Nanoclusters	15
1.5	History	15
1.6	Preparation Procedures	16
1.6.1	Brust's Synthesis	16
1.6.2	Synthesis in Reverse Micelles	18
1.6.3	Other Methods	19
1.7	Purification and Size Tuning	19
1.7.1	Solvent Extraction	20
1.7.2	Chromatography	20
1.7.3	Digestive Ripening	21
1.8	Characterization	21
1.8.1	UV-visible Spectroscopy	22
1.8.2	X-ray Diffraction (XRD)	23
1.8.3	Transmission Electron Microscopy (TEM)	23
1.8.4	Fourier Transform Infrared Spectroscopy (FTIR)	24
1.8.5	X-ray Photoelectron Spectroscopy (XPS)	25
1.8.6	Nuclear Magnetic Resonance (NMR)	25
1.8.7	Thermogravimetry/Differential Scanning Calorimetry (TG/DSC)	26
1.8.8	Scanning Probe Microscopes (SPM)	26
1.8.9	Electroanalytical Techniques	28
1.8.10	Other Characterization Techniques	29
1.9	Salient Features of MPCs	29
1.9.1	Core of MPCs	29
1.9.2	Capping Monolayer of MPCs	30
1.9.2.1	Functionality and Length Scale Control: Tailoring Property	31
1.9.2.2	Place Exchange Strategy: Control of ω-Functionality	32
1.10	Organization of MPCs	32
1.11	Properties	34
1.11.1	Optical Properties	34
1.11.2	Electronic Properties	35
1.11.3	Magnetic Properties	36
1.11.4	Electrochemical Properties	36
1.11.5	Other Properties	38

1.12	Applications of MPCs	39
1.12.1	Novel Optical Devices	39
1.12.2	Miniaturized Electronic Devices	40
1.12.3	Medical Diagnostics and Sensors	42
1.12.4	Other Applications	43
1.13	Conclusions and Perspectives	43
1.14	Motivation, Scope and Organization of the Thesis	44
1.15	Objective of the Present Study	44
1.16	References	49

Chapter 2

72-103

Synthesis and Characterization of Monolayer Protected Gold Nanoclusters: Temperature Effect on Au Nanoparticles Superstructures

2.1	Introduction	73
2.2	Experimental Section	75
2.2.1	Materials	75
2.2.2	Size Selective Synthesis of Au MPCs	75
2.2.3	Techniques Used for the Characterization of MPCs	77
2.2.3.1	UV-visible Spectroscopic Analysis	77
2.2.3.2	Transmission Electron Microscopic (TEM) Analysis	77
2.2.3.3	(a) X-ray Diffraction (XRD) Analysis *(b) In-situ* Temperature Controlled XRD Analysis	77
2.2.3.4	Nuclear Magnetic Resonance (NMR) Analysis	78
2.2.3.5	(a) Fourier Transform Infrared Spectroscopic (FTIR) Analysis (b) *In-situ* Temperature Controlled FTIR Analysis	78
2.2.3.6	Thermogravimetric (TG) Analysis	78
2.2.3.7	Differential Scanning Calorimetric (DSC) Analysis	79
2.3	Results for the Characterization of Au MPCs	79
2.3.1	UV-visible Spectroscopic Analysis	79
2.3.2	TEM Analysis	81
2.3.3	XRD Analysis	84
2.3.4	NMR Analysis	85
2.3.5	FTIR Analysis	87
2.4	Effect of Temperature on 3.72 nm Sized Au MPCs Superstructures	89
2.4.1	TEM Analysis	90
2.4.2	*In-situ* XRD and TG-DSC Analysis	91
2.4.3	*In-situ* FTIR Analysis	94
2.5	Discussion	97
2.6	Conclusions	98
2.7	References	100

Chapter 3

104-137

Single Electron Charging Features of Monolayer Protected Gold Clusters

3.1	Introduction	105
3.2	A Simplified Model to Understand the Charging Behaviour in Coulomb Blockade Nanostructure	107
3.3	Experimental Section	110
3.3.1	Materials	110
3.3.2	Synthesis of Au MPCs	111
3.3.3	Scanning Tunneling Microscope/Spectroscopic (STM/STS) Measurements	111
3.3.4	Electrochemical Measurements	111
3.4	Single Electron Charging Features of $Au_{1415}(DDT)_{328}$	112
3.4.1	STM/STS Measurements	112
3.4.2	Electrochemical Behaviour	116
3.4.2.1	Quantized Double Layer Charging	116
3.4.2.2	Adsorption features	129
3.5	Conclusions	134
3.6	References	135

Chapter 4

138-169

Interactions of Charged Monolayer Protected Gold Clusters in Electrolyte Solution

4.1	Introduction	139
4.2	Experimental Section	141
4.2.1	Materials	141
4.2.2	Synthesis of Au MPCs	141
4.2.3	Scanning Tunneling Microscope/Spectroscopic (STM/STS) Measurements	141
4.2.4	Electrochemical Measurements	142
4.3	Single Electron Charging Features of $Au_{2869}(DDT)_{541}$	142
4.3.1	STM/STS Results	143
4.3.2	Voltammetric Results	147
4.4	Interaction of Au MPCs	153
4.4.1	Chronoamperometric Results	155
4.4.2	Impedance Results	157
4.4.3	Effect of Charge Steps on Diffusion Coefficient	164

4.5	Conclusions	166
4.6	References	167

Chapter 5 *170-199*

Electrochemical Investigation of Monolayer Protected Silver Nanoclusters

5.1	Introduction	171
5.2	Experimental Section	172
5.2.1	Materials	172
5.2.2	Synthesis of Different Sized Ag MPCs	172
5.2.3	Characterization Techniques	173
5.3	Size Dependent Redox Features of Ag MPCs	174
5.3.1	Particle Characterization	174
5.3.2	Electrochemical Measurements	180
5.4	Synthesis of Ag Nanoparticles Using Triethylamine	186
5.4.1	Synthetic Procedure	187
5.4.2	Characterization of Ag Nanoparticles	187
5.4.3	Electrochemical Properties	192
5.5	Conclusions	195
5.6	References	196

Chapter 6 *200-205*

Conclusions and Future Prospects

List of Publications *206-207*

Erratum *208*

CHAPTER I

Preparation, Characterization and Applications of Nanomaterials: An Introduction

This chapter is an introduction to the thesis and gives a brief overview of basic aspects of self-assembled monolayers (SAMs), monolayer protected clusters (MPCs) and surface passivated one-dimensional metallic nanostructures. It also discusses the importance of one-dimensional nanostructures with respect to their optical, electronic and catalytic properties and efforts that have been made to achieve them. Besides, it also includes protocols used to synthesize 1D nanostructures. The different experimental techniques used during the course of the present work are also discussed in this chapter.

1.1 Introduction

The small world has big horizons. The revolutionary Feynman's vision of a powerful and general nanotechnology, based on nanomachines that build with atom-by-atom and molecule-by-molecule control, promises great opportunities and an unprecedented era of innovation across multiple disciplines and device applications [1,2]. With this vision of miniaturization, the chemists and physicists are no longer to be at the mercy of nature. Now, they can decide what properties they want a material to have and they go ahead and build it.

Today, Feynman's dream is surely being realized on a grand and global scale. The speed and functionality of computers have followed "Moore's Law" [3] doubling every year or two for the past 45 years. This remarkable increase in performance has required shrinking of the integrated circuits to smaller and smaller sizes and nanotechnology forms the basis of these advances. Within the last decade nanotechnology has reached the status of a leading science [4, 5] with fundamental and applied research prospects [6] in all basic sciences such as physical, life, and earth sciences: from chemistry and physics [7, 8], biology, and medicine [9-12] to astronomy and geology [13]. An important feature of nanotechnology, specifically nanomaterials, i.e., materials with atleast one dimension in the nanosize regime (1-100 nm) is its ability to bridge the crucial dimensional gap between the atomic and molecular fundamental sciences and the microstructural scale of engineering and manufacturing [14]. It is generally accepted that the quantum confinement of charge carriers by the potential wells of nanometer size structure provides one of the most powerful, yet versatile means to control the properties of these materials by modulating their size and shape.

At the end of the 20th century, most efforts were dedicated to develop synthesis [15,16] and characterization techniques [17-19] to produce and probe nanoparticles of smaller and smaller sizes. Such studies were rewarded by the generation of a new class of materials called quantum dots that are characterized by a zero dimensionality (0-D). Such materials have revealed fascinating size-induced physical and chemical properties due to quantum confinement effects and very high surface-to-volume ratios. One-dimensional (1-D) nanostructures, a new class of low dimensional and anisotropic

nanomaterials have emerged recently [20,21], whose lateral dimension is in the nanometer range and their longitudinal dimension ranges from hundreds of nanometer to hundreds of micron. Such characteristics give aspect ratios (length over diameter) of up to several thousand. The basic goals have been to develop synthesis techniques to produce large quantity of 0-D and 1-D building blocks in a controllable and fashionable way. Although, the control of the size has empirically and qualitatively been achieved, the strict control of the particle size over orders of magnitude has not yet been clearly demonstrated or quantitatively established. The control of the shape of nanocrystallites also represents an essential task to fulfill. The production of anisotropic nanomaterials has mostly been achieved using efficient chemical growth inhibitors, i.e. surfactants [22], or synthesis carried out in confined volume, i.e. microemulsion [23] to the detriment of the surface purity. The control of the orientation of anisotropic materials and the capability to generate aligned and ordered nanocrystallites onto a substrate are other important challenges. They are currently reached by using masking/patterning techniques such as template [24], lithography [25] or by epitaxial electrodeposition [26] on single crystalline substrates but very few approaches of direct growth methods of well-oriented and patterned structures have been reported. The ability to produce new devices with higher level of design and complexity, combining for instance ordered nanostructures with controlled size, shape and composition (hierarchical assemblies) is yet another important challenge.

In order to overcome these difficulties, several class of materials, including insulators, semiconductors, metallic, and supramolecular nanostructures have been synthesized to date [27-29]. However, the methods used to prepare these materials show strong limitations when up-scaling become an essential requirement. Indeed, the most serious challenge scientists and engineers have to face is to unfold the full potential of applications and prospects of nanotechnology, which includes the development of sustainable large-scale manufacturing techniques for the time and cost-effective productions of clean and reliable nanomaterials.

In an attempt to take part in the fascinating nanoworld, and to contribute to its ambitious challenges, the present thesis will expose novel synthetic protocols for the generation of nanomaterials especially one-dimensional nanomaterials and their

properties, focusing on some of their selected applications. The primary objective of this chapter is to summarize issues related to the synthesis and characterization of self-assembled monolayers (SAMs), monolayer protected metal nanoclusters (MPCs) as well as 1D nanostructures especially metallic nanowires. A brief description of the promising area of nanotechnology and reasons for the change in the properties of nanomaterials are given in section 1.2. Section 1.3 discusses history of nanotechnolgy while the basic aspects of SAMs, MPCs and 1D nanostructures are discussed in sections 1.4, 1.5 and 1.6 respectively. Other sections are devoted to describe the review of synthetic strategies, properties and applications of one-dimensional nanostructures and principles of the characterization techniques used in the present study. In such a broad field of nanomaterials, many fundamental questions are addressed everyday, which cannot be covered, in a single short chapter. Even restricting the scope to nanomaterials of metallic systems makes the task extraordinarily difficult. Therefore, here we mention selective and recent contributions in this emerging area, while few other important contributions are cited in the references. We hope that this brief summary will be helpful to understand the importance of nanomaterials and their fascinating physical and chemical properties as well as their possible potential for future technological applications.

1.2 How the properties of the materials change in Nano regime?

The physical and chemical properties of a material are determined by the type of motion its electrons are allowed to execute [30]. The latter is determined by the space in which the electrons are confined due to the forces they encounter. Unbound (unconfined) electrons have motion that is not quantized and can thus absorb any amount of energy. Once an electron is bound in an atom or in a molecule, its motion becomes highly confined and quantization sets in. The allowed types of motion in atomic or molecular orbitals are found to have well-defined energies. The smaller the space in which the motion is bound, the stronger the confinement and the larger the energy separation between the allowed energies of the different types of motion. The atomic confinement is the strongest type of electronic confined motion. In the hydrogen atom, the electron is confined to a length scale of ~50 pm. In a metal, electrons are highly delocalized over large space (i.e., least confined for example in a “free electron” model). This is a result of the fact that the separation between the valence and conduction bands

vanishes, giving the metal its conducting properties. As we decrease the size of the metal and confine its electronic motion, the separation between the valence and the conduction bands becomes comparable to or larger than kT (thermal energy), and the metal becomes a semiconductor. Higher confinement increases the energy separation further, and the material becomes an insulator. In the size domain at which the metal-to-insulator transition occurs, new properties are expected to be observed which are possessed neither by the metal nor by the molecules or atoms forming the metal. In noble metals, the decrease in size below the electron mean free path (the distance the electron travels between scattering collisions with the lattice centers) gives rise to intense absorption in the visible-near-UV region. This results from the coherent oscillation of the free electrons from one surface of the particle to the other and is called the surface plasmon absorption. Such strong absorption induces strong coupling of the nanoparticles to the electromagnetic radiation of light. This gives these metallic nanoparticles brilliant color in colloidal solution that intrigued scientists in the 17th century. Their technological application was ahead of semiconductor nanoparticles, as they were used to give stained glass (e.g. Lycurgus cup) its brilliant ruby color used in cathedrals at that time [31]. Faraday showed that the intense color is due to metallic gold in colloidal form [32]. It was not until 1908 when Mie [33] explained the phenomena by solving Maxwell's equations for the absorption and scattering of electromagnetic radiation by spherical metallic particles. This theory has been used to calculate the spectra of particles smaller than the wavelength of light for nanoparticles whose metallic dielectric function is known and which are embedded in an environment of known dielectric constant [34, 35].

1.3 History of nanotechnology:

The concept now known as nanotechnology was first proposed by Nobel laureate Richard P. Feynman in a dinner speech at the 1959 Annual Meeting of the American Physical Society. Feynman, a physicist who noted that "the principles of physics, as far as I can see, do not speak against the possibility of maneuvering things atom by atom" [1,2]. It would be several decades before the means to transform Feynman's dinnertime speculation into reality appeared on the horizon. In 1974 Tokyo Science University professor Norio Taniguchi coined the term "nanotechnology." So "nano" was well on its

way already in competing with “micro” [2]. The first to grasp the fact that those means were coming within reach was K. Eric Drexler [2]. He expanded the term nanotechnology, published the first scientific paper on the topic in 1981. In Drexler's conception, the goal of nanotechnology is to build molecular assemblers - nanoscale factories capable of constructing objects at any scale, atom by atom. Unlike conventional chemistry, in which innumerable molecules react en masse, Drexler's proposed method of "mechanosynthesis" involves positioning individual molecules close together so stronger chemical attractions can overcome weaker ones in a controlled way, depositing or removing atoms as desired. The invention of the Scanning Tunneling Microscope (STM) by Gerd Binnig and Heinrich Rohrer in 1981 at IBM's Zurich Research Laboratory and the Atomic Force Microscope (AFM) in 1986 by Gerd Binnig, Christoph Gerber and Calvin Quate, made it possible to realize the essence of nanotechnology and opened the door to images of what happens out of sight of the naked eye and manipulate matter with atomic level precision [2]. Another breakthrough came with the discovery of new shapes for molecules of carbon, the quintessential element of life. In 1985, researchers reported the discovery of the "buckyball," a lovely round molecule consisting of 60 carbon atoms. This led in turn to the 1991 discovery of a related molecular shape known as the "carbon nanotube [2]. With this rich history, research and development in many nanotechnology fields continues apace. At the turn of the new Millennium, nanotechnology has become not only very real but also a major driver in the future of human evolution.

1.4 Importance of Self-Assembly of Nanomaterials

Self-assembly is the most powerful tool to bring Drexler's dream of molecular assembly in reality. The broader nanotechnology community is waking up to the potential for dynamic self-assembly in a wide range of different applications and researchers are finding solutions to assemble atoms and molecules into smart materials and working devices. Self-assembly or supramolecular chemistry is the chemistry beyond the molecule, and molecules are being designed to self-assemble into larger structures. Nature works through self-assembly. In this case, biological system is a place to find inspiration: biology cells and their pieces are made from self-assembling biopolymers such as proteins and protein complexes. One of the things being explored

is synthesis of organic molecules by adding them to the ends of complementary DNA strands such as ----A and ----B, with molecules A and B attached to the end; when these are put together, the complementary DNA strands hydrogen bonds into a double helix, ====AB, and the DNA molecule can be removed to isolate the product AB. Self-assembly from seashells, which grow through the use of nanoparticles and polymer secretions. We recognize the power of self-assembly but we want to do it on our own terms, controlling it, directing it, speeding it up and nanotechnology gives the best solution.

1.5 Self-assembled monolayers

As discussed above organized molecular assemblies have been one of the intensely pursued areas of contemporary chemistry. Among the various methodologies used to make organized monolayer structures, self-assembled monolayers (SAMs) have been attractive to many materials chemists owing to the simplicity of the preparative method and high stability [36,37]. Self-Assembled Monolayers (SAMs) are usually formed as a result of spontaneous adsorption of (amphi-functional) species on the surfaces followed by their spontaneous organization as shown in figure 1.1. The spontaneous growth of many organic monolayers was suggested by Zisman and coworkers in 1946 [38]. They observed that alkyl amines adsorb on platinum, and consequently spontaneous formation of an ordered monolayer occurs. During the early period, the potential of SAMs was not recognized. In 1983, Nuzzo and Allara showed that SAMs of alkanethiolate on gold could be prepared by the adsorption of n-alkyl disulfides from dilute solutions [39]. Following this report, a rapid growth in SAMs research occurred. Several adsorbate/adsorbent combinations have been found [40, 41]. Among these, alkanethiol monolayers on coinage metals, especially gold, became the center of attraction because of its inertness (so that a clean absorbent can be made even in normal laboratory conditions) and owing to the fact that the formed monolayer is stable as Au–S bond is sufficiently strong (bond energy ~48 kcal/mol). The ability to tailor the monolayer–air interface makes SAMs ideal model systems for studies of interfacial phenomena. Some examples of suggested and implemented applications of these systems include sensors [42], corrosion inhibitors [43], molecular recognition [44], and molecular crystal growth [45]. SAMs provide the needed design flexibility, both at

the individual molecular and at the material levels, and offer a vehicle for investigation of specific interactions at interfaces, and of the effect of increasing molecular complexity on the structure and stability of two-dimensional assemblies. These studies may eventually produce the design capabilities needed for assemblies of three-dimensional structures [46]. Several approaches have been used to get at the energetics of thiol SAMs. Bain et al. [47] have determined the absolute activation energy for C22 thiol of 28 kcal/mol. Jung & Campbell [48] have determined the activation energy of »11 kcal/mol for zero chain length. The Blanchard group [49] determined the free energy of adsorption, 1Gads. They found that 1GadsD¡5.5 kcal/mol for C18 and ¡4.4 kcal/mol for C8 thiol SAMs.

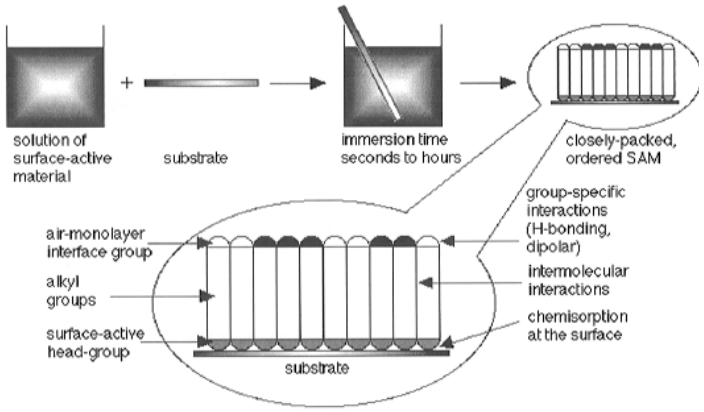

Figure 1.1 *Self-assembled monolayers are formed by simply immersing a substrate into a solution of the surface-active material. The driving force for the spontaneous formation of the 2D assembly includes chemical bond formation of molecules with the surface and intermolecular interactions. (Adopted from Ref. 37)*

It has been proved that the equilibrium structure of a SAM is the result of a delicate balance between competing forces. Organization of complex, semiflexible organic molecules within quasi 2D assemblies is the result of a delicate interplay between substrate-adsorbate interactions, nonbonded interactions between adsorbates, electrostatic and VDW forces and intramolecular interactions such as bond stretches, angle bends, and torsions.

The studies on SAMS have been further intensified since the successful preparation of stable metal clusters protected with monolayers. SAMs offer unique opportunities to increase fundamental understanding of self-organization, structure-property relationships, and interfacial phenomena as well as a versatile scaffold for the

introduction of chemical functionality to nanoparticles. The size and shape of nanoparticles and binding of surfactants or ligands on nanoparticle surface atoms is of fundamental importance in achieving size and shape control. Self-assembled monolayers of surfactants are proved to be excellent candidates for the size and shape control of nanomaterials.

1.6 Monolayer-protected nanoclusters (MPCs)

The possibility to prepare monodisperse metallic particles of pure materials in the nanometer size regime, associated with the capping of these particles by (typically) functionalized long-chain organic molecules (self-assembled monolayers), has thrown open an entire field of research. Metallic nanoparticles are finding myriad uses, ranging from traditional ones, such as coloring agents (in stained glass windows) and catalysts, to more novel ones, such as drug delivery, hypothermic cancer therapy, contrast agents in magnetic resonance imaging, magnetic and fluorescent tags in biology, solar photovoltaics, nano bar codes, and emission control in diesel vehicles. This field is, in certain ways, reaching maturity, and to go to the next step, it is becoming important to develop methods of scaling up the synthesis of these materials.

The usual synthetic route to prepare metal nanoparticles involves the reduction of a suitable metal salt (usually a halide) in solution in the presence of a stabilizer. The schematic presentation of monolayer-protected cluster is shown in figure 1.2. The first systematic studies of this method were carried by Michael Faraday who obtained colloidal gold by reducing an aqueous solution of $AuCl_4^-$ with phosphorus [32]. Since then, the discovery of various reducing agents and stabilizers have made possible the development of mild conditions that can be employed for the preparation of large amounts of nanoparticles of reproducible quality. Among these reduction methods, the best known is that developed by Brust et al. [50,51] which involves the phase transfer of $AuCl_4^-$ from aqueous to organic solutions followed by reduction with $NaBH_4$ in the presence of alkanethiols to yield gold nanoparticles in the size range of 1–3 nm. Ligand displacement reactions, developed by Murray and co-workers, have been successful in introducing multiple functionalities into these MPC systems in a stepwise fashion, relying on concentration equilibria [52]. Thiols are excellent stabilizers for capping gold

nanoparticles owing to strong Au-S bonding, which enables the isolation of the particles as solid materials following solvent evaporation [53]. The isolated particles can be readily redissolved in nonpolar solvents where they are indefinitely stable. Other good protective agents, such as phosphanes [54], phosphines [55], amines [56], chalcogen containing organic molecules [57], carboxylates [58], and selected functionalized polymers [59, 60] have been successfully used. The size and morphology of the nanoparticles can be tuned by varying the concentration ratio of capping agent to metal salts [61-63] and by choosing a suitable reducing agent. A weak reducing agent, such as citrate [64, 66] or tartarate, favors a slow reaction allowing particle growth over a long period to yield faceted and small (<1 nm) nanoparticles, whereas with relatively strong reducing agents, such as formamide [67] or o-anisidine [68] bigger and generally spherical nanoparticles are formed.

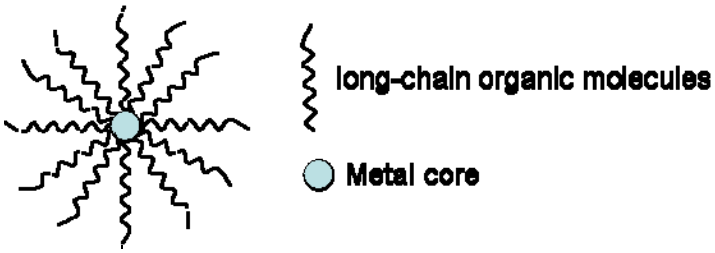

Figure 1.2 *Schematic diagram of monolayer protected nanocluster showing metal core functionalized with chains of organic molecules.*

1.7 One dimensional nanomaterials

Considering Zero dimensional (0D) nanostructures (or quantum dots) as ideal model systems, the relationship between fundamental properties with size can be easily investigated both experimentally and theoretically. For example, several chemical methods have already been developed to generate quantum dots with well-controlled dimensions and different types of quantum mechanical calculations have predicted their size and shape dependant optical, electrical and thermal properties. In comparison, one dimensional (1D) nanostructures provide a better system for the investigation of anisotropic confinement of electronic states and have been enthusiastically pursued for their applications such as switches, sensors and both interconnects and active components in fabricating future nanoscale electronic and photonic devices [69, 70]. In order to harness these applications, it is critical to synthesis 1D nanostructures

(specifically nanowires) with well-defined sizes and configurations. Consequently, extensive research activities have been carried out during the last few years to facilitate their successful preparation and characterization of 1D nanostructures using different approaches [71]. Nevertheless, the sparse advancement in 1D nanostructures has been mainly due to the difficulties associated with the synthesis and fabrication of these nanostructures having controlled dimensions, morphology, phase purity and chemical composition. Although each method developed for the production of 1D nanostructures has had success in achieving high quality materials, a general strategy, to make well-controlled nanowires with high purity and selectivity is missing.

1.8 Various methods for the generation of 1-D nanostructures

1.8.1 Template directed synthesis

Controlling the shape of nanoparticles has been most successfully achieved using templates since templates provide a constrained environment during the nanoparticle growth and thus shapes are tuned according to the template. Template directed synthesis is simple, high-throughput and cost effective which also allows the complex topology present on the surface of the template to be duplicated in a single step. Both the soft and hard templated approach to control the aspect ratio of nanomaterials shares the advantage of easy solution preparation and control of shape. For example, one dimensional templates such as channels in alumina or polymer membranes [72-74], mesoporous materials [75-77], carbon nanotubes [78-80], block co-polymers [81], DNA chains [82], rod shaped micelles [83], calix[4]hydroquinone nanotubes [84], and steps or edges on solid substrates [85] have been used for the synthesis of one dimensional nanostructures. The hard template methods are presently better suited for more rigorous alignment and connection of nanorods and nanowires. However, the exact mechanisms by which the growth proceeds are still not rigorously worked out. In practice, the presence of templates does not produce 100% shape monodispersity; rather, a significant fraction of thermodynamically favorable spheres are also formed. In addition, soft templates such as micelles may not be stable under the experimental conditions (e.g., boiling), and thus the template may not function [86-90]. A common reason for the failure of the template mechanism is the change in template

microstructures by reactants. Template methods for the synthesis of one-dimensional nanomaterials have several other disadvantages. For instance, templates based synthesis methods are complicated methods, which involve a series of procedures resulting into low yield often containing defects. In addition the need for complete removal of template to get continuous nanowires and nanorods requires harsh conditions, which can in some cases distort the shape. When the template is only involved physically, it is often selectively removed using post-synthesis treatment (such as chemical etching and calcination) in order to collect the resultant nanostructures. In a chemical process, the template is usually consumed as the reaction proceeds and it is possible to directly obtain the nanostructures as a pure product.

1.8.2 Seed mediated growth method

Another solution phase seeded growth method of generating high aspect ratio metal nanorods and nanowires has been demonstrated recently by Murphy's group. The basic principle for seeded growth method involves two steps: First, the preparation of small size spherical metal nanoparticles, and second, growth of the prepared spherical particle in rod-like micellar environment. Initial addition of preformed seeds has two advantages: first, it increases the overall reaction rate, and hence the growth rate; second, the particle size is controlled by varying the ratio of metal salt to seed, thus restricting the particle size to the nanometer regime. Murphy et al. have shown that the nanostructures can be synthesized by using a variety of different seeds with different sizes and surface functionalities [91]. A systematic study reveals that the nanorod dimension is influenced by various parameters such as concentration and size of seed, concentration of metal ions, ratio of concentration of seed to metal ions, concentration and nature of reducing agent, nature as well as chain length of capping agent [92]. The aspect ratio of the nanorods, to a large extent, increases as the seed size decreases. Further, it has been observed that seed mediated growth in presence of NaOH (at higher pH of reaction mixture) enables quantitative production of nanorods of high aspect ratio [93]. Recently this method has been improved by El-Sayed's group resulting in spectacular increase in nanorod yield [94].

1.8.3 Polyol method

The polyol method of generation of silver nanowires is similar to seed mediated growth except that this method used ethylene glycol as solvent as well as reducing agent. Polyol method, pioneered by Xia and coworkers [95,96] has proven to be very successful for the large-scale synthesis of silver nanowires. This method involves two steps: First the formation of Pt nanoparticles by reducing $PtCl_2$ with ethylene glycol refluxed at elevated temperatures. In this process, ethylene glycol serves as both solvent and reducing agent [96]. The second step involves, addition of $AgNO_3$ and poly(vinyl pyrrolidone) (PVP) to the refluxing solution that contained Pt seeds. It is believed that the formation of platinum seeds in the solution could effectively separate the subsequent nucleation and growth steps of silver and the use of a polymer surfactant could kinetically control the growth rates of various planes of face-center-cubic silver. In the presence of PVP, the growth of silver is directed into a highly anisotropic mode to form uniform nanowires with high aspect ratio as high as ~1000. According to the mechanism proposed by Xia et al. the PVP macromolecules interact more strongly with the {100} planes than with the {111} planes of silver. Each silver nanowire evolves from multiply twinned nanoparticles of silver with the assistance of PVP at the initial stage of the Ostwald ripening process. The anisotropic growth is maintained by selectively covering the {100} facets with PVP while leaving the {111} facets largely uncovered by PVP and thus highly reactive [95]. It has been verified that the morphology and aspect ratios of silver nanostructures could be varied from nanoparticles and nanorods to long nanowires by adjusting the reaction conditions, including the ratio of PVP to $AgNO_3$, reaction temperature, concentration of seeding solution and seeding conditions [96,97]. Polyol method has also been used for the synthesis of one-dimensional nanostructures of other metals [98].

On the other hand, Liz-Marzan and coworkers have reported the ability of N,N-dimethyl formamide (DMF), to reduce Ag^+ ions so that Ag nanowires can be synthesized using PVP as a stabilizer [99]. In this case, DMF plays the role of solvent as well as the reducing agent like EG in the above cases. Wei and co-workers have reported a novel chainlike and dendritic nanostructure of silver with fractal features, synthesized via a simple solvothermal method in the presence of poly(vinyl pyrrolidone) (PVP) [100]. This

method involves reaction of metal salt and PVP in EG at 180 °C for 3 h to form the silver chainlike nanostructures and it has been observed that morphology of nanostructures highly depends on reaction time and temperature. Though this method exhibits number of attractive futures such as high yield and low cost but often leads into mixed morphology products, which are to be separated using centrifugation. Also requirement of high temperature conditions limits the use of this method for the bulk production of nanowires.

1.8.4 Other methods

Many other solution phase chemical reduction processes are reported for generation of 1D nanostructures. For example, Murphy et al. have reported a method to make crystalline silver nanowires in water, in the absence of a surfactant or polymer to direct nanoparticle growth, and without externally added seed crystallites [101]. In this reaction silver salt is reduced to silver metal, at 100 °C, by sodium citrate, in the presence of NaOH. Hydroxide ion concentration is key to producing nanowires, which are up to 12 microns long. In another approach it has been shown that silver nanowires can be synthesized without the assistance of surfactants [102]. With this approach, silver nanowires can be synthesized by simple reduction of the silver ions with reductants such as glucose, sodium citrate, and sodium hypophosphite, etc., in the absence of the surfactants or capping reagents at the temperature from 80 to 200°C. The cyclic pentatwinned structures are concluded to play a key role in the growth of nanowires although the stability of some of these structures is questionable. Tian and co-workers have shown an interesting template and seed less method of generating silver nanowires using reduction of metal salt in presence of trisodium citrate and sodium dodecylsulfonate [103]. Similarly, Xu et al. have shown polymer-surfactant assisted sandwiched reduction method for synthesis of silver nanowires in which sandwich organometallic compound as a reducing agent results in the formation of elemental silver along certain axis in the xy plane and poly(ethylene)glycol provides microenvironments for confining 1D growth [104]. In a very recent study made by Adachi and co-workers it has been shown that citrate reduction of $AuCl^-_4$ ion with low concentration of citrate yields Au nanowires with 2D network [105].

1.8.5 Electrochemical method

Wang and co-workers have developed a method for the synthesis of Au nanorods via electrochemical oxidation/reduction within a simple two-electrode type cell [106]. The electrochemical cell comprises gold cathode and platinum anode electrodes immersed in an electrolytic solution consisting of a shape inducing cationic surfactant, hexadecyltrimethylammonium bromide (C16TAB), and a rod-inducing co-surfactant, tetraoctylammonium bromide (TC8AB). The C16TAB serves as the supporting electrolyte as well as the stabilizer for nanoparticles to prevent their further growth. During synthesis, the bulk gold metal is converted from the anode to form gold nanoparticles most probably at the interfacial region of the cathodic surface and within the electrolytic solution. The synthesis is conducted under an ultrasonication and a controlled temperature. The ratio between the surfactants controls the average aspect ratio of the Au nanorods. In later studies, it has been shown by same group how experimental conditions can be optimized further to improve the yield and controllability of aspect ratio of Au nanorods [107]. The advantage of this method is that it offers a relatively simple preparation procedure for the fabrication of the suspended nanorod particles while preserving a good controllability in the particles' dimensions. However, the stability of these Au nanorods under exposure to light or heat limits their future applications. Gosele and co-workers have demonstrated the preparation of monodisperse silver nanowires by dc electrochemical plating into monodomain porous alumina templates [108]. The electrochemical method of generation of nanorods/nanowires provides nanostructures with fairly good uniformity and controlled aspect ratio although its growth mechanism remains elusive. Also the electrochemical process is highly complex and involves various effects such as sonication and electric field, making it difficult to verify the mechanism of formation.

1.8.6 Photochemical method

Kim and co-workers have shown the synthesis of one-dimensional nanostructures with controlled aspect ratio by using photochemistry in the presence of metal ions. This process is highly promising for producing uniform nanorods, and more importantly it is useful in resolving the growth mechanism of anisotropic metal

nanoparticles due to its simplicity and the relatively slow growth rate of the nanostructures [109]. The synthesis strategy involves the reduction of Au ions by irradiation with UV light in presence of surfactants, C16TAB and TC8AB and different amounts of silver ions. Chen and co-workers have reported single-crystal silver dendritic supramolecular nanostructures prepared via an ultraviolet irradiation photoreduction technique at room temperature using poly(vinyl alcohol) (PVA) as a protecting agent [110] and it has been shown that the concentration of both $AgNO_3$ and PVA has a significant effect on the formation and growth of these nanostructures. Though nanorods with controlled aspect ratios have been synthesized via a simple photochemical process, their aspect ratio is very low and this method often leads to products with minor impurities from seeds.

1.9 Characterization techniques

The main emphasis of this thesis is the solution phase synthesis and characterization of monolayers and monolayer capped nanomaterials and exploring their properties and applications using different analytical techniques. Characterizing the properties of individual nanostructures is a challenge to many existing testing and measuring techniques because of the following constraints. First, the size (diameter and length) is rather small, prohibiting the applications of well-established testing techniques. Tensile and creep testing of a fiber-like material, for example, require that the size of the sample be sufficiently large to be clamped rigidly by the sample holder without sliding. This is impossible for nanostructured fibers using conventional means. Secondly, the small size of the nanostructures makes their manipulation rather difficult, and specialized techniques are needed for picking up and installing individual nanostructures. Therefore, new methods and methodologies must be developed to quantify the properties of individual nanostructures. Among the various techniques UV-Vis spectroscopy, Fourier Transform Infrared spectroscopy (FTIR), X-ray photoemission spectroscopy (XPS), Transmission Electron Microscopy (TEM), X-ray diffraction (XRD) and Cyclic voltammetry (CV), impedance etc. have been major tools in investigating the properties of individual nanostructures. This part of the chapter is devoted in explaining the basic principles on which different techniques are based and their application to understanding various aspects of formation of nanomaterials.

1.9.1 UV-Vis spectroscopy

The total energy of a molecule is the sum of its electronic, vibrational and rotational energy. The magnitude of these energy decreases in the following order: E_{elec}, E_{vib} and E_{rot}. Energy absorbed in the UV region produces changes in the electronic energy of the molecule resulting from transition of electrons in the molecule. The relationship between the energy absorbed in an electronic transition and the frequency (ν), wavelength (λ) and wavenumber ($\bar{\nu}$) of radiation producing the transition is,

$$\Delta E = h\nu = hc/\lambda = h\ \bar{\nu} c$$

where, h is Planck's constant, c is the velocity of light and ΔE is the energy absorbed in an electronic transition in a molecule from a low-energy state (ground state) to a high energy state (excited state). The energy absorbed is dependent on the energy difference between the ground state and the excited state; the smaller the difference in energy, the longer the wavelength of absorption. Since UV energy is quantized, the absorption spectrum arising from a single electronic transition should consist of a single, discrete line. A discrete line is not obtained since electronic absorption is superimposed on rotational and vibrational sublevels. The principal characteristics of an absorption band are its position and intensity. A more convenient expression of absorption intensity is that derived from the Lambert-Beer law, which establishes a relationship between the absorbance, the sample thickness and the concentration of the absorbing species. The relationship is expressed as,

$$A = abc$$

where, *A* is the measured absorbance, *a* is absorptivity , *b* is the cell-path length, and *c* is the analyte concentration.

As a consequence of reducing the size and the dimensionality of a material, its electronic properties change drastically as the density of states and the spatial length scale of the electronic motion are reduced [111-114]. When electromagnetic radiation falls on matter (especially metal), the electrons in the conduction band get excited and collective oscillations of electrons give rise to resonances [115]. These resonances are known as surface plasmons and these effects are sensitive to size, since they are absent in bulk materials [116]. The total extinction coefficient of small metallic particles is given in Mie's theory [33] as the summation over all electric and magnetic multipole

oscillations contributing to the absorption and scattering of the interacting electromagnetic field while for nanoparticles with much smaller size only dipolar term contributes and the extinction coefficient κ for *N* particles of volume *V* is then given by the following equation [117],

$$\kappa = \frac{18\pi N V \varepsilon_m^{3/2}}{\lambda} \frac{\varepsilon_2}{[\varepsilon_1 + 2\varepsilon_m]^2 + \varepsilon_2^2}$$

where λ is wavelength of the absorbing radiation and ε_m the dielectric constant of the surrounding medium (assumed to be frequency independent). ε_1 and ε_2 represent the real and imaginary parts of the material dielectric function, respectively

In case of spherical metallic nanoparticles, when they are irradiated by light, the oscillating electric field causes the conduction electrons to oscillate coherently. When the electron cloud is displaced relative to the nuclei, a restoring force arises from the coulomb attraction between electrons and nuclei resulting into oscillation of electrons relative to the nuclear framework. This oscillation frequency is determined by different factors such as (a) density of electrons, (b) effective electron mass, (c) shape and size of charge distribution. The electron density within a surface layer, the thickness of which is about equal to the screening length of a few angstroms, oscillate, whereas the density in the interior of the particle remains constant and this resonance is called as surface plasmon resonance.

For high aspect ratio nanostructures such as nanorods and nanowires, the plasmon absorption splits into two bands corresponding to the oscillation of the free electrons along (longitudinal bands) and perpendicular to the long axis (transverse bands) of the rods [118,119]. For example, UV-visible absorbance spectra of Au MPCs and Ag MPCs show a strong plasmon absorption band around 510-530 and 400-430 nm respectively depending upon the shape, size and protection layer while Au and Ag nanowires/nanorods show splitting of band with transverse band at around 510-530 and 400-430 nm and longitudinal bands at higher wavelengths < 530 and 430 nm respectively. Gans extended Mie theory for shape dependent surface plasmon absorption [120]. According to Gans, the extinction coefficient is given by the following

equation where, P_j values are the depolarisation factors for the three axes A, B, C of high aspect ratio material such as nanowire/nanorod with A > B =C.

$$\kappa = \frac{2\pi N V \varepsilon_m^{3/2}}{3\lambda} \sum_j \frac{(1/P_j^2)\varepsilon_2}{[\varepsilon_1+(1-P_j/P_j)\,\varepsilon_m]^2+\varepsilon_2}$$

UV–vis spectroscopy measurements of all the samples in the present case were performed on a UV-2101PC double beam spectrometer (Shimadzu) using quartz cells (path length 1 cm).

Thus UV-visible spectroscopy is the important analytical tool in understand the properties of nanomaterials, however, the solvent and substrate dependence limits the use of this technique for deep understanding of properties of the nanomaterials.

1.9.2 Fourier transform infrared spectroscopy (FTIR)

The atoms in a molecule do not remain in a fixed relative position and vibrate about some mean position. Due to this vibrational motion if there is a periodic alternation in the dipole moment then such mode of vibration is infrared (IR) active. The IR region of the electromagnetic spectrum is 100 μm – 1 μm wavelength. The vibrating molecule absorbs energy only from radiation with which it can coherently interact, i.e. the radiation of its own oscillation frequency. The appearance or non-appearance of certain vibrational frequencies gives valuable information about the structure of a particular molecule.

The frequency of vibration is given by the relation:

$$\nu = \frac{1}{2\pi} \sqrt{\frac{k}{\mu}}$$

where, *k* is force constant; μ is reduced mass.

FTIR is a powerful tool for exploring the surface of nanoparticles. The concentration of the capping material plays an important role in how a molecule interacts with that surface. It is important to understand the surface of the nanoparticles in question and how a ligand may adsorb onto their surfaces. FTIR spectroscopy can

reveal information about the local molecular environment of the adsorbed ligands and nanoparticles surfaces. For example, FTIR spectroscopy has been used previously to examine the conformational structure of the particle-bound organic surfactant monolayers, where the energies of the symmetric (d+) and antisymmetric (d-) stretching vibrations of the methylene units are taken as a sensitive diagnostic indicator for the ordering of the adsorbed alkanethiolate molecules [46,47]. The samples for FTIR analysis can be prepared by dropcasting the particle solutions onto a KBr plate or silicon wafer to form a thick film, and further dried in a gentle N_2 stream.

Alternately, Attenuated Total Reflection (ATR) is often used to characterize nanomaterials. For example, ATR-IR spectroscopy has been used to examine both bulk solutions and surface adsorption of dendrimers and dendrimer-encapsulated Pt nanoparticles onto wet and dry Al_2O_3 [121].

1.9.3 Raman spectroscopy

Raman spectroscopy is a form of vibrational spectroscopy, and Raman bands arise from a change in the polarizability. In many cases, transitions that are allowed in Raman are forbidden in IR, so these techniques are often complementary [122].

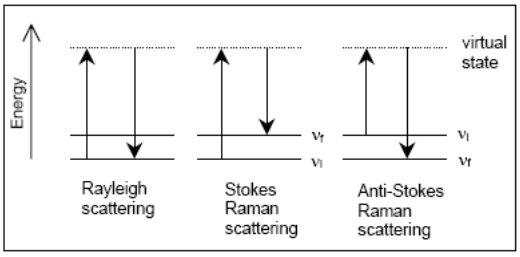

Figure 1.3 *Energy-level diagrams of Rayleigh scattering, Stokes Raman scattering, and anti-Stokes Raman scattering.*

When a beam of light is impinged upon a sample, photons are absorbed by the material and scattered. The vast majority of these scattered photons have exactly the same wavelength as the incident photons and are known as Rayleigh scatter, However, a small fraction of light (approximately 1 in 100 photons) is scattered at optical frequencies different from, and usually lower than, the frequency of the incident photons. The process leading to this inelastic scattering is termed the Raman effect. Most of the

Raman scattered photons are shifted to longer wavelengths (Stokes shift), but a small portion is shifted to shorter wavelengths (anti-Stokes shift). Figure 1.3 shows a diagram of Rayleigh scattering, Stokes Raman scattering, and anti-Stokes Raman scattering. In each case, the incident photon excites an electron into a higher virtual energy level (or virtual state) and then the electron decays back to a lower level, emitting a scattered photon. A Raman spectrum is a plot of the intensity of Raman scattered radiation as a function of its frequency difference from the incident radiation (usually in units of wavenumbers, cm^{-1}).

Raman spectroscopy is useful for analysis for several reasons: it exhibits high specificity, it is compatible with aqueous systems, no special preparation of the sample is needed and the timescale of the experiment is short. One limitation of conventional Raman spectroscopy is its low sensitivity, often requiring the use of powerful and costly laser sources for excitation. However, scattering efficiency can be enhanced by the factor up to 10^6 when compound is adsorbed on or near metal surfaces. The technique associated with this phenomenon is called as Surface Enhanced Raman Spectroscopy (SERS), which is especially more useful for the analysis of nanomaterials when nanoparticles are deposited on metal surfaces.

SERS arises from two mechanisms. The first is an enhanced electromagnetic field produced at the surface of the metal. When the wavelength of the incident light is close to the plasma wavelength of the metal, conduction electrons in the metal surface are excited into an extended surface electronic excited state called a surface plasmon resonance. Molecules adsorbed or in close proximity to the surface experience an exceptionally large electromagnetic field. The vibrational modes normal to the surface are most strongly enhanced. The second mode of enhancement is by the formation of a charge-transfer complex between the surface and analyte molecule. The intensity of the surface plasmon resonance is dependent on many factors including the wavelength of the incident light and the morphology of the metal surface. SERS exhibits extraordinary potential for the characterization of trace chemical species and hence widely used as one of the important tools for nanomaterials characterization.

1.9.4 Nuclear magnetic resonance spectroscopy (^{1}H NMR)

All atomic nuclei possess nuclear spin, I, which may be integral (i.e. 1,2,3 etc.) or half integral (i.e ½, 3/2, 5/2 etc.) Since nucleus possesses an electric charge, the spinning nucleus gives rise to a magnetic field whose axis coincides with the axis of spin. Thus each nucleus can be thought of being equivalent to a minute magnet having magnetic moment μ. Each nucleus with $I > 0$ has magnetic moment. If a magnetic nucleus is placed in a uniform magnetic field, it is found that the magnetic dipole assumes only a discrete set of orientations. The magnetic nucleus may assume any one of $(2I + 1)$ orientations with respect to the direction of the applied magnetic field. Thus, a proton ($I = ½$) will be able to assume only one of two possible orientations that correspond to energy levels of $\pm \mu H$ in a applied magnetic field, where H is the strength of the external magnetic field. The transition of a proton from one possible orientation to another may be affected by the absorption or emission of a discrete amount of energy such that

$$E = h\nu = 2\mu H,$$

where ν is the frequency of electromagnetic radiation absorbed or emitted.

In solution NMR, spectra consist of a series of very sharp transitions, due to averaging of anisotropic NMR interactions by rapid random tumbling. By contrast, solid-state NMR (SSNMR) spectra are very broad, as the full effects of anisotropic or orientation-dependent interactions are observed in the spectrum.

The monolayer binding, structure and dynamics of capping molecules within MPCs are generally obtained by NMR spectroscopy. For example, ^{13}C NMR measurements of the 3D RS/Au systems are very useful in assessing the changes associated with formation of the Au-S bond.[123] ^{1}H and ^{13}C NMR studies of alkanethiol capped Au particles show that the resonance at the first C next to the sulfur head group disappear upon binding to gold, indicating a strong interaction with the surface. NMR resonances of MPCs are characteristically broadened and shifted relative to those of free alkanethiols upon binding to the core, indicative of successful surface capping. Further, NMR is also useful to assess the purity content of the sample and all these results can be supplemented by the data obtained from FTIR.

Proton NMR spectra of the solutions of silver nanowires reported in the current study were recorded on a Bruker AC 200 MHz instrument and scanned in the range 0–15 ppm.

1.9.5 X-ray photoelectron spectroscopy (XPS)

XPS is based on the well-known photoelectric effect (a single photon in/electron out process) first explained by Einstein in 1905. Photoelectron spectroscopy uses monochromatic sources of radiation (i.e. photons of fixed energy given by relation, E = $h\nu$). In XPS the photon is absorbed by an atom in a molecule or solid, leading to ionization and the emission of a core (inner shell) electron. The kinetic energy distribution of the emitted photoelectrons (i.e. the number of emitted photoelectrons as a function of their kinetic energy) can be measured using any appropriate electron energy analyser and a photoelectron spectrum can thus be recorded. The one way to look at the overall process of photoionization is follows:

$$A + h\nu = A^{+} + e-$$

Conservation of energy then requires that:

$$E(A) + h\nu = E(A^{+}) + E(e-)$$

Since the electron's energy is present solely as kinetic energy (KE) this can be rearranged to give the following expression for the KE of the photoelectron:

$$KE = h\nu - (E(A^{+}) - E(A))$$

The final term in brackets, representing the difference in energy between the ionized and neutral atoms, is generally called the *binding energy* (BE) of the electron - this then leads to the following commonly quoted equation,

$$KE = h\nu - BE$$

The binding energies (BE) of energy levels in solids are conventionally measured with respect to the Fermi-level of the solid, rather than the vacuum level. This involves a small correction to the equation given above in order to account for the *work function* (ϕ) of the solid,

$$KE = h\nu - BE - \phi$$

Employing photons with fixed energy $h\nu$, it is obvious that if kinetic energy *KE* and work function ϕ of the sample are measured, it is possible to measure binding energy of

electron in solid. Binding energies being characteristic of atoms, different elements present in the sample under investigation are identified. Electrons traveling through a material have a relatively high probability of experiencing inelastic collisions with locally bound electrons as a result of which they suffer energy loss and contribute to the background of the spectrum rather than a specific peak. Due to inelastic scattering process, the flux of photoelectrons emerging from the sample is much attenuated.

XPS technique is widely used for the understanding the binding in nanomaterials. For example, self-assembled monolayers (SAMs) of alkylthiols on planar gold (2D SAMs) and nanoparticles (3D SAMs) have been intensely studied. The actual nature of the Au-S bonding can be characterized by XPS technique. The 2D and 3D SAMs show the Au $4f_{7/2}$ = 83.9 eV BE values which correspond to Au(0). While S 2p shows shift in the BE from 164.2 (for elemental S8) to 162 eV corresponding to a negative charge-bearing S adsorbed on Au [124].

For the work described in this thesis, XPS measurements were carried out on a VG Microtech ESCA 3000 instrument at a base pressure better than 1 x 10^{-9} Torr with un-monochromatized Mg Kα radiation (1253.6 eV energy). The measurements were made in the constant analyzer energy (CAE) mode at a pass energy of 50 eV and electron takeoff angle (angle between electron emission direction and surface plane) of 60°. This leads to an overall resolution of ~ 1 eV in the measurements.

It should be mentioned that there are limitations associated with this technique because it detects electrons. First, since electrons do not pass through air, these experiments must be run in vacuum. This also means that samples must be dried (water evaporates in a vacuum); this drying may impact the system or result in many chemical transformations. Also, since this technique is highly surface sensitive, it is less useful to analyze bulk properties; in fact, it may make it impossible to identify anything but interferences on a dirty surface.

1.9.6 Transmission electron microscopy (TEM)

TEM is a powerful tool for characterizing the atomic-scale structures of solid-state materials. A modern TEM is a versatile machine that not only can provide a real-space resolution better than 0.2 nm, but also can give a quantitative chemical and

electronic analysis from a region as small as 1 nm. It is feasible to receive a full structure characterization from TEM. In TEM analysis, a thin specimen is illuminated with electrons in which the electron intensity is uniform over the illuminated area. As the electrons travel through the specimen, they are either scattered by a variety of processes or they may remain unaffected by the specimen. The end result is that a nonuniform distribution of electrons emerges from the exit surface of the specimen that contains all the structural and chemical information about the specimen. Electron microscope is constructed to display this nonuniform distribution of electrons in two different ways.

Angular distribution of scattering can be viewed in the form of scattering patterns, usually called diffraction patterns, and spatial distribution of scattering can be observed as contrast in images of the specimen. The advantage of this arrangement is the possibility of directly viewing the area from which the diffraction pattern arises.

In the present study, TEM has been used for the size determination of nanostructures drop coated onto a carbon-coated copper grid. The TEM measurements were done on a JEOL model 1200EX instrument operated at an accelerating voltage of 120 kV. With the availability of slow-scan CCD cameras and the recent digital revolution, it is possible to treat the digital data of electron diffraction patterns and the corresponding TEM images recorded under low-dose conditions in a quantitatively rigorous manner.

1.9.7 X-ray diffraction (XRD)

X-rays are electromagnetic radiations with typical photon energies in the range of 100 eV-100 keV. The energetic X-rays can penetrate deep into the materials and provide information about the structural arrangement of atoms and molecules in a wide range of materials. X-rays are produced generally by either X-ray tubes or synchrotron radiation. In a X-ray tube, which is the primary X-ray source used in laboratory x-ray instruments, X-rays are generated when a focused electron beam accelerated across a high voltage field bombards a stationary or rotating solid target. As electrons collide with atoms in the target and slow down, a continuous spectrum of X-rays is emitted, termed also as Bremsstrahlung radiation. The high-energy electrons also eject inner shell

electrons in atoms through the ionization process. When a free electron fills the shell, an X-ray photon with energy characteristic of the target material is emitted. Common targets used in X-ray tubes include Cu and Mo, which emit 8 keV and 14 keV X-rays with corresponding wavelengths of 1.54 Å and 0.8 Å, respectively. (The energy E of an X-ray photon and it's wavelength is related by the equation $E = hc/\lambda$, where h is Planck's constant and c the speed of light). In recent years synchrotron facilities have become widely used as preferred sources for X-ray diffraction measurements. Synchrotron radiation is emitted by electrons or positrons traveling at near light speed in a circular storage ring.

X-rays primarily interact with electrons in atoms. When X-ray photons collide with electrons, some photons from the incident beam will be deflected away from the direction where they originally travel, much like billiard balls bouncing off one anther. If the wavelength of these scattered X-rays do not change (meaning that X-ray photons do not lose any energy), the process is called elastic scattering (Thompson Scattering) in that only momentum has been transferred in the scattering process. These are the x-rays that we measure in diffraction experiments, as the scattered X-rays carry information about the electron distribution in materials. On the other hand, in the inelastic scattering process (Compton Scattering), X-rays transfer some of their energy to the electrons and the scattered X-rays will have different wavelength than the incident X-rays. Diffracted waves from different atoms can interfere with each other and the resultant intensity distribution is strongly modulated by this interaction. If the atoms are arranged in a periodic fashion, as in crystals, the diffracted waves will consist of sharp interference maxima (peaks) with the same symmetry as in the distribution of atoms. Measuring the diffraction pattern therefore allows one to deduce the distribution of atoms in a material. The peaks in a X-ray diffraction pattern are directly related to the atomic distances. Figure 1.4 shows incident X-ray beam interacting with the atoms in the two different planes.

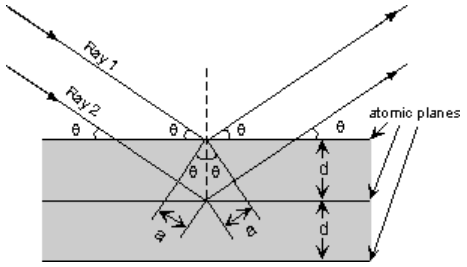

Figure 1.4 X-ray reflections from a crystal.

For a given set of lattice plane with an inter-plane distance of d, the condition for a diffraction (peak) to occur can be simply written as:

$$2d \sin\theta = n \lambda$$

which is known as the Bragg's law, after W.L. Bragg, who first proposed it. In the equation, λ is the wavelength of the X-ray, θ the scattering angle, and *n* an integer representing the order of the diffraction peak. The Bragg's Law is one of most important laws used for interpreting X-ray diffraction data.

In order to find out the particle size of the nanoparticles by XRD, Debye-Scherrer formula is used. If the crystallites of the powder are very small the peaks of the pattern will broaden. From the broadening it is possible to determine an average crystallite size by Debye-Scherrer formula:

$$D_{hkl} = k \lambda/\beta \cos\theta \text{ Å}$$

here k = 0.8 -- 0.9 (usually 0.9), λ-wavelength of the radiation λ_{Cu} = 1.54056 Å, β - FWHM (full width at half maximum, or half-width)in radiance, β = half-width (degree) Pi/180, θ-the position of the maximum of diffraction. The great advantage of the technique is that it does not require the growing and mounting of a single crystal. Powder diffraction also allows the sampling of larger objects. The great disadvantage is that the three dimensional information of the reciprocal space of a crystal gets collapsed into a one-dimensional diffractogram. XRD patterns of the samples synthesized in this study were recorded on a Phillips PW 1830 instrument operating at a voltage of 40 kV and a current of 30 mA with Cu-Ka radiation.

1.9.8 Electroanalytical techniques:

1.9.8.1. Cyclic Voltammetry: Cyclic voltammetry is one of the most versatile electroanalytical techniques for the study of electroactive species [125]. This technique has the capability for rapidly observing redox behavior over a wide potential range. It involves the cycling of the potential of a working electrode with respect to a reference electrode in an unstirred solution, and measuring the resulting current. The controlling potential applied across these two electrodes is an excitation signal. For cyclic voltammetry, the excitation signal is a linear potential scan with a triangular waveform (as shown in figure 1.5). A cyclic voltammogram is obtained by measuring the current at the working electrode during the potential scan. The voltammogram is a display of current versus potential.

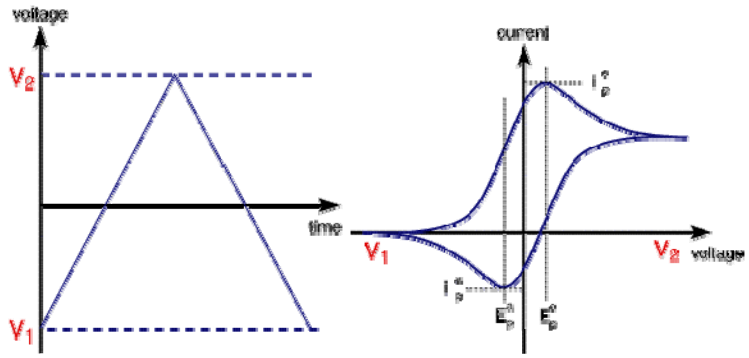

Figure 1.5: *Cyclic potential sweep,the voltage is swept between two values at a fixed rate, however now when the voltage reaches V_2 the scan is reversed and the voltage is swept back to V_1 (b) Resulting cyclic voltammogram is shown on the right hand side, where Ep^a, Ep^c are anodic and cathodic peak potentials and Ip^a, Ip^c are anodic and cathodic peak currents.*

The voltage-current curves are measured in a potentiostatic circuit. In a three-electrode arrangement the potentiostat controls the potential difference between the working electrode (WE) and the reference electrode (RE), which serves as the potential basis for the working electrode, to a predetermined value.

Previous reports indicate that monolayer protected nanoparticles behave as molecular capacitors in solutions, which are manifested by electrochemical coulomb

staircase characteristics. For instance, the double layer capacitance (C_{CLU}, F) of CTAB-protected silver clusters is so small (subattofarad 0.77 aF) [126], that single electron transfers to and from them occur at palpably large voltage intervals DV = e/C_{CLU} (e = the electron charge, 1.6 × 10^{-19} C) that are easily resolved at room temperature on the electrochemical potential. Chaki et al. has shown the size dependent electrochemistry of monolayer protected silver nanoparticles [127] where the appearance of the redox behaviour (7 nm diameter particles) with oxidation peak at 0.10 V and cathodic peak at -0.08 V is interesting.

1.9.8.2 Impedance analysis: Electrochemical impedance is another important electroanalytical technique based on the measurement of the response of an electrochemical cell in terms of the resultant ac voltage, of a circuit element to the application of an ac current. As any frequency may be applied, the impedance is a function of the frequency, and an impedance spectrum is a representation of the impedance of a circuit element as a function of frequency. When Impedance varies with frequency then real and imaginary parts come into picture. The components along the ordinate are assigned as imaginary and components along abscissa are real. If the real part is plotted on the Z axis and the imaginary part on the Y axis of a chart, "Nyquist plot" is obtained. Major shortcoming of the Nyquist plots is that it is not possible to identify the frequency at which the corresponding data was recorded. Another popular presentation method is the "Bode plot". The impedance is plotted with log frequency on the x-axis and both the absolute value of the impedance (|Z| =Z_0) and phase-shift on the y-axis.

The main advantage of ac, as compared to dc measurements is that the greater amount of information obtained usually allows the separate determination of the components of the metal-solution interface. It can give valuable information about surface coverage, dielectric constant, conductivity, concentration of carrier, diffusion-coefficients and electron transfer behaviour of nanomaterials both in solution and in solid state, however, interpretation of impedance is difficult. Also unique equivalent circuit cannot be used and change in the impedance model with frequency makes this technique more complicated. The response is often analyzed using the complex impedance presentation and the results are interpreted in terms of suitable equivalent circuits as shown in figure 1.6.

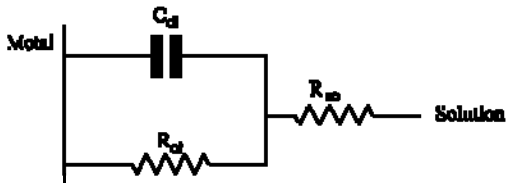

Figure 1.6: *The simplest linear equivalent circuit for a metal-solution interface consists of double layer capacitance (Cdl), charge transfer resistance (Rct), solution resistance (Rsol).*

1.9.9 Miscellaneous Characterization Techniques

Apart from these techniques, several other special characterization techniques, such as Scanning probe microscopy (STM, AFM), Scanning electron microscopy (SEM), Energy Dispersive X-ray analysis (EDAX), Electron Energy Loss Spectroscopy (EELS), Quartz Crystal Microgravimetry (QCM), Thermogravimetry, Ellipsometry etc. have been applied for investigations of nanomaterials.

Though several techniques are available for the charaterisation of nanometeials, esearch in nanomaterials faces many challenges in synthesis, property characterization, device fabrication, and system integration. The small size of nanostructures constrains the applications of the well-established testing and measurement techniques, thus new methods and approaches must be developed. The complimentary aspects of characterizing both organic and inorganic parts of these nanostructural materials bring down clearly that one or two techniques cannot provide reliable information. However a judicious application of a variety of techniques can provide all molecular level information like precise composition and purity of these nanostructured materials, which is an essential prerequisite before exploiting their unusual properties for tangible applications.

1.10 Properties of 1D nanomaterials

1.10.1 Thermal properties:

Nanowire thermal and thermoelectric properties are important for the thermal management of nanowire devices (optoelectronic, sensing, and computing) and

essential for the design of nanowires thermoelectric materials. For nanowire diameters smaller than the bulk mean free path of heat carriers, theory predicts that the thermal conductivity of nanowires will be reduced when compared to similar bulk materials. Theory predicts that during long-term annealing a nanowire tends to decrease its surface area and thus minimize the interfacial energy by decaying into a chain of nanospheres. Neumanna et al. have presented the results of annealing experiments performed on Cu nanowires that decay into a chain of nanospheres at temperatures much lower (500-600 ^{0}C) than the bulk melting point (T_{bulk} = 1200 °C) [128].

It is well documented that the melting point of a solid material will be greatly reduced when it is processed as nanostructures [129]. The remarkable reduction in melting point associated with nanowire has several important implications: (1) It is possible to perform zone refining to purify nanowires from the bulk materials at a modest temperatures (2) Reduction in melting point enables one to cut, interconnect, and weld nanowires at relatively mild temperatures. This capability may provide new tool to integrate these 1D nanostructures into functional devices and circuitry. In a series of studies, El-Sayed and co-workers used spectroscopic methods to investigate the photothermal melting and shape transformation of gold nanorods dispersed in micellar solutions [130]. They found that the nanorods were melted and transformed into spherical particles when they were exposed to femtosecond laser pulses at moderate energies. At higher energies or when exposed to nanosecond laser pulsed, these nanorods were fragmented and then transformed into spherical particles with smaller dimensions. They also determined that an average energy of ~60 fJ was required to melt a single gold nanorod dispersed in an aqueous medium. Thermal stability of 1D nanostructures is of critical importance for their implementation as building blocks in nanoscale electronic and photonic devices.

1.10.2 Mechanical properties

Materials with reduced size and dimensionality such as nanowires, nanotubes, or metallic clusters may present exceptional properties compared to those of the corresponding macroscopic materials. The mechanical behavior of materials at the nanoscale is often different from that at macroscopic scale. Fernandez and co-workers used AFM tool to measure the change in the length of Au nanowires during elongation-

compression cycles [131]. They found that the Au nanowires elongated under stretching in quantized steps up to three integer multiples of 0.176 nm and that they spontaneously shorten in steps of 0.152 nm when relaxed. They explained these observations by assuming that the sliding of crystal planes within the Au nanowires created stacking faults and thus changed the local structure from ccp to hcp. These results provide some direct evidence for the mechanism responsible for the plastic deformation of a nanowire when it undergoes mechanical stretching or compression. This approach can further extended to examine the atomic events occurring during the plastic failure of various metals and their alloys. Boland and co workers have measured the Young's modulus values for Au nanowires ranging from 40 nm to 250 nm in diameter. The average measured value is 70 $\pm$11 GPa. [132] In a related study, an STM supplemented with a force sensor was adopted to investigate the mechanical properties of a freely suspended chain of single Au atoms by Rubio et al. [133]. It was found that the bond strength of the nanowires is approximately twice that of a bulk metallic bond. Computational studies on this system indicate that the total effective stiffness of the nanowire has a strong dependence on the local arrangement of atoms at the chain bases. In another study, Rubio et al. [134] simultaneously measured the electrical conductance and cohesive force of an atomic-scale gold wire as it is formed and ruptured. They observed steps of order $G_0 \approx 2e^2 = h$ in the conductance, which were synchronized with a sawtooth structure with an amplitude of order 1 nN in the force. Similar results were obtained independently by Stalder and Du¨rig [135]. It was noted that the tensile strength of the nanowire in the final stages before rupture exceeds that of macroscopic gold by a factor of 20, and is of the same order of magnitude as the theoretical value in the absence of dislocations [134]. This is consistent with the recent finding of Rodrigues et al. [136] that such nanowires are, in fact, typically free of defects in their central region [137]. Nanowires also show potential applications as high aspect ratio probes in atomic force microscopes due to the mechanical stability during operation.

1.10.3 Optical properties

The size-confinement plays an important role in determining the energy levels of a nanowire once its diameter has been reduced below a critical value (the Bohr radius). The plasmon resonance for nanorods splits into two bands. As the aspect ratio

increases, the energy separation between the resonance frequencies of the two-plasmon bands also increases. The high-energy band corresponds to the oscillation of the electrons perpendicular to the major axis of the rods and is referred to as the transverse plasmon absorption. The other absorption band, which is red-shifted to lower energies, is caused by the oscillation of the electrons along the major axis of the nanorods and is known as the longitudinal surface plasmon absorption. The transverse plasmon absorption has linear dependence on the aspect ratio and the dielectric constant of the medium. For nanorods made of noble metals such as Au and Ag, their surface plasmon resonance (SPR) properties have been extensively studied by El-Sayed and coworkers and other research groups [138]. Different from their 0D counterparts, the 1D nanostructures exhibit two SPR modes, corresponding to the transverse and longitudinal excitations. While the wavelength of transverse mode is essentially fixed around 520 nm for Au and 410 nm for Ag, their longitudinal modes can be easily tuned to span across the spectral region from visible to near infrared by controlling their aspect ratios. It was demonstrated that gold nanorods with an aspect ratio of 2.0-5.4 could fluoresce with a quantum yield more than one million times that of the metal [139]. These properties, coupled with biological inertness make Au and Ag nanorods ideal candidates for use as colourimetric markers or sensors and contrast-enhancing reagents for in-vivo optical imaging [140].

Additionally, molecules adsorbed to the surface of gold and silver nanoparticles undergo enhanced surface-enhanced Raman scattering (SERS) effects, due to the coupling of the plasmon band of the irradiated metal with the molecules' electronic states. Murphy et al. have investigated the relationship between the SERS and fluorescence enhancement factor (the degree to which the metal nanoparticle increases the Raman signals of adsorbed molecules) and excitation resonance with longitudinal plasmon absorption for gold and silver nanorods [141]. These results suggest that molecules adsorbed to substrates that have plasmon absorption in resonance with the excitation source show 10-100-fold greater SERS enhancement than those adsorbed to gold or silver nanoparticles in the off-resonance condition.

1.10.4 Electrical properties

The electron transport properties of nanowires are expected to lead to new discoveries of nanoscience facilitating fabrication of novel electronic devices. Indeed, there are several appealing features of nanowires for the bottom-up approach to nanoelectronics. First, the size of the nanowire building blocks can be readily tuned to sub-100 nm and smaller, which should lead to a high density of devices on a chip. Second, the material systems for the nanowires are essentially unlimited, which should give researchers great flexibility to select the right materials for the desired device functionality. Metal nanowires exhibit a number of interesting properties: their electrical conductance is quantized, their shot-noise is suppressed by the Pauli principle, and they are remarkably strong and stable. Thus a nanowire is a strip of a conducting material (10 nm or less in width/thickness) that displays quantum-mechanical effects. Xia and co-workers have shown the electrical conductivity measurements on individual silver nanowires having diameter 40 nm. A linear I-V curve, V(mV) = 0.43 +0.974I (μA) from which an electrical conductivity of $0.8x10^5$ S/cm was calculated. This value represents a reasonable number for such a thin nanowires compared to the conductivity of bulk silver is $6.2 X10^5$ S/cm [95,96].

Gold represents a metal whose electron-transport properties have been extensively studied in the form of short nanowires as thin as a single, linear chain of atoms [142]. Because these wires are extremely short in length (usually a few atoms across, sometimes also referred to as point contacts), their conductance has been shown to be in the ballistic regime with the transverse momentum of electrons becoming discrete. A ballistic conductor is one in which an electron injected at one end will emerge at the other with certainty. Therefore, there is no backscattering of electrons, which yields an intrinsic electric resistance and would follow Ohm's Law.

The transport phenomenon observed in this kind of 1D system is found to be independent of material [143]. Hirose and Fujimoto have investigated transport properties of single-row gold nanowires and shown that wires possess a quantized conductance of about 1 G_0 at the average bond length of less than 2.7 Å [144]. For the optimized nanowire, the conductance decreases during elongation, and it is close to zero when the average bond length is larger than 3.1 Å. These results show that a

metal–insulator transition occurs in the optimized 4-atom wire while the average bond length is from 2.8 to 3.0 Å, and that its conductance is 0.54 G_0 at (d) = 2.9 Å which is equal to the nearest-neighbor atomic distance of the gold crystal. Using an STM tip with a voltage applied, conductance measurements have been made on nanowires produced using the STM. It was found that the conductance occurred in jumps as the wire was elongated. The jumps occurred in intervals of G [G = 2(e^2)/h]. It was also found that longer wires (l>10nm) exhibit localization behavior, which is an exponential dependence of the resistance on the square of l (lnR~l^2) [145].

1.11 Applications of 1D nanomaterials

Nanotechnology refers to emerging set of tools, techniques and unique applications involving the structure and composition of materials at the near-atomic, or nanometer level. Designing and creating materials at the nanoscale often leads to products that achieve exceptional performance – possibly enabling more efficient and less expensive manufacturing processes. The intense interest in nanotechnology is being driven by visions of a stream of new nanotech commercial applications. The commercialization of new nanomaterials promises to have a profound effect on multiple industries in the coming decades. These applications of 1D nanomaterials include, but are not limited to, the following:

1.11.1 Sensing applications

One of the major applications for 1D nanostructures is related to the sensing of important biological molecules, and gases with a significant impact in many important and quickly developed areas like medical diagnostics, environmental monitoring, pharmacy, biotechnology, (bio)chemical warfare and or national security. These new capabilities offer unprecedented challenges and opportunities for developing highly sensitive and selective multifunctional sensor arrays beyond what conventional (bio) sensors can do. The inherent high surface-to volume ratios associated with these nanostructures make their electrical properties extremely sensitive to species adsorbed on surfaces. For example, Tao and co-workers have demonstrated this concept using arrays of Cu nanowires that contained nanoscale gaps generated through an automated electrochemical process and have also shown changes in the conductivity of gold

nanowires upon sensing thiols or amines [146,147]. Upon the adsorption of organic molecules onto these Cu nanowires, the quantized conductance was reduced to a fractional value as a result of the scattering of conduction electrons by the absorbates. In another demonstration, Penner and co-workers fabricated hydrogen sensors with Pd nanowires supported on the surface of a polymeric thin film. Since each nanowire contained may break junctions along their longitudinal axis that could be reduced as hydrogen gas was absorbed into the crystal lattice, the resistance of these nanowires exhibited a strong dependence on the concentration of hydrogen gas [148]. The response time could be as short as 75 ms. Nanowires can also be functionalized with chemical or biological reagents appropriate for biological sensing applications. However, the nansensors display less than ideal sensitivity, and sometimes uses conducting polymers, which suffer from low mechanical strength and stability.

1.11.2 Catalytic applications

It is widely known that transition metal nanoparticles such as Fe, Co, and Ni play an essential role in many processes including the growth of carbon nanotubes. For example, Yen et al. have recently shown that the multi-walled carbon nanotubes (CNTs) can be successfully synthesized in presence of metal nanowires of Fe, Co, and Ni. This study reveals that the nanowire catalyst strongly affects not only the alignment but also the microstructure of CNTs. Nanotubes grown from Fe and Ni nanowires show the best alignment and their walls also exhibit to be composed of reasonably good graphitized layers. Carbon nanotubes grown from Ni and Fe nanowires demonstrate better field emission properties than those from Co nanowires [149]. El-Sayed and co-workers have shown that the transition metal nanoparticles are very attractive to be used as catalysts due to their high surface-to-volume ratio and their high surface energy, which makes their surface atoms very active and also shown the effect of the shape of the nanomaterials on the catalytic activity [150].

Apart from the above applications of 1D nanostructures are used in several other fields such as Micro/Nano Electromechnical Systems (MEMS/NEMS), molecular electronics etc. Many new applications of one-dimensional nanostructures are being discovered almost daily and the use of nanowires may occur in the microelectronics

industry in the face of smaller and smaller devices. There are many other applications and uses, which have yet to be discovered.

While nanomaterials create a wealth of new opportunities, they also pose tremendous environment and human risks. Potentially harmful effects of nanotechnology might arise as a result of the nature of the nanoparticles themselves, the characteristics of the products made from them, or aspects of the manufacturing process involved. The large surface area, crystalline structure, and reactivity of some nanoparticles may facilitate transport in the environment or lead to harm because of their interactions with cellular material. The size of nanomaterials could facilitate and exacerbate any harmful effects caused by the composition of the material. Little is known about the fate, transport, and transformation of nanomaterials after they enter the environment. Although there have been few studies to date on the potential toxicity of nanomaterials, research efforts should be intensified in order to prevent the possibility of damage to human health and the environment.

1.12 Conclusion and Perspectives

From the above critical reviews it is clear that several aspects on the preparation, characterization, properties and various applications of SAMs and nanomaterials are not completely elucidated despite their importance in the emerging importance of nanotechnology. The present study is an attempt to provide some of these information and consequently most of the recent developments of monolayers and monolayers capped 0 and 1 dimensional nanostructures have been presented in this chapter with particular emphasis on metal nanostructures. Although nanowire-based devices possess a variety of interesting properties and promising functions, the development for industrial products and commercialization of nanowires have been relatively slow. This is due to difficulties associated with the synthesis of 1D nanostructures with well-controlled size, phase purity, crystallinity, chemical composition, and especially an integration of individual nanowires into complete devices in mass production process. Further in-depth investigations integrating chemistry and nanotechnology will be required to fully achieve these important challenging goals; knowing how to translate the rules of tailoring

molecular-level functions into large-scale complex systems will be crucial to the fabrication of nanoparticle-based functional devices.

1.13 Motivation, Scope and Organization of the Thesis

The thesis addresses some of the major issues related to the synthesis and characterization of self-assembled monolayers (SAMs), monolayer protected metal nanoclusters (MPCs) as well as 1D nanostructures especially metallic nanowires and the motivation being both fundamental and technological applications in nanotechnology. Indeed, several synthetic strategies have been demonstrated during the last few years to synthesize 1 D nanostructures with controllable size, shape and confinement, the sparse advancement (in comparison with that of simple nanoparticles) has been mainly due to the difficulties associated with synthesis and fabrication of these nanostructures having controlled dimensions, morphology, phase purity and chemical composition. Towards this end, we have proposed few new synthetic routes to synthesize one-dimensional nanostructures along with their characterization and few properties for their future possible applications in electronic and photonic devices. Further, the effects of different parameters such as temperature and solvent on these nanowires have been studied in order to provide detailed mechanism of formation of these structures. Main emphasis is given on finding out the electrochemical aspects of these 1 D nanostructures and their comparison with the electrochemical behaviour of metallic quantum dots. Detailed study of electrochemical behaviour and effect of solvent on metallic nanoparticles has been studied using various electroanalytical techniques. This study provides a crucial role of solvent in guiding electron transfer properties of metallic nanoclusters which can be advantageously used to control selectivity of reactions catalyzed by metal clusters. We have also investigated the role of in-situ generated metal nanoparticles as a catalyst in organic reactions especially Wolff rearrangements of diazoketones. We believe that this study gives a significant achievement in the understanding the role of silver compounds and co-reagents in Wolff rearrangement and these results may prove germane to the understanding of the catalysis of several organic reactions by metal-nanoclusters. Further we have shown a new approach of using self-assembled molecular layers (SAMs) of aromatic molecules as high-efficiency cathodes, which may give birth to new generation of batteries. This strategy of using layered mesoassemblies of molecular

nanostructures could open up new possibilities of creating lightweight and miniaturized rechargeable energy generation and storage modules with extended lifetimes that can be integrated with logic and memory devices

1.14 Objective of the Present Study

The specific objectives of the work embodied in this thesis are set out in this perspective as follows:

(a) To explore novel methods for the synthesis of one-dimensional nanostructures (especially nanowires) of gold and silver in aqueous and non-aqueous medium.

(b) To form the hierarchical, custom designed one-dimensional assembly of nanoparticles silver nanoparticles.

(c) To accomplish the characterization and effect of different parameters on synthetic procedures for 1 D nanomaterials of gold and silver and their various properties.

(d) To understand the solvent dependent electrochemical behaviour of monolayer protected silver nanoparticles.

(e) To elucidate the electrochemical behaviour of 1 D nanostructures and to compare electron transfer behaviour of monolayer protected spherical quantum dots and 1D nanostructures.

(f) To explore the applications of monolayers (SAMs) as possible nanocathodes in lithium batteries.

(g) To demonstrate the proof of involvement monolayer protected nanoparticles as electrocatalysts in organic reactions.

Thus present thesis addresses some important issues related to the synthesis and characterization of monolayer protected metal nanoclusters as well as one-dimensional structures like nanowires. Some of the possible applications of these hybrid materials

are also included highlighting their size and shape dependant properties together with a brief discussion of their main limitations.

The thesis consists of seven chapters. **Chapter one** gives an introduction along with a brief overview on the synthesis of 2D and 3D self assembled monolayers (SAMs) and monolayer protected nanostructures. Different methods of synthesizing these nanomaterials especially 1D nanostructures have been discussed with special emphasis on their properties and applications. Besides these, the chapter also describes the physical principals and limitations of different techniques that are extensively used for the characterization of nanomaterials. More specifically it includes an elementary discussion of UV-visible Spectroscopy, Fourier Transform Infrared Spectroscopy, Raman Spectroscopy, Scanning Electron Microscopy, Transmission Electron Microscopy, X-ray Diffraction, Nuclear Magnetic Resonance Spectroscopy, Cyclic Voltammetry, Impedance Analysis and other electrochemical techniques. The complimentary aspects of these techniques clearly indicate that one or two techniques alone cannot provide reliable information. Hence, a judicious selection of a variety of techniques is important to provide reliable molecular level information.

In the **second chapter**, we demonstrate a completely new template-less approach of assembling 2-D networks of nanowires at room temperature by the agitation of Au nanoparticles in toluene-aqueous mixtures. These nanowires have a uniform diameter of ~5-7 nm consisting of coalesced face centered cubic (fcc) nanocrystals. In many cases, the networks fold into 3-D cage-like structures. It is proposed that Toluene molecules do passivate the Au surfaces via π-electron interactions during nanoparticle coalescence, rendering the nanowire surfaces hydrophobic, simultaneously enabling the transfer of the nanowires into the toluene layer. Similar methods can be used to obtain networks of Ag nanowires and the extension of similar strategies through the manipulation of solvent chemistry and convective conditions could offer potential ways to tailor the nanowire aspect ratio, lengths, orientations, and network connectivity. Changing the aromatic solvent alters the balance between nanoparticle coalescence and surface passivation rates, resulting in partially networked morphology. Such template-less, low-temperature assembly of mesostructures from nanoscale blocks would also open up new possibilities of using liquid mixtures to create a variety of architectures for

applications such as self-supporting nanocatalyst and sensing networks, nanowires for device interconnection, and porous high-strength nanofillers for composites.

The **third chapter** deals with a novel route for synthesizing custom designed superstructures of silver nanoparticles in one dimension using an organometallic chiral molecule as a source of silver. It has been previously shown that monodispersed silver nanoparticles can be synthesized using triethyl amine (TEA) as a capping as well as reducing agent necessitating only a single step In this chapter, we demonstrate the synthesis of silver nanowire architectures using silver dibenzoyl tartaric acid as a starting material and TEA as a reducing agent. Silver nanoparticles (3-5 nm) are generated using TEA while the chiral molecule plays an important role during the spatial confinement of these particles to form organized assemblies. Extensive analysis of these nanowires using different techniques including electrochemical characterization clearly shows their different electron transfer behavior compared to that of the nanoparticles. Thus we believe that the use of chiral molecules can offer a unique advantage in terms of a high degree of organization and ease of chemical modification.

Several reports are available on the generation of nanoparticles in non-aqueous media; however, the use of non-aqueous medium limits their utility in several biological applications. Hence considerable efforts have been expended in last few years to facilitate the successful preparation of *water-dispersible* nanoparticles. In the **fourth chapter**, accordingly, we demonstrate a simple, one step synthesis of *water-dispersible* silver nanoparticles and networks of nanowires at room temperature. The use of partially water-soluble triethyl amine helps to form a complex with aqueous silver ion and the control over the morphology can be achieved by varying the ratio of metal ion to the capping agent.

Chapter five deals with the study of solvent mediated electron transfer behavior of silver nanoclusters. The cyclic voltammetry and impedance study reveals the crucial role of solvent in guiding electron transfer properties of benzoic acid protected silver nanoclusters. The analysis suggests that the electron transfer properties of metal nanoclusters are governed by a judicious control of electrostatic interactions between solvent molecules and an electrical double layer of clusters which can be advantageously used to control the selectivity of reactions catalyzed by metal clusters.

In **chapter six** we present some selected applications of self-assembled monolayers and monolayer-protected nanoclusters. First, we reveal the experimental proof that silver compounds can accept or donate electron either from various co-reagents like α-diazoketone to form silver atoms that spontaneously grow into silver nanoclusters, presumably catalyzing the Wolff rearrangement of α-diazoketones. Secondly, we demonstrate the proof-of-concept of using self assembled molecular nanocathodes of aromatic thiol molecules such as diphenyl disulfide (DDS) as active elements for rechargeable Li^+-ion batteries. Potential advantages of this novel approach include high-surface area, facile fabrication and scalability, and high power-weight ratios. The presence of phenyl rings in a conjugate configuration in DDS provides a higher electrical conductivity than SAMs of thiol-terminated alkane chains. The spacing between individual molecules allows ion transfer pathways to the metallic substrate, similar to that reported in micro array electrodes. We also envision that the flexibility of phenyl rings would allow readjustment of molecular orientation in the SAMs, thereby facilitating Li^+ ion transport across the SAMs during the charge-discharge operations.

The **last chapter** (chapter seven) outlines a summary of all major conclusions of present studies suggesting the general principles of synthesis and characterizations of monolayer protected nanoclusters and one-dimensional nanostructures (nanowires). The future prospects of these materials are outlined in terms of their fundamental chemistry along with important and promising applications.

These results clearly suggest the benefits offered by the chemical routes to synthesize nanostructures, some in non-aqueous and some in aqueous medium enabling several applications of nanotechnology. Furthermore, the study of electron transfer properties of self assembled monolayers and monolayer protected clusters indicates their clear potential in applications in electrocatalysis and electrochemical power sources. Though, several methods have been proposed in this work to synthesize nanostructures, each method has its own limitations. For example, the Template-less nanowire synthesis limits their use in different solvents and often yields nanoparticles or partially grown nanowires in other solvents while the water dispersible nanowire synthesis suffers with low thermal stability and purity. Despite these limitations, these methods offer an elegant one step, template-less route to synthesize metal

nanoparticles and nanowires in moderate quantities and with well-controlled dimensions under favorable conditions. Besides the applications indicated above, such approaches are likely to find use in several other future nano electronic devices.

References

[1] Feynman, R. P. *There's Plenty of Room at the Bottom*. Sat. Rev. **1960**, *43*, 45.

[2] (a) *Societal Implications of Nanoscience and Nanotechnology*; Roco, M. C.; Bainbridge, W. S., Eds.; National Science Foundation Report: Arlington, VA, 2001 and also published by Kluwer Academic Publishers: Boston, MA, 2001. (b) http://www.nano.gov. (c) www.its.caltech.edu%7efeynman.html

[3] Moore, G. E. *Electronics* **1965**, *38*, 114.

[4] Regis, E.; Chimsky, M. *Nano: The Emerging Science of Nanotechnology*, Little, Brown & Co. ***1996***.

[5] Wilson, M.; Simmons, M.; Smith, G.; Kannangara, K. (Eds.) *Nanotechnology: Basic Science and Emerging Technologies,* CRC, **2002.**

[6] Nalwa, H. S. *Encyclopedia of Nanoscience and Nanotechnolog*y, ASP, (Ed.) **2003**.

[7] Bard, A. J. *Integrated Chemical Systems: A Chemical Approach to Nanotechnology*, Wiley, **1994.**

[8] Klabunde, K. J. *Nanoscale materials in chemistry*, Wiley, (Ed.) **2001.**

[9] Robinson, D.; Coombs, R. *Nanotechnology in Medicine and the Biosciences*, Gordon & Breach, (Ed.) **1996**.

[10] Hoch, H. C.; Jelinski, L. W.; Craighead, H. G. *Nanofabrication and Biosystems: Integrating Materials Science, Engineering, and Biology*, Cambridge University Press. (Eds.) **1996.**

[11] Freitas Jr.; R. A. Landes, *Nanomedicine, Bioscience,* **1999.**

[12] Mosznert, N. *Int. J. Nanotechnol*., **2004**, *1(1/2),*130.

[13] Hochella, M.F. *Earth Planet*. *Sci. Lett*., **2002,** *203*, 593.

[14] Bhushan, B. *Fundamentals of Tribology and Bridging the Gap between the Macro and Micro/Nanoscales*, Kluwer, (Ed.) **2001**.

[15] Edelstein, A. S.; Cammarata, R.C. *Nanomaterials: synthesis, properties, and applications,* IOP, (Eds.) **1998.**

[16] Hofmann, H.; Rahman, Z.; Schubert, U. *Nanostructured Materials*, Springer-Verlag. (Eds.) **2002.**

[17] DiNardo, N. J. *Nanoscale Characterization of Surfaces and Interface*, VCH, (Ed.) **1994**.

[18] Gardener, J. W.; Hingle, H.T. *From Instrumentation to Nanotechnology*, Gordon and Breach, (Eds.) **1991.**

[19] Wang, Z. L. *Characterization of Nanophase Material*s, Wiley, (Ed.) **2000.**

[20] Lieber, C.M. *Solid State Comm*., **1998,** *107*, 607.

[21] Huang, Y.; Duan, X.; Wei, Q.; Lieber, C.M. *Science*, **2001**, *291*, 630.

[22] Peng, X.; Manna, L.; Yang, W.; Wickham, J.; Scher, E.; Kadavanich, A.; Alivisatos, A. P. *Nature* **2000**, *404*, 59.

[23] Zarur, A. J.; Ying, J. Y. *Nature* **2000,** *403*, 65.

[24] Martin, C. R. *Chem. Mater*. **1996**, *8*, 1739.

[25] Xia, Y.; Rogers, J. A.; Paul, K. E.; Whitesides, G. M. *Chem. Rev*. **1999**, *99*, 1823.

[26] Liu, R.; Vertegel, A.; Bohannan, E. W.; Sorenson, T. A.; Switzer, J. A. *Chem. Mater*., **2001,** Vol. *13,* 508.

[27] Adachi, M.; Harada, T.; Harada, M.; *Langmuir*, **1999,** 15, 7097

[28] Kasuga, T.; Hiramatsu, M.; Hoson, A.; Sekino, T.; Niihara, K. *Langmuir* **1998**, *14*, 3160.

[29] Whangbo, M.-H.; and Koo, H.-J. *Solid State Comm*., **2000**, *115*, 675.

[30] El-Sayed, M. *Acc. Chem. Res*., **2001**, *34*, 258.

[31] Kerker, M. *J. Colloid Interface Sci.* **1985,** *105*, 297.

[32] (a) Faraday M. *Phil. Trans. R. Soc. London* **1857**,*147*, 145. (b) M.C. Daniel and D. Astruc, *Chem. Rev*. **2004**, *104*, 293.

[33] (a) Mie, G*. Ann. Phys.* **1908**, *25*, 329. (b) Mie, G. *Ann. Phys*. **1908,** *25,* 377.

[34] Creighton, J. A.; Eadon, D. G. *J. Chem. Soc., Faraday Trans*. **1991**, *87*, 3881.

[35] Mulvaney, P. *Langmuir* **1996**, *12*, 788.

[36] Ulman, A. *An Introduction to Ultrathin Organic Films*; Academic Press: Boston, **1991**.

[37] Ulman, A. *Chem. Rev*. **1996**, *96*, 1533.

[38] Bigelow, W. C.; Picket, D. L.; Zisman, W. P. *J. Coll. Inter. Sci*. **1946,** *1*, 513.

[39] Nuzzo, R. G.; Allara, D. L. *J. Am. Chem. Soc*. **1983**, *105*, 4481.

[40] Sagiva, J.; Taya, K. *J. Am. Chem. Soc*. **1980,** *102*, 92.

[41] Ogawa, H.; Chihera, T.; Taya, K. *J. Am. Chem. Soc.* **1985,** *107*, 1365.

[42] Kepley, L. J.; Crooks, R. M.; Ricco. A. J.; *Anal. Chem*. **1992,** 64, 3191.

[43] Yamamoto, Y.; Nishihara, H.; Aramaki. K. *J. Electrochem. Soc.* **1993,** *140*, 436.

[44] Häussling, L.; Michel, B.; Ringsdorf, H.; Rohrer. H. *Angew. Chem. Int. Ed. Eng.* **1991,** *30*, 569.

[45] Frostman, L. M.; Bader, M. M.; Ward. M. D. *Langmuir* **1994,** *10,* 576.

[46] Ball, P. *Designing the Molecular World*; Princeton University Press: Princeton, **1994**.

[46] Templeton, A. C.; Wuelfing, M. P.; Murray, R. W. *Acc. Chem. Res*. **2000**, 33, 27.

[47] Bain, C. D.; Troughton, E. B.; Tao, Y.; Evall, J.; Whitesides, G. M.; Nuzzo, R. G. **1989**. *J. Am*. Chem. Soc. *111*, 321.

[48] Jung, L. S.; Campbell, C.T. *Phys. Rev. Lett.* **2000**, *84*, 5164.

[49] Karpovich D. S.; Blanchard G. J. *Langmuir* **1994**, *10*, 3315. Schessler, H. M.; Karpovich D. S.; Blanchard, G.J. *J. Am. Chem. Soc*. **1996**, *118*, 9645.

[50] Brust, M.; Walker, M.; Bethell, D.; Schiffrin, D. J.; Whyman, R. *J. Chem. Soc. Chem. Commun.* **1994**, 801.

[51] Brust, M.; Fink, J.; Bethell, D.; Schiffrin, D. J.; Kiely, C. J. *J. Chem. Soc., Chem. Commun*. **1995**, 1655.

[52] Templeton, A. C. Hostetler, M. J.; Warmoth, E. K.; Chen, S. W.; Hartshorn, C. M.; Krishnamurthy, V. M.; Forbes, M. D. E.; Murray, R. W. *J. Am. Chem. Soc.* **1998**, *120*, 4845.

[53] Schmid G.; Corain B. *Eur. J. Inorg. Chem.* **2003**, *17*, 3081.

[54] Schmid G.; Lehnert A. *Angew. Chem. Int. Ed. Engl.* **1989,** *28,*780.

[55] Weare, W. W.; Reed, S. M.; Warner, M. G.; Hutchinson, J. E. *J. Am. Chem. Soc*. **2000**, *122*, 12890.

[56] Leff, D. V.; Brandt, L.; Heath J. R. *Langmuir* **1996**, *12*, 4723.

[57] Brust. M.; Stuhr-Hansen, N.; Norgaard, K.; Christensen, J. B.; Nielsen, L. K.; Bjornholm T. *Nano Lett.* **2001**, *1*,189.

[58] Yao H, Momozawa O, Hamatami T, Kimura K. *Chem. Mater*. **2001**, *13*, 4692.

[59] Corbierre, M. K, Cameron, N. S.; Sutton, M.; Mochrie, S. G. J.; Lurio, L. B.; *J. Am. Chem. Soc.* **2001**, *123,* 1041.

[60] Tan, Y.; Dai, X.; Li. Y.; Zhu, D.; *J. Mater. Chem.* **2003**, *13*, 1069.

[61] Heath, J. R.; Knobler, C. M.; Leff, D. V.; *J. Phys. Chem. B* **1997,** *101*, 189.

[62] Hostetle,r M. J.; Wingate, J. E.; Zhong, C. J.; Harris, J. E.; Vachet, R. W.; *Langmuir* **1998**,14, 30

[63] Leff, D. V.; Ohara, P. C.; Heath, J. R.; Gelbart, W. M. **1995**, *J. Phys. Chem. 99,* 7036.

[64] Zhu, T.; Vasilev, K.; Kreiter, M.; Mittler, S.; Knoll, W. *Langmuir* **2003**, *19,* 9518.

[65] Frens, G. *Nat. Phys. Sci.* **1973,** 241.

[66] Turkevich, J.; Stevenson, P. C.; Hillier, J. *Discuss. Faraday Soc.* **1951,** *11,* 55.

[67] Han, M. Y.; Quek, C. H.; Huang, W.; Chew, C. H.; Gan, L. M. *Chem. Mater.* **1999,** *11*, 1144.

[68] Dai, X.; Tan, Y.; Xu, J. *Langmuir* **2002,** *18*, 9010.

[69] Hu, J.; Odom, T. W.; Lieber, C. M. *Acc. Chem. Res*. **1999,** *32*, 435.

[70] *A special issue in MRS Bull*. **1999**, *24*, 20.

[71] Xia, Y.; Yang, P.; Sun, Y.; Mayers, B.; Gates, B.; Kim, F.; Yan, H. *Adv. Mater.* **2003**, *15*, 253.

[72] Martin, C. R. *Science*, **1994**, *266*, 1961.

[73] Martin, B. R.; Dermody, D. J.; Reiss, B. D.; Fang, M.; Lyon, L. A.; Natan, M. J.; Mallouk, T. E. *Adv. Mater*. **1999**, *11*, 1021.

[74] Zhang, Z.; Gekhtman, D.; Dresslhaus, M. S.; Ying, J. Y. *Chem. Mater*. **1999**, *11*, 1659.

[75] Han, Y. J.; Kim, J. M.; Stucky, G. D. *Chem. Mater*. **2000**, *12*, 2068.

[76] Huang, M. H.; Choudrey, A.; Yang, P. *Chem. Commun*, **2000**, 1063.

[77] Bhattacharyya, S.; Saha, S. K.; Chkravorty, D. *Appl. Phys. Lett*. **2000**, *77*, 3770.

[78] Ugarte, D.; Chatelain, A.; DeHeer, W. A. *Science* **1996**, *274*, 1897.

[79] Govindaraj, A.; Satishkumar, M.; Nath. M.; Rao, C. N. R. *Chem. Mater*. **2000**, *12*, 202

[80] Sloan, J.; Wright, D. M.; Woo,H.-G.; Bailey, S.; Brown, G.; York, A. P. E.; Coleman, K. S.; Hutchison, J. L.; Green, M. L. H. *Chem. Commun*. **1999**, 699.

[81] Zhang, D.; Qi, L.; Ma, J.; Cheng, H. *Chem. Mater*. **2001,** *13*, 2753.

[82] Braun, E.; Eichen, Y.; Sivan, U.; Ben-Yoseph, G. *Nature* **1998**, *391*, 775.

[83] Jiang, X.; Xie, Y.; Lu, J.; Zhu, L.; He, W.; Qian, Y. *J. Mater, Chem*. **2001**, *11*, 1775.

[84] Hong, B. H.; Bae, S. C.; Lee, C.-W.; Jeong, S.; Kim, K. S. *Science*, **2001**, *294*, 348.

[85] Song, H. H.; Jones, K. M.; Baski, A. A. *Sci, Technol. A* **1999**, *17*, 1696.

[86] Heywood, B. R.; Rajam, S.; Mann, S. *J. Chem. Soc., Faraday Trans*. **1991**, *87*, 735. [87] Wash, D.; Mann, S. *Nature* **1995,** *377*, 320.

[88] Hopwood, J. D.; Mann, S. *Chem. Mater*. **1997**, *9*, 1819.

[89] Rees, G. D.; Evans-Gowing, R.; Hammond, S. J.; Robinson, B. H. *Langmuir* **1999**, *15*, 1993.

[90] Filankembo, A.; Pileni, M. P. *J. Phys. Chem. B* **2000**, *104*, 5865.

[91] Gole, A.; Murphy, C. *J. Chem. Mater.* **2004**, *16(19)*, 3633.

[92] Gao, J.; Bender, C. M.; Murphy, C. J. *Langmuir* **2003**, *19*, 9065.

[93] Busbee, B. D.; Obare, S. O.; Murphy, C. J. *Adv. Mater*. **2003**, *15*, 414.

[94] Nikoobakht, B.; El-Sayed, M. A. *Chem. Mater*. **2003,** *15*, 1957.

[95] Sun, Y.; Mayers, B.; Herricks, T.; Xia, Y.; *Nano Lett*. **2003**, *3(7),* 955.

[96] Sun, Y.; Gates, B.; Mayers, B.; Xia, Y. *Nano Lett*. **2002**, *2*, 165.

[97] (a) Sun, Y.; Xia, Y. *Adv. Mater*. **2002**, *14*, 833. (b) Sun, Y.; Yin, Y.; Mayers, B. T.; Herricks, T.; Xia, Y. *Chem. Mater.* **2002,** *14*, 4736.

[98] Kim, F.; Connor, S.; Song, H.; Kuykendall, T.; Yang, P. *Angew. Chem. Int. Ed*. **2004**, *43,* 3673.

[99] (a) Giresig, M.; Pasoriza, I.; Liz-Marzan, L. *J. Mater. Chem*. **2004**, *14,* 607. (b) Santos, I. P.; Liz-Marzan, L. M. *Nano Lett*. **2002**, *2*, 903.

[100] Wei, G.; Nan, C.-W.; Deng, Y.; Lin, Y.-H. *Chem. Mater*. **2003**, *15(23)*, 4436.

[101] Caswell, K. K.; Bender, C. M.; Murphy, C. J. *Nano Lett*. **2003**, *3(5*), 667.

[102] Zhang, S.-H.; Jiang, Z.-Y.; Xie, Z.-X.; Xu, X.; Huang, R.-B.; Zheng, L.-S.;*J. Phys. Chem. B*. **2005**, *109(19),* 9416.

[103] Hu, J.-Q. Chen, Q. Xie, Z.-X. Han, G.-B. Wang, R.-H. Ren, B. Zhang, Y. Yang, Z.-L. Tian, Z.-Q. *Adv. Funct. Mater*. **2004**, *14*, 183.

[104] Xiong, Y.; Xie, Y.; Wu, C.; Yang, J.; Li, Z.; Xu F. *Adv. Mater*. **2003,** *15*, 405.

[105] Pei, L.; Mori, K.; Adachi, M. *Langmuir* **2004**, *20*, 7837.

[106] Yu, Y. Y.; Chang, S. S.; Lee, C. L.; Wang, C. R. C. *J. Phys. Chem. B* **1997**, *101*, 6661.

[107] Chang, S. S.; Shih, C. W.; Chen, C. D.; Lai, W. C.; Wang, C. R. C. *Langmuir* **1999**, *15*, 701.

[108] Choi, J.; Sauer, G.; Nielsch, K.; Wehrspohn, R. B.; Gosele, U. *Chem. Mater*. **2003**, *15(3)*, 776.

[109] Kim, F.; Song, J. H.; Yang, P.; *J. Am. Chem. Soc*. **2002**, *124(48),* 14316.

[110] Zhou, Y.; Yu, S. H.; Wang, C. Y.; Li, X. G.; Zhu, Y. R.; Chen, Z. Y.*Adv. Mater*. **1999**, *11*, 850.

[111] Henglein, A. *J. Phys. Chem*. **1993**, 97, 8457.

[112] Schmid, G. *Clusters and Colloids: From Theory to Application;* VCH: Weinheim, **1994.**

[113] Perenboom, J. A. A. J.; Wyder, P.; Meier, P. *Phys. Rev*. **1981**, 78,173.

[114] Hughes, A. E.; Jain, S. C.; *Adv. Phys*. **1979**, *28*, 717.

[115] Kreibig, U.; Vollmer, M. *Optical Properties of Metal Clusters*;Springer: Berlin, **1995**.

[116] Bohren, C. F.; Huffman, D. R. *Absorption and Scattering of Light by Small Particles*; Wiley: New York, **1983.**

[117] Papavassiliou, G. C. *Prog. Solid State Chem*. **1980,** *12*, 185.

[118] vd. Zande, B. M. I.; Bohmer, M. R.; Fokkink, L. G. J.; Schonenberger, C. *J. Phys. Chem. B* **1997**, *101*, 852.

[119] Foss, C. A.; Hornyak, G. L.; Tierney, M. J.; Martin, C. R. *J. Phys. Chem*. **1992**, *96*, 9001.

[120] Gans, R. *Form of Ultramicroscopic Particles of Silver*. *Ann. Phys*.**1915**, *47*, 270.

[121] Liu, D.; Gao, J.; Murphy, C. J.; Williams, C. T. *J. Phys. Chem. B*. **2004,** *108(34),* 12911.

[122] Schrader, B. *Infrared and Raman Spectroscopy*; Schrader, B. ed., VCH Publishers Inc.: New York, **1995**; Chapter 4.

[123] (a) Badia, A.; Demers, L.; Dickinson, L.; Morin, F. G.; Lennox, B.; Reven, L. *J. Am. Chem. Soc.* **1997**, *119*, 11104. (b) Badia, A.; Demers, L.; Cuccia, L.; Lennox, R. B. *J. Am. Chem. Soc.* **1997**, *119*, 2682.

[124] Bourg, M.-C.; Badia, A.; Lennox, R. B.*J. Phys. Chem. B*. **2000**, *104(28),* 6562.

[125] Bard, A.J. Faulkner, L. R. Electrochemical *Methods, Fundamentals and Applications*, (Ed) John Wiley And Sons, New York, **2001**.

[126] Chen, S.; Murray, R. W.; Feldberg, S. W. J. Phys. Chem. B **1998**, *102*, 9898.

[127] Chaki, N. K.; Sharma, J.; Mandale, A. B.; Mulla, I. S.; Pasricha, R.;Vijayamohanan, K. *Phys. Chem. Chem. Phys.* **2004**, *6*, 1304.

[128] Toimil Molares, M.E.; Balogh, A. G.; Chtanko, N.; Cornelius, T. W.; Neumann, R. *Adv. Mater*. **2001**,*13*, 62.

[129] Buffat, P.; Borel, J.-P. *Phys. Rev*. **1976,** *13*, 2287.

[130] Link, S.; Burda, C.; Mohamed, M. B.; Nikoobakht, B.; El-Sayed, M. A. *Phys. Rev.* **2000,** *61*, 6086.

[131] Marszalek, P. E.; Greenleaf, W. J.; Li, H.; Oberhauser, A. F.; Fermamdez, J. M. *PNAS* **2000**, *97*, 6282.

[132] Wu, B.; Heidelberg, A; Boland, J. J. *Nature Materials* **2005**, *4*, 525.

[133] Rubio-Bollinger, G.; Bahn, S. R.; Agralit, N.; Jacobsen, K. W.; Vieira, S. *Phys. Rev*. Lett. **2001**, *87*, 026101.

[134] Rubio, G.; Agrai¨t, N.; Vieira, S. *Phys. Rev. Lett*. **1996,** *76*, 2302.

[135] Stalder, A.; Du¨rig, U. *Appl. Phys. Lett*. **1996,** *68*, 637.

[136] Rodrigues, V.; Fuhrer, T.; Ugarte, D. *Phys. Rev. Lett*. **2000,** *85*, 4124.

[137] Gall, K.; Diao, J.; Dunn, M. L. *Nano Lett*. **2004**, *4*, 2431.

[138] El-Sayed, M. A. *Acc. Chem. Res*. **2001**, *34*, 257.

[139] Mohamed, M. B.; Volkov, V.; Link, S.; El-Sayed, M. A. *Chem. Phys. Lett*. **2000**, *317*, 517.

[140] Sun, Y.; Xia, Y. *Anal. Chem*. **2002**, *74*, 5297.

[141] Murphy, C. J. *Anal. Chem*. **2002**,*74(19)*, 520A.

[142] Yanson, A. I.; Bollinger, G. R.; van den Brom, Araot. N.; van Ruitenbeek, *Nature* **1998**, *395*, 783.

[143] van Houten, H.; Beenakker, C. *Phys. Today* **1996**, *3*, 22.

[144] Fujimoto, Y.; Hirose, K. *Nanotechnology* **2003,** *14*, 147.

[145] Costa-Kramer, J. L. *Physical Review B*. **1997**, *55(8),* 5416.

[146] Li, C.Z.; He, H. X.; Bogozi, A.; Bunch, J. S.; Tao, N. J. *Appl. Phys. Lett*. **2000**, *76,* 1333.

[147] Li, C. Z.; Sha, H.; Tao, N. J. *Phys. Rev. B* **1998**, *58,* 6775.

[148] (a) Walter, E.C.; Favier, F.; Penner R. M.; *Anal. Chem.* **2002,** *74,* 1546. (b) Favier, F.; Walter, E.; Zach, M.; Benter, T.; Penner, R. M. *Science* **2001,** *293,* 2227.

[149] Yen, J. H.; Leu, I. C.; Wu, M. T.; Lin, C. C.; Hon, M. H. *Diamond & Related Materials* **2005**, *14,* 841.

[150] Narayanan, R.; El-Sayed M. A. *J. Phys. Chem. B* **2005,** *109*, 12663.

CHAPTER II

Template-less assembly of gold and silver nanowires at room temperature

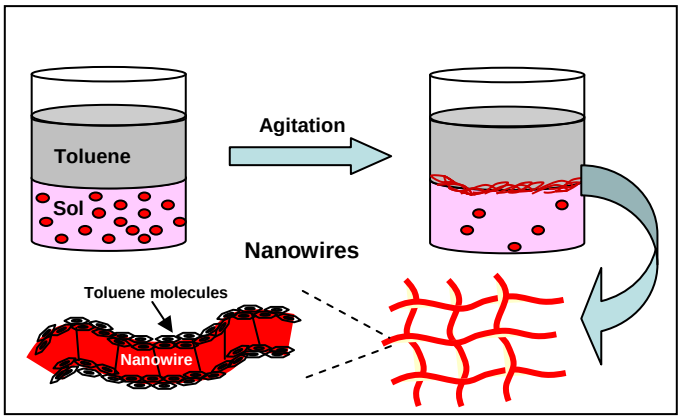

This chapter describes a new wet-chemical approach for assembling Au and Ag nanoparticles at room temperature into nanowire networks, without the use of lithographic templates. Five to 35 nm-diameter wires passivated with a thin organic layer were synthesized by mechanically agitating a biphasic liquid mixture of an aqueous hydrosol containing the nanoparticles and toluene. Nanowire structure and surface chemistry are discussed based on microscopy and spectroscopy techniques.

---

*A part of the work reported in this chapter has been published in **Chem. Commun**., 2004, 1435 and another part in **Langmuir**, 2004, 20, 5583.*

2.1 Introduction

Nanostructured materials having at least one dimension in the nano-size regime (1-100 nm) have attracted considerable attention recently from the standpoints of both fundamental science and technology [1-5] due to their conspicuous size and shape dependant physicochemical properties like thermal, mechanical, electronic, catalytic, and optical behaviour [6-11] facilitating their unique applications superior to that of bulk materials [12,13]. For most of these applications, the shape and size of nanostructures may represent the ultimate limit to the miniaturization of currently existing functional devices. Especially, one dimensional (1D) nanostructures (nanowires, nanotubes, nano-rods, nano-belts) provide a better system for the investigation of anisotropic confinement of electronic states and are attractive for their possible applications such as switches, sensors and both interconnects and active components in fabricating future nanoscale electronic and photonic devices [14,15]. In order to harness these applications, it is critical to synthesis 1D nanostructures (specifically nanowires) with well-defined sizes and configurations [16]. The sparse advancement in 1D nanostructures (in comparison with that of simple nanoparticles) has been mainly due to the difficulties associated with synthesis and fabrication of these nanostructures having controlled dimensions, morphology, phase purity and chemical composition.

Indeed, several synthetic strategies have been demonstrated during the last few years to synthesize metal nanowires with controllable size, shape and confinement. For instance, nanowire morphology and aspect ratio can be tailored using hard templates of mesoporous materials [17], zeolites [18], carbon nanotubes [19], steps or edges of solid substrates [20], or soft templates such as DNA chains [21], rod shaped micelles [22], and polymers [23]. As shown recently by Hsia et al., the use of silica shell templates ensures a good control over the morphology of silver nanowires with high yield [24]. Recently, Weizmann and co-workers [25] have generated Au nanowires using Telomer template (DNA based template). However, since template removal is often difficult, and may limit the use of such approaches in specific applications, there is significant interest in exploring template-less synthetic strategies. Consequently, there has been a great deal of recent activities to assemble nano-scale building blocks into larger scale

structures via template-less wet-chemical approaches due to the enormous process flexibility offered by these methods to controllably create a variety of architectures. For example, nanowires can now be synthesized using micelles [26] and from surfactant-stabilized biphasic microemulsions [27], stringing nanoparticles with molecular connectors [28], and room-temperature coalescence of molecularly-linked nanoparticles [29]. In addition, Sun et al. used an approach based on polyol process for the large-scale synthesis of uniform silver nanowires [30]. This method involves the reduction of silver nitrate using ethylene glycol in the presence of polyvinyl pyrollidone. However, this method needs high temperatures as high as 160 5°C, and yields mixtures of nanowires and particles. Electrochemical routes [31-33] such as arc discharge or electrodeposition have also been used to synthesize metal nanowires, but low yields, polycrystallinity and irregular morphologies are drawbacks that need to be circumvented. As a result, it is still desirable to develop a template-less, method capable of generating metal nanowires in moderate quantities and with well-controlled dimensions, crystallinity and morphology and purity under favorable conditions.

In this chapter, a completely new, template-less room-temperature approach of assembling 2-D networks of nanowires by the agitation of Au nanoparticles in toluene-aqueous mixtures has been demonstrated. The nanowires have a uniform diameter of ~5-7 nm, and consist of coalesced *fcc* nanocrystals. In many cases, the networks fold into 3-D cage-like structures. Toluene molecules passivate the Au surfaces via π-electron interactions during nanoparticle coalescence, rendering the nanowire surfaces hydrophobic and enabling the transfer of the nanowires into the toluene layer. Extensions of similar strategies through the manipulation of solvent chemistry and agitation conditions could offer potential ways to tailor the nanowire aspect ratio, lengths and orientations, and network connectivity. Changing the aromatic solvent alters the balance between nanoparticle coalescence and surface passivation rates, and results in partially networked morphologies. Such template-less low-temperature assembly of mesostructures from nanoscale blocks would open up new possibilities of using liquid mixtures to create a variety of architectures for applications such as self-supporting nanocatalyst networks, nanowires for device interconnection, novel fluid heat-transfer agents and porous high-strength nanofillers for composites.

2.2 Experimental section

2.2.1 Materials:

Hydrogen tetrachloroaurate ($HAuCl_4.3H_2O$), silver nitrate ($AgNO_3$), sodium borohydride ($NaBH_4$), potassium chloride (KCl) and toluene were obtained from Aldrich Co. and used as received. In all the experiments, deionized water from a Milli-Q system was used.

2.2.2 Synthesis of nanowires:

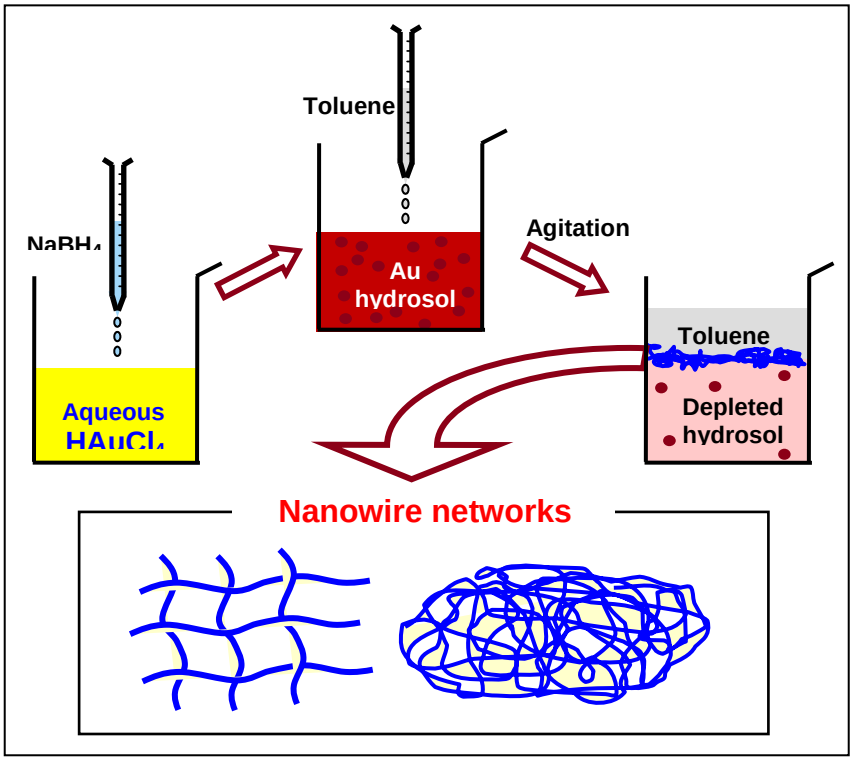

Scheme 2.1*The synthetic scheme to form nanowire networks at room temperature. The reduction of a $HAuCl_4$ aqueous solution (pale yellow) with $NaBH_4$ results in a wine red colored colloidal gold solution. The Au hydrosol is then mixed with toluene and agitated leading to the spontaneous formation of black-colored nanowire networks (depicted here in blue for clarity) at the aqueous/toluene interface.*

Scheme 2.1 shows a schematic representation of the method for forming gold nanowires. Hydrosols of Au and Ag were synthesized by reducing 500 ml of 1 mM of chloroauric acid ($HAuCl_4$) and silver nitrate ($AgNO_3$) solutions, respectively, with 7.4 mM sodium borohydride ($NaBH_4$), added drop-by-drop over 1 hour at 5 °C. No organic capping agents were used, unlike conventional synthesis methods [35] where short molecules (e.g., octanethiol) or polymers are added to transfer metal ions into an organic solvent layer prior to reduction. The initially pale yellow solution was transformed into a wine red (Au) and dark brown (Ag) coloured solutions respectively due to the formation of nanoparticles. The strong surface plasmon peak at 518 nm for Au and 420 nm for Ag hydrosols indicates an average size of ~5 nm which was independently confirmed from the TEM image of gold nanoparticles as shown in figure 2.3. The hydrosol was mixed with toluene in a 1:2 ratio. Vigorous agitation of this mixture (e.g., with a magnetic stirrer at 600 rpm for 10 min) depleted the nanoparticles from the aqueous layer, and resulted in the spontaneous formation of black-colored agglomerates that migrated to the toluene-water interface (see scheme 2.1).

2.2.3 Characterization:

These nanowires were characterized with various techniques such as scanning electron microscopy (SEM), transmission electron microscopy (TEM), UV-vis spectroscopy, Fourier transform infrared (FTIR) spectroscopy, thermogravimetric analysis (TGA), surface enhanced Raman scattering spectroscopy (SERS) and cyclic voltammetry (CV).

SEM measurements were carried out in a JEOL JSM-6330F microscope equipped with a field emission gun operated at 5 keV. Samples for TEM analysis were prepared by lifting the nanowire at the water-toluene interface on carbon-coated copper TEM grids and allowed to dry prior to measurement. TEM measurements were carried out in a CM12 microscope operated at an accelerating voltage of 120 kV. Lattice resolution images of the nanowires were obtained in a JEOL 2010 instrument operated at 200 kV.

UV-Vis spectroscopy measurements of all the samples were performed in a Varian Cary 500 Scan UV-Vis-NIR spectrophotometer operated at a resolution of 2 nm.

FTIR measurements of the gold nanowire were carried out on a Perkin-Elmer, Paragon 1000 spectrometer in the transmission mode at an 80° incident beam angle to the surface normal. To understand the strength of interaction of toluene with the nanowire, we carried out TGA measurements using a Mettler Toledo TGA/SDTA851e instrument by heating the nanowire samples from room temperature to 900°C at 10 °C/min under 50 mL/min N_2 flow. XPS measurements were performed using a VG Scientific ESCA LAB Mk II spectrometer, which was operated at a pressure better than 10^{-9} Torr using a monochromatic Mg Kα source (*hv* = 1253.6 eV). All regions, viz. C 1s, Ag 3d and Au 4f were measured with 50 eV pass energy. The spectra have been background corrected using the Shirley algorithm prior to curve resolution and core levels were aligned with respect to the C 1s B. E. of 285 eV. The gold nanowires were also characterized by micro-Raman spectroscopy using a Renishaw S 2000 Raman spectroscope with a 514.5 nm argon ion laser. CV measurements were carried out on a Autolab PGSTAT30 (ECO CHEMIE) instrument in an oxygen-free atmosphere using a three-electrode cell comprised of a Pt wire working electrode, a large-area platinum flag counter electrode, and Ag/Ag^+ reference electrode in 0.1 M KCl as the supporting electrolyte.

2.3 Results and discussion

2.3.1 Scanning electron microscopy and optical microscopy results*:*

Figure 2.1 shows scanning electron microscopy (A) and optical microscopy images (B) for gold nanowires. It is evident from the SEM image that porous networks of nanowires are formed at the toluene-water interface having a uniform diameter and different lengths, unlike the dispersed nanowires. The pores are of the dimensions 100-1000 nm. Also several folds are observed in the nanowire networks, which may grow into cocoon shaped nanostructures.

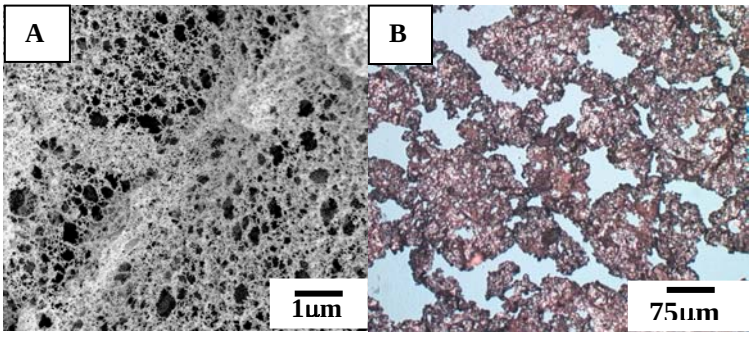

Figure 2.1 *Scanning electron (A) and optical micrograph (B) of gold nanowires*

2.3.2 Transmission electron microscopy results:

Figure 2.2 shows a Transmission electron micrograph of typical gold nanoparticles synthesized by the reduction of a $HAuCl_4$ aqueous solution (pale yellow) with $NaBH_4$ having an average particle size of 5-7 nm.

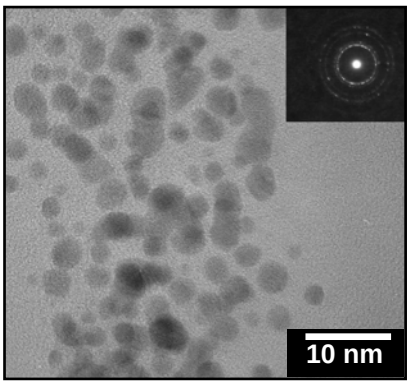

Figure 2.2 *Transmission electron micrograph of gold nanoparticles. Inset shows corresponding electron diffraction pattern of gold nanoparticles.*

Transmission electron microscopy (TEM) images in figure 2.3 reveal that the agglomerated structures at the toluene-water interface are 2-D networks of gold nanowires with a uniform diameter of ~ 5 nm (Figures 2.3a and 2.3b). In many cases, the 2-D networks fold into cocoon-shaped 3-D cage-like structures (Figure 2.3c) of sizes between 100s of nm to several 100 μm. Electron diffraction patterns (e.g., Figure 2.3d) indicate that the nanowires are comprised of coalesced *fcc* nanocrystals. Figure 2.3e shows a high-resolution lattice image of a single nanowire consisting of randomly oriented grains whose average diameter is identical to that of the nanoparticles in the hydrosol. The grain boundaries are at a 90° (±20°) angle to the nanowire axis (see

arrows in Figure 2.3e) and do not show significant curvature, indicating that the nanowires are not merely linear aggregates of nanoparticles, but are melded through particle impingement and coalescence.

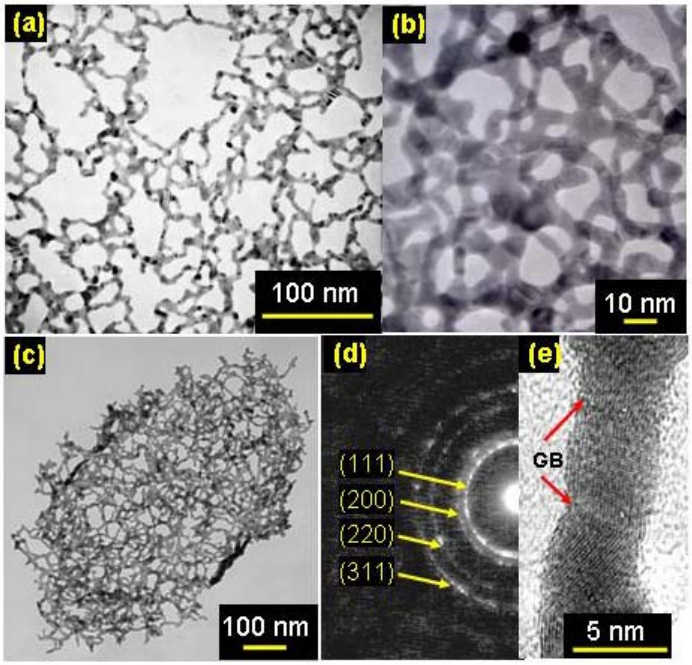

Figure 2.3 *Representative TEM micrographs and diffraction pattern obtained from gold nanowire networks dispersed on a carbon-coated TEM grid, in a CM 12 microscope operated at 120 kV. (a) A 2-D network of nanowires, (b) a higher magnification view from a different area, (c) a cocoon-shaped 3-D nano-cage comprised of interwoven Au nanowires, and (d) a selected-area electron diffraction pattern. (e) A lattice-resolution image of a single polycrystalline nanowire obtained in a JEOL 2010 instrument operated at 200 kV. Red arrows point to grain boundaries (GB).*

Once the agitation of the hydrosol-toluene mixture is stopped, the nanowire networks migrate to the toluene-water interface rather than sinking to the bottom of the aqueous layer, indicating the hydrophobic passivation of the nanowire surfaces. In contrast, agitating the hydrosol *without* toluene results in aggregated structures whose smallest feature sizes of ~0.5-1 μm are more than 1000-fold larger than that of the nanowires which precipitate to the container bottom in a lump. These aggregates also take 100-fold larger time frames (e.g., >10 hours) to form compared to that taken for nanowires (~5-15 minutes) to form from toluene-hydrosol mixtures, suggesting the participation of toluene in nanowire formation and passivation.

Representative bright field transmission electron (TEM) micrographs in figure 2.4 show the evolution of silver nanostructures from quasi-zero-dimensional (0-D) to 1-D morphology, which co-relate well with our UV-visible spectroscopy results. Figure 2.4(a) shows as-prepared poly-dispersed and quasi-spherical silver nanoparticles with an average size of ~6 nm. Upon agitation in toluene, slightly larger nanoparticles are seen along with few twinned particles as shown in figure 2.4(b).

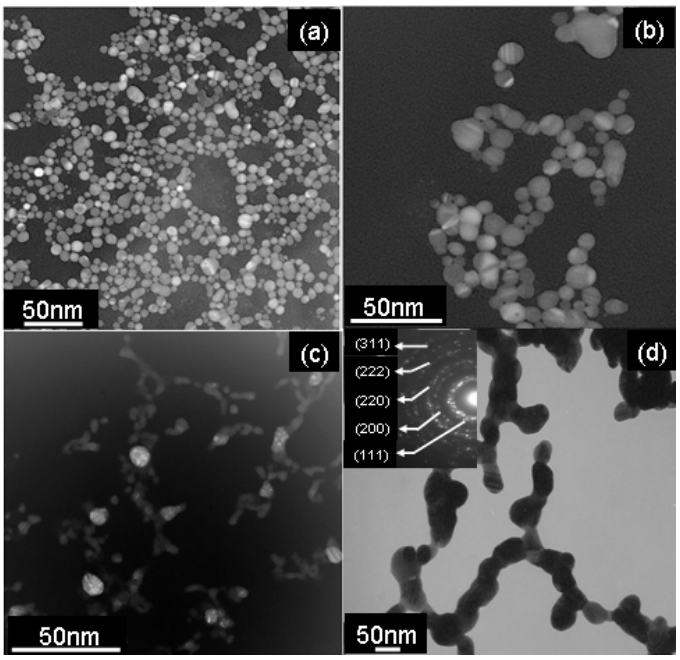

Figure 2.4 *Representative TEM micrographs and diffraction pattern obtained from silver nanowire networks dispersed on a carbon-coated TEM grid, in a CM 12 microscope operated at 120 kV. (a) A 2-D network of nanowires synthesized by the agitation of a mixture of toluene and Ag hydrosol, (b) a higher magnification view from a different area, (c) a selected-area electron diffraction pattern.*

Twinned nanostructures are favored due to the resultant surface energy minimization. These twin boundaries may also serve to attract other silver atoms to diffuse towards its vicinity during agitation. Figure 2.4(c) shows a mixture of nanoparticles, and nanowires having the same diameter as that of nanoparticles. Figure 2.4(d) shows the completely grown network of silver nanowires of ~35 nm diameter, with a standard deviation of ~5 nm.

A representative diffraction pattern (inset figure 2.4d) obtained from an individual silver nanowire is also shown for comparison. Analysis of this pattern indicates that each silver nanowire is not a single crystal because the diffraction rings/spots, arise from multiple crystals, and can be indexed as (111), (200), (220), (311) and (222) reflections respectively corresponding to cubic structure of silver [35].

2.3.3 UV-Visible Spectroscopy results*:*

The above results and inferences are consistent with the features of UV-visible spectra obtained from the hydrosols before and after nanowire formation (Figure 2.5a).

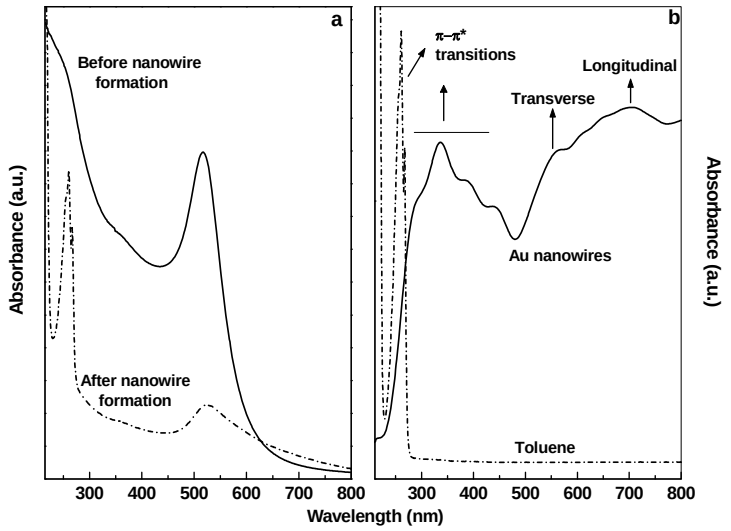

Figure 2.5 *UV-Visible absorption spectra from (a) gold hydrosols before and after vigorous agitation with toluene, and (b) gold nanowires drop coated on a quartz slide after vigorous washing with de-ionized water and drying in N_2.*

The strong surface plasmon peak at 518 nm in as-prepared hydrosols indicates an average nanoparticle size of ~5 nm [4]. Remnant hydrosols after nanowire formation (and removal) show a significantly lower intensity plasmon peak, which extends towards higher wavelengths due to nanoparticle depletion and coalescence. The additional peak observed at ~260 nm (with a shoulder at ~270 nm) is due to π-π^* transitions in toluene dissolved in the hydrosol during agitation. Spectrum obtained from the gold nanowires (Figure 2.5b) (vigorously washed in de-ionized water and dried in N_2) shows very broad plasmon band with additional peaks in the 600-800 nm range [36] arising from the

longitudinal component due to aspect-ratio increase [37]. The merging of this peak with the transverse component in the range 580-640 nm is likely due to interconnected nanowires of different lengths, unlike those previously reported for well-dispersed nanowires [38]. We attribute the 230-480 nm range peaks with a maximum at ~350 nm to the π-π^* transitions of adsorbed toluene. The red shift in these peaks (~75 nm) with respect to corresponding 260 nm peak seen in pure toluene suggests strong binding interaction between toluene and gold.

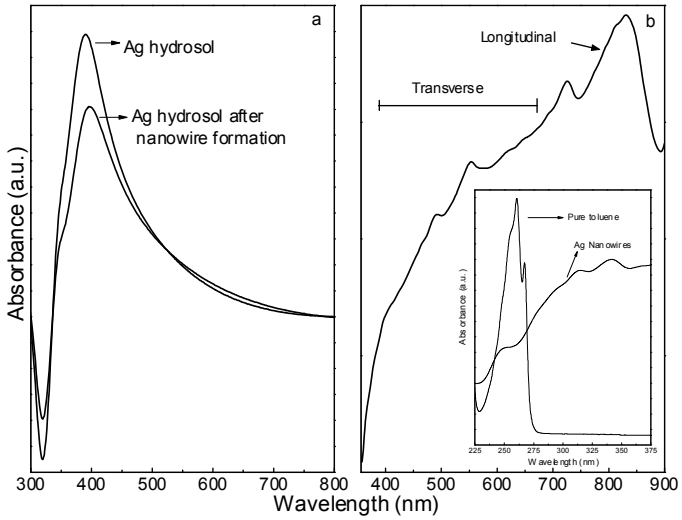

Figure 2.6 *UV-Visible absorption spectra of (a) silver hydrosols before and after vigorous agitation with toluene and (b) silver nanowires (vigorously washed with de-ionized water and dried in N_2) coated on a quartz slide. Inset shows superimposed UV spectra of Ag nanowires and pure toluene in the range 300 to 350 nm.*

Figure 2.6a shows the UV-Visible spectra of the Ag hydrosol before and after agitation in toluene. Spectra obtained from hydrosols prior to agitation exhibit a strong surface-plasmon resonance peak at 389 nm with a shoulder at 350 nm indicating the formation of nanometer-sized silver particles [39]. The broad full width at half maximum (FWHM) of ~70 nm with a tail stretching over 800 nm indicates polydispersity [Figure 2.6(a)]. Upon the agitation of the hydrosol in toluene, the nanoparticle size increases, as seen from the shifting of the surface plasmon peak to 406 nm. The decrease in the peak intensity is seen due to nanoparticle depletion from the hydrosol and formation of nanowire at liquid-liquid interface. The silver nanowires formed by nanoparticle agitation show characteristic absorption signatures in UV-visible region (Figure 2.6b). The broad

bands in the 350-700 nm range, and the 750 to 900 nm range, are due to transverse and longitudinal surface plasmon modes, respectively [39]. Inset in Figure 2.6b shows the UV-Vis spectrum of nanowires superimposed on that obtained from pure toluene. The nanowires also show broad low-intensity peaks due to π-π^* transitions characteristic of toluene, suggesting that toluene molecules are adsorbed on the nanowires surface via π-cation interactions. The proposed π-cation interactions are consistent with the observed slight red shift of the π-π^* signatures in the nanowires, when compared to the corresponding peaks in pure toluene.

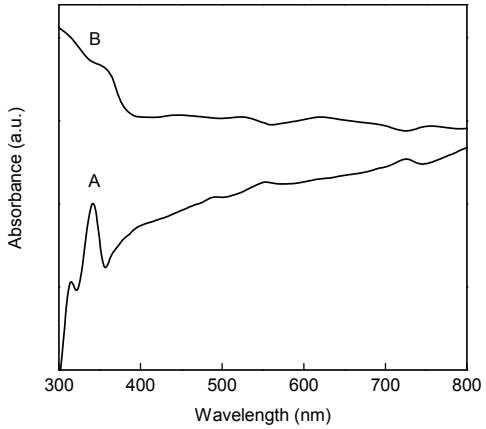

Figure 2.7 *The comparison of UV-visible spectra of silver nanowires (A) before and (B) after annealing to 300 ^{0}C in the range 300-800 nm. The spectra were obtained using a Varian Cary 500 Scan UV-VIS-NIR spectrophotometer*

The above results, and the interpretation, are confirmed by the absence of the π-π^* signatures in nanowires samples annealed to 300 ^{0}C. Figure 2.7 shows the comparison of UV-Visible spectra of silver nanowires before (2.7A) and after annealing (2.7B) to 300 ^{0}C. The UV features associated with the π-π^* signatures in silver nanowires before annealing (peak at 370 nm) are absent in the annealed sample while the surface plasmon peaks are seen even after annealing. The red-shift of the surface plasmon peaks is likely due to the agglomeration of nanowires after the desorption of toluene.

2.3.4 Fourier Transform Infrared Spectroscopy*:*

FTIR spectra obtained from the 'as-prepared' nanowires networks, after vigorous washing and sonication in de-ionized water and drying in N_2, confirm toluene passivation on the nanowires surfaces (see Figure 2.8).

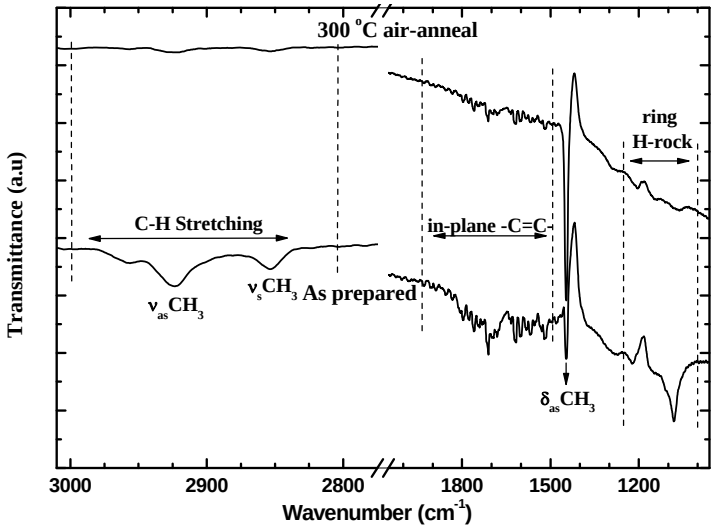

Figure 2.8 *FTIR spectra obtained from nanowires networks before and after air-annealing at 300 ^{0}C in air for 1 hour. The spectra were obtained in a Perkin Elmer, Paragon 1000 spectrometer operated in the transmittance mode at an 80^0 incident beam angle to the surface normal.*

The *in-plane* skeletal –C=C- stretching modes and their overtones in the ~1480-1945 cm^{-1} range [40] and ring hydrogen rocking modes between ~1000 and 1250 cm^{-1} are typical of aromatic hydrocarbons. The C-H deformation mode [41] at ~1445 cm^{-1} (δ_{as} CH_3), and C-H stretching vibrations (ν_s and ν_{as} CH_3) between 2800-3000 cm^{-1}, also support the presence of toluene.

The relatively low-intensity of the skeletal modes observed in the nanowires, compared to that of pure toluene, suggests toluene immobilization on Au nanowires via π-electron interactions. The *in-plane* –C=C– and C-H stretch modes, and ring hydrogen rocking vibrations either strongly diminish in intensity or entirely disappear upon annealing the nanowires in air for 1 hour at 300 ^{0}C due to toluene desorption. The annealed nanowires, however, show an increase in the C-H deformation mode intensity,

which is most likely due to aliphatic hydrocarbon residue formed through toluene decomposition on the nanowires surface.

Similarly, in case of silver nanowires the *in-plane* skeletal –C=C- stretching modes in the ~1400-1800 cm^{-1} range and ring hydrogen rocking modes between ~1000 and 1250 cm^{-1}, are typical of aromatic hydrocarbons (Figure 2.9). The presence of C-H stretching vibrations (ν_s and ν_{as} CH_3) between 2800-3000 cm^{-1}, also support the presence of toluene [42,43].

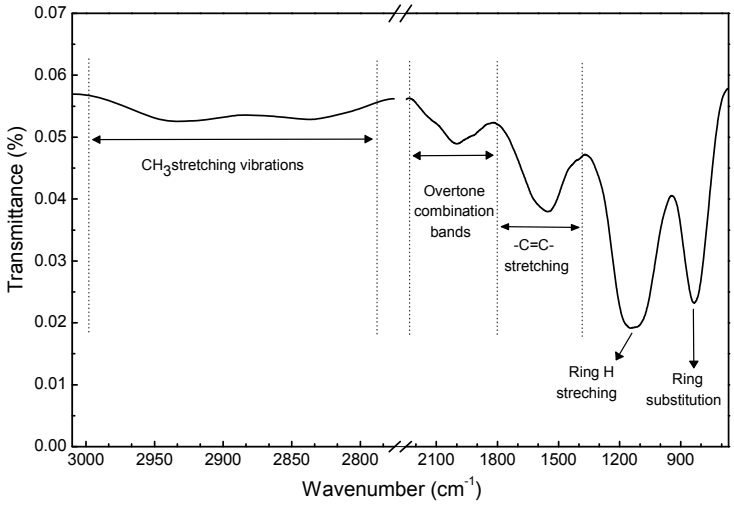

Figure 2.9 *FTIR spectra obtained from Ag nanowire networks.*

The relatively low-intensity of the skeletal modes observed in the nanowires, compared to that of pure toluene, suggests toluene immobilization on the metal surface via π-electron interactions.

2.3.5 Thermogravimetric analysis*:*

Toluene desorption and decomposition during annealing are corroborated by TGA mass loss characteristics of the gold nanowires (see Figure 2.10), which are similar to desorption of chemisorbed anthracene and benzene on gold [44]. The onset of mass loss at ~110 ^{0}C close to the boiling point of toluene is due to vaporization of toluene. The total 4.6 wt % loss between 110 to 765 ^{0}C corresponds to desorption/decomposition of chemisorbed toluene.

Similarly silver nanowires show a 3.6 wt % mass loss between 110 and 639 ^{0}C. Two steps have been seen, first step of wt loss is consistent with desorption of physisorbed toluene from the Ag nanowires while the second step in the range 500-600 ^{0}C is probably due to desorption of chemisorbed molecules or small sized nanoparticles. The thermogravimetric results indicate that the approximate toluene-to-Au ratio is 1:10 while the toluene-to-Ag ratio is 1:22. The variation in the ratios for gold and silver concurs with the fact that greater diameter nanowires are seen in case of silver.

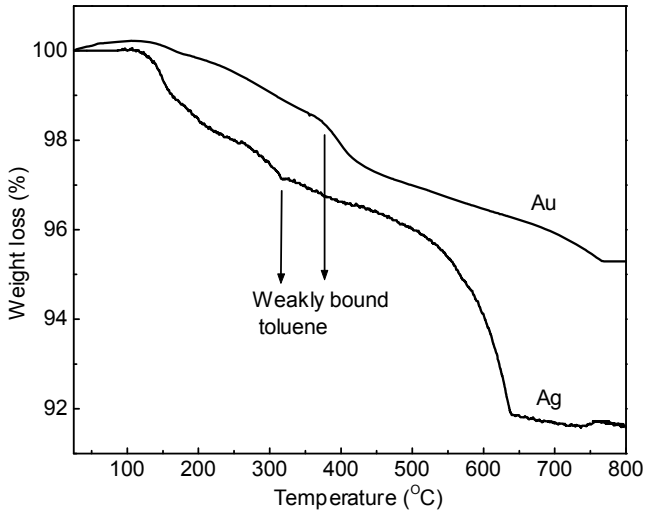

Figure 2.10 *Mass loss characteristics of Au and Ag nanowires obtained by TGA in a Mettler Toledo TGA/SDTA851^e instrument during heating from room temperature to 800 ^{0}C at 10 ^{0}C/min under 50 mL/min N_2.*

2.3.6 Transmission electron microscopy analysis:

Surface depassivation by toluene removal during annealing is accompanied by the coarsening of the nanowires as seen from TEM micrographs (see Figure 2.11), which show that the average diameter of annealed nanowires is nearly 65 % higher than that of the as-prepared ones. Simultaneous coarsening of nanowires and surface depassivation indicates that adsorbed organic molecules on the nanoparticle surfaces inhibit nanoparticle coalescence.

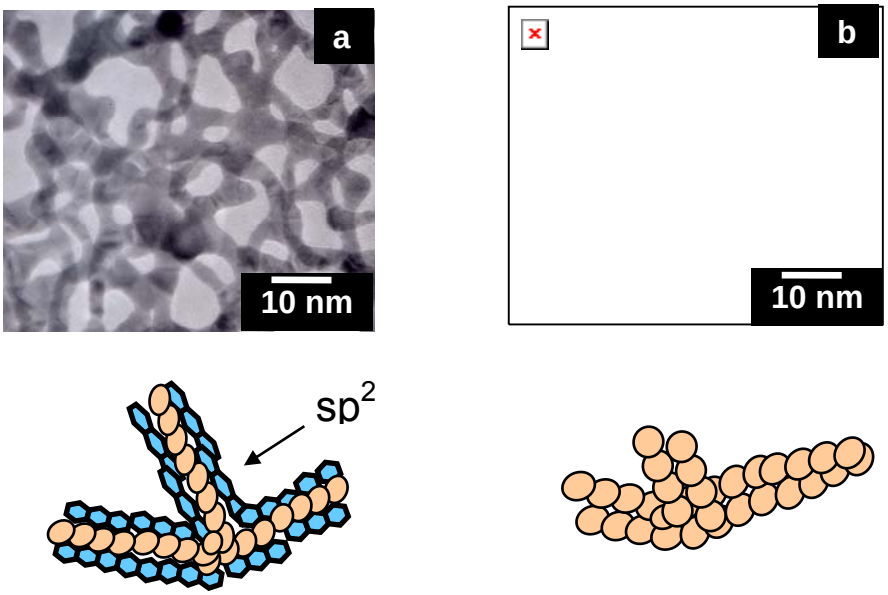

Figure 2.11 *Bright field TEM micrographs from Au nanowires networks obtained (a) in the as-prepared state, and (b) after annealing the same sample-containing grid at 300 ℃ for 1 hour in air with corresponding schematic representation.*

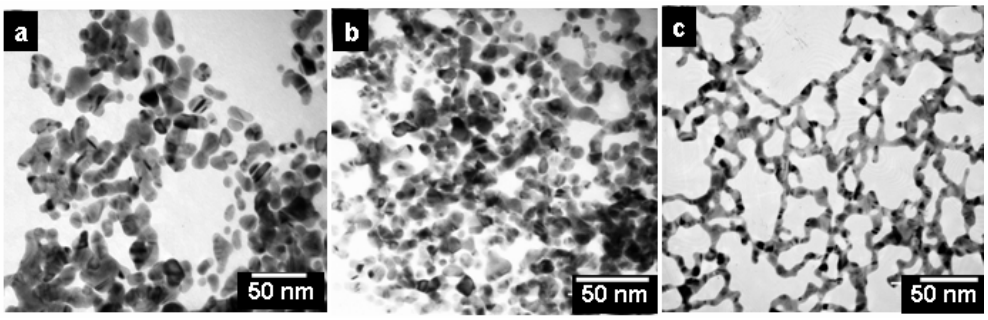

Figure 2.12 *Bright-field TEM images obtained from Au nanostructures synthesized by agitation of 5-nm-dia nanoparticles in (a) benzene, and (b) xylene. In both cases, partially networked structures are formed and transferred to the organic-aqueous interface. Note that the average sizes of both the structures are larger than the average diameter of nanowires (see Figure 2.3) synthesized with toluene from 5-nm-dia nanoparticles.*

Replacing toluene with benzene or xylene in our synthesis process results in partially-networked nanowires and agglomerated nanoparticles in the ~5-20 nm size range (e.g., Figure 2.12). These partially coalesced structures were transferred to the

organic layer, indicating hydrophobic surface passivation as in the toluene case. The morphology of the coalesced nanoparticles is determined by the relative rates of nanoparticle impingement and surface passivation. The microstructure formed in toluene-aqueous mixtures suggests nanoparticle diffusion-limited impingement with a sticking probability close to unity, and coalescence at a rate slightly faster than the rate of surface passivation by toluene.

Lower coalescence rates result in partially networked structures such as that obtained in the case of benzene and xylene. This is consistent with higher viscosity of both these liquids (0.65 and 0.81 cP, respectively) compared to that of toluene (0.59 cP) [45][Table 2.1]. If surface passivation is very slow or absent (e.g., in an extreme case where there is no toluene), we would observe a coarse morphology as described earlier.

Table 2.1 *A comparison of important parameters such as polarity, solubility, surface tension and viscosity data for different solvents, governing nanowires growth*

Solvent	Log P* (polarity)	Solubility in H_2O (mM @ 25^0C)	Surface tension (dynes/cm)	Viscosity (cP)
Toluene	2.69	5.5	28.53	0.59
Xylene	3.2	1.7	30.03	0.81
Benzene	2.13	22.8	28.00	0.654
Water	-	-	72.80	1

P* is measured as the electric dipole moment of a solvent

Agitation of gold nanoparticles synthesized from $HAuCl_4$ reduction by sodium citrate ($C_6H_8O_7Na$) instead of $NaBH_4$ does not result in any observable nanoparticle coalescence or nanowires formation. This is confirmed by identical UV-visible spectra obtained from citrate-reduced hydrosols before and after agitation. Perhaps, the strong binding of $C_6H_8O_7^-$ ions to the nanoparticle surface [46] inhibits nanoparticle coalescence and toluene passivation.

2.3.7 Surface-enhanced Raman scattering spectroscopic analysis (SERS)*:*

The Raman spectra of 'as prepared' gold nanowires, before and after annealing at 200 and 300 ^{o}C in the crystalline (powder) state are shown in figure 2.13.

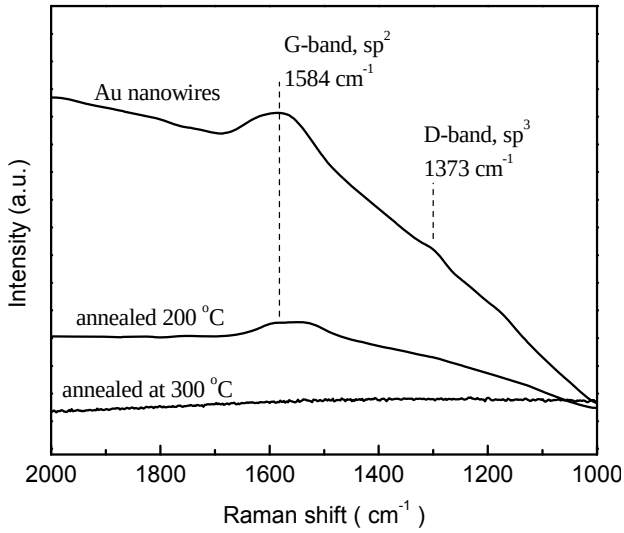

Figure 2.13 *Raman spectra of as prepared gold nanowires, and after annealing at 200 and 300 ^{0}C respectively.*

The 1150-1600 cm^{-1} region of the Raman spectra is dominated by skeletal vibrations of the C-C stretching modes and C-CH_3 symmetric bending modes, CH_2 rocking modes which are all sensitive to the conformation of hydrocarbon chain. The assignments to the bands in the 1100-1600 cm^{-1} are well established and have been used to probe the lateral chain interaction and conformational disorder. The SER spectrum for the 'as prepared' gold nanowires sample (Figure 2.13) shows the relatively high intensity for the 1584 cm^{-1} and low intensity peak at 1373 cm^{-1}. This is about 3 times as intense as the band for the 200 ^{0}C annealed sample. However, on annealing the sample to 300 ^{0}C, this bands losses the intensity. Thus, we can conclude from the SER spectra of gold nanowires before and after annealing that the CH_2 rocking modes and C-CH_3 symmetric bending modes originate from the toluene molecules. Further comparison of the band intensities with the annealed samples confirms a Raman process from the molecules of toluene adsorbed at the nanowires surface.

2.3.8 X-ray photoelectron spectroscopic analysis*:*

XP spectra were taken for both gold and silver nanowires in order to support toluene encapsulation. The nanowires were drop casted in the form of a film onto a Si(111) substrate and analyzed by XPS. The general scan spectrum of the nanowires showed the strong C 1s, Ag 3d and Au 4f core level signals with no evidence of

impurities. The Au 4f and Ag 3d core levels were recorded from the Au and Ag nanowires as shown in figure 2.14.

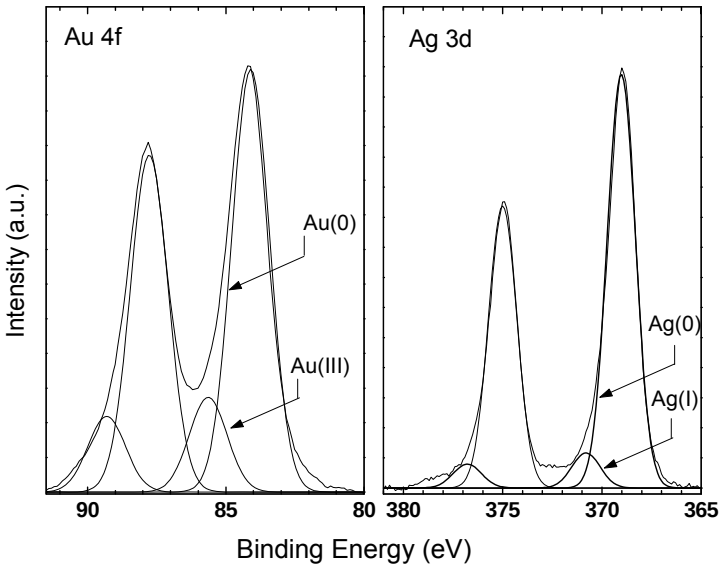

Figure 2.14 *Core level spectra from nanowires dispersed on a Si substrate. The higher energy sub-bands correspond to Au(III) and Ag(I) states. The spectra were obtained using a PHI 5400 instrument with a Mg* K_α *probe them.*

Au 4f high-energy component is obtained with sub-bands centered at 85.6 eV [44]. Ag 3d core level spectrum could be deconvoluted into two chemically distinct spin-spin pairs and binding energy of two chemically distinct Ag $3d_{5/2}$ components at 368 and 370 eV respectively [47]. The low BE component is attributed to electron emission from the silver metal nanocore while the high BE component arises from the silver ions. Passivation via borates or chloride formation is unlikely because neither B nor Cl was detected by XPS.

Also the electrochemical measurements were carried out to understand the surface chemistry and mechanism of formation of nanowire networks.

2.3.9 Cyclic voltammetric measurements*:*

In order to understand the role of toluene in the nanowire formation, electrochemical measurements were carried out using cyclic voltammetry. The cyclic

voltammogram of Auric chloride (Figure 2.15a) exhibits a well-defined redox behavior, with a cathodic peak at +0.5 V and anodic peak at +1.1 V respectively and the other couple appears (shown in inset of Figure 2.15) at the –0.58 V (cathodic) and -0.4 V (anodic) respectively. There is an asymmetry in the peaks and anodic peak currents are significantly larger. In the cathodic scan, Au reductive adsorption ($Au^{+} \rightarrow Au^{0}$) may occur while the anodic process is complex due to the presence of different charged species such as Au^{III} and Au^{I} [48,49].

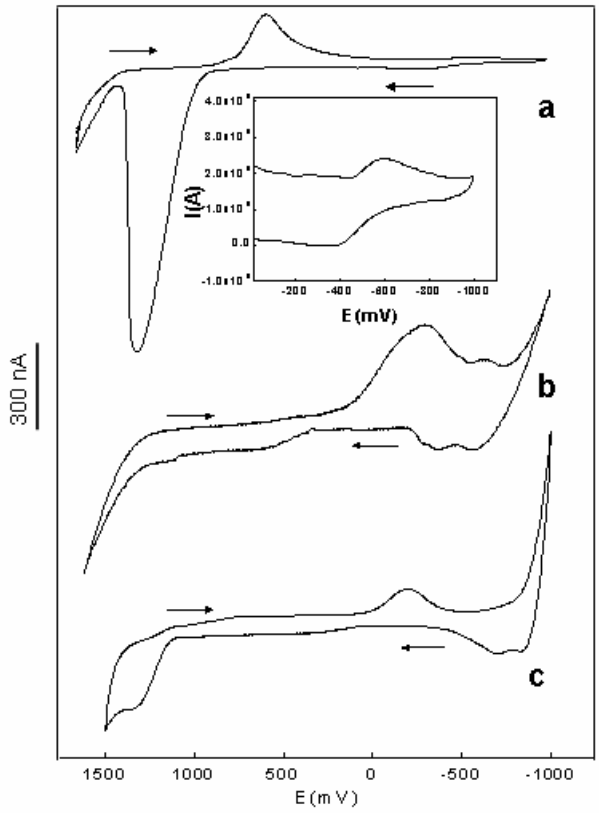

Figure 2.15 *Cyclic voltammograms of Auric chloride solution (a), gold hydrosol solution before nanowires formation (b), and gold hydrosol after nanowires formation(c) acquired at a scan rate 100 mV.cm^{-2} using a Pt working electrode, Pt flag counter electrode, and Ag/Ag^{+} reference electrode, in 0.1 M aqueous KCl. Arrow indicates the direction of the scan. Inset of fig. 2.15 gives the magnified CV of second couple obtained in auric chloride*

Figure 2.15b shows the cyclic voltammogram of the Au hydrosol before nanowire formation at 100 mV scan rate. In sharp contrast to above voltammogram (Figure 2.15a), the cathodic and anodic peaks appear in totally different potential range. The cathodic

peaks appear at -0.25 V, -0.65 V and anodic peaks appear at –0.6 V and –0.3 V respectively. The charge transfer process seen may be due to the presence of $AuCl^-_2$ species adsorbed on the nanoparticle surface. Also the presence of –OH species in the hydrosol due to the reduction of Au salt with sodium borohydride may slightly change the redox potentials of the Au species. Figure 2.15c shows cyclic voltammogram of Au hydrosol after the nanowires formation using the same electrochemical system. The figure shows two redox couples. The first couple arises with the cathodic peak at +0.7 V and anodic peak at +1.3 V respectively and the other couple is seen with cathodic peak at +0.2 V and anodic peak at –0.65 V. Furthermore, the first couple shows characteristics similar to that presented in figure 2.15a while the second couple shows the electrochemical behavior as presented in figure 2.15b. This interesting reappearance of the former redox couple as seen in gold chloride solution (Figure 2.15a) and presence of the other couple as seen in the hydrosol before nanowires formation (Figure 2.16b), suggests that the species present in gold chloride solution reappear in the hydrosol solution after the nanowire formation.

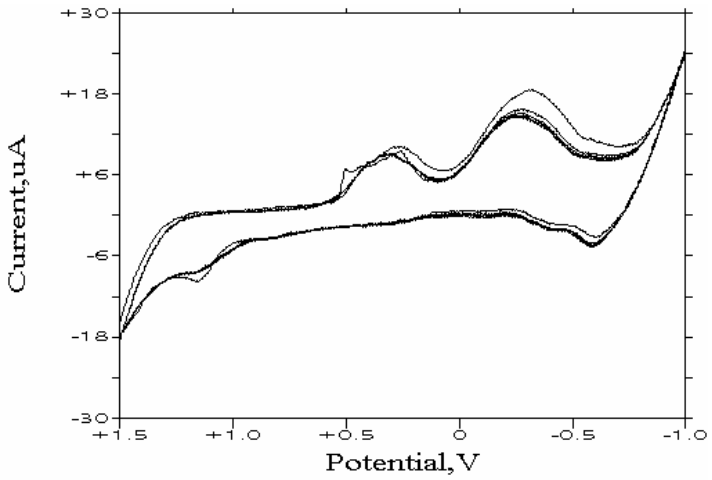

Figure 2.16 *Cycle-dependent voltammograms of mixture of 1 mM auric chloride and gold hydrosol solution added in equal quantities*

This was further confirmed by adding 1mM Auric chloride solution in gold hydrosol solution. Similar CV characteristics are seen here, along with slight shift in the peak potentials as shown in figure 2.16. This gives a compelling evidence for the reappearance of the species present in the Auric chloride solution during the nanowires

formation. The analysis clearly indicates that toluene molecules displace the ionic species adsorbed on the nanoparticles surfaces leading to the destabilization of hydrosol.Toluene molecules have different interactions with different crystallographic planes of gold nanoparticles, which lead to the anisotropic aggregation of gold nanoparticles and results into the nanowire formation.

We also believe that this process is kinetically driven in which gold hydrosol–toluene interface plays an important role demonstrating the importance of the effect of interfaces on nanowire formation. This interface can be tuned by changing the stirring rate of toluene-gold hydrosol biphasic solution, which indicates the role of convective mode of mass transfer in controlling the network topology.

Although the main principles governing the formation of nanowires is well understood, there is, as yet, no possibility of accurate prediction of the kinetics of formation and surface charges on the nanoparticles. In this case the interaction between the nanoparticle surface charges and toluene molecules is sensitive to the variations of environmental parameters. Here we extend our studies to explore the effects of different parameters such as Ionic strength, pH, rate of agitation, and the amount of precursor on the nanowire formation.

2.4 Effect of different parameters on network topology

2.4.1 Effect of stirring rate*:*

Figure 2.17 shows the effect of stirring rate on nanowire formation. More specifically, the stirring rate was varied from 200, 300, 400, 500 to 600 rpm respectively during the agitation of hydrosol with toluene and UV spectra were recorded from the hydrosol at each stirring rate, which gives the estimation of depletion of nanoparticles from the hydrosol for the nanowires formation (figure 2.17A).

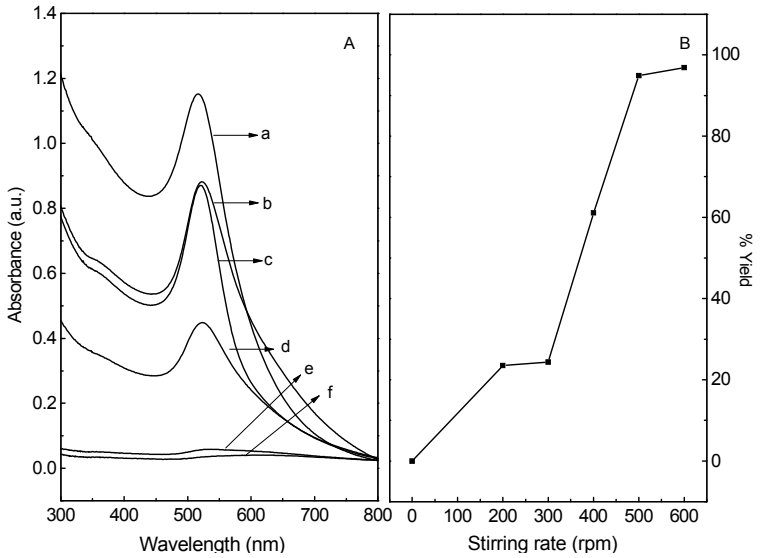

Figure 2.17 *(A) UV-Vis spectra of the Au hydrosol in the presence of toluene at different stirring rates 200, 300, 400, 500 and 600 rpm respectively. (B) The plot of the variation of yield (%) of nanowires at different stirring rates.*

At the zero stirring rate (i.e., no stirring), there is no formation of nanowires, suggesting that mechanical stirring plays an important role during the nanowire formation which was confirmed from the lack of change in the intensity of surface plasmon peak as compared to the case of hydrosol alone (520 nm). It is seen that the surface plasmon peak intensity decreases with increasing the stirring rate from 0 to 600 rpm, which in turn increases the nanowire yield. Figure 2.17B shows the gradual increase in the nanowire yield with increasing the stirring rate. These results indicate that at high stirring rate the turbulence intensity increases, which increases the interfacial area between toluene molecules and nanoparticles and the collision rate of nanoparticles.

2.4.2 Effect of metal /toluene ratio*:*

The effect of ratio of starting material/toluene on nanowire formation was investigated by UV-Vis spectroscopy since the ratio of starting material to ligand can be used to manipulate the nanowires yield [50]. Figure 2.18A shows that the intensity of surface plasmon peak decreases with increasing the amount of toluene to gold. There is

no change in the intensity of the surface plasmon peak if the molar ratio is increased beyond 1:2. Accordingly, figure 2.18B shows the increase in the nanowires yield with increasing the molar ratio of toluene.

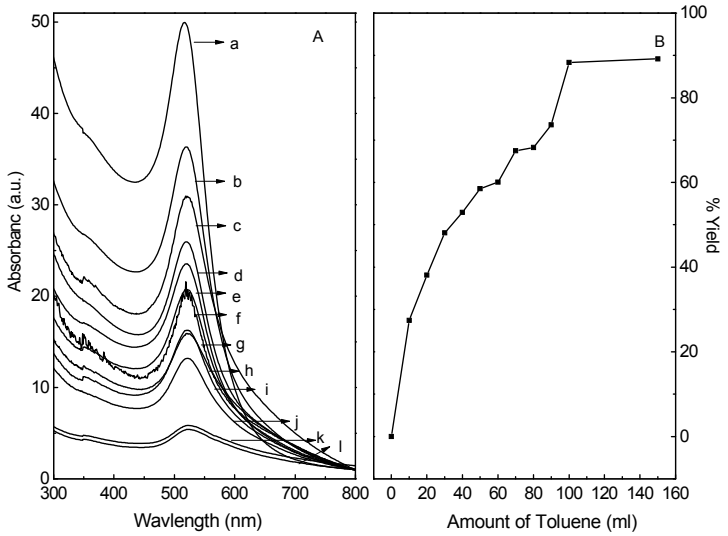

Figure 2.18 *(A) The effect of amount of toluene on the nanowire formation. UV-visible spectra of Au hydrosol after putting (a) 0 (b) 10%, (c) 20%, (d) 30%, (e) 40% (f) 50% (g) 60% (h) 70% (i) 80 %, (j) 90%, (k) 100% and (l) excess toluene. (B) The plot of the variation of % yield of nanowires with at various amount of toluene.*

This supports our previous conclusion that at the aqueous-organic liquid interface, strong electrostatic attraction between the charged nanoparticles and the π-electrons of the aromatic solvent molecules takes place. As the number of toluene molecules increases, the consequent hydrophobic passivation of gold nanoparticles increases which results into maximum nanowires yield at high molar ratio. Once the gold nanowires are fully passivated with the toluene molecules, there is no further nanowire formation, which is seen from the figure 2.18B where the yield is almost constant even after adding excess of toluene.

It is clear from the above discussion that toluene plays an important role during the nanowires formation by decreasing the electrostatic repulsion between the nanoparticles by passivating the nanoparticle surface and thus allowing the nanowires to grow in the specific direction during the aggregation. In order to understand more details of the mechanism, we performed further experiments using a strategy to reduce the

electrostatic repulsion between the particles by adding an electrolyte like KCl in presence of toluene.

2.4.3 Effect of ionic strength*:*

Previous studies of the effect of ionic strength on gold nanoparticle kinetics have shown that the salt induced precipitation destabilizes the colloidal solution of nanoparticles leading to the formation of aggregates. Here, we have studied the effect of salt on nano-collidal gold during the formation of nanowires in presence of toluene. Figure 2.19 (A) is the UV-visible spectra of Au hydrosol after the nanowire formation as a function of KCl concentration. The salt concentration was varied from 0.1, 0.5, 1, 2, 3 M respectively and it is seen from the figure that the surface plasmon peak intensity decreases with increase in the salt concentration. Figure 2.19(B) is the variation of yield of nanowires with ionic strength (salt concentration). These results show that higher the concentration of salt, the higher will be the screening of nanoparticles surface charges by counter ions in the solution, which in turn increases the agglomeration of nanoparticles. However, the toluene molecules interact with the screened nanoparticles and these interactions may be stronger that the particle-particle interactions thus leading to a higher proportion of nanowires.

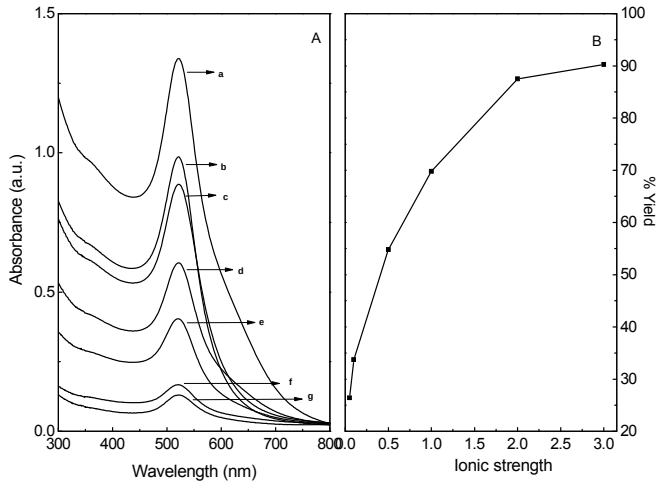

Figure 2.19 *(A) The effect of ionic strength on nanowires formation. UV-visible spectra of Au hydrosol at different ionic strengths (a) 0, (b) 0.1, (c) 0.5, (d) 1 (e) 2 and (f) 3. (B) The plot of the variation of % yield of nanowires with ionic strength.*

Earlier reports suggest that the average inter-particle distance decreases with increasing the ionic strength due to screening of the charges by ionic clouds and at high ionic strength, repulsive interaction is reduced and van-der-Waals attraction starts to dominate [51,52]. Hence borohydride molecules adsorbed on nanoparticle surfaces start to desorb leading to the instability of the colloidal suspension and these screened particles get encapsulated with toluene molecules at liquid/water interphase to form stable nanowires networks. Since the yield of nanowires increases with increasing the salt concentration, it would be interesting to test the yield as a function of solution pH during the nanowires synthesis.

2.4.4 Effect of pH*:*

Figure 2.20 shows the variation of yield with pH, which shows that the maximum yield is obtained by lowering the pH. The UV-vis spectra of Au hydrosol after nanowires formation at different pH [53]. Shows the gradual decrease in the surface plasmon peak intensity (Figure not shown).

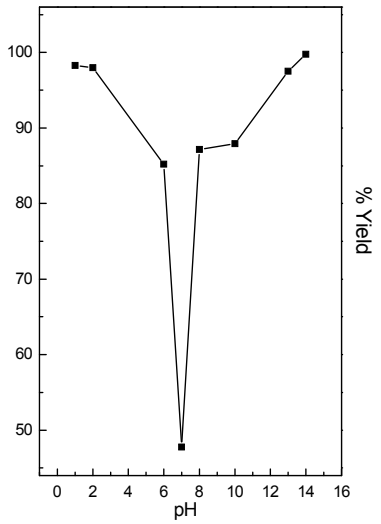

Figure 2.20 *The plot of variation of % yield of nanowires with pH.*

Also on further decreasing the pH of the solution, the decrease in the peak intensity is seen revealing maximum reduction in peak intensity both at at higher (pH14) and lower (pH 1) pH. These results are in good agreement with above ionic strength results which states that with increasing or decreasing the pH of the Au hydrosol the

screening of nanoparticles occur which destabilses the particles and allows the particles to agglomerates. However, at the same time the adsorption of toluene molecules forms stable nanowires networks.

The salient features of nanowires formation via nanoparticle coalescence in biphasic media can be quantitatively understood based upon the following description. The nanoparticles used in our experiments possess a slight positive surface charge due to the presence of partially reduced $HAuCl_4$ species, and are weakly solvated by anionic species such as OH^- and BO_3^- ions in the hydrosol. Agitation of this hydrosol with an immiscible low-viscosity organic liquid[1] forms a number of transient high-mobility aqueous-organic liquid interfaces, thereby providing a mechanism for facile nanoparticle transport and impingement. At the aqueous-organic liquid interface, strong electrostatic attraction between the charged nanoparticles and the π electrons of the aromatic solvent molecules results in the aromatic molecules displacing the weakly solvating anions on the gold surface. The consequent hydrophobic passivation inhibits further coalescence, as indicated by our annealing experiments and notably the lack of nanowire formation from strongly-passivated nanoparticles.

2.5 Conclusions

We have demonstrated a new, simple, room-temperature strategy for assembling gold nanowire networks through the coalescence of nanoparticles by agitation of gold hydrosol-toluene mixtures. These nanowires have a uniform diameter identical to that of the nanoparticles. During coalescence, toluene displaces the weak solvating agents and adsorbs onto the Au surface, enabling the transfer of the nanowire networks to the organic layer. Here we have elucidated the impact of pH, ionic strength, choice of solvent, stirring rate and precursor concentration on the nanowires formation and our electrochemical measurements allow us to understand the species present in the hydrosol and their possible role to form nanowires. With increasing pH, ionic strength, stirring rate and toluene molar ratio, the nanowires yield seems to be increasing suggesting the screening of nanoparticles induced by salt effects. At the same time toluene plays an important role in encapsulation providing microenvironments to confine the one-dimensional growth of the nanowires. As long as nanoparticles form the

hydrosol influx at the liquid/water interface, the toluene encapsulated confined growth of nanowires do takes place.

Extending our methodology to other materials systems would open up the possibility of low-temperature synthesis of new mesoscale structures from nanounits, for applications such as self-supporting catalyst networks, nanowires for devices, and porous nanofillers for composites.

References

[1] Schmid, G. Ed. *Clusters and Colloids*; VCH: Weinheim, **1994**.

[2] Kreibig, U.; Vollmer, M. *Optical Properties of Metal Clusters*, Springer Verlag; New York, **1995.**

[3] Hu, J. T.; Odom, T. W.; Liber, C. M. *Acc. Chem. Res*. **1999**, *32*, 435.

[4] Link, S.; El-Sayed, M. A. *J. Phys. Chem. B* **1999,** *103*, 8410.

[5] Creighton, J. A.; Eadon, D. G. *J. Chem. Soc. Faraday Trans*. **1991**, *87*, 3881.

[6] Weller, H. *Angew. Chem*. **1993**, *105*, 43.

[7] Halperin, W. P. *Rev. Mod. Phys*. **1986**, *58*, 533.

[8] Bradly, J. S.; Millar, J. M.; Rill, E. W. *J. Am. Chem. Soc.* **1991,** *11*, 4016.

[9] Brus, L. *J. Chem. Phys*, **1983**, *79*, 5566.

[10] Alivisatos, P. *Science* **1996,** *271*, 933.

[11] Schmid, G. Chem. Rev. **1992**, *92*, 1709.

[12] Handbook of nanostructured materials and nanotechnology, (Eds: H. S. Nalwa) Academic press, New York, **2000.**

[13] Alivisatos, P.; Barbara, P. F.; Castleman, A. W.; Change, J.; Dixon, D. A.; Kline, M. L.; McLendon, G. L.; Miller, J. S.; Ratner, M. A.; Rossky, P. J.; Stupp, S. I.; Thompson, M. I. *Adv. Mater*. **1998,** *10*, 1297.

[14] Xia, Y.; Yang, P.; Sun, Y.; Wu, Y.; Mayer, B.; Gates, B.; Yin, Y.; Kim, F.; Yan, H. *Adv. Mater.* **2003**, *15*, 353.

[15] Moffit, M.; Eisenberg, A. *Chem. Mater.* **1995**, *7*, 1178.

[16] Wang, Z. L. *Adv. Mater.* **2000**, *12*, 1295.

[17] Han, Y.J.; Kim, J. M.; Stucky, G. D. *Chem. Mater.* **2000**, *12*, 2068.

[18] Edmondson, M. J.; Zhou, W.; Sieber, S. A.; Jones, I. P.; Gameson, I.; Anderson, P. A.; Edwards, P. P*. Adv. Mater*. **2001**, *13*, 1608.

[19] Govindaraj, A.; Satishkumar, M.; Nath, M.; Rao, C. N. R. *Chem. Mater*. **2000**, *12*, 202.

[20] Song, H. H.; Jones, K. M.; Baski, A. A. *J. Vac. Sci. Technol. A* **1999**, *17*, 1696.

[21] Braun, E.; Eichen, Y.; Sivan, U.; Ben-Yoseph, G. *Nature* **1998**, *391*, 775.

[22] Jiang, X.; Xie, Y.; Lu, J.; Zhu, W. He.; Qian, Y. *J. Mater. Chem*. **2001**, *11*, 1775.

[23] Wei, G.; Nan, C.; Deng, Y.; Lin, Y. *Chem. Mater*. **2003**, *15*, 4436.

[24] Hsia, C.-H.; Yen, M.-Y.; Lin, C.-C.; Chiu, H.-T.; Lee, C.-Y. *J. Am. Chem. Soc.* **2003,** *125*(33), 9940.

[25] Weizmann, Y.; Patolsky, F.; Popov, I.; Willner, I. *Nano Lett.* **2004**, *4*(5), 787.

[26] Lisiecki, I.; Billoudet, F.; Pileni, M. P. *J. Phys. Chem.* **1996**, *100*, 4160.

[27] Rees, G. D.; Evans-Gowing, R.; Hammond, S. J.; Robinson, B. H. *Langmuir* **1999**, *15*, 1993.

[28] Lu, Q.; Gao, F.; Zhao, D. *Nano Lett.* **2002**, *2*, 725.

[29] Wang, X.; Li, Y. *J. Am. Chem. Soc.* **2002**, *124*, 2880.

[30] Sun, Y.; Mayers, B.; Herricks, T.; Xia, Y. *Nano Lett*. **2003,** *3*(7), 955.

[31] Romanska, D.; Mazur, M. *Langmuir* **2003**, *19*(11), 4532.

[32] Pan, H.; Liu, B.; Yi, J.; Poh, C.; Lim, S.; Ding, J.; Feng, Y.; Huan, C. H. A.; Lin, J. *J. Phys. Chem. B.* **2005**, *109(8),* 3094.

[33] Tian, M.; Wang, J.; Kurtz, J.; Mallouk, T. E.; Chan, M. H. W. *Nano Lett.* **2003,** 3*(7),* 919.

[34] Brust, M.; Bethell, D.; Kiely, C. J.; Schiffrin, D. J. *Langmuir* **1998**, *14*, 5425.

[35] Sun, Y.; Yin, Y.; Mayers, B. T.; Herricks, T.; Younan, X. *Chem. Mater*. **2002,** 14, 4736.

[36] Jana, R.; Gearheart, L.; Murphy, C. J. *J. Phys. Chem. B* **2001,** *105*, 4065.

[37] (a) van der Zande, B. M. I.; Bohmer, M. R.; Fokkink, L. G. J.; Schonenberger, C. *Langmuir* **2000,** *16*, 451. (b) Foss, C. A.; Hornyak, G. L.; Stockert, J. A.; Martin, C. R. *J. Phys. Chem.*, **1994**, *98*, 2963.

[38] Caswell, K. K.; Bender, C. M.; Murphy, C. J. *Nano Lett.* **2003**, 3*(5),* 667.

[39] Tao, A.; Kim, F.; Hess, C. J.; Goldberger, R.; Sun, Y.; Xia, Y.; Yang, P. *Nano lett.* **2003,** *3*, 1229.

[40] Manna, A.; Chen, P.; Akiyama, H.; Wei, T.; Tamda, K.; Knoll, W. *Chem. Mater.* **2003**, *15*, 20.

[41] Hostetler, M. J.; Strokes, J. J.; Murray, R. W. *Langmuir* **1996**, *12*, 3604.

[42] *The Aldrich library of FT-IR spectra*, 2nd ed.; Sigma-Aldrich: Milwaukee, **1997**, 2, 1625.

[43] Cross, A. D. *An introduction to practical infrared spectroscopy*, 2nd ed.; Butterworths: London, **1964**; p 63.

[44] Kumar, A.; Mandal, S.; Mathew, S. P.; Selvakannan, P. R.; Mandale, A. B.; Chaudhari, R. V.; Sastry, M. *Langmuir* **2002**, *18*, 6478.

[45] *Lange's Handbook of Chemistry*, 15th ed.; McGraw-Hill: New York, **1999.**

[46] Li, G.; Lauer, M.; Schulz, A.; Boettcher, C.; Li, F.; Fuhrhop, J.-H. *Langmuir* **2003**, *19*, 6483.

[47] McNeillie, A.; Brown, D. H.; Smith, W. E.; Gibson, M. Watson, L. *J. Chem. Soc., Dalton Trans.* **1980**, 767.

[48] Kavanoz, M.; Gulce, H.; Yildiz, A. *Turk J. Chem,* **2004**, *28*, 287.

[49] Mokrani, C.; Fatisson, J.; Guérente, L.; Labbé, P. *Langmuir* **2005**, *21*, 4400.

[50] Xu, S.; Zhou, H.; Li, Y. *Langmuir*, **2002,** *18,* 10503.

[51] Kooij, E. S.; Brouwer, E. A. M.; Wormeester, H.; Poelsema, B. *Langmuir,* **2002**, *18*, 7677.

[52] Brounwer, E. A. M.; Wormeester, H.; Poelsema, B. *Langmuir*, **2003**, *19,* 8102.

[54] Busbee, B. D.; Obare, S. O.; Murphy, C. J. *Adv. Mater***, 2003**, *15*, 414.

CHAPTER III

Hierarchical architectures of silver nanoparticles: use of chiral molecules as a precursor

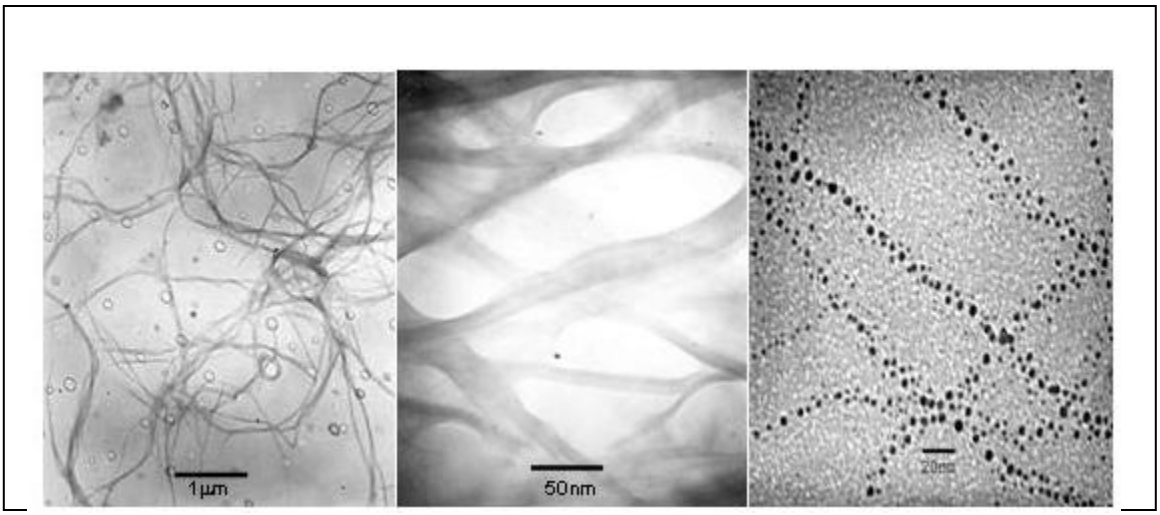

This chapter describes the intriguing and unprecedented formation of custom designed silver nanowires by supramolecular self-assembly of nanoparticles in the presence of organometallic chiral molecules. Specifically, a facile synthesis of extensive 1D arrays of silver nanoparticles using optically active silver salt of dibenzoyl tartaric acid (Ag-DBTA) as a starting material and triethyl amine as a reducing agent is found to form stable and monodispersed silver nanowires having the diameters 35±5 nm and length in few micrometers at room temperature. Another substantial result emerging from this study is that nanowires are formed when D(+) or L(-) DBTA is used as a starting material while spherical nanoparticles are formed with their racemic mixture. The influence of the starting compound as well as the other parameters on the formation of these one-dimensional superstructures is investigated using diverse types of techniques including transmission electron microscopy, UV-vis, IR, Raman spectroscopy and cyclic voltammetry.

*A part of the work reported in this chapter has been communicated to **J. Am. Chem. Soc.**, 2006.*

3.1 Introduction

Nanomaterials, especially quantum dots and one-dimensional nanostructures with distinct size and shape dependant physical and chemical properties have recently emerged to be important in understanding both fundamental concepts and methodologies for fabricating nanodevices [1-5]. The synthesis of metal nanoparticles with controllable size, shape, configuration and their spatially ordered assemblies in predefined geometries is the first step towards the construction of nanodevices. In order to exploit the size and shape tunable optical and electronic properties of the individual nanoparticles in a device, the assembly of nanoparticles in hierarchical architectures became a challenging issue [6-7]. As a consequence, several bottoms-up approaches for the assembly of these nanoparticle building blocks into novel superstructures have been extensively pursued over last few years [8]. Most of the previous methods traditionally involve the synthesis of narrow sized nanoparticles, surface passivation and patterned organization using various techniques such as solvent evaporation [9,10], template method [11], Langmuir-Bloddget film [12], formation of self-assembled mono or multilayers [13], and layer-by-layer assembly [14]. In these methods, the length of the passivating agent, core size and nature of the core materials play key roles in determining the ordered organization of nanomaterials, which in turn controls the collective interactions. For example, Korgel et al. have shown the synthesis of silver nanowires by self-assembly of ellipsoidal silver nanoparticles using dodacanethiol ligand [15] while Tang et al. have reported the spontaneous organization of CdTe nanoparticles in one-dimensional assembly by the controlled removal of the protective shell of organic stabilizer [16]. Recently, the formation of silver nanowires by the oriented aggregation of silver nanoparticles using Poly(vinylpyrrolidone) and dimethylformamide has been shown by Liz-Marzan and co-workers [17]. Considering these studies related to one-dimensional assemblies of nanoparticles, more emphasis is given on concentration of precursor, ratio of surfactant, reaction conditions, use of the template assemblies or use of chelating agents. While these approaches have shown remarkable capabilities in assembling nanoparticles in one-dimensional nanostructures, the use of the precursor-based assembly of 1D structures remains poorly studied. Few approaches such as, a solution phase precursor route of synthesis of SnO_2 and In_2O_3 nanowires have been shown earlier [18]; however, the use of organic chiral molecules as a possible reagents

has not been realized. Chirality is an important and intriguing structural physical property of molecules. Since Pasteur's discovery that the three dimensional crystals of the salt of the tartaric acid exist in two entatiomers, the influence of molecular chirality on the two and three dimensional ordering of molecules has attracted a lot of interest [19]. Tartaric acid (TA) is one of the most important chiral compounds, with a rich history and countless current applications. Tartaric acid and its derivatives are used as chiral building blocks, reagents, ligands, and resolving agents in organic synthesis. These molecules can serve as good candidates to offer a high degree of organization of nanoparticles, ease of chemical modification, and naturally occurring self-assembly motifs inherent in these systems, which is of interest for the preparation of novel nanomaterials.

In the previous chapter, we have described a templateless, room-temperature strategy for assembling gold and silver nanowire networks through the coalescence of nanoparticles by agitation of metal hydrosol-toluene mixtures. This chapter, in comparison, describes a novel route for synthesizing a large amount of custom-designed one-dimensional superstructures of silver nanoparticles using an organometallic chiral molecule as a source of silver. Specifically, we here demonstrate a single step room temperature synthesis of silver nanowire architectures using optically pure silver salt of dibenzoyl tartaric acid (Ag-DBTA) as a starting material and triethyl amine as a reducing agent as well as capping agent. In order to understand the mechanism behind the formation of these nanostructures using optically active salts, the experimental procedure was repeated with both optically active (+) and (-) stereomers of DBTA as well as their racemic optically inactive mixture (±) DBTA. A simple combination of molecular driving forces is exploited in this chiral molecule mediated strategy, which is used for one-dimensional organization of silver superstructures. The objective of this research is two fold: one is to develop a single processing route for the production of nanoparticles at room temperature and other is to form organized assemblies and study the variation in their properties with respect to nanoparticles. These types of structures are expected to be useful in future for fabricating various nanoelectronic devices such as integrated-circuit interconnects, quantum computing devices, transistors and sensors.

3.2 Experimental section

3.2.1 Materials:

Silver nitrate ($AgNO_3$), benzoyl chloride, L-Tartaric acid [(*R,R*)-(+)-tartaric acid], D-tartaric acid [(S,S)-(-)-tartaric acid] and DL-tartaric acid, triethylamine and all solvents were purchased from Aldrich. The single enantiomers had an optical purity of 99%. All chemicals were used without further purification, Deionized water from a Milli-Q system was used in all experiments.

3.2.2 Synthesis of dibenzoyl tartaric acid:

The dibenzoyl-d-tartaric was synthesized according to published procedures [20,21]. In brief, one mole of tartaric acid was mixed with 3.2 moles of benzoyl chloride and the reaction mixture was refluxed for 3 h at 150 ^{o}C (as shown in scheme 3.1).

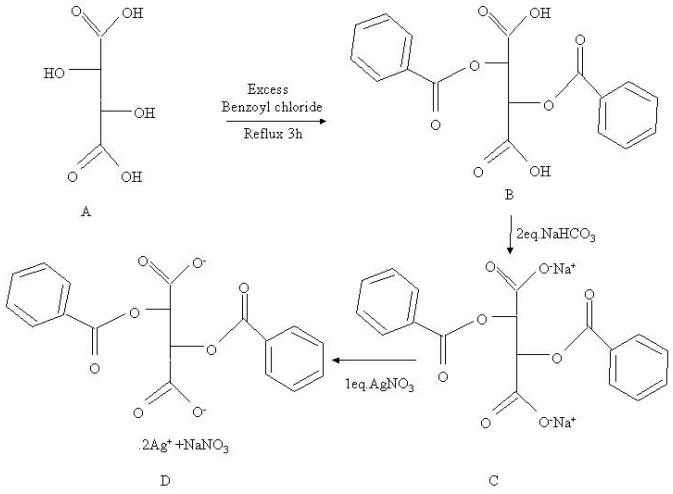

Scheme 3.1 *Schematic illustration of the synthesis of silver salt of dibenzoyl tartaric acid (Ag-DBTA).*

The contents of the flask were removed and ground in a mortar and subsequently, benzoic acid and excess of benzoyl chloride were removed by extracting with benzene. The product, i.e., dibenzoyl-d-tartaric (DBTA) anhydride was filtered, air dried and characterized using IR and NMR spectroscopy. The use of chiral bulky dibenzoyl molecule could essentially separate the nucleation and growth rate of silver nanoparticles and kinetically control the tendency of the silver nanoparticles to self-

assemble into one dimensional nanostructures. Since TA is unable to present large hydrophobic surfaces, the substitution of hydroxyl functions with bulky aromatic groups to form DBTA, may facilitate the organized assembly of nanoparticles [22]. Using this property of DBTA, Na-DBTA was initially formed by treating DBTA with two equivalent $NaHCO_3$ and further it was treated with 1 equivalents of aqueous silver nitrate (as shown in scheme 3.1). The resulting Ag-DBTA salt formed by the interaction of carboxy group and silver clusters was filtered and used after extensive washing.

3.2.3 Synthesis of nanowires:

DBTA precursor was subsequently used in the synthesis of silver particles as well as their one dimensional organized assemblies. A typical procedure is as follows: In a three necked round bottom flask, silver salt of dibenzoyl tartaric acid (27 mg of Ag-DBTA in 25 ml of solvent) was suspended in acetonitrile or toluene solvent and the reaction mixture was stirred (with a magnetic stirrer at 600 rpm) under inert atmosphere. Dilute solution of triethyl amine in acetonitrile (0.125 ml of TEA in 25 ml of acetonitrile) was added drop-by-drop over 1 h to this solution. The surface of the white silver tartarate powder gradually turned to brown and the insoluble precursor finally disappeared, to generate a highly homogeneous dispersion of silver nanowires in solution (over ~12 h of reaction). The resulting brown colored solution was shaken with 10 mM $NaHCO_3$ in order to remove excess of silver salt and further removal of uncoordinated amine molecules was effected by centrifugation. The final precipitate was re-dispersed in acetonitrile after repeated washings. Silver nanowires isolated as powder were readily redispersed in nonpolar solvent such as acetonitrile or toluene, showing no signs of precipitation for few months. In order to understand the effect of chirality on the mechanism of formation of silver nanoparticle assemblies, the above synthetic procedure was conducted for silver-l-dibenzoyl tartarate and silver-d-dibenzoyl tartarate chiral molecules as well as for the recemic mixture of both the salts. The corresponding transmission electron micrographs were taken to study the shape and size distribution.

3.2.4 Characterization:

These nanowires were characterized by various techniques such as scanning electron microscopy (SEM), transmission electron microscopy (TEM), High-resolution transmission electron microscopy (HRTEM), UV-vis spectroscopy, Fourier transform infrared (FTIR) spectroscopy, Nuclear magnetic resonance spectroscopy (NMR), surface enhanced Raman scattering spectroscopy (SERS) and cyclic voltammetry (CV).

SEM measurements were carried out in a JEOL JSM-6330F microscope equipped with a field emission gun operated at 5 keV. In preparing SEM samples, the reaction products were spotted on silicon substrates as small droplets and were allowed to dry at room temperature. TEM measurements were carried out in a CM12 microscope operated at an accelerating voltage of 120 kV. Lattice resolution images of the nanowires were obtained in a JEOL 2010 instrument operated at 200 kV. The TEM samples were prepared by placing small droplets of the reaction solutions on carbon coated copper grids and samples were allowed to dry at room temperature prior to taking the images.

UV-vis spectroscopy measurements of all samples were performed in a Varian Cary 500 Scan UV-vis-NIR spectrophotometer at a resolution of 2 nm. FTIR measurements of the DBTA and silver nanowires were carried out on a Perkin-Elmer, Paragon 1000 spectrometer in the transmission mode at an 80° incident beam angle to the surface normal. A few drop of each solution was placed onto the silicon substrate for the Raman studies and allowed to dry at room temperature. The Raman spectra were obtained in the region from 2500 to 800 cm^{-1} for these solutions using the Renishaw S 2000 Raman spectroscope with a 514.5 nm argon ion laser. The background spectrum of silicon was subtracted from each subsequent spectrum and an acquisition time of 15 min was used always to obtain a good signal-to noise ratio. Purified powder of silver nanowires was dissolved in $CDCl_3$ + DMSO-d_6, and the proton (1H) NMR spectra were recorded on a Bruker AC 200 MHz instrument and scanned in the range 0-15 ppm using trimethylsilane internal standard. For comparison, the proton NMR spectrum of pure benzoic acid was also recorded in $CDCl_3$. CV measurements were carried out on a Autolab PGSTAT30 (ECO CHEMIE) instrument in an oxygen-free atmosphere using a three-electrode cell comprised of a Pt microelectrode (50 μm) working electrode, a large-

area platinum flag counter electrode, and Ag/Ag^+ reference electrode in 0.1 M $LiClO_4$ as the supporting electrolyte in acetonitrile (98 %)-water (2 %) solution.

3.3 Results and discussion

3.3.1 UV-vis spectroscopic analysis:

Figure 3.1 shows comparative UV-vis spectra of solutions of silver nanostructures at different stages of synthesis, which clearly indicate unique and shape dependent surface plasmon resonance (SPR) properties.

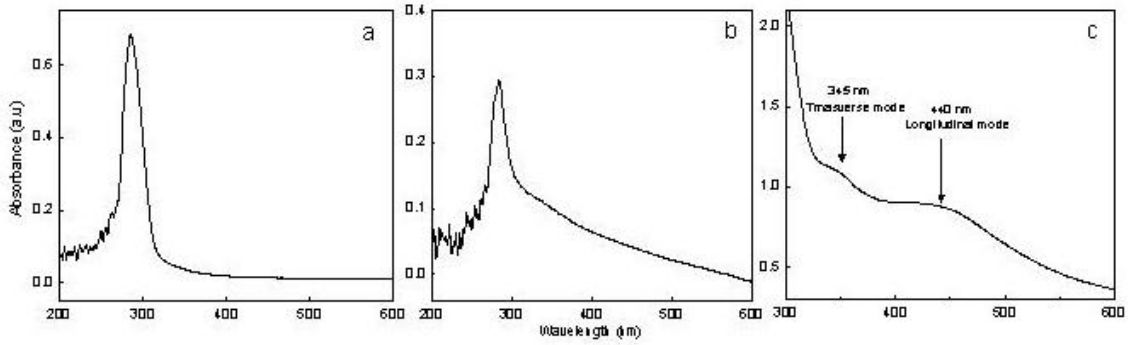

Figure 3.1 *UV visible spectra of solutions of silver nanostructures at different stages of synthesis (a) 1 h (b) 6 h (c) 12 h.*

As seen in spectrum 3.1(a), during the initial stages of synthesis (1 h), spherical silver nanoparticles having uniform size ~ in the range 5-15 nm are formed as evident from the single sharp characteristic surface plasmon band with absorption maxima at 320 nm. These results are in agreement with earlier reports on silver nanoparticles. For example, Henglein et al. has reported the occurrence of surface plasmon peak at 320 nm for the particles in the range 3-15 nm [23a]. When the reaction is continued, the colour of the solution gradually changes from yellow to yellowish-brown. In the UV-visible spectrum of solution obtained after the six hours of reaction, the presence of the surface plasmon band at 310 nm is still seen with a decrease in the absorption intensity as shown in figure 3.1(b). This presumably indicates the depletion in the amount of spherical nanoparticles as the reaction continues although the appearance of a broad absorption band in the range 300-400 nm, suggests the possible aggregation of silver nanoparticles to generate anisotropic nanostructures having different aspect ratios [23b-

25]. Interestingly, the UV visible spectrum of the silver nanostructures obtained after the 12 h of the reaction (i.e., when the colour of the solution turns dark brown) shows a complete disappearance of the features as seen in figure 3.1a and b. A broad hump like characteristic absorption band at 345 nm is seen along with another broad peak at 440 nm. It is well known that two plasmon resonances, the transverse and longitudinal plasmon bands, are expected for anisotropic metallic nanoparticles like silver nanowires. The observed two peaks at 345 nm and 440 nm could be attributed to the presence of longitudinal and transverse modes of surface plasmon in silver nanowires respectively. These results are consistent with the earlier reports on the appearance of two peaks due to the formation of one-dimensional silver nanowires by Catherine et al. [26]. Therefore, the presence of the peak at 342 due to longitudinal bands and appearance of another broad peak at 440 nm in figure 3.1(c) could be attributed to the formation of one-dimensional, high-aspect ratio superstructures of silver nanoparticles. The stability of silver nanostructures can be confirmed by the invariance of these surface plasmon features when the dark brown colored solution is stored over 90 days. With regard to the emerging use of metal enhanced fluorescence in sensing applications [27] the method and protocols presented here for the synthesis of silver nanowires that are grown from chiral compounds could be a useful tool for the simpler production of silver wire. These silver nanowires can be deposited on a glass substrate, which, could significantly improve the sensitivity of fluorescence based biological assays and can be utilized in biotechnological applications such as high-throughput screening and drug discovery based on enhanced fluorescence detection. Further studies in this direction are under progress.

3.3.2 Scanning electron microcopy analysis:

Figure 3.2 shows typical scanning electron micrograph of silver nanostructures synthesized at room temperature revealing a large quantity of wire like nanostructures with length in the range of several micrometers, and diameter in the range 20 nm to 40 nm. A high-magnification SEM image (Figure 3.2b) shows the abundance of uniform strongly interwoven structures with random orientation and each wire in turn, is quite uniform along its length. A closer look by SEM indicates that some of the wires could aggregate into bundles, which appear thicker under low magnification.

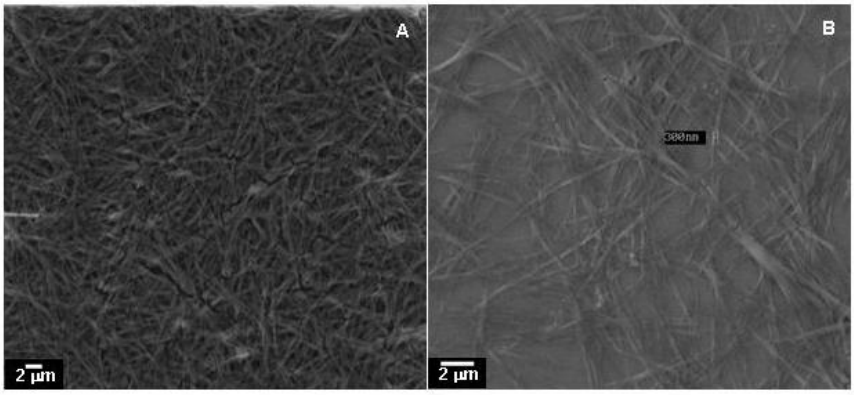

Figure 3.2 *(A) SEM image of uniform silver nanowires prepared at room temperature at low magnification. (B) SEM image at high magnification revealing the wires having width of 20-40 nm and length up to several microns.*

3.3.2 Transmission electron microcopy analysis:

Figure 3.3 displays transmission electron microcopy (TEM) images (also high resolution -HRTEM) of the silver nanostructures obtained from the silver salt of optically pure DBTA, along with the selected area diffraction pattern (SAED) and particle size histogram.

The TEM image with low magnification (Fig. 3.3a), shows long nanowires with high yield having the average diameter of the nanowires statistically measured to be 35-40 nm (by sampling 100 nanowires) along with length in few micrometers. At higher magnification (Fig. 3.3b), it can be clearly seen that the silver nanowires have fine wire like morphology and interestingly they form networks of nanowires under these synthesis conditions (Temperature 40 ^{o}C). Figure 3.3c reveals selected area electron diffraction pattern (SAED), in which several concentric rings could be assigned as diffraction from {111}, {200}, {220}, and {311} planes of face-center-cubic (*fcc*) silver from the center most ring, respectively. The preferred growth direction and the nature of single crystallinity of the nanowires could be verified by HRTEM image.

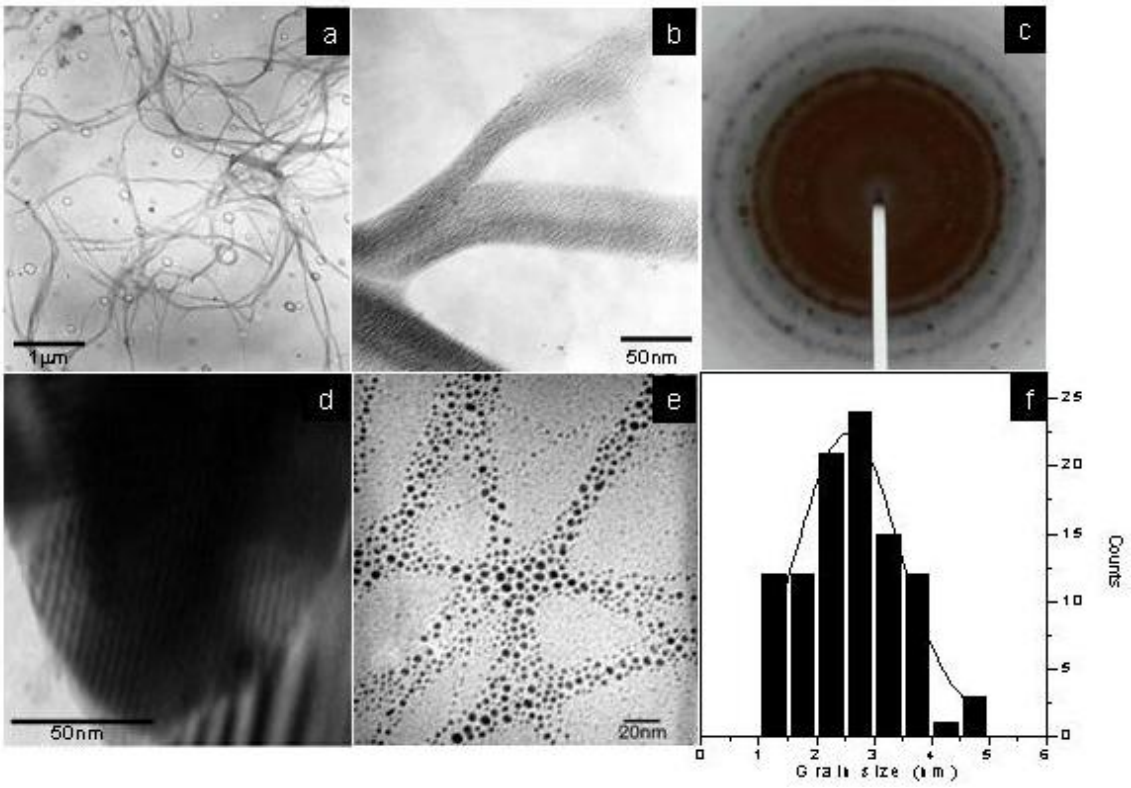

Figure 3.3 *TEM images of silver nanowires at (a) low and (b) high magnification along with the (c) SAED pattern; high resolution TEM images are in (d), (e) while (f) shows the histogram of silver nanoparticles corresponding to image (e).*

Figure 3e is a HRTEM image of silver nanowires and it can be seen from the figure that nanowires are composed of a continuous string of precisely ordered nanoparticles and an average particle size of nanoparticles is seen to be 2.7 ± 0.2 nm as shown in the histogram (Fig. 3.3f). It is evident from the figure that nanowires are nothing but the one-dimensional arrangement of spherical nanoparticles. Sometimes these chains of nanoparticles are seen to get merged with other chains to form branched, more complex architectures and hence the diameter of the structures varies at intersections. This fact indicates that the structures mainly consist of chains of coalesced primary particles and the growth process depends on the collective behavior of nanoparticles. The adsorption and confirmation of DBTA molecules on the nanoparticle surfaces also plays an important role in nanowire growth mechanism. This type of counter ion effect on the surface of ZnO nanowires has been previously explained by Pacholski et al. where the adsorption of acetate ions from the precursor salt is reported

as the one of the reasons for the formation of oriented growth of ZnO nanowires [8b]. Liz-Marzan and co-workers recently showed a similar process of formation of nanoparticle stripes with silver quantum dots when the suitable crystallographic facets of particles are facing each other [17]. In contrast, Lin et al. has reported the formation of chain like silver dendritic nanostructure due to nucleation of silver nanoparticles having same spacing (1.50 Å) and growth direction (220 plane)[7b].

No difference in the morphology of the nanostructures is seen when optically active silver salts of (-) DBTA or (+) DBTA are used in the synthesis as a chiral starting material. However, when racemic mixture of silver salt of (±) DBTA is used as a starting material, silver nanoparticles having average diameter in 7-15 nm are obtained without any traces of nanowires (as shown in figure 3.4). This could be explained because a variation in the precursor confirmation and its distribution over nanoparticle surface has a significant effect on the ordering of nanoparticles. Thus the electrostatic and hydrophobic interactions capable of producing wired assembly of nanoparticles are believed to be present in the optically active D(+) or L(-) DBTA, while this process is hindered in case of racemic mixture. Preliminary analysis suggests the two probable factors which influence the formation of nanowire structures, first, the multidentate behaviour of ligand and second the chirality. It is quite difficult to quantify the individual effects of these factors and further investigations are needed to separate out these factors. The enantioselectivity is proven for the synthesis of organic nanotubes formation and the use of selective and directional nature is ideally suited for the construction of complex molecular architectures. There have been accounts of successful capture of the tubule shape through use of the lipid assembly as a template for the deposition of more rugged materials, such as nickel, copper, or magnetic alloys. For example, pioneering work on this type of structures was carried out by Ghadiri and co-workers for cyclic D, L-peptides with eight to twelve residues [28] while other research groups have introduced amino acids [29,30], cystine based ureas [31] and bisamides [32] as well as aromatic rings [33].

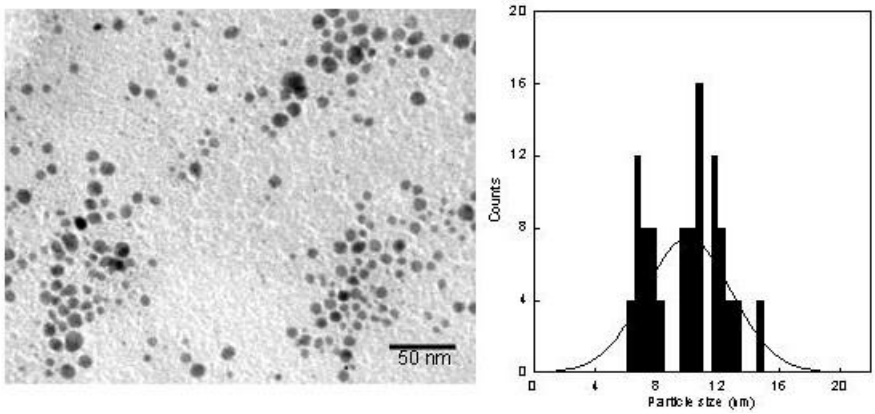

Figure 3.4 *Transmission electron microscopy image of silver nanoparticles obtained by using racemic mixture of silver salt of DBTA as a starting material with corresponding histogram showing diameter of nanoparticles in the range 7-15 nm.*

3.3.3 X-ray diffraction analysis of silver nanowires:

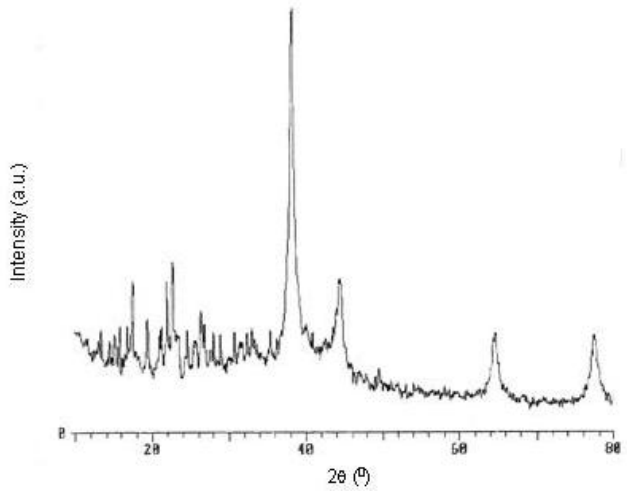

Figure 3.5 *Powder X-ray diffraction (XRD) pattern of silver nanowires.*

The crystal structure of these silver nanowires is further studied using XRD and the XRD pattern (Figure 3.5) exhibits peaks corresponding to the (111), (200), (220), and (311) diffraction peaks of the cubic structure of metallic Ag, respectively, indicating that the thin film is composed of pure crystalline silver [34, 35]. Relatively broad XRD peaks reveal small size of silver crystals and the average size of the silver nanostructures determined from the half width of the intense (111) reflection according to the Debye-

Scherrer equation [34b] is approximately 35 nm which is consistent with the mean size of nanowires as determined from by TEM.

3.3.4 Fourier Transform Infra-Red spectroscopy of silver nanowires:

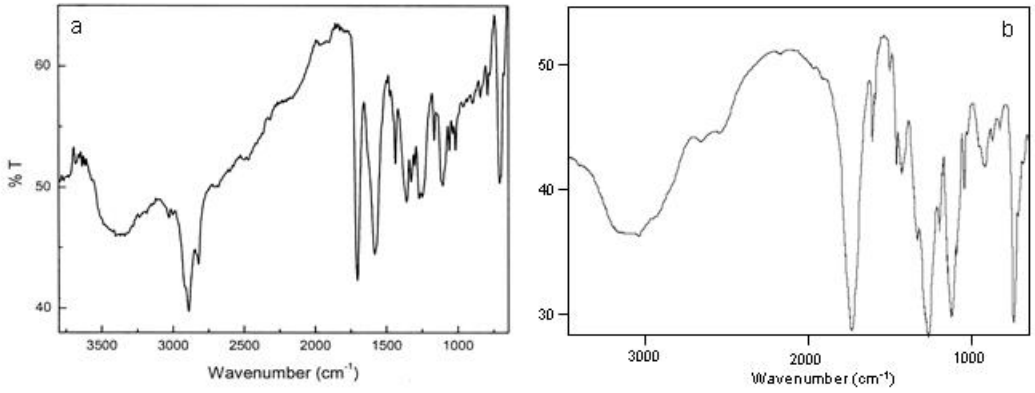

Figure 3.6 *FTIR spectra of (a) silver nanowires prepared from Ag-DBTA and (b) neat DBTA.*

Figure 3.6 shows a comparison of the FTIR spectra of the triethylamine capped (a) silver nanowires prepared using single source precursor DBTA and (b) neat DBTA and corresponding IR peak assignments are shown in Table 3.1. The spectrum for silver nanowires predominantly shows the same features relative to those of neat DBTA. The neat DBTA bands are in the region ~1660 cm^{-1} (C=O stretch), ~1600 cm^{-1} (C=C vibrations). The bands of the nanowires are in the same regions and have the same features as those of the neat DBTA with following exceptions: (1) the broad band from 3300 to 3600 due to Ag_n-O stretching (2) the band at 1662 due to Ag_n-O-C=O stretch, both are with increased intensity relative to that of neat amine. Such effects are not surprising, given the proximity of the metal surface with DBTA in these motions. (3) Another striking feature in spectrum 'a' is the presence occurrence of new bands at 2936 and 2876 cm^{-1}, due to the methylene antisymmetric and symmetric stretching vibrations of the hydrocarbons respectively [36,37]. The presence of these vibrations in the nanowires sample confirms that nanowires are coated with triethylamine. These signatures thus present additional evidence for the involvement of the triethyl amine in the silver nanowires formation in the vicinity of DBTA.

Table 3.1 *IR peak assignments for DBTA and triethylamine capped (a) silver nanowires prepared using single source precursor DBTA*

Compound	IR frequency (cm^{-1})	Band assignment
DBTA	1660 1600-1400	-C=O stretching -C=C- benzene ring stretching
Silver nanowires	1600-1400 1660 1662 3600-3400 2936 2876	C=O stretching -C=C- benzene ring stretching Ag_n-O-C=O stretch Ag_n-O- stretching $-CH_2$- antisymmetric stretching $-CH_2$- symmetric stretching

3.3.5 *Raman Spectroscopy of silver nanowires:*

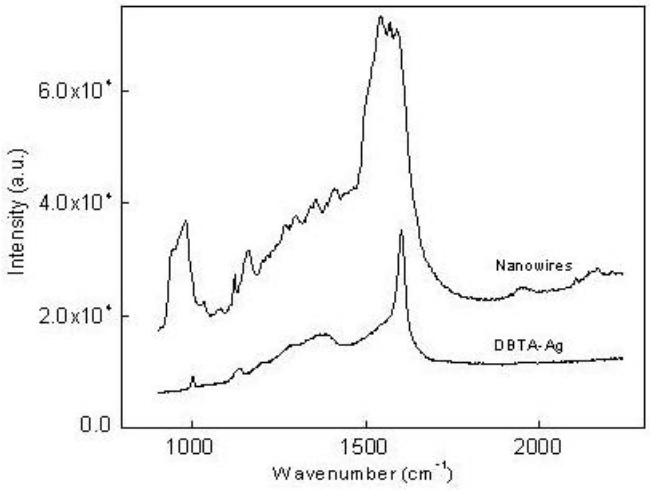

Figure 3.7 *Raman spectra of silver salt of DBTA and silver nanowires.*

A comparison of the Raman spectra of Ag-DBTA starting material, and silver nanowires provides more details about the modes of binding. The Raman spectra in the region from 3500 to 2200 cm^{-1} are not shown since there are no spectral features present in this region for both samples. The major band seen in the spectra is the band at 1613 cm^{-1} due to the ring stretching as shown in figure 3.7. The overall position of this band is same for both the samples except broadening and enhanced intensity of the peak for the nanowire sample. The new spectral features observed on the nanowires originate from the plasmon coupling between Ag nanoparticles and the underlying

substrate. While, there is no direct evidence for the change in the relative orientation of aromatic rings, changes in spectral features in nanowires sample suggest a possible change in the packing geometry of the aromatic ring planes. Similar observations have been reported by Gao et al., where the probable reason for the moderate enhancement in the breathing mode of pyrrolidone ring is attributed to the ring tilting on the surfaces of silver nanowires [38a]. The band at 929 cm^{-1} appears to be the ring-breathing mode that has downshifted from 1005 cm^{-1} due to the electron transfer that takes place from the ring to the metal, thus weakening the π electron system [38b]. The 1150-1600 cm^{-1} region of the Raman spectra is dominated by skeletal vibrations of the C-C stretching modes and C-CH_3 symmetric bending modes, CH_2 rocking modes which are all sensitive to the conformation of hydrocarbon chain from triethyl amine entities. The Raman spectrum of silver nanoparticles shows similar characteristics as seen for nanowire sample except the broadening and splitting of the band at 1613 cm^{-1}. This band is rather sharp and intense in case of silver nanoparticles.

3.3.6 Nuclear Magnetic Resonance Spectroscopy of silver nanowires*:*

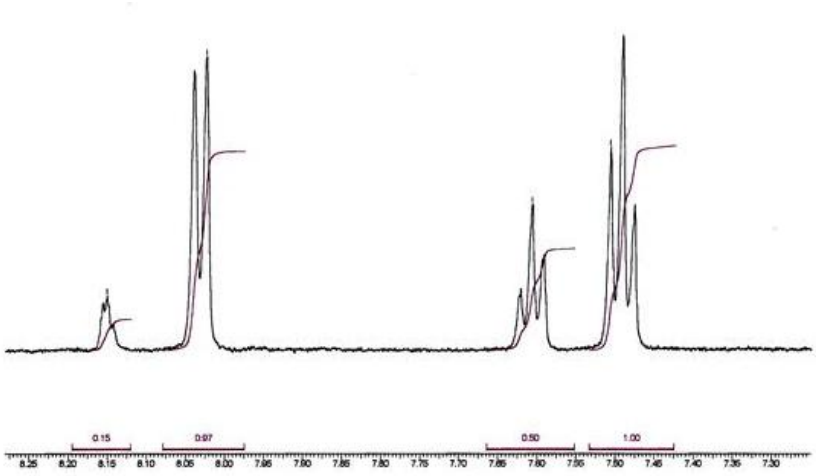

Figure 3.8 *Proton magnetic resonance spectrum of silver nanowires in $CDCl_3$ + DMSO-d_6 solvent system using tetramethylsilane internal standard.*

The ^1H NMR spectra of silver nanowires show (Figure 3.8) a fine splitting pattern of five contiguous protons due to aromatic protons and also the dishielding of all signals is seen compared to that of neat free acid as well as Ag-DBTA salt. The significant

pattern of aromatic protons give two broad resonances around δ= 7.51 and δ= 8.02 respectively in ^{1}H NMR spectrum, indicating the absence of bulk paramagnetic nature due to large particle size.

3.3.7 Effect of temperature on the synthesis of nanowires:

Interestingly, during the synthesis of nanowires we notice that the color change of silver nanowires solution is highly sensitive to the temperature and varies slightly over the fluctuations of the room temperature. To investigate whether the temperature dependence of the colour change of silver nanowires is associated with the shape of nanoparticles, surface plasmon characteristics of silver nanoparticles were studied by varying the reaction temperature viz: 20, 25, and 30 and 35°C under similar synthetic conditions of stirring under inert atmosphere in a temperature-controlled mantle. The Uv-visible spectra of each solution prepared at these different temperatures were recorded after 12 h of reaction. Figure 3.9 shows such UV-visible absorbance spectra of silver nanostructures synthesized at 20, 25, and 30 and 35°C. UV-vis spectrum of the reaction solution prepared at 20 °C (sample a), shows a single broad surface plasmon band at 450 nm, suggesting the sole presence of spherical silver nanoparticles

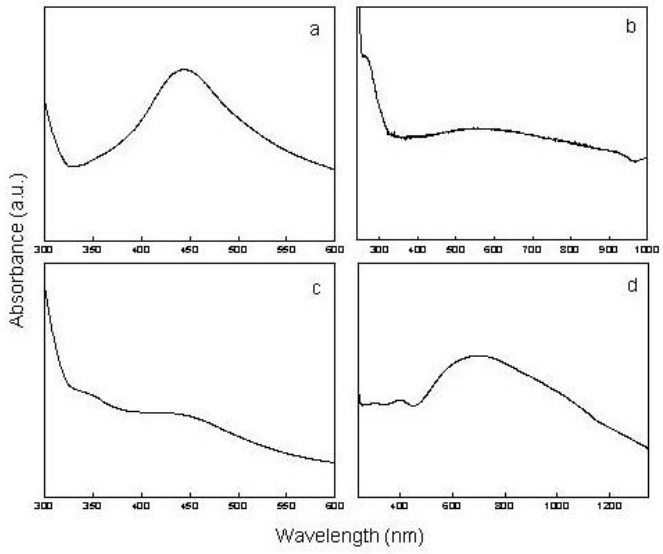

Figure 3.9 *UV visible spectra of silver nanostructures prepared at various temperature conditions (a) 20 (b) 25 (c) 30 and (d) 35°C*

The UV-Vis spectrum of the reaction solution prepared at 25 °C (sample b) shows the appearance of small hump like signatures at 300 nm. And also the band observed at 450 nm in sample 'a' becomes broad in case of sample 'b' with drastic reduction in the intensity. These features indicate the change in the morphology of the silver nanoparticles and formation of anisotropic nanostructures. These features are more prominent in the samples prepared at higher temperatures (30 °C) which shows the presence of transverse surface plasmon band at the 340 nm while the longitudinal modes are seen at the wavelength 450 nm. At still higher temperature (35-40 °C) the fully-grown silver nanostructures are seen which is evident from the presence of sharp features of transverse band at 350 nm and red shifted broad surface plasmon band in the range 500-800 nm due to longitudinal modes. These features suggest that the long aspect ratio nanostructures are formed at this temperature of synthesis. Further increase in the temperature shows similar features suggesting no change in the morphology of nanostructures. Similarly, Sun and co-workers have shown the effect of temperature on the dimensions of silver nanowires [24a]. When the reaction temperature is lower than 160^0C, the length of nanowires is decreased. While El-Sayed and co-workers have shown the changes in the optical features when the shape of particles is changed from spherical to rod and have reported the linear dependence of the absorption maximum on the aspect ratio of metal nanorods [24b].

Corresponding changes in the morphology of these structures were studied using transmission electron microscopy. Figure 3.10 shows the corresponding TEM micrographs of samples obtained from the above solutions a, b, c and d respectively. Sample a shows the presence of polydispersed silver nanoparticles having diameter in the range 10-50 nm while sample b shows the presence of nanostructures having mixed morphology such as triangular, spherical, and elongated nanoparticles. The TEM image of the sample obtained at 30 °C shows the presence of low aspect ratio nanowires with 3-4 micrometers length and sample d shows the presence of long, high aspect ratio nanowires having diameters in the range 35-40 nm and it is difficult to calculate the length of these structures.

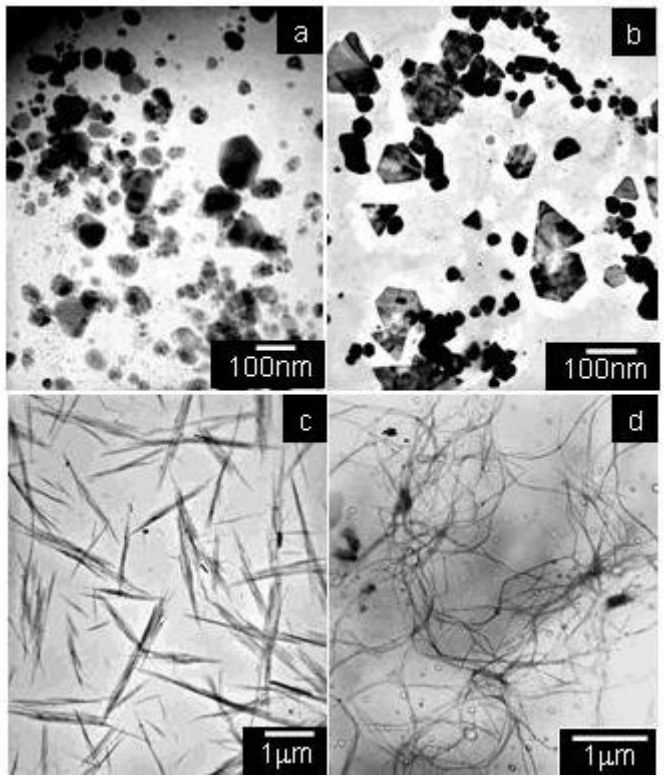

Figure 3.10 *TEM images of silver nanostructures prepared at various temperatures of (a) 20 (b) 25 (c) 30 and (d) 35 °C.*

3.3.8 Effect of solvent:

Many studies have been carried out to understand the effect of solvent refractive index on the optical properties of metal nanowires. These studies show that the shift in the surface plasmon absorption of nanoparticles occurs when solvent refractive index is varied. For example, Mulvaney *et al*. [39] has shown a 23 nm shift in the absorption maximum when the solvent refractive index is changed from 1.336 to 1.583. Recently, a 30 nm shift in the surface plasmon absorption maxima for gold nanoparticles has been shown by Pal and co-workers [40] as a function of solvent refractive index. These spectral shifts agree well with the predictions of Mie theory [41].

Here we show the dependence of the surface plasmon resonance spectrum of the silver nanowires as a function of the refractive index of solvent. Figure 3.11 shows UV-visible spectra of silver nanowires in different solvent and corresponding surface plasmon absorption maxima are summarized in table 3.2.

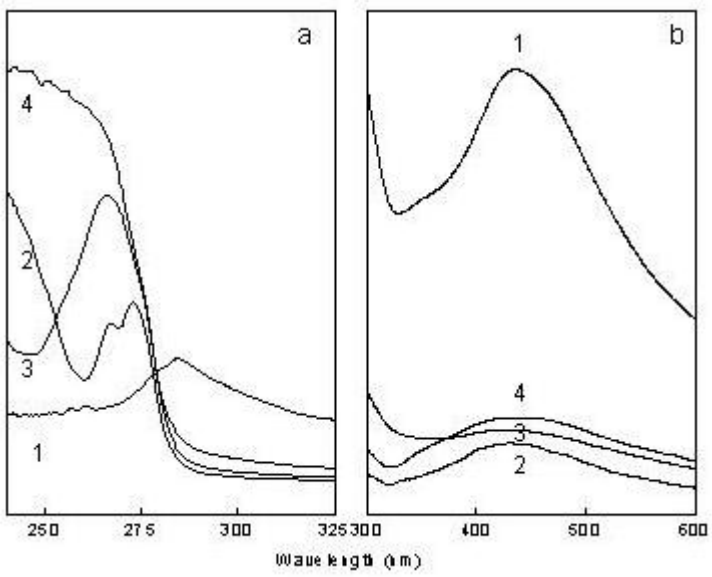

Figure 3.11 *UV visible spectra of silver nanowires shown (a) transverse and (b) longitudinal surface plasmon resonance in various solvents (1) Acetonitrile (2) Tetrahydronfuran (3) 1,4 Dioxan and (4) Dichloromethane of varying refractive indices.*

As the solvent refractive index is changed from 1.34 to 1.42, the transverse surface plasmon absorption maxima (λ_1) shows a red shift from 245 to 272 nm. The position of longitudinal surface plasmon absorption maxima is fairly constant however; peak intensities are decreased with change in the refractive index of the surroundings medium. These results indicate the profound effect of solvent refractive index on absorption characteristics of silver nanowires. These characteristics of silver nanowires may find suitable use in optical sensors and solvent assisted catalytic reactions.

Table 3.2 *Absorption maxima of Surface plasmon resonances of silver nanowires in solvents (1) Acetonitrile (2) Tetrahydronfuran (3) 1,4 Dioxan and (4) Dichloromethane of varying refractive indices.*

No.	Solvent	Refractive index (η)	λ_1 (nm)	λ_2 (nm)
1	Acetonitrile	1.344	243	432
2	Tetrahydrofuran	1.407	248	422
3	1,4 Dioxan	1.422	263	430
4	Dichloromethane	1.424	272	426

3.3.8 Electrochemical measurements:

Earlier electrochemical studies on silver nanostructures are primarily confined to spherical shaped nanoparticles. For example, Chaki et al. have shown the size dependent electrochemistry of monolayer protected silver nanoparticles [42] where the appearance of the redox behaviour (7 nm diameter particles) with oxidation peak at 0.10 V and cathodic peak at -0.08 V is interesting. Aoki et al. have shown the voltammetry of silver stearate stabilized nanoparticles with a reduction wave at -0.6 V and an oxidation wave at 1.1 V [43]. Here we report the electrochemical behaviour of silver nanoparticles and how this behaviour changes with their assembly in one-dimensional nanostructures such as nanowires. Figure 3.12 shows the cyclic voltammograms of silver nanoparticles using working Pt microelectrode and Pt flag counter electrode in acetonitrile-water solution containing 0.1 M $LiClO_4$ as different scan rates. At lower scan rate (0.02 V/s) the redox couple is seen with a prominent oxidation peak at 0.067 V and less intense reduction peak at -0.086 V.

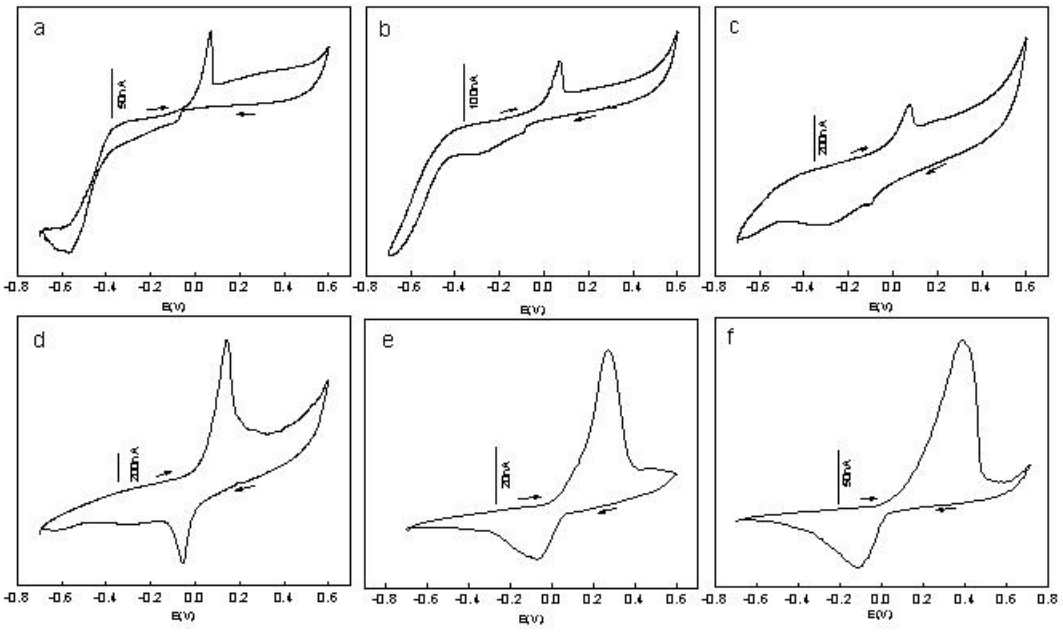

Figure 3.12 *Cyclic voltammograms of silver nanoparticles using Pt microelectrode as a working electrode and Pt flag counter electrode in acetonitrile-water solution containing 0.1 M $LiClO_4$ at various scan rates (a) 0.02 V/s (b) 0.05 V/s (c) 0.5 V/s (d) 1 V/s (e) 3 V/s (f) 5 V/s. Arrows indicate direction of scan.*

At low scan rates, significant reduction in the cathodic peak current arises while anodic peak shows prominent features over the whole range of scan rates, suggesting the preference of these nanoparticles to stay in the oxidized form. However, with increasing the scan rate, the anodic peak shows a tendency to move in the anodic direction and species become more difficult to oxidize while cathodic peak begins to grow and a prominent cathodic peak is seen at higher scan rates. These features indicate that the charge transfer process is relatively free from the control of mass transfer process in the low scan rate region. Also the ratio of Ipa/Ipc becomes very small at much higher scan rates (~30 V/s).

In comparison, cyclic voltammetric features for silver nanowires in acetonitrile-water solution are seen in totally different potential window than for the silver nanoparticles. Figure 3.13 represent typical cyclic voltammograms of silver nanowires illustrating the redox nature at much lower scan rates with oxidation peak at -0.705 V and cathodic peak at -0.96 V. Similar to the features seen for nanoparticles, here cathodic peak currents are much smaller than the corresponding anodic peak currents at lower scan rates.

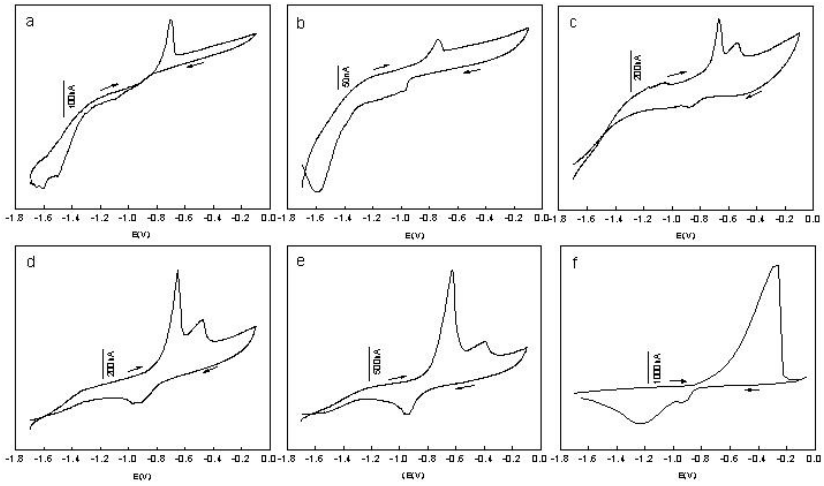

Figure 3.13 *Cyclic voltammograms of silver nanowires using Pt microelectrode as a working electrode and Pt flag counter electrode in acetonitrile-water solution containing 0.1 M $LiClO_4$ at various scan rates (a) 0.02 V/s (b) 0.05 V/s (c) 0.2 V/s (d) 0.5 V/s (e) 1 V/s (f) 3 V/s. Arrows indicate direction of scan.*

The results differ, on the other hand from those of silver nanoparticles at higher scan rates. More discernible changes are seen in the anodic peaks, for example, as we approach the scan rate 0.2 V/s, a the presence of single distinct cathodic wave at -0.888 V (FWHM = 0.049, Ipc=4.857x $x10^{-9}$ A) while anodic peak shows remarkable splitting of the wave into two peaks at -0.668 V (FWHM= 0.046 V, Ipa = 1.9795x $x10^{-7}$ A) and -0.540 V (FWHM= 0.06 V, Ipa = 5.976$x10^{-8}$ A) respectively. Remarkably, at much higher scan rates (0.5 V/s) the cathodic peak grows into a full peak along with the merging of anodic peaks and splitting of cathodic wave.

In summary, the optically pure chiral molecule offers a uniquely organized environment of spatial confinement to form nanowires architectures. TEA capped silver nanoparticles can be organized into ordered arrays to form nanowire structures; this suggests that interparticle-coupling phenomenon can be achieved by using chiral molecules to form the superstructures of nanoparticles without the use of templates. If directional forces like σ-bond, van-der-Waals' interactions etc. are within the material (i.e. part of the building block of clusters), then it is possible to have independent assembly of clusters to form different structures and use of templates can be discarded.

The high stability of the resulting aggregates suggests significant pre-organization of the chiral units and a strongly cooperative assembly process. The most convincing evidence from these analysis is that the assembly is driven by optically active chiral molecules and these assemblies are absent in the presence of optically inactive racemic mixture of these entities. Variations within this basic framework alter the organization of nanoclusters in definite shape. These molecules might apparently assemble in such a fashion that with that chiral bulky dibenzoyl molecule could essentially separate the nucleation and growth rate of silver nanoparticles and kinetically control the tendency of the silver nanoparticles to self-assemble into one dimensional nanostructure. We believe that chiral molecules can serve as good candidates to offer a high degree of organization of nanoparticles, ease of chemical modification, and naturally occurring self-assembly motifs inherent in these systems.

3.4 Conclusion

In conclusion, we have developed a new approach towards the synthesis of silver nanowires by using specially designed organometallic chiral molecules as precursors. The characterization of these structures confirms that nanowires having uniform diameters in the range 30-40 nm and lengths in few micrometers are formed without the use of any extraneous template. The use of chiral and bulky dibenzoyl molecule could essentially separate the nucleation and growth rate of silver nanoparticles and kinetically control the tendency of the silver nanoparticles to self-assemble into one-dimensional nanostructures. Also the synthesis protocol offers a high degree of reproducibility and high yield of nanostructures with controlled morphology.

These materials have excellent stability and show similar characteristics after several months of storage. Also nanowires are highly sensitive to temperature, suggesting that shape of the nanostructures can be altered by temperature. The extensive analysis of these nanowires has been carried out using different techniques and the electrochemical characterization shows completely different electron transfer behavior when compared with that of nanoparticles. We believe that this synthesis can be extended to generate potential 1D nanostructures from other materials that include both metals and semiconductors and the molecular arrangement and final overall architecture of such systems may thus be expected to reflect the light on their future applications in nanodevices.

References

[1] Antonietti, M.; Ozin, G. A. *Chem. Eur. J*. **2004**, *10*, 28.

[2] Chang, Y.-C.; Sanders, G. D. *Phys. Rev B* **1992**, *45*, 9202.

[3] Brus, L. E. *J. Phys. Chem.* **1994,** *98*, 3575.

[4] Stafford, C. A.; Sarma, S. D. *Phys. Rev. Lett*. **1994**, *72,* 3590.

[5] Wong, E.; Sheehan, P.; Lieber, C. M. *Science* **1997**, *277*, 1971.

[6] Mirkin, C. A. *Inorg. Chem*. **2000**, *39*, 2258.

[7] (a) Shenton, W.; Davies, S. A.; Mann, S. *Adv. Mater*. **1999**, *11*, 449. (b) Wei, G.; Nan, C-W.; Deng, Y.; Lin, Y-H. *Chem. Mater*. **2003**, *15*, 4436.

[8] (a) Collier, C. P.; Vossmeyer, T.; Heath, J. R*. Ann. Rev. Phys. Chem*. **1998**, *49*, 371 and references therein. (b) Pacholski, C.; Kornowski, A.; Weller, H. *Angew. Chem. Int. Ed*. **2002**, *41*, 1188.

[9] Murray, C. B., Kagan, C. R.; Bawendi, M. G. *Annu, Rev. Mater. Sci.* **2000**, *30*, 545.

[10] Pileni, M. P. *J. Phys. Chem. B* **2001**, *105,* 3358.

[11] (a) Martin, C. R. *Chem. Mater*. **1996**, *8*, 1739. (b) Martin, C. R. *Science* **1994**, *266*, 1961.

[12] Kotov, N. A.; Meldrum, F. C.; Wu, C.; Fendler, J. H. *J. Phys. Chem*. **1994**, *98*, 2735.

[13] Fendler, J. H. *Chem. Mater*. **1996**, *8*, 1616.

[14] Kotov, N. A. *Multilayer Thin Films,* Wiley-VCH, Weinheim, Germany, **2003**, Ch. 8.

[15] Korgel, B. A.; Fitzmaurice, D*. Adv. Mater*.**1998**, *10*, 661.

[16] Tang, Z.; Kotov, N. A.; Giersig, M. *Science,* **2002,** 297, 237.

[17] Giresig, M.; Pasoriza, I.; Liz-Marzan, L. *J. Mater. Chem*. **2004**, *14*, 607.

[18] Wang, Y.; Jiang, X.; Xia, Y. *J. Am. Chem. Soc*. **2003**, *125*, 16176.

[19] Pasteur, L.; *C. R. Hebd. Seances Acad. Sci*. **1848**, *26*, 535.

[20] Butler,C. L.; Leonard H.; Cretcher, M. *J. Am. Chem. Soc.*; **1933**, *55(6),* 2605.

[21] Zetzsche and Hubacher, *Helu. Chim. Acta*, **1926**, *9*, 291.

[22] Kovari, Z.´N.; Bocskei, Z.; Kassai, C.; Fogassy, E.; Kozma, D.; *Chirality* **2004** *S23–S27*, 16*.*

[23] (a) Henglein, A. *J. Phys. Chem.* **1993**, *97(21),* 5457. (b) Dickson, R. M.; Lyon, L. A. *J. Phys. Chem. B* **2000**, *104*, 6095.

[24] Sun, Y.; Gates, B.; Mayers, B.; Xia, Y.; *Nano Lett*. **2002** *2(2*), 165. (b) Link, S.; Mohamed, M. B.; El-Sayed, M. A. *J. Phys. Chem. B*. **1999**, *103(16)*, 3073.

[25] (a) Lin, S.; Li, M.; Dujardin, E.; Girard, C.; Mann S. *Advanced Mater*. **2005**, *17*, 2549. (b) Sharma, J.; Chaki, N. K.; Mahima, S. Gonnade, R. G.; Mulla, I. S.; Vijayamohanan, K. *J. Mater. Chem*. **2004**, *14*, 970.

[26] (a) Jana, N. R.; Gearheart, L.; Murphy, C. J. *Chem. Commun*. **2001**, *2001*, 617. (b) Murphy, C. J.; Jana, N. R. *Adv. Mater*. **2002**, *14*, 80.

[27] (a) Geddes, C. D.; Aslan, K.; Gyrczynski, I.; Malicka, J.; Lakowicz, J. R. *In Rev. Fluoresc.* **2004**, 365 and references therein.(b) Aslan, K.; Leonenko, Z.; Lakowicz, J. R.; Geddes, C. D. *J. Phys. Chem. B*. **2005**, *109(8)*, 3157.

[28] Bong, D. T.; Clark, T. D.; Granja, J. R.; Ghadiri, M. R. *Anguw. Chem. Int. Ed*. **2001**, *40*, 988.

[29] Seebach, D.; Matthews, J. L.; Meden, A.; Wessels, T.; Baerlocher, C.; McCusker, L. B. *Helv. Chim. Acta* **1997**, *80*, 173.

[30] Clark,T. D.; Buehler, L. K.; Ghadiri, M. R. *J. Am. Chem. Soc*. **1998**, *12*0, 651.

[31] Ranganathan, D.; Lakshmi, C. Karle, I. L. *J. Am. Chem. Soc.* **1999**, *121*, 6103.

[32] Ranganathan, D.; Haridas, V.; Sundari, C. S.; Balasubramanian, D.; Madhusudanan, K.; Roy, P. R.; Karle, I. L. *J. Org. Chem*. **1999**, *64*, 9230.

[33] Ranganathan, D.; Haridas, V.; Gilardi, R.; Karle, I. L. *J. Am. Chem. Soc*. **1998**, *120*, 10793.

[34] (a) Lin, X. Z.; Teng, X.; Yang, H. *Langmuir*, **2003**, *19*, 10081. (b) Culity, B. D. *Elements of X-ray Diffraction*, 2nd ed.; Addison-Wasley: Menlo Park, CA, **1978**.

[35] Sun, Y.; Yin, Y.; Mayers, B. T.; Herricks, T.; Xia, Y. *Chem. Mater*. **2002**, *14,* 4736.

[36] Hostetler, M. J.; Stokes, J. J.; Murray, R. W. *Langmuir* **1996**, *12,* 3604.

[37] Gole, J. L.; Stout, J. D.; Burdo, C.; Lou, Y.; Chen, X. *J. Phys. Chem. B* **2004**, *108(4*), 1230.

[38] (a) Gao, Y.; Jiang, P.; Liu, D. F.; Yuan, H. J.; Yan, X. Q.; Zhou, Z. P.; Wang, J. X.; Song, L.; Liu, L. F.; Zhou, W. Y.; Wang, G.; Wang, C. Y.; Xie, S. S.; Zhang, J. M.; Shen, D. Y. *J. Phys. Chem. B* **2004**, *108*, 12877. (b) Daniels, J. K.; Chumanov, G. *J. Phys. Chem. B* **2005**, *109*, 17936.

[39] Underwood, S.; Mulvaney, P. *Langmuir*, **1994**, *10,* 3427.

[40] Ghosh, S. K.; Nath, S.; Kundu, S.; Esumi, K.; Pal, T. *J. Phys. Chem. B* **2004**, *108*, 13963.

[41] Mie, G. *Ann. Phys*. **1908**, *25*, 377.

[42] Chaki, N. K.; Sharma, J.; Mandale, A. B.; Mulla, I. S.; Pasricha, R.;Vijayamohanan, K. *Phys. Chem. Chem. Phys.* **2004**, *6,* 1304.

[43] Aoki, K.; Chen, J.; Yang, N.; Nagasawa, H. *Langmuir* **2003**, *1*9, 9904.

CHAPTER IV

One step synthesis of *water-dispersible* silver and gold nanostructures and their organized assemblies

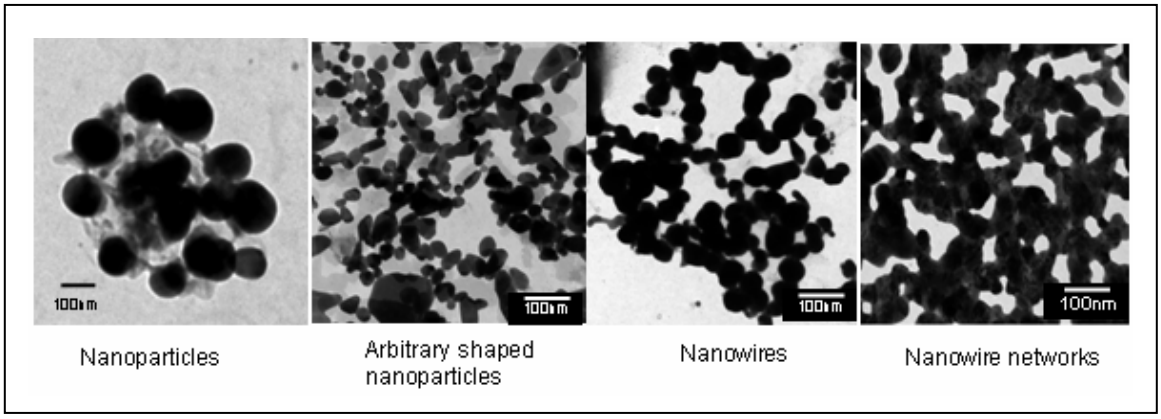

This chapter describes one-step room temperature synthesis of *water-dispersible* nanostructures such as nanoparticles and nanowires of silver and gold using triethyl amine by adjusting the ratio of metal ions to ligand. The control of nanoparticles shape can be achieved by a systematic variation of the experimental conditions. Spectroscopic characterization of nanowires confirms the interaction between amine molecules and silver atoms on the surface while the electrochemical analysis of these nanostructures allows us to understand the variation in their electron transfer properties with shape.

A part of work reported in this chapter has been communicated to ***J. Mat. Chem****., 2006.*

4.1 Introduction

Monolayer protected nanostructured materials have attracted a great deal of attention in recent years because of their unique chemical and physical properties that can be exploited for a wide variety of possible technological applications including optical, electronic and magnetic devices [1-3]. In order to realize these possibilities, it is critical to synthesize the nanomaterials with well-defined size, shape and configuration [4,5]. Earlier, Brust et al. have described the synthesis of isolable, stable; alkanethiolate passivated gold nanoparticles [6]. Since then, considerable efforts have been made to functionalize nanoparticles by simple chemical transformations, with a wide variety of structural units such as aromatic thiolates, ω-substituted alkane-thiolates, and polyhetero-ω-functionalized alkanethiolates [7-9]. Recent advances have demonstrated one phase synthesis of organoamine-protected nanoparticles of Au, Ag and Cu in organic solvents [10]. These monolayer-protected nanoparticles have led to significant interest in developing them as building blocks in catalytic, optical, and electronic applications. Despite these advantages, poor dispersibility of these materials in water hinders their potential applications in biological systems such as biolabeling, molecular markers, biosensors [11,12].

Progress in designing water-soluble monolayer protected clusters has been demonstrated over the last several years. For example, semiconductor quantum dots (QDs) are used as fluorescent tags in biology, magnetic Fe_2O_3 particles are used as contrast agents in magnetic resonance imaging (MRI), and Pd particles are used as green catalysts [13-16].

A considerable development in designing water-soluble monolayer-protected clusters (MPCs) is driven by the type of monolayer. For example, capping agents such as tiopronin [11,17], poly(ethylene glycol) [18], glutathione [19], 4-hydroxythiophenol [20], mercaptobenzoic acid [21], mercaptosuccinic acid [22], lysine [23], sulfonic acid [24] and trimethyl(mercaptoundecyl)ammonium chloride [25] have been used to synthesize water soluble nanoparticles. In spite of the ability of these monolayers to synthesize *water-dispersible* nanoparticles, it is relatively difficult to have a precise control over their desired size, and shape Furthermore, these methods are often

characterized by elevated temperature and result into low yield of nanoparticles. Hence, the synthesis of *water-dispersible* nanostructures at room temperature with well controllable structures still remains a challenge.

As the shape of these nanoparticles, along with the characteristic dimensions, plays an important role in governing the unique material properties, studies of particle shape evolution will provide a mechanistic insight into the manipulation and control of the properties and functions. In chapter 2 and 3, we have discussed novel synthetic methods for the generation of one-dimensional nanostructures. More specifically, chapter two describes the templateless approach to synthesize metallic nanowires by agitation of nanoparticles in aqueous-toluene biphasic mixture while chapter 3 describes synthesis of superstructures of silver nanoparticles in one dimension using an organometallic chiral molecule. In comparison, the present chapter describes an one step synthesis of silver nanoparticles and their nanowire networks in an aqueous phase by using silver nitrate as a starting material with triethyl amine as a stabilizing as well as cluster forming reagent at room temperature just by controlling the metal ions to ligand ratio.

4.2 Experimental section

4.2.1 Materials:

Silver nitrate ($AgNO_3$, 99.9%), Auric chloride ($HAuCl_4$), Silver benzoate, Triethyl amine, and Tetrabutylammonium hexaflurophosphate were purchased from Aldrich Chemicals and were used as received. Water used for all the experiments was deionized with a Milli-Q-reagent water system.

4.2.2 Synthesis of nanowires:

In a typical experiment, 0.1 ml of triethyl amine was added dropwise to a stirred solution of 10 ml of aqueous 1, 2, 5, and 10 mM silver nitrate ($AgNO_3$) and the mixtures were stirred for 10 min. Within 1-10 min, colour of the resulting solution varies (from transparent yellow to dark brown colour) with the initial amount of silver ions, which is indicative of Ag wires with different aspect ratio or morphology. In order to remove uncoordinated amine molecules, resulting solutions were subjected to centrifugation and

the collected precipitate was redispersed in deionized water for further measurements.

4.2.3 Characterization:

UV–visible absorption measurements were carried out at room temperature on a UV-2101PC double beam spectrometer (Shimadzu) using quartz cells (path length 1 cm). Transmission electron micrographs (TEM) were taken by JEOL Model 1200 EX instrument operated at an accelerating voltage of 100 kV. Specimens were prepared by spreading a small drop of diluted dispersions on a carbon-coated copper grid. Thermogravimetric analysis of silver nanowire powder was performed on TGA-7 Perkin-Elmer instrument from 50 to 600 ^{o}C at a scanning rate of 10 ^{o}C/min. FTIR measurements were carried out in the diffuse transmittance mode at a resolution of 4 cm^{-1} on a Shimadzu FTIR-8201 PC instrument using the drop-coated samples on Si(111) wafers. The XPS measurements were carried out using a VG MicroTech ESCA 3000 spectrometer operated at a pressure of 10^{-9} Torr using a monochromatic Mg-Kα source ($h\nu$ = 1253.6 eV) at a pass energy of 50 eV and electron takeoff angle 60^{o}. The overall resolution was ~1 eV for XPS measurements. The alignment of the binding energy was carried out using the C 1s binding energy of 285 eV as a reference. X-ray diffraction of the silver nanowires was carried out at room temperature using a Philips 1730 X-ray diffractometer at 40 kV and 30 mA (1200 W) with filtered Cu-Kα line (λ = 1.5404 Å). All electrochemical measurements were carried out using a three-electrode cell comprised of a Pt micro-electrode (50 μm) as the working electrode, a Pt wire as the counter electrode, and Ag/AgCl reference electrode in an aqueous cluster solution containing tetrabutylammoniumhexafluorophosphate (TBAHFP) supporting electrolyte. Cyclic voltammograms were recorded on Potentiostat/galvanostat (Autolab PGSTAT-30 with GPES software) whereas impedance measurements were carried out in an impedance analyzer (Autolab PGSTAT-30 with FRA software). The alternating current signal amplitude was 10 mV, and the frequency range employed was 100 kHz to 10 mHz; the data was recorded with averaging over three cycles for each frequency.

4.3 Results and discussion

4.3.1 UV-vis spectroscopic analysis:

The interaction between the nucleating metal surface and the organic amine molecule is an important factor to control the structure and morphology of the product. Figure 4.1 shows UV-vis spectra of silver nanostructures prepared with different concentrations of silver nitrate viz.; 1mM (a), 2mM (b), 5 mM (c), and 10 mM (d). At lower concentration (1mM), the UV-vis spectrum exhibits a single surface plasmon peak at 430 nm [26] indicating the sole appearance of silver nanoparticles. On the other hand, as the concentration of starting material increases, the surface plasmon band splits into two bands, as expected for the anisotropic nanostructures. Formation of anisotropic nanostructured materials is evident from the appearance of an additional peak (around 600-800 nm) due to longitudinal surface plasmon along with a former transverse plasmon band at 420 nm for solutions B, and C. These results are in agreement with earlier reports on silver nanowires and nanorods.

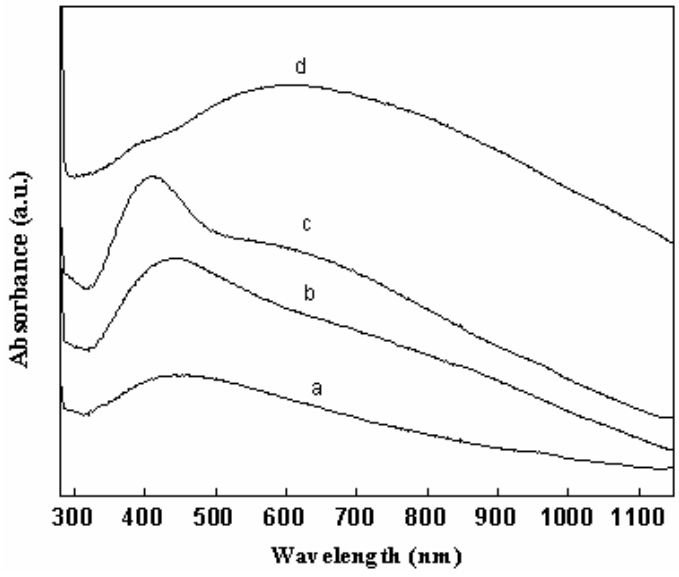

Figure 4.1 *UV-vis spectra of silver nanostructures prepared by varying the concentration of starting material from 1 mM (a), 2 mM (b), 5 mM (c), and 10 mM (d).*

For example, Murphy et al. have reported that the silver nanowires show the appearance of transverse surface plasmon band at 400 nm while a longitudinal surface plasmon band appears in the range 500-700 nm and have shown that the longitudinal plasmon band is red shifted when the aspect ratio was changed from 1-6 [27]. Similarly, at higher precursor concentration (Figure 4.1D), the spectrum exhibits a weak transverse surface plasmon peak at 400 nm and broad longitudinal surface plasmon band in the range 400-1000 nm. It is noted that the transverse plasmon band is blue shifted and shows significant decrease in the intensity. These results are in agreement with the increase in the aspect ratio of nanowires and the formation of nanowire networks at higher concentration of silver salt [27,28]. There is virtually no separation between the transverse and longitudinal plasmon bands unlike those seen for well-dispersed nanowires, possibly due to the formation of interconnected networks of nanowires.

4.3.2 Transmission electron microscopy analysis:

Figure 2 shows typical TEM images taken from the solutions that were used for UV-visible spectroscopy studies as shown in figure 4.1. The change in the electron microscopy images correlates well with optical features. At lower concentrations (1 mM), spherical nanoparticles are predominantly formed with average size in the range 25-50 nm (Figure 4.2A). As the concentration of silver ions increases (2 mM), particles with mixed morphology are produced (Figure 4.2B) in larger quantities. For example, different nanostructures of silver such as spherical particles (~28 %), triangles (~18 %), arbitrary shaped nanostructures (~33 %), and rod like structures (~21 %) are formed at this concentration of 2 mM. At 5 mM concentration of $AgNO_3$, these elongated nanostructures in the process of formation of nanowires are seen (Figure 2C).

These nanowires exhibit coarse surface, which perhaps could be attributed to the directed aggregation and growth of primary particles. The TEM image at a higher concentration (10 mM) shows the formation of nanowires networks having diameter ranging from 30-50 nm and length in few micrometers (Figure 4.2D). Further increasing the concentration of silver shows similar nanowire networks formation.

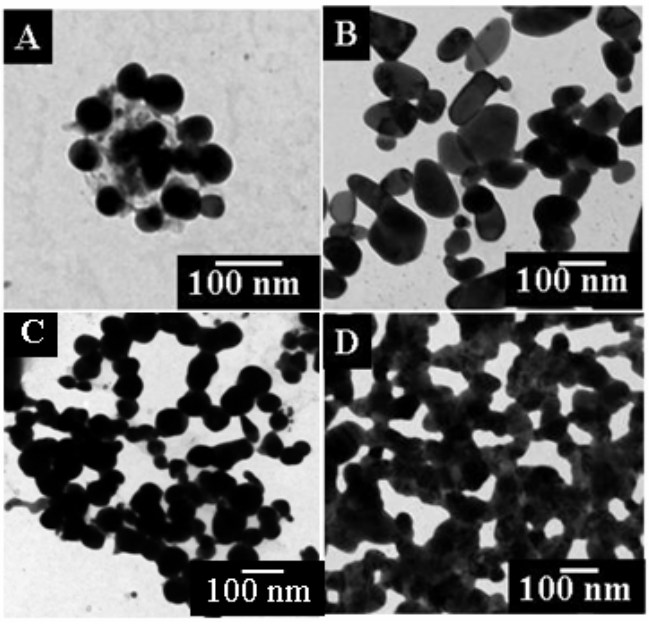

Figure 4.2 *TEM images showing (A) silver nanoparticles (B) mixed morphology nanostructures (C) nanowires, and (D) nanowires networks*

For comparison, other metal salts have also been used as starting material for synthesis of nanowires. Figure 4.3 shows transmission electron micrographs of (A) silver nanowires prepared using silver benzoate and (B) gold nanowires using gold chloride substrate utilizing triethyl amine as capping agent. In both cases branched nanowires with coarse edges have been obtained.

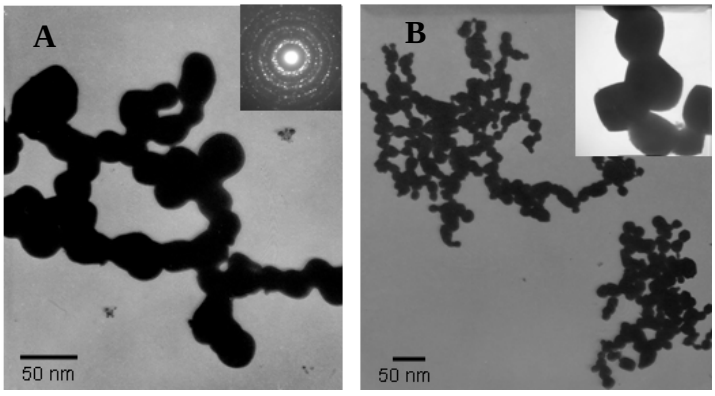

Figure 4.3 *TEM of (A) silver nanowires obtained using silver benzoate substrate with corresponding diffraction pattern in inset, and (B) gold nanowires obtained using similar method using auric chloride as the starting material with magnified image in inset.*

4.3.3 Thermogravimetric analysis:

It is important to study the nature of interaction between the surface-bound amine molecules and the silver surface (core) in terms of strength of the bond and its chemical nature. Hence, TGA measurements were carried out on carefully weighed amounts of purified powders of silver nanowires from 50 to 600 °C and the data obtained is shown in figure 4.4.

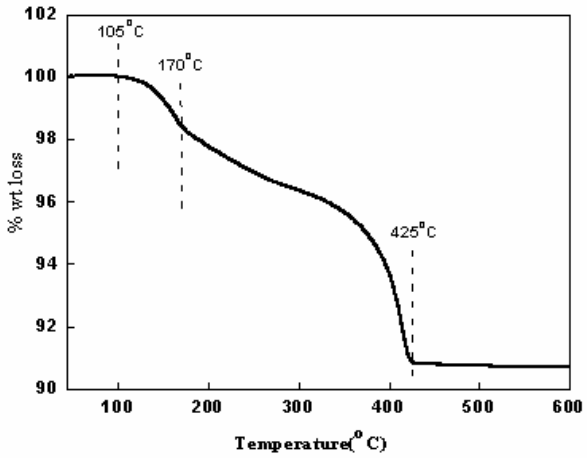

Figure 4.4 *TGA mass-loss characteristics recorded from purified powders of TEA capped silver nanowires during heating from 50 to 600 ^{0}C at 10 ^{0}C/min under 50 mL/min N_2*

It can be seen from the curve that initial 2 % weight loss takes place at 105 °C which is attributed to the unadsorped amine molecules while a distinct weight loss (ca. 6% wt. loss) is seen in the range 170-450 °C which is most likely due to the desorption of strongly bound amine entities. The temperature at which maximal rate of mass loss occurs agrees well with TGA data reported in the literature on desorption of alkanethiols/alkylamines covalently bound to colloidal metal. For example, previous reports on octadecyl amine (ODA) capped silver nanoparticles show similar weight loss (11.5 wt % at 112 °C) for ODA molecules that are covalently bound to silver particles [29]. These TGA results have particular significance since they strongly indicate that the silver surfaces of these organically-capped nanocyrstals are almost exclusively covered by amine molecules.

4.3.4 Fourier Transform Infrared spectroscopy results:

FTIR spectroscopy provides a convenient means of monitoring the attachment of the triethyl amine to silver ions. The FTIR spectrum of triethyl amine obtained from NIST standard reference data has been shown as curve (a) and the spectrum recorded from the silver nanowires deposited on Si (111) substrates is shown as curve (b) in figure 4.5.

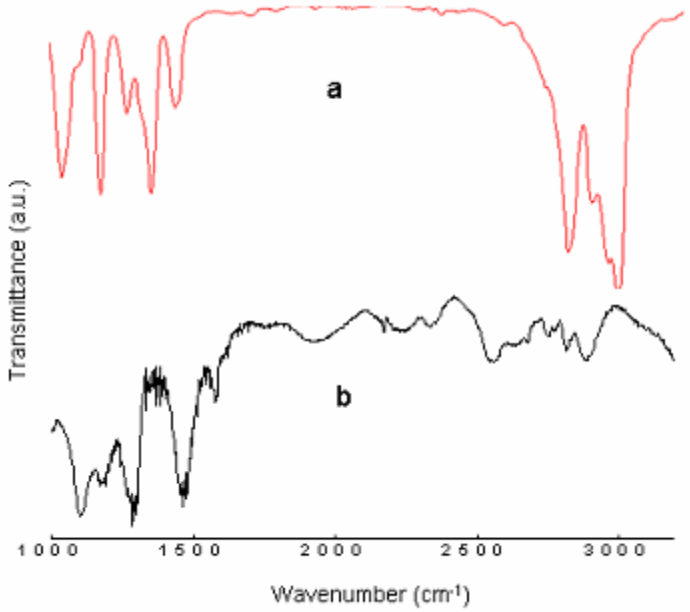

Figure 4.5 *FTIR spectra of triethyl amine obtained from the standard NIST data (curve a) and the silver nanowires deposited on a Si (111) substrate (curve b).*

The methylene antisymmetric and symmetric vibrations [30] of the hydrocarbons were observed to occur at 2936 and 2876 cm^{-1}, respectively in curve 'a' while these bands with reduced intensity appear in curve 'b' with slight shift to lower wavenumber. The presence of these vibrations in the nanowire sample (curve b) confirms that nanowires are coated with triethylamine. The reduction in the intensity of the methylene antisymmetric and symmetric vibration bands in the nanowire sample is perhaps, due to the considerable reorganization of the chains during the formation of nanowire. Figure 4.5a shows prominent and sharp resonance at about 1235 cm^{-1}, which is assigned to the stretch mode of C-N present in the triethylamine [31]. The absorption band at 1235 cm^{-1} has shifted to 1282 cm^{-1} in case of nanowire sample with significant reduction in the

intensity (Figure 4.5b) clearly indicating that the Ag atoms have complexed through amine groups. Similarly, previous reports on FTIR study of primary amine capped gold nanoparticles suggest the disappearance of N-H stretching vibrations of amines. These signatures thus present additional evidence for the involvement of the triethyl amine in the silver nanowires formation.

4.3.5 X-ray photoelectron spectroscopy analysis:

XPS measurements were carried out to gain more insight into the chemical linkage between nanoparticles and the capping agent [32]. The nanowires were drop casted in the form of a film onto a Si(111) substrate and analyzed by XPS. The general scan spectrum of the nanowires shows strong C 1s, Ag 3d and N 1s core levels with no evidence of impurities.

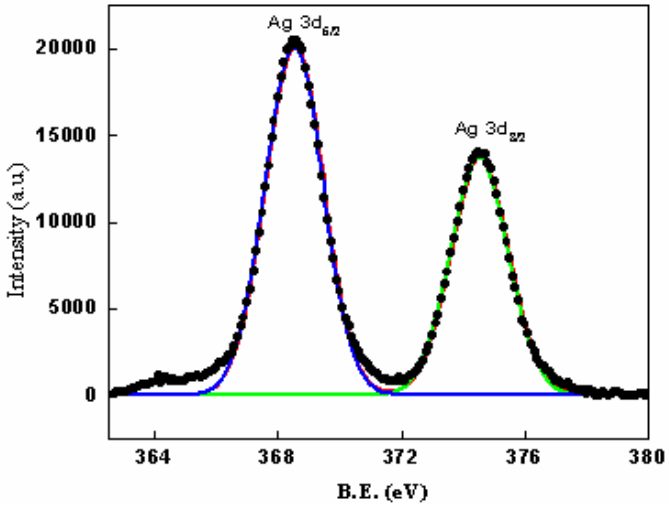

Figure 4 6 *Ag 3d core level spectrum recorded from silver nanowires.*

Figure 4.6 represents the XPS signatures of the Ag 3d doublet (Ag $3d_{5/2}$ and Ag $3d_{3/2}$) for silver nanowires. The peak positions, line shapes, and peak to-peak distance of the Ag 3d doublet are standard measure of the silver oxidation state. The two silver bands i.e. Ag $3d_{5/2}$ and Ag $3d_{3/2}$ are identified at 368.6±0.1 and 374.6±0.1 respectively (splitting of the 3d doublet of ca. 6.0 eV). While shift in the Ag binding energies to the lower values has been reported by Gao *et al.* for poly(vinylpyrrolidone) (PVP) capped silver nanowires having diameter in the range (BE 367.7, 373.8 eV) due to the change

in the silver environment [34]. All experimental values compare well with the standard values for Ag^0. If Ag^+ was present, it would be expected to show up as a peak (or atleast a shoulder on the Ag $3d_{5/2}$ peak) near 370 eV. The absence of peak near 370 eV rules out the presence of any features due to Ag^+ [34].

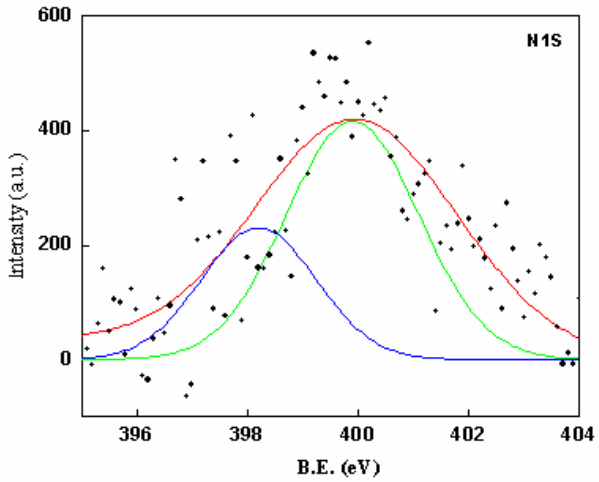

Figure 4.7 *N 1s core level spectrum recorded from silver nanowires*

The most interesting spectrum is of N 1s core level which could be fit into two Gaussians centered at 398.5 and at 400.5 eV BE respectively and is shown in figure 4.7. The lower BE component is tentatively assigned to nitrogen from the un-ionized amine groups (possibly those bound to the silver surface) while the higher BE component arises due to electron emission from the amine groups.

4.3.6 X-ray diffraction analysis:

Figure 4.8 shows the XRD pattern which was taken from collection of silver nanowires of several syntheses, deposited on a Si(111) substrate. All the peaks in the XRD pattern can be indexed as face center cubic (*fcc*) Ag phase with cell parameter *a* = 0.408 nm, which is close to that of the reported data for PVP capped silver nanowires having diameter in the range of 50-70 nm [34]. The four sharp peaks occurring at 38.1^0, 44.3^0, 64.5^0 and 77.8^0 can be assigned to the {111} {200} {220} and {311} diffraction peaks of metallic silver respectively indicating that the silver nanowires synthesized using this method are crystallized in a *fcc* structure similar to bulk silver [34]. Relatively

broad XRD peaks reveal small size of silver crystals and according to the Scherrer diffraction formula the average particle size is approximately 12-30 nm, which is slightly smaller than the size obtained from the TEM micrographs.

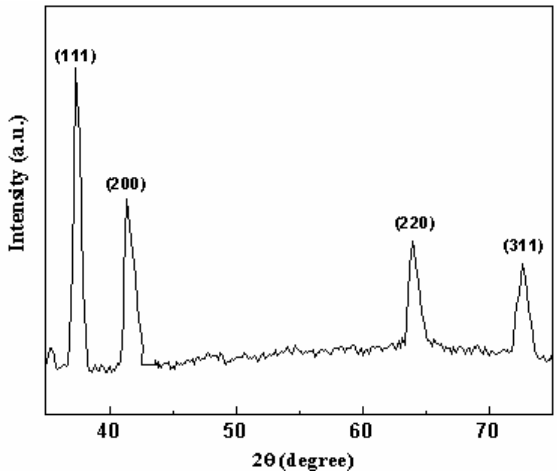

Figure 4.8 *XRD pattern of silver nanowires deposited on Si(111) substrate in the range 35-80^0.*

4.3.7 Cyclic voltammetric analysis:

Previous reports indicate that monolayer protected nanoparticles behave as molecular capacitors in solutions, which are manifested by electrochemical coulomb staircase characteristics. For instance, the double layer capacitance (C_{CLU}, F) of CTAB-protected silver clusters is so small (subattofarad 0.77 aF) [35,36], that single electron transfers to and from them occur at palpably large voltage intervals $\Delta V = e/C_{CLU}$ (e = the electron charge, 1.6×10^{-19} C) that are easily resolved at room temperature on the electrochemical potential axis [37-39]. These studies indicate that electrochemical properties of monolayer protected nanoclusters are sensitive to core size, monolayer thickness, temperature, and dielectric properties [35,36,39,40]. However, the shape dependent electrochemical behavior of monolayer protected clusters remains largely unexplained. Here we discuss the variation in electron transfer behaviour of silver nanostructures with morphological change (corresponding electron micrographs are shown in inset of Figure 4.9) Variation in electron transfer behaviour of nanostructures is evident from the comparison of cyclic voltammograms of all the four samples prepared under similar conditions using different concentrations of $AgNO_3$.

Figure 4.9 shows the cyclic voltammograms of (A) silver nanoparticles (B) arbitrary shaped nanoparticles, (C) nanowires, and (D) nanowire networks at the scan rate 0.01 Vs^{-1} and insets show corresponding transmission electron micrographs.

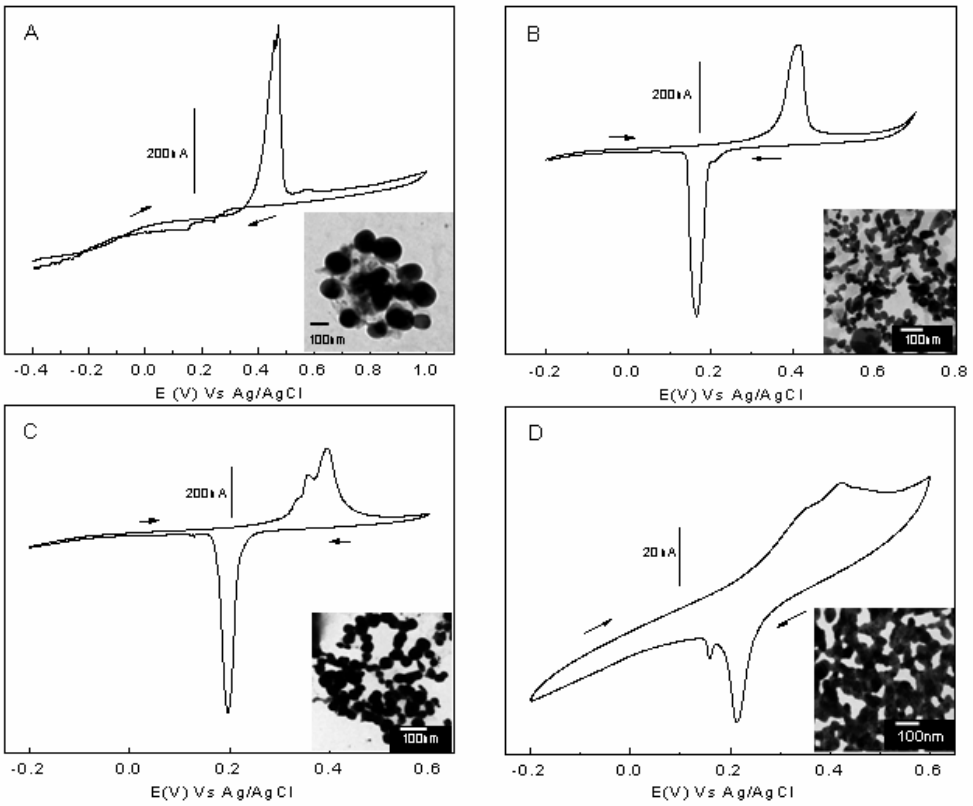

Figure 4.9 *Cyclic voltammograms of (A) silver nanoparticles (B) arbitrary shaped nanoparticles, (C) nanowires, and (D) nanowire in 0.1 M TBAHFP solution. The scan rate was 0.1 V/s and the arrow indicates the scan direction and inset shows corresponding transmission electron micrographs.*

Cyclic voltammogram of triethyl amine capped silver nanoparticles with diameter in the range 50-60 nm using a platinum microelectrode at the scan rate 0.01 Vs^{-1} reveals the presence of a unique redox couple. Voltammogram 'A' depicts a predominant anodic peak at 0.47 V with a full width at half maxima (FWHM) of about 0.047 V and cathodic peak at 0.14 V. There is a large asymmetry in the peaks (Area under the anodic curve 2.42 x 10^{-6} C while area under the cathodic peak is 1.376 x 10^{-7} C) and anodic peak

currents are significantly large. The dynamic nature of the amine molecules attached on the cluster is responsible for this difference.

Table 4.1 *Cyclic voltammetric features of silver nanostructures at different concentrations of $AgNO_3$ at the scan rate 0.1 V/s*

Conc. of $AgNO_3$ (mM)	Shape of silver Nano-structures	Ep_a (V)	Ep_c (V)	ΔEp (V)	$E_{1/2}$ (V)	Ip_a (x 10^{-7}) (A)	Ip_c (x 10^{-7}) (A)	Ip_a/Ip_c	Anodic peak FWHM (V)	Cathodic Peak FWHM (V)
1	Particles	0.47	0.13	0.34	0.17	4.38	0.13	33.69	0.050	0.065
2	Anisotropic structures	0.41	0.16	0.25	0.12	2.65	4.77	0.55	0.047	0.034
5	Nanowires	0.35 0.39	0.19 -	0.16 -	0.12 -	0.53 1.6	7.19 -	0.07 -	0.013 0.028	0.028
10	Nanowires networks	0.34 0.42	0.21 0.15	0.13 0.27	0.065 0.135	0.02 0.05	0.31 0.05	0.064 1	0.049 0.058	0.034 0.010

*Note that all the parameters summarized in table are obtained from the cyclic voltammograms of silver nanostructures (A to D) for second cycle at the scan rate 0.1 V/s as shown in figure 4.9

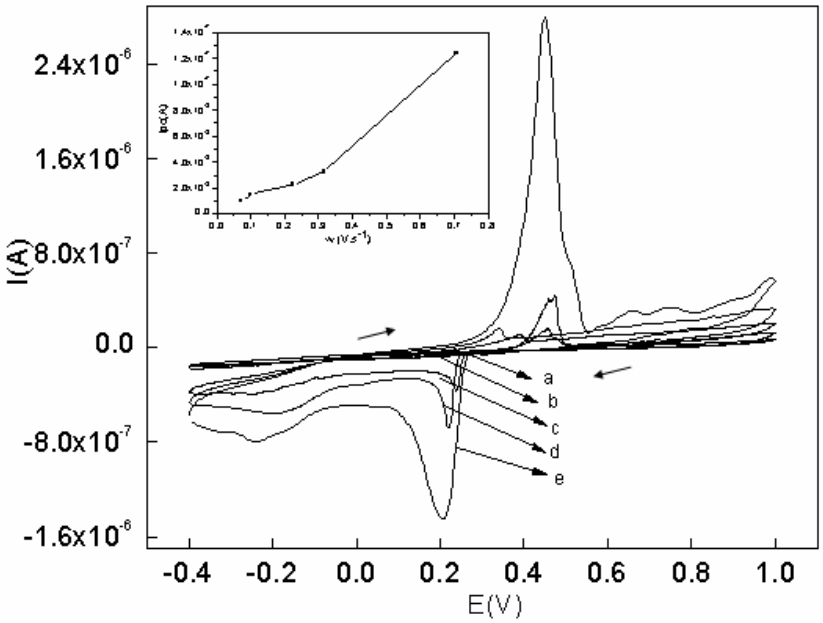

Figure 4.10 *Cyclic voltammograms of silver nanoparticles in 0.1 M $Bu_4NF_6PO_4$ solution at different scan rates 0.005 Vs^{-1}(a), 0.01 Vs^{-1}(b), 0.05 Vs^{-1}(c), 0.1 Vs^{-1}(d), and 0.5 Vs-1 (e).*

Figure 4.10 shows the scan rate dependent behaviour of these silver nanoparticles. In sharp contrast to above voltammogram at 0.01 Vs^{-1} (Figure 4.9A), here cathodic peak becomes more intense with scan rate. At low scan rate, significant

reduction in the anodic peak currents arises due to the inaccessible times scales for reduction suggesting the reorganization of amine on cluster surfaces. Cathodic peak becomes distinct at 0.5 Vs^{-1}. A variation in the Ipc with $\sqrt{\nu}$ is shown in the inset of figure 4.10, where the linear increase in the peak intensities is seen with the scan rate.

Figure 4.9B shows the cyclic voltammogram of silver nanostructures obtained by varying the concentration of silver nitrate to 2 mM and the corresponding transmission electron micrograph is shown in figure 4.2B. Voltammogram shows that the couple is centered around 0.41 V and the cathodic peak at the 0.16 V. In contrast to the cathodic peak (Ip_c:1.857x10^{-8} A) for the spherical nanoparticles (Figure 4.9A), in this case (Figure 4.9B) cathodic peak is distinct at lower scan rates (Ip_c: 4.726x10^{-7} A). Importantly the ratio Ipa/Ipc becomes nearly equal to unity at the scan rate 1 Vs^{-1}.

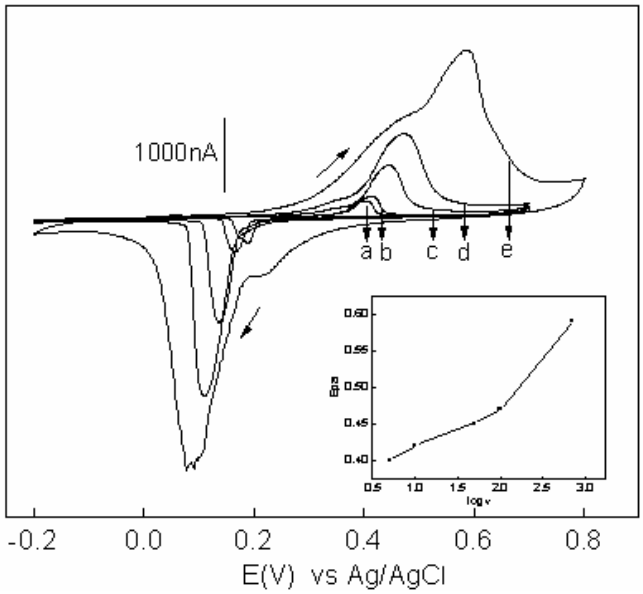

Figure 4.11 *Cyclic voltammograms of silver nanoparticles in 0.1 M TBAHFP solution at different scan rates 0.005 Vs^{-1}(a), 0.01 Vs^{-1}(b), 0.05 Vs^{-1}(c), 0.1 Vs^{-1}(d), and 0.5 Vs-1 (e). The scan rate was 0.1 and the arrow indicates the scan direction. Inset shows the plot of Epa vs. log of scan rate (ν).*

Figure 4.11 shows the scan rate dependent cyclic voltammograms of the anisotropic nanostructures capped with triethyl amine. It is seen from the cyclic voltammograms that the reversible couple observed at lower scan rate becomes quasi-reversible in nature with increasing scan rate. Furthermore, with increasing scan rate the

anodic peak is shifted more towards the anodic side and cathodic peak is shifted in the cathodic direction. This shift in the anodic and cathodic peak potentials is clearly seen in the plot of Ep_a versus log of scan rate (ν) as shown in the inset of figure. 4.11. In contrast to the cyclic voltammograms of the silver nanoparticles (Figure 4.9a) and the anisotropic nanostructures (Figure 4.9b) a predominant cathodic peak is seen for silver nanowires (Figure 4.9c). A close analysis of the voltammograms reveals the presence of single distinct cathodic wave at 0.197 V (FWHM = 0.028, Ip_c=7.157x x10^{-7} A) while anodic peak shows remarkable splitting of the wave in to two peaks at 0.355 V (FWHM= 0.013 V, Ip_a = 5.375x x10^{-8} A) and 0.396 V (FWHM= 0.028 V, Ip_a = 1.569x10^{-7} A) respectively. The second peak potential corresponds to the oxidation peak potential of the redox couple while the appearance of the first peak with low peak intensity suggests interesting changes in the electron transfer behaviour of silver nanowires compared to other shapes as shown in figure 4.9 a and b.

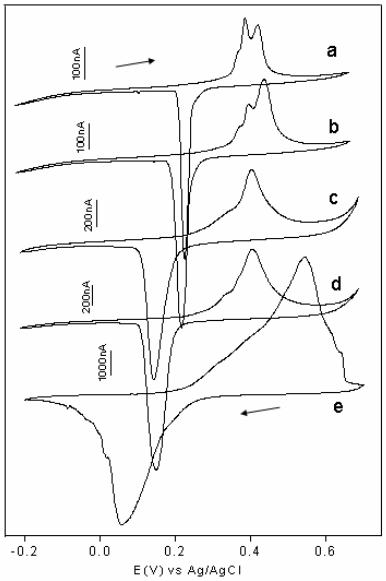

Figure 4.12 *Cyclic voltammograms of silver nanowires in 0.1 M TBAHFP solution at different scan rates 0.005 Vs^{-1}(a), 0.01 Vs^{-1}(b), 0.05 Vs^{-1}(c), 0.1 Vs^{-1}(d), and 0.5 Vs-1 (e).*

The splitting of anodic peak is prominent at the lower scan rates (0,005, 0.01 Vs^{-1}), which shows a subsequent decrease in the first peak at higher scan rates (Figure 4.12). Although the splitting in anodic peak is seen for nanowires sample, the trend in

the shift of anodic peak in the anodic direction and the cathodic peak in the cathodic direction is not changed.

Cyclic voltammograms of networks of silver nanowires (Figure 4.13) show similar electrochemical response except the presence of two redox couples. Cyclic voltammograms of wires clearly depicts the splitting of anodic as well as cathodic peak while in this case cathodic peak splitting is more prominent at lower scan rates (as shown in Figure 4.13). Anodic peaks appear at 0.343 V (FWHM = 0.043, Ip_{a1} = 1.93x10^{-9} A) and 0.423 V (FWHM = 0.064, Ip_{a2} = 6.09x10^{-9} A) and cathodic peaks appear at 0.214 V (FWHM = 0.034, Ip_{c1} = 3.12x10^{-8} A) and 0.159 V (FWHM = 0.01, Ip_{c2} = 5.92x10^{-9} A) respectively. The first couple is prominent at lower scan rates but the peak currents are drastically reduced and cyclic voltammogram shows only single couple features.

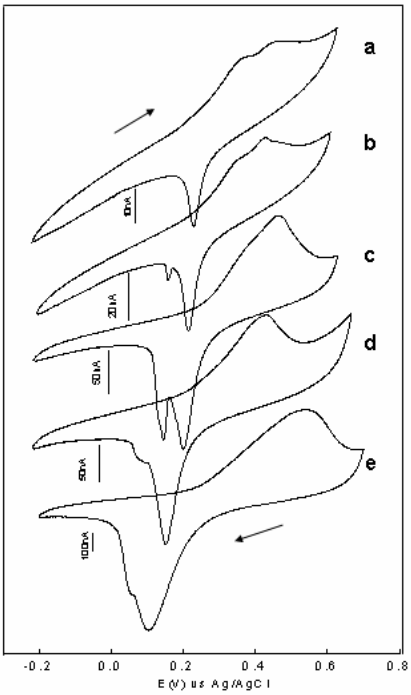

Figure 4.13 *Cyclic voltammograms of solution of networks of silver nanowires in 0.1 M TBAHFP at different scan rates (a) 0.005 Vs^{-1}, (b) 0.01 Vs^{-1}, (c) 0.05 Vs^{-1}, (d) 0.1 Vs^{-1}, and (e) 5 Vs^{-1}.*

In order to understand the effect of shape on the electrochemical properties of the silver nanoclusters, we co-related the peak potential values and ratio of anodic and cathodic peak currents (as summarized in Table 4.1). With changing morphology from

nanoparticles to nanowire (A to D) (see insets Figure 4.9), the anodic peak shows a tendency to move more towards zero potential indicating more facile oxidation when shape changes from particle to wire while cathodic inflection point begins to grow into a peak with an inclination to shift in the cathodic direction. It should be noted that there is a gradual decrease in peak separation (ΔEp), accompanied with a splitting of peaks for nanowires. The considerable decrease in ΔEp value can be co-related to increase in the electron transfer property of silver nanostructures when shape is changed from A to D (Figure 4.9).

Individual peak potentials as well as ratio of peak currents varies as a function of shape change indicating crucial role of kinetic effects on electron transfer properties of Ag_n. The ratio of peak currents shows gradual decrease from 33.5 to 0.06 with change in shape from spherical to wire. Interestingly, a drastic reduction in Ipa/Ipc is seen when shape was changed from spherical to any other shape as seen from table 4.1. These striking differences in the nature of cyclic voltammograms of nanostructures with different morphologies give significant evidence of the change in the electrochemical properties of monolayer protected nanomaterials with shape. However, the detailed reaction mechanism remains largely unknown at the moment and detailed studies are desired to explain all these features.

4.3.8 Impedance analysis:

The changes in electron transfer properties resulting from the change in the shape of nanomaterial can be monitored more accurately by alternate current impedance analysis. A common feature of the impedance plots for all the samples is the semicircle seen at high frequencies. Figure 4.14 shows comparison of impedance plots (Z' vs. Z" plot) of silver nanoparticles (figure 4.14a) and silver nanowires (Figure 4.14b) respectively using Pt disc electrode having diameter 0.5 mm in an aqueous solution containing tetrabutylammonium hexafluorophosphate (TBAHFP) supporting electrolyte. The impedance data shows a (fitted) semicircle at higher frequency region and a straight line in the low frequency region for both nanoparticles and nanowires. The results show that charge transfer resistance (R_{ct}) can be obtained as 1.17 kΩ.cm^{-2} (W_{max} = 152 Hz) and 0.58 kΩ.cm^{-2} (W_{max} = 67 Hz) for nanoparticles and nanowires respectively. The

reduction in R_{ct} value for nanowires as compared to nanoparticles indicates the significant changes in the electron transfer properties. The semicircle domains are reduced with reduction in R_{ct} value suggesting the decrease in charge transfer resistance in case of nanowires. Thus both CV and impedance studies indicate that electron transfer properties are shape dependent and more studies are desired to correlate these with the known ballistic electron transfer properties of individual silver nanowires.

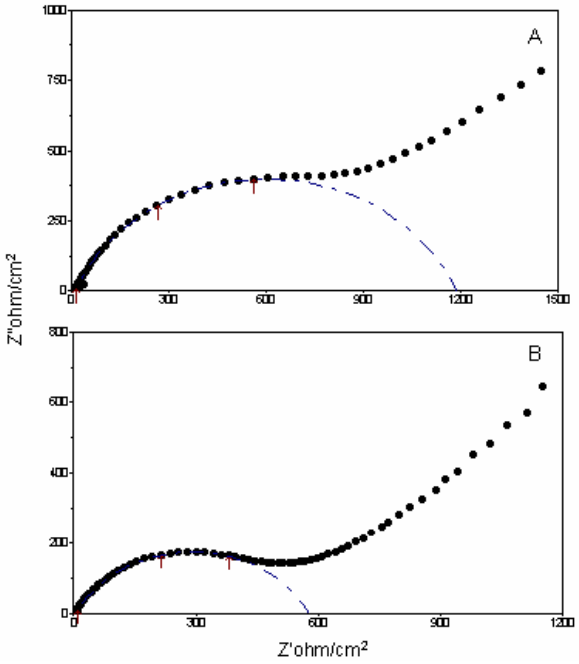

Figure 4.14 *Complex plane impedance plots (Z' vs. Z") of silver nanoparticles (A) and nanowires (B) in aqueous solution using Pt disc (0.5mm, diameter). The frequency range used is 100 kHz–10 mHz with a 10 mV rms signal.*

4.4 Conclusions

In this chapter, we report a new procedure for the one step synthesis of hydrophilic silver nanoparticles and nanowire networks functionalized with tertiary amine. Specifically, we show the usefulness of this simple procedure for controlling the aspect ratios of metal nanostructures with the help of amine surface passivation through results obtained from TEM, UV-vis, FTIR, TGA, XRD, and XPS, as primary characterization

techniques. This extensive characterization leads to the conclusion that the use of partially water-soluble triethyl amine forms a complex with aqueous silver ions regulating the reduction and this controlled variation of metal ion renders the confined growth of the nanoparticles to form nanowire networks. The study of effect of morphologies on electrochemical properties by cyclic voltammetry and impedance analysis shows the striking differences in the nature of electron transfer behaviour. This variation in the electron transfer behaviour suggests possible use of these different morphological structures in electrochemical analysis along with providing new information on the fundamental difference in the electron transfer dynamics in nanowires and nanoparticles.

References

[1] Halperin, W. P. *Rev. Mod. Phys*., **1986**, *58*, 533.

[2] Alivisatos, A. P. *Science* **1996**, *271*, 933.

[3] Xia, Y.; Yang, P. *Adv. Mater.* **2003**, *15(5)***.**

[4] Xia, Y.; Yang, P.; Sun, Y.; Wu. Y.; Mayers, B.; Gates, B.; Yin, Y.; Kim, F.; Yan, H. *Adv. Mater.* **2003**, *15,* 353*.*

[5] Link, S.; El-Sayed, M. A. J. Phys. Chem B **2000**, *104*, 1153.

[6] (a) Brust M., Walker, M. Bethell, D. Schiffrin, D. J. Whyman, R. *J. Chem. Soc., Chem. Commun.*, **1994**, 801.(b) Fink, J. Kiely, C. J. Bethell, D. Schiffrin, D. *J. Chem. Mater.* **1998**, *10*, 922.

[7] (a) Johnson, S. R.; Evans, S. D.; Mahon, S. W.; Ulman, A. *Langmuir* **1997**, *12*, 51. (b) Brown, L. O.; Hutchison, J. E. *J. Am. Chem. Soc.* **1997**, *119*, 12384.

[8] (a) Chen, S.; Huang, K. *Langmuir* **2000**, *16*, 2014. (b) Ingram, R. S.; Hostetler, M. J.; Murray, R. W*. J. Am. Chem. Soc.* **1997**, *119*, 9175.

[9] Hostetler, M. J.; Green, S. J.; Stokes, J. J.; Murray, R. W. *J. Am. Chem. Soc*. **1996**, *118*, 4212.

[10] (a) Hiramatsu, H.; and Osterlob, F. E. *Chem. Mater*., **2004**, *13*, 2509. (b) Chaki, N. K.; Sudrik, S. G.; Sonawane H. R.; and Vijayamohanan, K. *Chem. Commun.,* **2002**, 76.(c) Kumar, A.; Mandal, S.; Selvakannan, P.R.; Pasricha, R.; Mandale, A. B.; Sastry M. *Langmuir* **2003,** *19,* 6277.

[11] Templeton, A. C.; Chen, S.; Gross, S. M.; Murray, R. W. *Langmuir* **1999**, *15*, 66.

[12] Christou, P. *Plant J.* **1992**, *2*, 275.

[13] Dubertret, B.; Skourides, P.; Norris, D.; Noireaux, V.; Brivanlou, A.; Libchaber, A. *Science* **2002**, *298*, 1759.

[14] Perez, J. M.; Josephson, L.; O'Loughlin, T.; Hongemann, D.; Weissleder, R. *Nat. Biotechnol.* **2002**, *20*, 816.

[15] Li. Y.; Hong, X. M.; Collard, D. M.; El-Sayed, M. A. *Org. Lett*. **2000**, *2*, 2385.

[16] Bruchez, J. M.; Moronne, M.; Gin, P.; Weiss, S.; Alivisatos, A.P. *Science* **1998**, *281*, 2013 (b) Chan, W. C. W.; Nie, S. *Science* **1998**, *281*, 2016. (c) Mattoussi, H.; Mauro, J. M.; Goldman, E. R.; Anderson, G. P.; Sundar, V. C.; Mikulec, F. V.; Bawendi, M. G. *J. Am. Chem. Soc.* **2000***, 122,* 12142. (d) Wang, Y. A. Li, J. J.; Chen, H. Y.; Peng, X. G. *J. Am. Chem. Soc.* **2002**, *124*, 2293.

[17] Templeton, A. C.; Cliffel, d. E.; Murray, R. W. *J. Am. Chem. Soc.* **1999**, *121*, 7081.

[18] Wuelfing, W. P.; Gross, S. M.; Miles, D. T.; Murray, R. W. *J. Am. Chem. Soc*. **1998**, *120*, 12696.

[19] Schaff, T. G.; Knight, G.; Shaffigulin, M. N.; Borkman, R. F.; Whetten, R. L. *J. Phys. Chem. B.* **1998**, *102,* 10643.

[20] Chen, S. *Langmuir* **1999**, *15,* 7551.

[21] Johnson, S. R.; Evans, S. D.; Brydson, R. *Langmuir* **1998**, *14,* 6639.

[22] Chen, S.; Kimura, K. *Langmuir* **1999**, *15,* 1075.

[23] Selvakannan, P. R.; Mandal S.; Phadtare, S.; Pasricha, R.; Sastry, M. *Langmuir* **2003**, *19*, 3545.

[24] Shon, Y. S.; Wuelfing, W. P.; Murray, R. W. *Langmuir* **2000**, *17*, 1255.

[25] Cliffel, D. E.; Zamborini, F. P.; Gross, S. M.; Murray, R. W. *Langmuir* **2000**, 16, 9699.

[26] Schwartz, H.; Harel, Y.; Efrima, S. *Langmuir* **2001,** *17*, 3884.

[27] (a) Jana, N. R.; Gearheart, L.; Murphy, C. J.; *J. Phys. Chem. B* **2001**, *105*, 4065. (b) Jana, N. R.; Gearheart, L.; Murphy, C. J.; *Chem. Comm.* **2001**, 617.

[28] (a) Tao, A.; Kim, F.; Hess, C.; Goldberger, J.; He, Rongrui, Sun, Y.; Xia, Y.; Yang, P. *Nanolett.* **2003**, *3*, 1229. (b) Zong, R.-L.; Zhou, J.; Li, Q.; Du, B.; Li, B.; Fu, M.; Qi, X, W.; Li, L. T.; Buddhudu, S.; *J. Phys. Chem. B*. **2004**, *108*, 16713.

[29] (a) Patil, V; Sastry, M. Langmuir **2000**, *16*, 2207. (b) Leff, D. V.; Brandt, L.; Heath, J. R. *Langmuir* **1996**, *12*, 4723.

[30] (a) Hostetler, M. J.; Stokes, J. J.; Murray, R. W. *Langmuir* **1996**, *12,* 3604. (b) Gole, J. L. Stout, J. D.; Burdo, C.; Lou, Y.; Chen, X. *J. Phys. Chem. B* **2004**, *108(4*), 1230.

[31] The Aldrich library of FT-IR spectra, 3nd ed.; Sigma-Aldrich: Milwaukee, **1997**; Vol. 3, pp 175.

[32] Shon, Y.-S.; Gross, S. M.; Dawson, B.; Porter, M.; Murray, R. W. *Langmuir* **2000**, *16*, 6555.

[33] Moulder, J. F.; Stickle, W. F.; Sobol, P. E.; Bomben, K. D. In *Handbook of X-ray Photoelectron Spectroscopy **1995**,* Chastain, J., King, R. C., Jr., Eds.; Physical Electronics: Eden Prairie, MN.

[34] (a) Gao, Y.; Jiang, P.; Liu, D. F.; Yuan, H. J.; Yan, X. Q.; Zhou, Z. P.; Wang, J. X.; Song, L.; Liu, L. F.; Zhou, W. Y.; Wang, G.; Wang, C. Y.; Xie, S. S.; Zhang, J. M.; Shen, D. Y. *J. Phys. Chem. B* **2004**, *108*, 12877. (b) Selvakannan, P. R.; Swami, A.; Srisathiyanarayanan, D.; Shirude, P. S.; Pasricha, R.; Mandale, A. B.; Sastry, M.; Langmuir, **2004**, *20*, 7825.

[35] Chang, W.; Dong, S.; Wang, E. Electrochem. Commun. **2002**, *4*, 412.

[36] (a) Chen, S.; Murray, R. W.; Feldberg, S. W. *J. Phys. Chem. B* **1998**, *102*, 9898. (b) Hicks, J. F.; Templeton, A. C.; Chen, S.; Sheran, K. M.; Jasti, R.; Murray, R. W.; Debord, J.; Schaaff, T. G.; Whetten, R. L. *Anal. Chem*. **1999**, *71*, 3703.

[37] Templeton, A. C.; Wuelfing, W. P.; Murray, R. W. *Acc. Chem. Res.* **2000**, *33*, 27.

[38] Green, S. J.; Stokes, J. J.; Hostetler, M. J.; Pietron, J.; Murray, R. W. *J. Phys. Chem. B* **1997**, *101*, 2663.

[39] (a) Ingram, R. S.; Hostetler, M. J.; Murray, R. W.; Schaaff, T. G.; Khoury, J. T.; Whetten, R. L.; Bigioni, T. P.; Guthrie, D. K.; First, P. N. *J. Am. Chem. Soc.* **1997**, *119*, 9279. (b) Chen, S.; Ingram, R. S.; Hostetler, M. J.; Pietron, J. J.; Murray, R. W.;

Schaaff, T. G.; Khoury, J. T.; Alvarez, M. M.; Whetten, R. L. *Science* **1998**, *280*, 2098.

[40] Chaki, N. K. Sharma, J., Mandale, A. B., Mulla, I. S., Pasricha, R., Vijayamohanan, K. *Phys. Chem. Chem. Phys.* **2004**, *6,* 1304.

CHAPTER V

Solvent mediated electron transfer behaviour of triethylamine capped silver nanoclusters

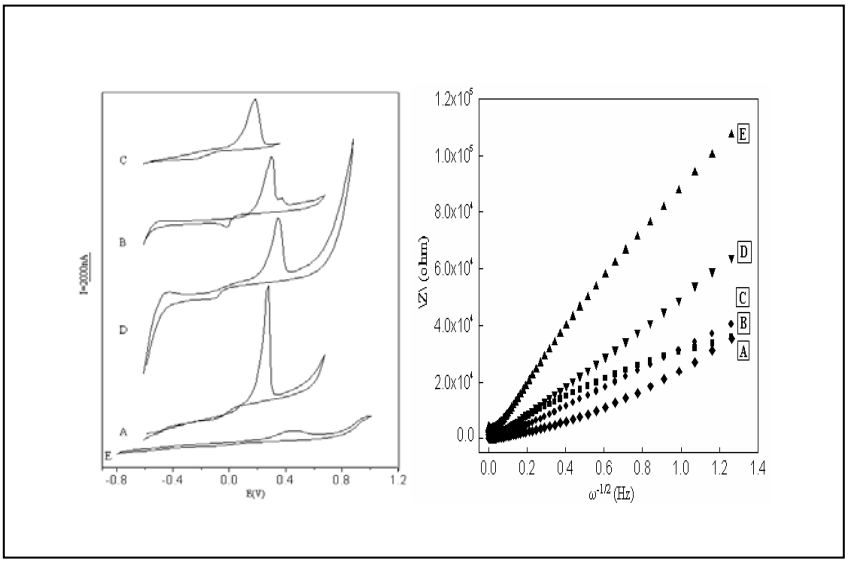

This chapter demonstrates the significance of solvent effects on the electron transfer behaviour of metal nanoclusters. More specifically, in the present work, we delineate the role of solvent molecular properties in guiding the redox behaviour of Ag_n^0/Ag_n^+ couple using cyclic voltammetry and impedance analysis. The study suggests that electron transfer properties of metal nanoclusters in solution are governed by a judicious balance of electrostatic interactions between solvent molecules and an electrical double layer (Stern layer) of clusters and this could be advantageously used to control the selectivity of reactions catalyzed by many metal clusters.

A part of work reported in this chapter has been communicated to ***J. Phys. Chem. B*** *2006*

5.1 Introduction

Monolayer protected clusters with unique electronic structure comprising of a core of metal atoms surrounded by a shell of dielectric capping molecules are subject of intense investigations due to the unique physical, spectral, optical, and electronic properties associated with these artificial molecular entities [1-5]. In particular, increasing availability of these type of nanostructures with highly controllable optical properties have created a widespread interest in photonic crystals, plasmonic waveguides, chemical or biological sensors, optical filters, and optically triggered drug delivery [6,7]. It is well known that noble metal nanoparticles exhibit a strong absorption band in the visible region and this is indeed a small particle effect since they are absent in the individual atom as well as in the bulk. In last few decades, several research groups have been actively pursuing the effects of different parameters, like size, shape, nature of capping molecule, intercluster coupling and chain length on optical properties of these metal nanoparticles [8-10]. These studies reveal that the real-time monitoring of the optical properties of a system of metallic nanoparticles need to consider the presence of a stabilizing ligand shell, a solvent layer on the top of the particles and the electromagnetic interactions between particles [11]. More specifically, the dependence of surface plasmon absorption on bulk properties such as refractive index of the medium play an important role in governing optical characteristics of metal nanoclusters [12,13]. The linear variation of the maxima of surface plasmon with refractive index of the solvent can be treated within the framework of Drude model, where the surface plasmon position λ is related to refractive index of surrounding medium with (n) by the relation,

$$\lambda^2 = \lambda p^2 (\varepsilon^{\infty} + 2\varepsilon_m) \text{ ---------- 1}$$

where, λp is bulk metal plasmon wavelength, ε^{∞} is the high-frequency dielectric constant and ε_m *(=* n^2*)* is the optical dielectric function of the medium [9]. These investigations provide distinct information that accounts for the effect of solvent refractive index on optical properties of nanomaterials [12,13].

Since optical properties of these nanoclusters are found to change with the nature of the solvent, it is natural for us to expect similar variation in electrochemical

properties of monodisperse nanoparticles, which would be the key for a clear understanding of the effects of core size, monolayer thickness and solvent dielectric constant. For example, Murray et al. and Bard et al. have shown that the optical band gap as well as electrochemical peak positions can be critically linked to the quantum confinement of monolayer protected metal and semiconducting nanoclusters respectively. [4,14-15] The voltammetric response of monodispersed metal nanoclusters exhibits quantized oxidative as well as reductive double layer charging and electrochemical equivalent of the coulomb staircase, when e/C_{CLU} is grater than k_BT/e, where e is the electronic charge, C_{CLU} is the integral capacitance of the monolayer protected spherical nanoparticle, k_B is the Boltzmann distribution coefficient and T is the absolute temperature. C_{CLU} can be estimated from the concentric sphere model, $C_{CLU} = 4\pi\varepsilon\varepsilon_0(r/d)(r + d)$, where e is the electronic charge, ε is the monolayer dielectric constant, r is the core radius and d is the monolayer thickness. Recently, Chaki et al. have shown that the nature and chain length of the capping molecules along with core size plays a crucial role in controlling Coulomb blockade behaviour of gold nanoparticles [16]. The *I-V* results demonstrate a Coulomb blockade effect with larger band gaps for clusters passivated with longer chain length, while the aromatic nature of phenyl ring gives nearly linear *I-V* characteristics. These studies reveal that electron-transfer (ET) properties of monolayer-protected clusters are sensitive to the particle core size, monolayer thickness, and dielectric properties [16-19]. These studies reveal that electron-transfer (ET) properties of monolayer-protected clusters are sensitive to the particle core size, monolayer thickness, and dielectric properties [17-19].

The pioneering studies by Marcus recognized the key role of dielectric medium on the electron-transfer properties irrespective of its homogeneous or heterogeneous nature [20, 21]. This theory considered a classical description of the solvent fluctuations, which was subsequently handled in terms of quantum mechanical theory of solvents modes, developed by Levich and co-workers [22]. The Marcus approach is capable to handle ET process provided that the nuclear contribution is dominated by the re-organization of the exterior solvent [20, 21], which is described by the relation,

$$\Delta G^{*}_{os} = - N_o e_o^{\,2}/32\pi\varepsilon_o r_A[(1 - 1/n_D^{\,2}) - (1 - 1/\varepsilon_s)] \quad \text{------- 2}$$

where, N_0 is the Avagadro constant, e_o the fundamental electron charge, r_A the radius of the reactant *A* represented as sphere, n_D the refractive index of solvent, ε_0 the permittivity of free space and ε_s is the static dielectric permittivity.

Alternatively, the mean spherical approximation (MSA) theory provides a promising description of primitive model of ET, in which solute ions in an electrolyte solution are modeled as electrically charged hard spheres of different diameters, while solvent is treated as a continuous dielectric medium [23]. Subsequently, related advanced theories derived an exact solution for the solvation dynamics within the framework of the MSA, which predicts the entire hierarchy of the effect of solvents on the kinetics and thermodynamics of the ET reactions [24]. On the basis of MSA, the expression for Gibbs outer sphere reorganization energy is given by,

$$\Delta G^*_{os} = -N_o e_o^2/32\pi\varepsilon_0[(1 - 1/n_D^2) -(1 - (1/\varepsilon_s) (1/(1 +\delta_{sA}/ r_A)] \text{ ---------- } 3$$

Where δ_{sA} is the MSA distance parameter appropriate for ion and the other symbols are as in eq. 2.

Electrochemical studies on medium effects on the redox potential of the transfer reactions are reported in detail by Fawcett et al. [24b] who have given possible experimental evidence for the involvement of solvent properties such as dielectric permittivity, viscosity, solvent acidity, basicity, and solvent longitudinal relaxation time in ET reactions. These studies suggest significant solvent effects on the electron transfer reactions.

Recent advances in the study of dynamics of electron transfer in monolayer protected clusters show the possible use of solvent dielectric properties in controlling the electrochemical properties [14-19, 25]. Hence, further generic approaches for the study of nanoparticle electron-transfer dynamics, particularly spatial correlations of the solvent in the vicinity of the MPCs, would be valuable.

We aim here to understand the effects of solvent on spectroscopic and electrochemical properties of triethyl amine capped silver nanoclusters. In previous chapter, we have described the synthesis of *water-dispersible* triethyl amine capped

silver nanoclusters and nanowires and studied their shape dependent electron transfer properties while in this chapter, we report the solvent dependent electron transfer behaviour of silver nanoparticles. We envisage that the electron transfer properties of silver nanoclusters can also be governed by the judicious control of electrostatic interactions between solvent molecules and an electrical double layer of clusters, which can be advantageously used to control selectivity of reactions catalyzed by clusters. This is especially significant for several classes of organic reactions where silver nanocluster redox couple shows unique electrocatalytic role like that has been recently reported for Wolff rearrangement [16b].

5.2 Experimental section

5.2.1 Materials:

Sodium benzoate (AgOCOPh), silver nitrate, triethylamine, tetrabutylammonium hexaflurophosphate (TBAHFP), Lithium perchlorate ($LiClO_4$) were obtained from Aldrich Chemicals and were used as received. All solvents like acetonitrile, dichloromethane, methanol, and benzylamine (AR grade) were purchased from Merck and were used after further purification. Water (16 MΩ) used for all the experiments was deionized with a Milli-Q-reagent water system.

5.2.2 Preparation of silver benzoate:

Silver benzoate was prepared by mixing equivalent solutions of silver nitrate and sodium benzoate as described elsewhere [26]. The precipitate was recrystallized from water and the pure crystalline solid was dried in a vacuum oven.

5.2.3 Synthesis of silver nanoclusters

The preparation of triethylamine capped silver nanoparticles was carried out in a single-phase system. In a typical experiment, silver nanoclusters were prepared by dropwise addition of 2 ml of triethyl amine in a stirred solution of silver benzoate (50 mg) in 8 ml of acetonitrile or toluene. Then the solution slowly turned pale yellow and solution showed no further change in colour, implying the completion of the reaction. This

method is reproducible and the organosol prepared by this method remained stable for a couple of months even if stored at room temperature.

5.2.4 Characterization:

UV–visible absorption measurements were carried out at room temperature on UV-2101PC double beam spectrometer (Shimadzu) using quartz cells (path length 1 cm). Cyclic voltammograms were recorded on a Potentiostat/galvanostat (Autolab PGSTAT-30 with GPES software) using conventional three-electrode cell comprised of a Pt micro-electrode (50 μm) as the working electrode, a Pt wire as the counter electrode, and Ag/AgCl reference electrode. Impedance measurements were conducted on an impedance analyzer, Autolab PGSTAT-30 with FRA software. The working electrode was a polycrystalline platinum disk with a diameter 1-mm embedded in teflon rod. A Pt wire and Ag/AgCl electrode were used as counter and the reference electrodes, respectively. Prior to all measurements, the Pt electrodes were polished using alumina slurry down to 0.05 mm on a polishing cloth, followed by sonicating in water and ethanol. The electrodes were then subjected to electrochemical etching by applying rapid potential sweeping in 0.1 M H_2SO_4 within the potential range of -0.5 to +0.6 V at 10 V/s for 5 min. Subsequently the electrodes were then rinsed with a copious amount of deionized water and dried under a stream of N_2. All electrochemical experiments were conducted in a cluster solution containing 0.1 mM tetrabutylammonium hexafluorophosphate (TBAHFP) supporting electrolyte unless otherwise stated and solutions were prepared with deionized water treated with a water purification system (Millipore Corp.). All solvents were deoxygenated by bubbling with high-purity N_2. After deoxygenating, all electrochemical experiments were conducted under a nitrogen atmosphere at the ambient temperature.

5.3 Results and discussion

5.3.1 UV-vis spectroscopic analysis:

The optical properties of triethylamine stabilized silver nanoparticles in various solvents were studied by measuring their absorption due to surface plasmon resonance.

Specifically, aliquot of 30 μl of silver nanoparticles prepared by the method mentioned in the experimental section was diluted to 2 ml with desired solvents and the normalized surface plasmon resonance of all the solutions was measured using UV-visible spectroscopy. Figure 5.1 shows the UV-vis spectra of silver nanoparticles in various solvents such as (A) toluene, (B) acetonitrile, (C) dichloromethane (D) benzyl amine in acetonitrile and (E) methanol. The plot shows that with increase of solvent refractive index, from methanol (1.33) to toluene (1.50), the plasmon peaks linearly shift to longer wavelength (from 428 nm to 442 nm, ~14 nm shift) [9,11,27]. The positions of the surface plasmon maxima as a function of solvent refractive index are illustrated in table 5.1. Different trends in the absorption maximum in benzyl amine may be attributed to the damping of surface plasmon by ligand (due to benzyl amine complexation with silver clusters) and also due to change in refractive index of the solvent due to the presence of acetonitrile as a possible co-solvent.

Table 5.1 Absorption maxima observed for silver nanoclusters in solvents of varying refractive indices

Solvent	Refractive index (n)	λ_{max} (nm)
Methanol	1.326	428
Acetonitrile	1.341	438
Dichloromethane	1.424	440
Toluene	1.494	442
Benzyl amine	1.542	430

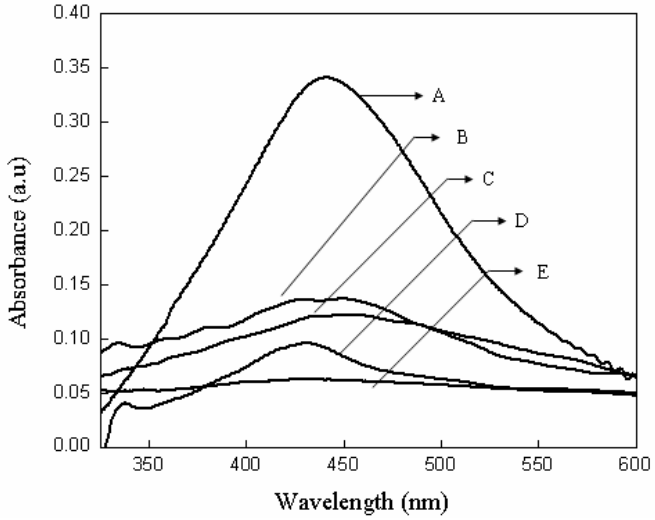

Figure 5.1 *UV-vis spectra of silver nanoparticles having size and concentration in (A) toluene, (B) acetonitrile, (C) dichloromethane (D) benzyl amine in acetonitrile and (E) methanol.*

Figure 5.2 shows the plot of square root of absorption maxima (λ_{max}) as a function of twice of the medium dielectric function. It is evident from the figure that λ_{max} depends linearly on the refractive index of the solvent [28]. This is in agreement with Drude model, which suggests that solvent refractive index alters the surface plasmon band position in a straightforward manner as illustrated by the equation 1, $\lambda^2 = \lambda p^2 (\varepsilon^{\infty} + 2\varepsilon_m)$. These results suggest that electromagnetic field of silver remains extended to sense the refractive index changes occurring at the interface of amine surfactant and bulk. This is in accordance with the Mie theory [29], which states that, the addition and removal of electrons from colloidal particles produces changes in the plasmon band position. The amount of available electrons varies with solvent, which results in variation in the λ_{max} value.

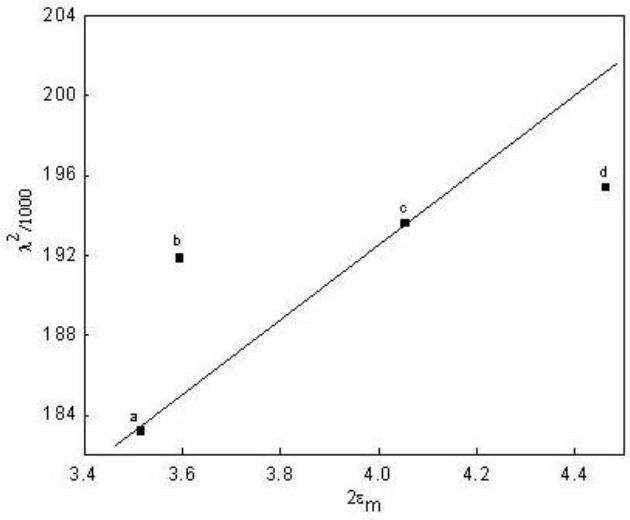

Figure 5.2 *Plot of square root of the absorption maxima as a function of twice the medium dielectric function (ε_m was determined from the expression, $\varepsilon_m = n^2$) for (a) methanol (b) acetonitrile (c) dichloromethane and (d) toluene.*

Though the changes in the wavelength maxima are not very noticeable, full width at half maxima (FWHM) is found to be sensitive to the dielectric constant of medium. UV-visible spectra reveal the ~ 47 nm increase in the FWHM in the surface plasmon

peak of silver nanoclusters when dielectric constant is varied from 2.4 (toluene) to 36.6 (acetonitrile). Also the distinct features of the surface plasmon peak seen in the case of toluene are suppressed with increasing the dielectric constant of the solvent. These results provide distinct information in accounting the effect of solvent dielectric constant on optical properties of clusters and are in agreement with the previous studies on effect of solvent refractive index on the surface plasmon absorbance on monolayer protected nanoclusters of Cu, Ag, and Au [11,20,30]. In order to understand corresponding changes in the electrochemical properties, cyclic voltammetry and impedance analysis of silver nanoclusters were carried out in various solvents systems.

5.3.2 Cyclic voltammetric analysis:

Cyclic voltammetric analysis of silver nanoclusters in acetonitrile reveals the presence of a unique redox couple. The origin of this redox couple can be ascribed to the reaction presented by, $Ag^{+}_{n} + e^{-} \rightarrow Ag^{0}_{n}$

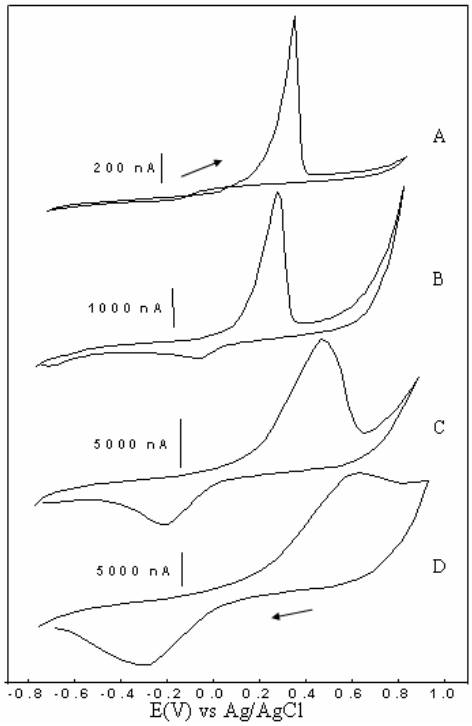

Figure 5.3 *Cyclic voltammograms of silver nanoclusters in acetonitrile solution (using 50 mM TBAHFP supporting electrolyte) at different scan rates (A) 0.05 V/s, (B) 1.5 V/s, (C) 10 V/s, and (D) 30 V/s. Voltammograms*

are recorded using platinum microelectrode and are referred to non-aqueous Ag/Ag^+ electrode. All voltammograms represent the second cycle of the scan. Arrows indicate the scan direction.

At low scan rates the couple exhibits the distinct behavior having features of both quasireversible and irreversible behavior. Voltammogram A (ν = 0.05 Vs^{-1}) (Figure 5.3) shows a strong anodic peak at 0.19 V with full width at half maxima (FWHM) of about 0.04 V and an inflection point around -0.17 V for the cathodic process. With increasing scan rate, the oxidation peak tends to move in the anodic direction (more difficult to oxidize) and an inflection point begins to grow into a full peak with a tendency to move in the cathodic direction. Individual peak potential as well as the ratio of peak current vary as a function of scan rate (ν) indicating the crucial role of kinetic effects on electron transfer properties of Ag_n. The overall behavior is very similar to those observed with dopamine capped silver nanoclusters as reported elsewhere [31].

Voltammogram B (Figure 5. 3: ν = 1.5 Vs^{-1}) represents such a situation, with oxidation peak at 0.25 V (FWHM = 0.13V) and reduction peak at –0.05 V. The couple is centered at 0.1 V with the ratio of peak current (Ip_a/Ip_c) of about 5.2 and the difference in peak potential (ΔEp) around 0.3 V. At high scan rates, quasi-reversibility is evidenced by increased values of ΔEp. The voltammogram (ν = 10 Vs^{-1}) shows more anodically shifted oxidation peak around 0.33 V (FWHM = 0.18 V) along with more cathodically shifted reduction peak around –0.18 V (FWHM = 0.21 V). The couple is centered at 0.08 V with reversal parameters Ip_a/Ip_c around 2.5 and ΔEp of about 0.51 V. However, at higher scan rate, a unique behavior, typically represented by the voltammogram D (ν = 30 Vs^{-1}) is observed. The couple exhibits the most significant behavior having features reminiscent of the reversible electron transfer process around scan rate of 30 Vs^{-1}. The voltammograms D (Figure 5.3) depicts the couple centered at 0.09 V with anodic peak at 0.45 V and cathodic peak at –0.27 V. The ΔEp has a magnitude of about 0.72 V while ratio of peak current (Ip_a/Ip_c) as well as ratio of peak area of anodic to cathodic are nearly equal to the unity. Additionally, the magnitude of FWHM of anodic (0.30 V) and cathodic (0.31 V) peak becomes nearly equal. Further increase in the scan rate reveals no deviation from this behavior as well as the peak potential. According to Feldberg, this higher magnitude of ΔEp offers a unique possibility to perform nonclassical electron

transfer process, in which a chemical reaction is interposed between the reversible electron transfer processes [17,32]. Several factors play important roles in governing the electron transfer properties of the chemical reactions including solvent effect. Towards this end, it is interesting to follow the changes in cyclic voltammetric features of silver nanoclusters in presence of various solvent systems.

Figure 5.4 shows the cyclic voltammograms of silver nanoclusters in various solvents such as (A) acetonitrile, (B) acetonitrile-water, (C) methanol, (D) benzyl amine, and (D) dichloromethane at the scan rate 0.1 V/s. For comparison purpose, all the electrochemical data for silver nanoclusters in various solvents is summarized in table 5.2. A redox couple is observed in acetonitrile with anodic peak at 0.23 V and cathodic peak at -0.12 V at the scan rate 0.1 V/s while in aqueous acetonitrile solution peak positions differ from that in pure acetonitrile. These relative differences in voltammetric features of silver nanoclusters in aqueous acetonitrile suggest the dominant role of water in fine-tuning the electron transfer properties of the Ag_n^0/Ag_n^+ couple, presumably due to solvation, in addition to its well-known nucleophillic behavior.

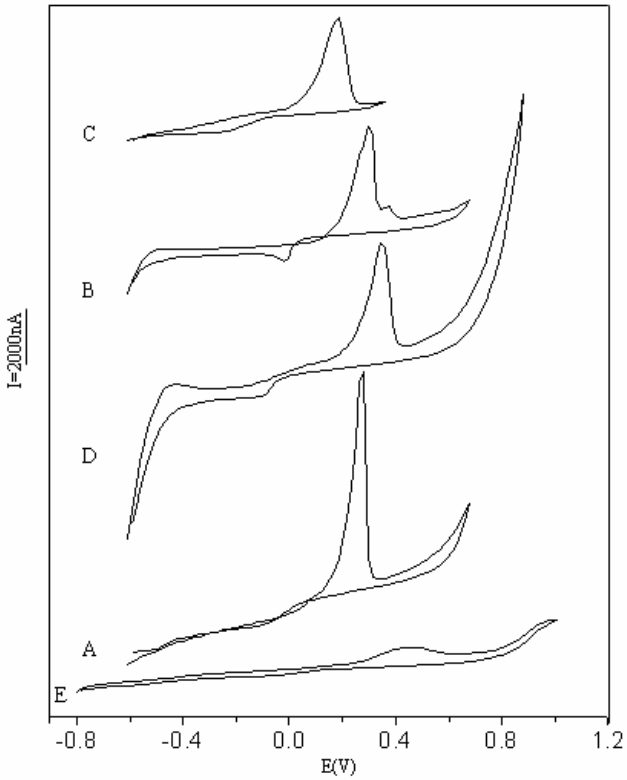

Figure 5.4 *Cyclic voltammograms of silver nanoclusters in various solvents (A) acetonitrile, (B) acetonitrile-water, (C) benzyl amine, (D) methanol, and (E) dichloromethane at the scan rate 0.1 V/s. Voltammograms are recorded using platinum microelectrode and are referred to non-aqueous Ag/Ag^{+} electrode. All voltammograms represent the second cycle of the scan.*

Table 5.2 *Cyclic voltammetric features of silver nanoclusters (size = 5-7 nm) in various solvents at the scan rate 0.1 V/s.*

Solvent	Epa (V)	Epc (V)	ΔEp (V)	Ipa ($\times 10^{-6}$) (A)	Ipc ($\times 10^{-8}$) (A)	Anodic Peak FWHM (V)	Cathodic Peak FWHM (V)	ΔG^{*}_{os} (kJ mol^{-1})
Acetonitrile	0.23	-0.12	0.35	1.0	4.9	0.045	0.194	18.31
Aqu. acetonitrile	0.25	-0.04	0.29	0.31	8.3	0.075	0.075	18.42
Benzyl amine	0.14	-0.25	0.39	0.42	3.4	0.105	0.194	18.43
Methanol	0.29	-0.12	0.41	0.51	5.6	0.090	0.150	-
Dichloromethane	0.42	-0.05	0.47	0.056	1.0	0.209	0.209	13.19

Voltammogram B depicts a predominant anodic wave at 0.25 V having full width at half maxima (FWHM) 0.075 V with another small inflection at 0.32 V (FWHM = 0.014

V) while a cathodic peak appears at -0.047 V. As illustrated in figure 5.4B, the cathodic peak shifts more towards the zero potential (indicating the more facile reduction in aqueous acetonitrile system) and anodic peak moves more towards the anodic direction, while the ΔEp value shows slight decrease in the magnitude (Table 5.2). This shift in the peak potentials in aqueous acetonitrile solution suggests the profound effect of water on electron transfer properties silver nanoclusters.

When the solvent system is changed to benzyl amine-acetonitrile, drastic changes are seen in the positions of peak potentials along with a reduction in the potential window is observed (as shown in Figure 5.4 C). The redox couple is seen with anodic peak at 0.14 V with FWHM 0.105 V and cathodic peak at -0.25 V with FWHM 0.19 V. The redox couple shows the shift towards cathodic direction with peak centered at 0.12 V. Most striking feature of these voltammograms is that with increasing the scan rate, there is no change in the magnitude of ΔEp as compared to other solvent systems. The ΔEp value differs only by 0.05 V when scan rate was changed from 0.1 V to 1 V while negligible variation in ΔEp_c is observed.

Cyclic voltammograms in methanol show the presence of a redox couple with anodic peak at 0.29 V and cathodic peak at -0.12 V (Figure 5.4D). Although these peak potentials of the redox couple are unperturbed in methanol as compared to that in acetonitrile, anodic peak currents are much lower than that in acetonitrile.

Interestingly, cyclic voltammograms of silver nanoclusters in dichloromethane show significant changes as compared to other solvent systems (Figure 5.4E). The anodic wave appears at 0.42 V while a cathodic peak appears at -0.05 V. The shift in the anodic peak potential is more towards the anodic side while shift in the cathodic peak potential is more towards zero potential indicating a facile reduction. However, with increasing scan rate, the anodic peak shows a tendency to move in the anodic direction while cathodic peak shifts in the cathodic direction. It should be noted that there is a significant peak separation (ΔEp increase), accompanied with an increase in FWHM at higher scan rates, perhaps due to increased contribution due to double layer charging.

With this tendency of anodic and cathodic peaks to move in the opposite direction, the redox couple is trying to maintain its thermodynamic value and is predominantly reflected in the linear plot of half wave potential $E_{1/2}$ verses logarithm of the scan rate in all solvents as shown in figure 5.5.

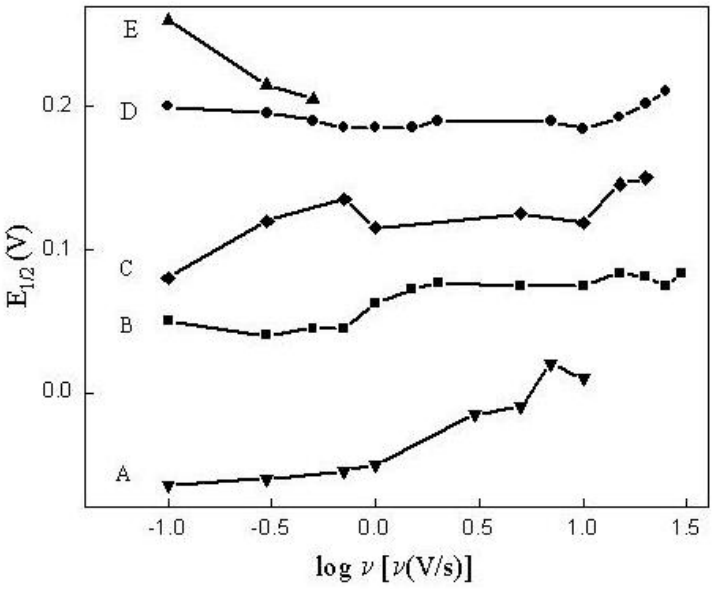

Figure 5.5 *Plots of $E_{1/2}$ vs. log ν for (A) Benzyl amine in acetonitrile, (B) Acetonitrile, (C) methanol, (D) Aqueous acetonitrile, and (E) dichloromethane.*

Figure 5.6 shows plot of ΔEp vs. log ν for all solvent systems. At faster scan rates the process becomes quasireversible as indicated by a significant increase in the peak separation. In the low scan rate region, both the anodic and cathodic currents are unequal and charge transfer process is relatively free from the control of mass transfer process and the reversal parameter ΔEp is greater than 0.2 V.

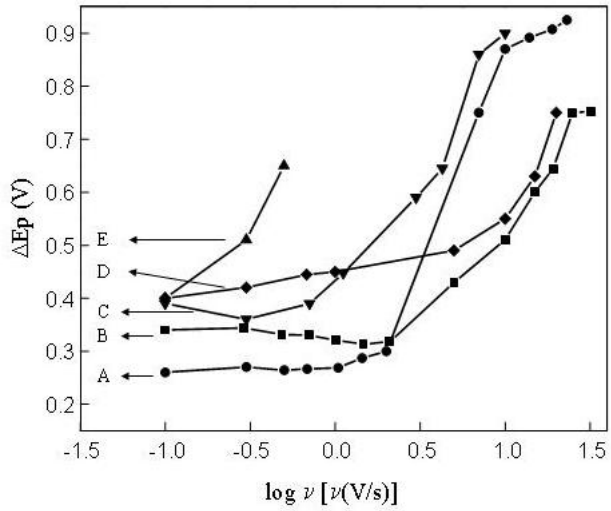

Figure 5.6 *Plots of ΔEp vs. log ν for (A) Aqueous acetonitrile (B) Acetonitrile (C) Benzylamine in acetonitrile (D) methanol (E) dichloromethane.*

Values of ΔG^*_{os} estimated using the Marcus theory (equation 2) are recorded in table 5.2 using the assumption that the reactant radius is 0.5 nm. ΔG^*_{os} varies somewhat, from low 13.19 kJ mol^{-1} for dichloromethane to a high of 18.43 kJ mol^{-1} for methanol. The calculated estimates of ΔG^*_{os} using Marcus relationship are perhaps higher and some contribution from inner reorganization can be expected. These results are in agreement with the previously reported Gibbs solvation energies for the electroreduction reaction of benzophenone in different media [33].

The electrochemical transfer coefficient (α) can be calculated from the equation $\alpha = S_a/(S_a-S_c)$ as stated by Chen [34,35] where S_a and S_c are the slopes of the lines obtained from the plot of cathodic and anodic peak potential vs. ln ν. The linear regression for the plots of Ep_c and Ep_a vs. ln ν shows two straight lines whose slopes are *Sc* and *Sa* respectively and the estimated values of α for silver clusters in various solvents are compiled in table 5.3. These values vary from 0.14 in acetonitrile to 0.98 in dichloromethane. The electron transfer coefficient varies with the solvent but no trend is apparent. The solvation effects are different with each solvent, which is often discussed in terms of solvent dielectric constant. The significant effect of solvent on electron transfer coefficient suggests that the energy barrier for electron transfer is more symmetric in case of methanol as compared to other solvent systems. The structure of

double layer and the field gradient at the reaction site also depends on the solvent. Hence the values of α may be used to assess the possible variation in the relative positions of reaction plane (rp) and outer Helmholtz plane (OHP).

Table 5.3 Variation in slope and transfer coefficient of silver nanoclusters in different solvents obtained from the plot of cathodic and anodic peak potential as a function of ln ν.

Solvent	$Slope_a$ (S_c)	$Slope_c$ (S_a)	α
Acetonitrile	-0.0017	-0.0103	0.14
Aqu. acetonitrile	0.0037	0.008	0.32
Methanol	0.038	0.053	0.42
Benzyl amine in acetonirile	0.035	0.019	0.65
Dichloromethane	0.014	0.0003	0.98

The value of α is close to 0.5 in the case of methanol, although it is somewhat smaller in the case of acetonitrile and its aqueous mixtures, whereas in the case of DCM and benzylamine, it is larger. These results can be interpreted as evidence that the rp is closer to the electrode with respect to OHP in acetonitile but further away in DCM and benzylamine. This situation was convincingly demonstrated by Fawcett and Jaworski in the study of the electroreduction of dicyanobenzene and anthracene in different solvents where the change in the electron transfer coefficients is attributed to the change in the positions of reaction planes with solvent nature [36].

Nature of the plot of Ip vs. $\sqrt{\nu}$ (Figure 5.7) in low scan rate region reveals the dependence of the charge transfer process on linear diffusion of Ag_n towards the electrode. Significantly, the peak current is proportional to the square root of scan rate and the tiny magnitude of slope in this region indicates that the charge transfer process is relatively free from the control of mass transfer process.

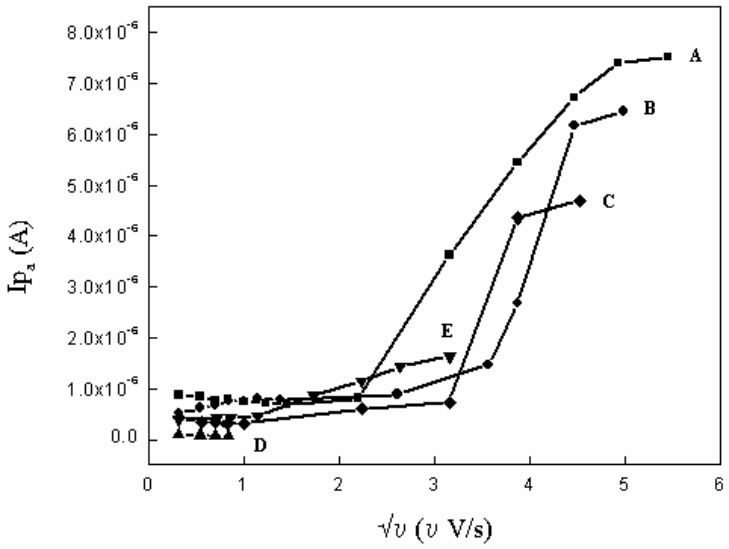

Figure 5.7 *Ip_a vs. $\sqrt{\nu}$ for silver clusters in different solvents (A) acetonitrile, (B) aqu. acetonitrile, (C) methanol, (D) dichloromethane and (E) benzylamine in acetonitrile*.

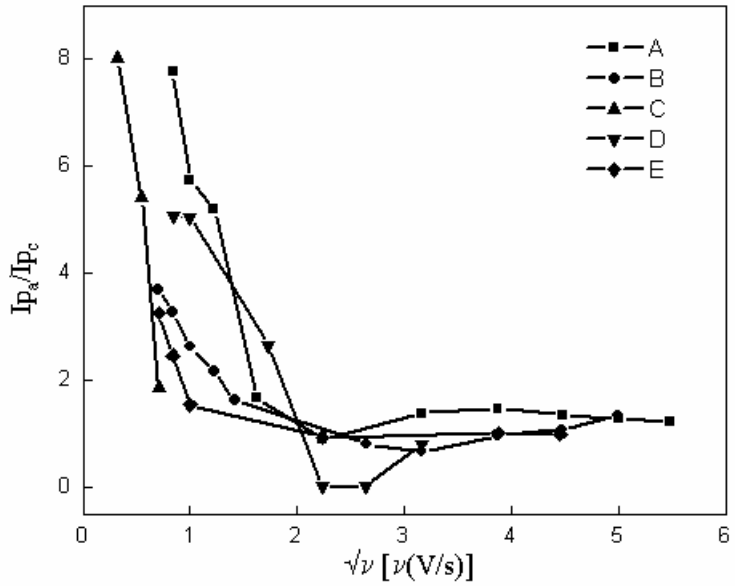

Figure 5.8 *Ip_a/Ip_c vs. $\sqrt{\nu}$ plot of different solvents (A) acetonitrile (B) aqu. acetonitrile (C) dichloromethane (D) benzylamine in acetonitrile (E) methanol.*

This transitional behavior of the redox couple as a function of scan rate is prominently reflected in the plot of Ip_a/Ip_c vs. $\sqrt{\nu}$ (Figure 5.8). At slow scans the anodic peak current is considerably greater than the cathodic peak current. At very rapid scans

the peak currents are equal, and the process appears quite reversible by standard criteria.

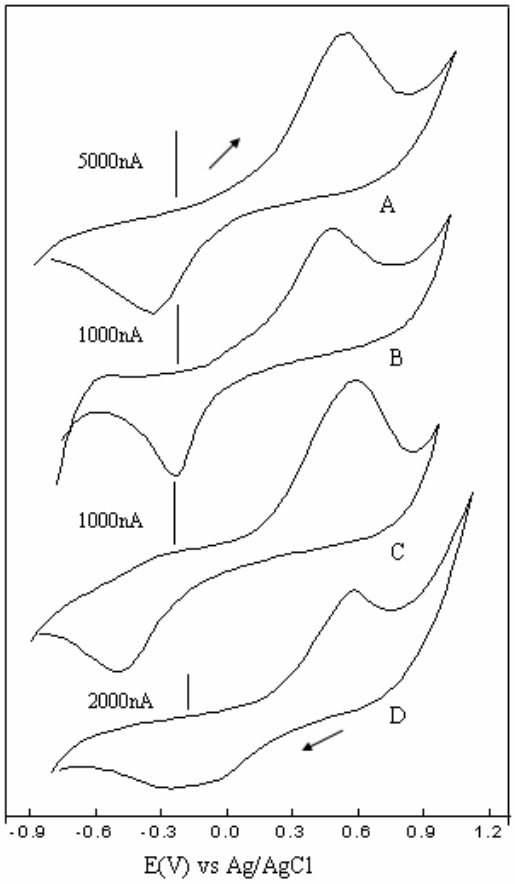

Figure 5.9 *Superimposed cyclic voltammograms of silver clusters (Ag_n) in different solvents (A) Acetonitrile, (B) Methanol, (C) Benzyl amine in acetonitrile, and (D) aqueous acetonitrile at the scan rate of 30, 5, 10, 15 V/s respectively at which the ratio Ip_a/Ip_c = 1. Arrows indicate the scan direction.*

Figure 5.9 shows superimposed cyclic voltammograms of silver clusters (Ag_n) in different solvents (A) Acetonitrile, (B) Methanol, (C) Benzylamine in acetonitrile, and (D) aqueous acetonitrile at scan rates of 30, 5, 10, and 15 V/s respectively at which the ratio Ip_a/Ip_c = 1 in each solvent. These plots show that the ratio Ip_a/Ip_c = 1 at different scan rates for each solvent The CV for dichloromethane is not shown here, since ratio of $Ip_a/Ip_c \neq 1$ in the given range of scan rates. Cyclic voltammetric data for various solvent

systems estimated from these voltammograms for similar silver clusters is presented in table 5.4 indicating an interesting variation in electron properties of silver nanoclusters with solvent. Although there is a significant solvent effect on the peak currents and redox potentials, an exact correlation between the dielectric constant and peak potentials in different solvent systems is difficult to obtain. Since few of the solvents (such as acetonitrile, methanol) have essentially the same dielectric constant and that of dichloromethane is much lower, the solvent effect can also be related to the Gutmann solvent acceptor/donor number (AN/DN) [37] rather than the solvent polarity; further studies in this direction are in progress.

Table 5.4 Solvent dependent electron transfer behavior of silver nanoclusters

Solvent	ε	ν^* (V/s)	Ep_a (V)	Ep_c (V)	ΔEp (V)	$E_{1/2}$ (V)
Acetonitrile	35.9	30	+0.45	-0.27	0.72	+0.09
Aqueous Acetonitrile	40.0	15	+0.55	-0.11	0.66	+0.22
Methanol	32.7	5	+0.37	-0.18	0.55	+0.01
Benzyl amine in acetonitrile	4.6	10	+0.46	-0.44	0.90	+0.01

*Scan rate at which the ratio of peak currents become nearly equal to one for different solvent systems. (Cyclic voltammograms are shown in Figure 5.9). For dichloromethane the peak currents ratio does not become zero at the range of scan rates from 0.1 to 100 V/s and is hence not included here.

Cyclic voltammetry of silver nanoclusters in presence of different concentrations of tetrabutylammonium hexafluorophosphate and lithium perchlorate was carried out in order to understand the effect of nature and the quantity of the electrolyte on the redox behaviour of silver nanoclusters. Accordingly, Figure 5.10 shows voltammetric behaviour of silver nanoclusters recorded using various concentrations of (a) tetrabutylammonium hexafluorophosphate and (b) lithium perchlorate electrolytes respectively. Significantly, this unique transitional behavior of the redox couple as a function of ν is unperturbed by either the nature or by concentration of the supporting electrolyte except a slight shift in anodic peak potentials.

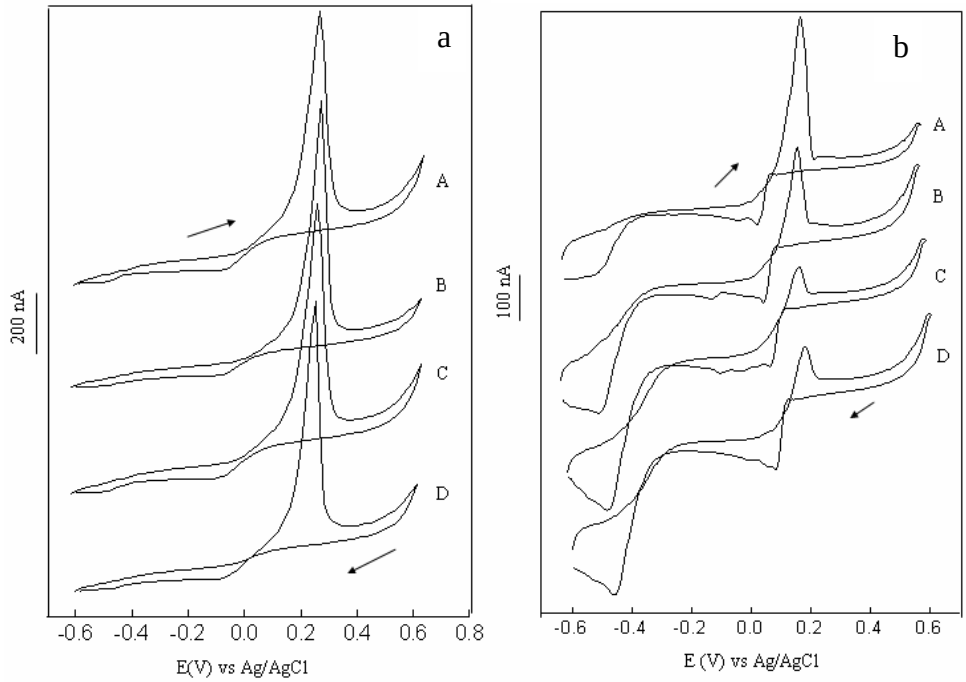

Figure 5.10 *Superimposed cyclic voltammogram of silver nanoclusters (AgN) at different concentrations (A) 10 mM, (B) 15 mM, (C) 20 mM, and (D) 30 mM of supporting electrolyte Tetrabutylammonium hexafluorophosphate (a) and Lithium perchlorate (b). Arrows indicate the scan direction.*

5.3.3 Impedance analysis:

The impedance technique is a powerful approach to understand the ET dynamics and the mass transport features of the electroactive materials in the solution [38]. For example, Figure 5.11 shows a plot of the modulus of real and imaginary parts of impedance data vs. $\omega^{-1/2}$ for silver nanoparticles in different solvents. The plot shows the linear dependence of the modulus of the real and imaginary parts of the impedance data with $\omega^{-1/2}$ and the σ value was obtained from the slops of the graphs for each solvent. The Warburg impedance (W) is given by $W = \sigma\omega^{-1/2} - j\sigma\omega^{-1/2}$, where σ is a constant. The diffusion coefficient can be calculated from the relationship, $\sigma = \sqrt{2}RT/An^2F^2D^{1/2}C$, where n =1, A is the area of electrode, D is diffusion coefficient, C is the MPC concentration in the solution. An approximate estimation of diffusion coefficient shows a decreasing order, beginning from benzyl amine solution in acetonitrile (1.1×10^{-5} cm^2/s) through aqueous acetonitrile (6.5×10^{-6} cm^2/s), methanol (2.5×10^{-6} cm^2/s) up to dichloromethane

($8.0x10^{-7}$ cm^2/s) and these values are consistent with previous electrochemical measurements of diffusion coefficients of various MPCs [16, 39]. The standard rate constant has been calculated using the relationship, $k^0 = RT/n^2F^2R_{CT}C$, assuming, n =1, T = 300 K, C = $9.0x10^{-7}$mol.cm^{-3} and R_{CT} values are obtained from the impedance plots of silver nanoparticles in different solvent. In particular the high frequency data of impedance plot could be fitted to a semicircle, which give rise charge transfer resistance of clusters in each different solvents. The standard rate constant values obtained are $6.01x10^{-5}$ cm/s, $2.27x10^{-5}$ cm/s, $3.56x10^{-5}$ cm/s, $1.93x10^{-5}$ cm/s, $1.15x10^{-5}$ cm/s in aqueous acetonitrile, pure acetonitrile, methanol, dichloromethane and benzyl amine respectively.

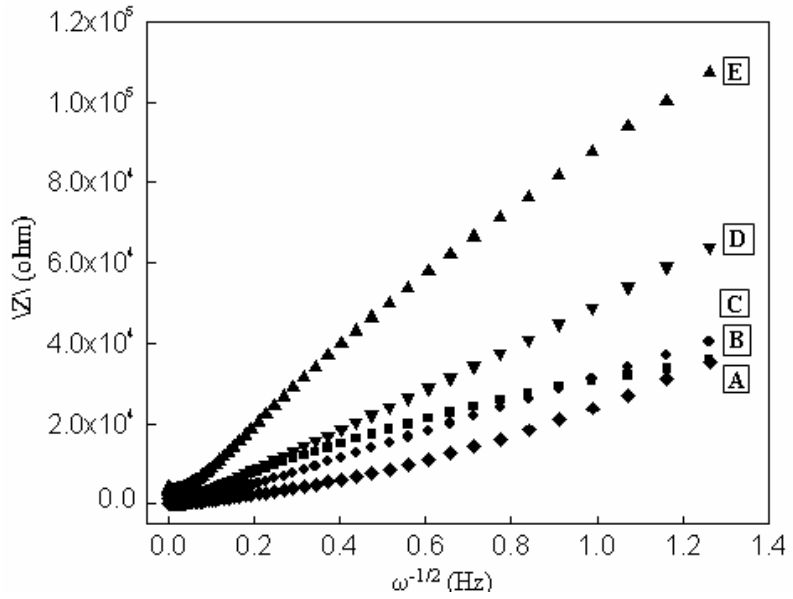

Figure 5.11 */Z/ vs.* $\omega^{-1/2}$ *plots for different solvents (A) benzyl amine in acetonitrile, (B) aqueous acetonitrile, (C) acetonitrile, (D) methanol, and (E) dichloromethane.*

5.4 Conclusions

The present experiments demonstrate significant medium effects on the optical and electrochemical properties of the silver nanoparticles. UV-visible spectra reveal a 14 nm red shift as the solvent refractive index is varied from 1.326 to 1.494 that is in accord with the prediction of Mie theory. With the help of cyclic voltammetry and impedance techniques we have revealed the crucial role of solvent in guiding electron transfer properties of benzoic acid protected silver nanoclusters. The Ag_n^0/Ag_n^+ couple exhibits unique transitional behavior as a function of scan rate, having voltammetric features reminiscent of quasireversible as well as reversible electron transfer process in the above mentioned group of solvents except dichloromethane. The variation in solvent reorganization energies calculated using Marcus theory, gives the possible reason for the changes in electron transfer properties of silver nanoparticles in various solvents. The estimation of rate constants and diffusion coefficients using Impedance analysis of MPCs in various solvents gives the compelling evidence for the significant solvent effects on electron transfer properties. All this information will pave the way for understanding the significant media effects on nanoclusters electron transfer properties that could find wide range of applications in the catalysis reactions in organic solvents.

References

[1] Brust, M.; Walker, M.; Bethell, D.; Schiffrin, D. J.; Whyman, R. *J. Chem. Soc., Chem. Commun.* **1994**, 801.

[2] Terrill, R. H.; Postlethwaite, T. A.; Chen, C.-h.; Poon, C.-D.; Terzis, A.; Chen, A.; Hutchison, J. E.; Clark, M. R.; Wignall, G.; Londono, J. D.; Superfine, R.; Falvo, M.; Johnson, C. S., Jr.; Samulski, E. T.; Murray, R. W. *J. Am. Chem. Soc.* **1995**, *117*, 12537.

[3] Hostetler, M. J.; Murray, R. W. *Curr. Opin. Colloid & Interface Sci.* **1997**, *2,* 42 and references therein.

[4] Templeton, A. C.; Wuelfing, W. P.: Murray, R. W. *Acc. Chem. Res*. **2000**, *33*, 27.

[5] Brown, L. O; Hutchison, J. E. *J. Am. Chem. Soc*. **1999**, *1221*, 882.

[6] (a) Schmid, G. Ed., *Clusters and Colloids* (VCH, Weinheim, Germany, **1994**).(b) Liang, Z.; Susha, A.; Caruso. F. *Chem. Mater*. **2003**, *15,* 3176.

[7] (a) Storhoff, J. J.; Elghanian, R.; Mucic, R. C.; Mirkin, C. A.; Letsinger, R. L. *J. Am. Chem. Soc*. **1998**, *120*, 1959. (b) Knoll, B.; Keilmann, F. *Nature* **1999,** *399*, 134.

[8] Tukervich, J.; Stevenson, P. C.; Hillier, J. Discuss. Faraday Soc., **1951**, *11*, 55.

[9] Mulvaney, P. *Langmuir*, **1996**, *12*, 788.

[10] Alvarez, M. M.; Khoury, J. T.; Schaft, T. G.; Shafigullen, M. N.; Vezmer, I.; Whetten, R. L. *J. Phys. Chem. B* **1997**, *101*, 3706.

[11] Papavassiliou, G. C*. Prog. Solid State Chem*. **1980,** *12*, 185.

[12] Kreibig, U.; Vollmer, M. *Optical Properties of Metal Clusters*; Springer-Verlag: Heidelberg, Germany, 1995; Vol. 25.

[13] Hilger, A.; Cu¨ppers, N.; Tenfelde, M.; Kreibig, U. *Eur. Phys. J. D* **2000**, *10*, 115-118.

[14] Chen, S.; Ingram, R. S.; Hostetler, M. J.; Pietron, J. J.; Murray, R. W.; Schaaff, T. G.; Khoury, J. T.; Alvarez, M. M.; Whetten, R. L. *Science* **1998**, *280*, 2098.

[15] Haram, S. K.; Quinn, B. M.; Bard, A. J. *J. Am. Chem. Soc*. **2001**, *123*, 8860.

[16] (a) Chaki, N. K.; Aslam, M.; Gopakumar, T. G.; Sharma, J.; Pasricha, R.; Mulla, I. S.; Vijayamohanan, K. *J. Phys. Chem. B* **2003**, *107*, 13567. (b) Sudrik, S. G.; Chaki, N. K.; Chavan, V. B.; Chavan, S. P.; Chavan, S. P.; Sonawane, H. R.; Vijayamohanan, K. *Chem Eur. J.*, **2005**, *11*, 1.

[17] (a) Chen, S.; Murray, R. W.; Feldberg, S. W. *J. Phys. Chem. B* **1998**, *102*, 9898.

(b) Remacle, F.; Levine, R. *J. Am. Chem. Soc.* **2000**, *122*, 4084., (c) Nakanishi, T.; Ohtani, B.; Uosaki, K. *J. Phys. Chem. B* **1998**, *102*, 1571.

[18] (a) Andres, R. P.; Bein, T.; Dorogi, M.; Feng, S.; Henderson, J. I.; Kubiak, C. P.; Mahoney, W.; Osifchin, R. G.; Reinfenberger, R. *Science* **1996**, *272*, 1323. (b)

Andres, R. P.; Bielefeld, J. D.; Henderson, J. I.; Janes, D. B.; Kolagunta, V. R.; Kubiak, C. P.; Mahoney, W. J.; Osifchin, R. G. *Science* **1996**, *273*, 1690.

[19] (a) Dorogi, M.; Gomez, J.; Osifchin, R.; Andres, R. P.; Reifenberger, R. *Phys. Rev. B* **1995**, *52*, 9071. (b) Amman, M.; Wilkins, R.; Ben-Jacob, E.; Maker, P. D.; Jaklevic, R. C. *Phys. Rev. B* **1991**, *43*, 1146.

[20] (a) Marcus, R. A. *J. Chem. Phys*. **1956**, *24*, 966. (b) Marcus, R. A. Ibid. **1956**, *24*, 979. (c) Marcus, R. A. *Annu. Rev. Phys. Chem*. **1964,** *15*, 155.

[21] Hwang, J. K.; Warshel, A. *J. Am. Chem. Soc*. **1987**, *109*, 715.

[22] (a) Levich, V. G.; Eyring, H.; Henderson, D.; Jost, W. '*Physical Chemistry: An Advanced Treatise'*, Eds.; Academic press: NewYork, *9B,* **1970**. (b) Levich, V. G. *Adv. Electrochem. Electrochem. Eng.* **1966**, *4*, 249.

[23] (a) Wolynes, P. *J. Chem. Phys.* **1987,** *86*, 5133.(b) Wertheim, M. S. *J. Chem. Phys*. **1971**, *55*, 4291. (c) Blum, L. *J. Chem. Phys.* **1974**, *61*, 2129. (d) Wei, D.; Blum, L. *J. Chem. Phys.* **1987**, *67*, 2999.

[24] (a) Blum, L.; Rosenfeld, Y. *Stat. Phys.* **1991**, *63*, 1177. (b) Blum. L.; Fawcett, W. R. *J. Phys. Chem.* **1992**, *96*, 408.

[25] Pietron, J. J.; Hicks, J. F.; Murray, R. W. *J. Am. Chem. Soc*. **1999**, *121*, 5565.

[26] Lee, V.; Newman, M. S. *'Ethyl 1-Naphthylacetate Org. Syn. Coll'*. **1988**, *5*, 613.

[27] Templeton, A. C.; Pietron, J. J.; Murray, R. W.; Mulvaney, P. *J. Phys. Chem. B* **2000**, *104*, 564.

[28] Ghosh, S. K.; Nath, S.; Kundu, S.; Esumi, K.; Pal, T. *J. Phys. Chem. B* **2004**, *108*, 13963.

[29] (a) Mie, G. *Ann. Phys*. **1908**, *25*, 377.(b) Furstner, A. *Active Metals: Preparation Characterization Applications*; John Wiley & Sons: New York, **1995**. (c) Henglein, A.; Mulvaney, P.; Linnert, T. *Discuss. Faraday Soc*. **1991**, *92*, 31. (d) Ung, T.; Giersig, M.; Dunstan, D.; Mulvaney, P. *Langmuir* **1997**, *13*, 1773.

[30] Sudrik, S. G.; Maddanimath, T.; Chaki, N. K.; Chavan, S. P.; Chavan, S. P.; Sonawane, H. R.; Vijayamohanan, K. *Org. Lett.* **2003**, *5*, 2355.

[31] Chen, S.; Pei, R. *J. Am. Chem. Soc*. **2001**, 10607.

[32] Nelson, R. F.; Feldberg, S. W. *J. Phys. Chem.* **1969,** *73***,** 2623.

[33] Fawcett, W. R.; Fedurco, M. *J. Phys. Chem*. **1993**, *97,* 7075.

[34] Chen, S. *J. Phys. Chem. B* **2000**, *3*, 664.

[35] Chaki, N. K.; Singh, P.; Dharmadhikari, C. V.; Vijayamohanan, K. P. *Langmuir* **2004**, *20,* 10208.

[36] Fawcett, W. R.; Jaworski, J. S. *J. Phys. Chem*. **1983**, *87,* 2972.

[37] (a) Almlof, J.; Faegri, K., Jr.; Korsell, K. *J. Comput. Chem*. **1982***, 3,* 385. (b) Saebo, S.; Almlof, J. *Chem. Phys. Lett.* **1989,** *154*, 83.

[38] Bard. A. J.; Faulkner, L. R. *Electrochmical Methods, Fundamentals and Applications*, 2nd ed.; John Wiley & Sons; New York, **2001**.

[39] Hicks, J. F.; Miles, D. T.; Murray, R. W. *J. Am. Chem. Soc.* **2002**, *124*, 13322.

CHAPTER VI-A

Application of silver nanoparticles as a catalyst in Wolff-rearrangement reaction

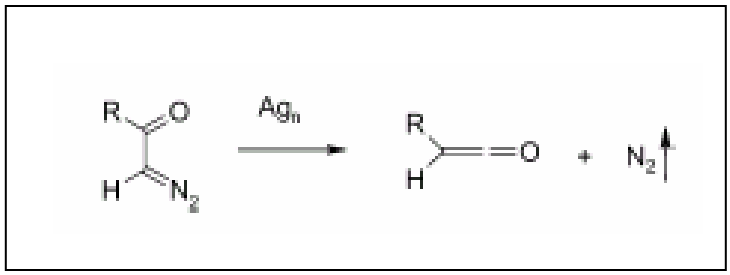

This chapter presents the experimental results suggesting that silver compounds can accept or donate electron either from various co-reagents like α-diazoketone to form silver atoms that spontaneously grow into silver nanoclusters, presumably catalyzing the Wolff rearrangement of α-diazoketones.

*A part of the work reported in this chapter has been published in **Org. Lett**. 2003, 5, 2355.*

6A.1 Introduction

Metal particles in nanoscales have become a subject of intense interest in various fields of chemistry and physics during the past few decades [1-4]. The interest in these particles stems from their unique optical [5], electronic [6] and catalytic [7] properties which are different from their bulk counterparts and hence lead to novel applications in chemical sensors [8], catalysts for a variety of chemical and photochemical reactions [9,10], nanoelectronic devices [11] etc. In particular, they have a characteristic high surface-to-volume ratio, and consequently large fractions of the metal atoms are on the surface and thus are accessible to reactant molecules enabling unique properties [12]. It has been experimentally demonstrated that metal nanoparticles have high catalytic activities for hydrogenation, hydroformylation, carbonylation, hydration, and various other reactions [13-18]. In heterogeneous catalysis, porous materials such as alumina, silica, and zeolite, have many advantages as supports for the formation of nanoparticles because of their high surface areas, shape/size selectivity, and easy separation from the reaction mixtures [19-22]. However, these complex methods of generation of catalysts, always lead to the formation of amorphous nanoparticles. Other methods involve the stabilization of metal nanocatalysts using polymers, complex ligands, or surfactants [15-17,23-25]. However, this kind of stabilization affects the catalytic activity of metal particles. A detailed examination is necessary to evaluate the usefulness of these particles in catalysis. This will enable a much better understanding of what kind of nanoparticles are suitable for catalysis and also to provide an insight on how to make the nanoparticles more stable maintaining their catalytic activity. Previous research reflects on the investigation of the catalytic properties of metal catalysts in colloidal solutions, as well as the effects of the micro-environment on catalytic properties [26]. However, not much emphasis has been given on *in-situ* generation of nanoparticles especially when they are catalyzing organic reactions of industrial significance.

In previous chapter, we have described the synthesis of benzoic acid capped silver nanoparticles and crucial role of solvent in guiding electron transfer properties of these clusters. The analysis suggests that the electron transfer properties of clusters are

governed by judicious control of electrostatic interactions between solvent molecules and an electrical double layer of clusters. This property can be advantageously used to control selectivity of reactions catalyzed by metal clusters.

To further extend this idea, it would be interesting to study the role of silver nanoclusters in catalysis of organic reactions. In this chapter, we discuss results of our efforts to understand the catalysis of organic reactions especially Wolff rearrangements of diazoketones by *in-situ* generated metal nanoclusters. These results may prove germane to the understanding of the catalysis of several organic reactions by metal-nanoclusters especially the co-relation of cluster size with catalytic activity.

Catalytic reactions of α-diazocarbonyl compounds have become an integral part of the modern organic synthesis and the Wolff-rearrangement has a distinguished recognition. The *Z*-configuration specific, Wolff-rearrangement [27-31] of α-diazocarbonyl compounds is a part of the well-known Arndt-Eistert one carbon homologation of carboxylic acids. In addition, it serves as a powerful technique to achieve the ring contraction of cyclic α-diazoketones (Scheme-6A.1).

$$RCOX + CH_2N_2 \rightarrow RCOCHN_2 \quad \ldots\ldots\ldots\ldots \quad (I)$$

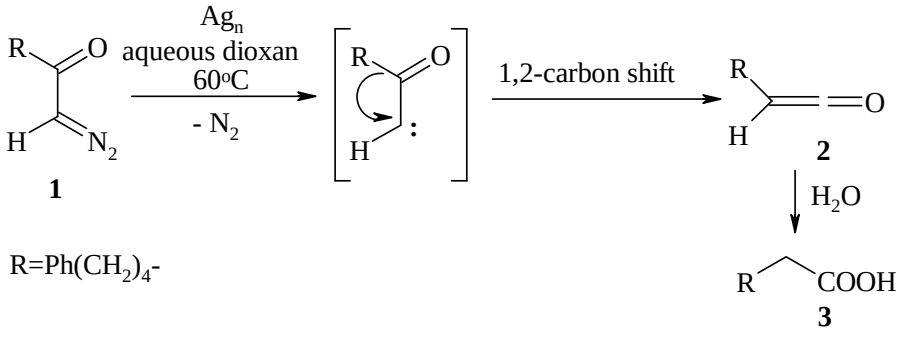

………………………………. (II)

***Scheme 6A.1** Arndt-Eistert reaction: Step (I) involves the reaction between acyl halides and diazomethane to prepare diazoketones. Wolff rearrangement occurs in the second step (II) on treatement of diazoketone with silver oxide or with silver benzoate and triethylamine in presence of water to yield carboxylic acid.*

The rearrangement involves stereospecific 1,2-carbon shift following or accompanying the loss of dinitrogen to ketene via transient, singlet α –ketocarbene [32-34] intermediate. The α -elimination of dinitrogen can be initiated under the influence of thermal energy, ultraviolet light, transition metal catalysts, ultrasound [35] in presence of silver(I) ions or more recently by microwave [36,37]. Among these, transition metal catalysis is widely practiced with the use of several silver(I)-catalysts. Silver(I)nitrate along with aqueous ammonia [31], silver(I) oxide in the presence of either triethyl amine [38,39] (Et_3N) or sodium thiosulfate [40] and silver(I) benzoate [41,42] (AgOCOPh) in combination with Et_3N are more frequently used. The use of co-reagents along with silver(I) compounds leads to more reproducible [39] formation of the rearrangement product in relatively higher yields at much lower temperatures. For example, AgOCOPh [41,42] in combination with Et_3N catalyzes the Wolff-rearrangement of α-diazoketones at room temperature. Although, several suggestions such as reduction of the activation energy, solvent action on the silver(I) compounds leading to catalysis under homogenous conditions or as a base to abstract the most acidic ∝-hydrogen resulting in the formation of carbanion have been made, neither the function of the co-reagents nor the catalytic cycle is well understood.

As a modest beginning in this direction, the nature of the catalyst before and after the reaction was scrutinized, in addition to the usual characterization of products. This chapter demonstrates an experimental proof [1,43,44] of the electron donation by the additives to silver(I) compounds leading to the formation of silver-nanoclusters (Ag_n) during the reaction, which subsequently catalyzes the Wolff-rearrangement of α-diazoketones. The evidence from the surface plasmon absorption of silver nanoclusters formed during the reaction along with transmission electron micrographs (TEM) give unambiguous confirmation for the involvement of nanoclusters.

6A.2 Experimental section

6A.2.1 Materials:

Silver nitrate ($AgNO_3$, 99.9%), silver benzoate (AgOCoPh) Trietylamine (99%), all these high-grade chemicals were purchased from Aldrich chemical company and used without further purification. Dichloromethane (CH_2Cl_2, Fisher, 99.9%), acetonitrile

CH_3CN, Fisher, 99.9%), toluene (Fisher), 1-4 dioxane ($C_4H_8O_2$), methanol (CH_3OH), N, N-dimethylformamide (DMF) solvents were all used as received. Low-conductivity water was obtained from a Millipore Nanopure water purification system.

6A.2.2 Preparation of silver benzoate:

Silver benzoate was prepared by mixing equivalent solutions of silver nitrate and sodium benzoate. The precipitate was collected, washed and dried in a vacuum oven.

6A.2.3 Preparation of Newman's silver reagent:

Addition of 0.5 g (0.002 mole) of silver benzoate in 5 ml of triethylamine gives the orange coloured Newman's silver reagent. Extreme dryness of silver benzoate is desirable as moisture causes precipitation of silver oxide on dissolving in triethyl amine.

6A.2.4 Characterization:

The optical properties of silver nanoparticles and Newman's reagent were monitored on a Hewlett-Packard diode array spectrophotometer (model HP-8452) operated at a resolution of 2 nm. TEM samples of the silver nanoparticles were prepared by placing drops over carbon-coated copper grids and allowing the solvent to evaporate. TEM measurements were performed on a JEOL model 1200EX instrument operated at an accelerating voltage at 120 kV. Purified powder of silver nanoparticles was dissolved in $CDCl_3$, and the proton (1H) NMR spectra were recorded on a Bruker AC 200 MHz instrument and scanned in the range 0-15 ppm. For comparison, the proton NMR spectrum of pure benzoic acid was also recorded in $CDCl_3$. Scanning electron microscopy (SEM) of silver agglomerate was carried on a Leica Stereoscan-440 SEM equipped with a Phoenix Energy dispersive analysis of X-rays (EDX) attachment. X-ray diffraction (XRD) analysis was carried out on a Philips PW 1830 instrument operating at a voltage of 40 kV and a current of 30mA with Cu Kα radiation.

6A.3 Results and discussion

6A.3.2 UV-vis spectroscopic analysis:

The development of orange colour during the preparation of Newman's silver reagent [41-42] using silver (I) benzoate (AgOCOPh) and triethyl amine (Et_3N) gives preliminary indication of the formation of silver clusters.

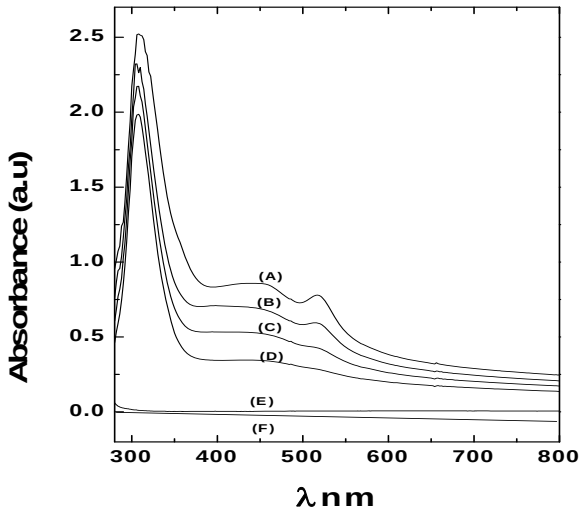

Figure 6A.1 *UV-visible spectroscopic follow-up of the formation of Newman's silver reagent prepared by mixing triethylamine and silver(I) benzoate (A) 1min, (B) 5 min (C) 10 min, (15 min; UV-visible spectra in aqueous 1,4-dioxan of (E) triethylamine, (F) silver(I) benzoate.*

Figure 6A.1 shows the UV-visible spectra recorded from Newman's silver reagent prepared by mixing Et_3N and AgOCOPh at different time interval. Comparison of these spectra with the UV-visible spectrum of Et_3N or AgOCOPh alone gives the evidence for the presence of charge transfer species. UV-visible spectra show a charge transfer absorption band at 308 nm and 517 nm. With time, the intensity of the band (at 517 nm) in the visible range decreases along with concomitant rise in the peak intensity of the band at 308 nm in the ultraviolet region. Significantly, this latter absorption (around 308 nm) corresponds to surface plasmon characteristic of silver nanoclusters (Ag_n) [1], since

silver ions are devoid of any UV-visible absorption and also the metallic sliver absorbs in the vacuum UV region.

The surface plasmon resonance band obtained at 308 nm shifts bathochromically with time to give a relatively stable optical response around λ = 436 nm after 12 h as shown in figure 6A.2.

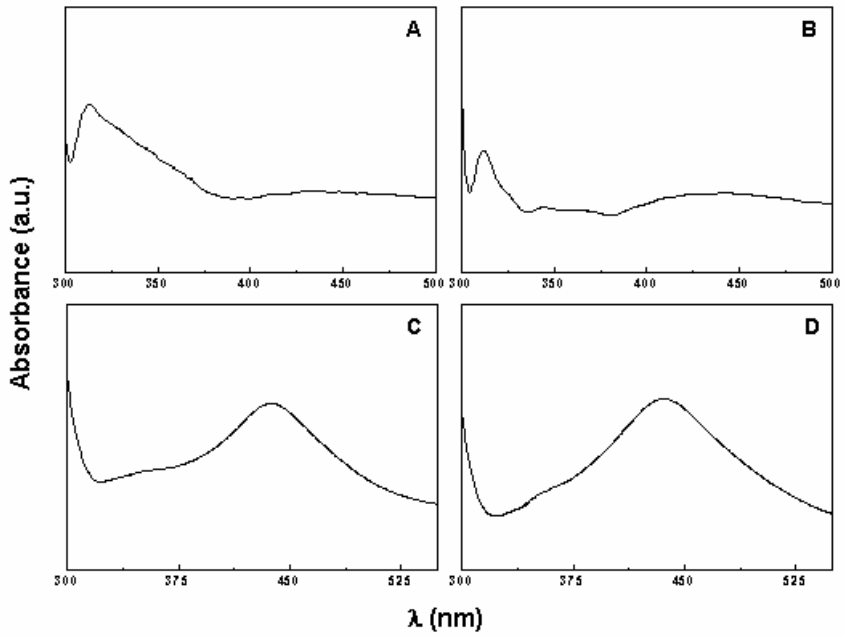

Figure 6A.2 *UV-visible spectra of the Newman's silver reagent (Ag_n) in Toluene at different time intervals, (A) 30 min (B) 12 h (C) 24 h (D) seven days.*

6A.3.3 Transmission electron microscopy analysis:

This phenomenon of appearance of surface plasmon peak and shift in the peak position can be understood in terms of growth of particles of chemically identical silver clusters (Ag_n). TEM and selected area diffraction (SAED) of the sample specimen was taken at different intervals to provide conclusive evidence in this direction. Figure 6A.3 shows the TEM image of Newman's silver reagent prepared using silver benzoate and triethyl amine at different time intervals of 0.5 h (A) and 12 h (B) along with the particle size distribution. The corresponding diffraction pattern is shown in the inset.

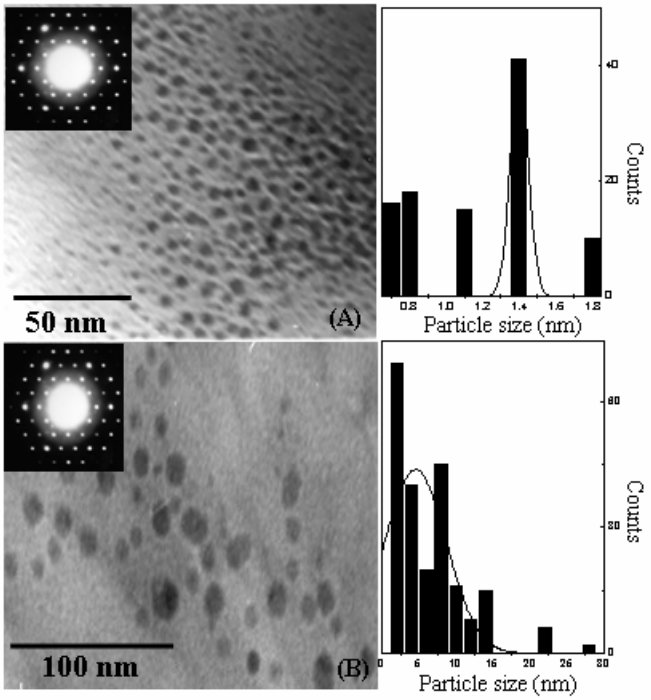

Figure 6A.3 *Transmission electron micrographs of the Newman's silver reagent prepared using silver (I) benzoate and triethylamine at different time intervals (A) 0.5 h; (B) 12 h along with particle size distribution. The corresponding electron diffraction pattern is shown in an inset.*

The TEM image (Figure 6A.3A) obtained after half an hour shows the presence of nearly monodispersed spherical particles having an average size of 1.4 nm ($\sigma \pm 0.048$ nm), while similar analysis performed after 12 h (Figure 6A.3B) formed relatively larger clusters (0.5-15 nm) having average particle size of 4.6 nm ($\sigma \pm 4.2$). Importantly, all the electron diffraction patterns [inset of Figure 6A.3 (A), (B)] are identical to the structure of metallic silver (fcc, a= 4.104 Å).

6A.3.4 UV-visible spectroscopy results:

The optical properties of nanoclusters depends on a number of factors, among which particle size as well as shape are the most important [1,45,46]. In addition, surface plasmon is strongly influenced by the dielectric constant of the medium, which is another significant feature of these Ag_n clusters. Figure 6A.4 shows the UV-visible spectra of

Newman silver reagent (Ag_n) in different solvents such toluene (A), dichloromethane (B), 1,4-dioxane (C), methanol (D), acetonitrile (E) and N, N-dimethylformamide (F).

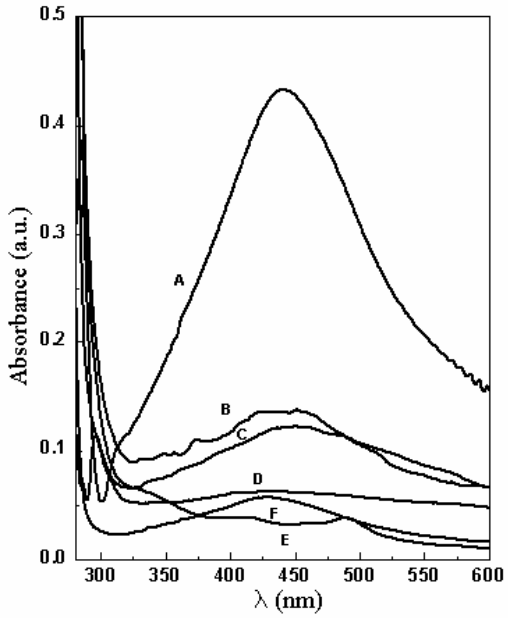

Figure 6A.4 *UV-visible spectra of the Newman's silver reagent (Ag_n) in various solvents, (A) Toluene, (B) Dichloromethane, (C) 1,4-Dioxan, (D) Methanol, (E) Acetonitrile, (F) N, N-Dimethylformamide.*

With increasing dielectric constant, the strong absorption at λ= 439 nm in toluene with full width at half maxima (FWHM) of 55.39 nm is gradually suppressed to show a nearly plateau like nature around λ= 436 nm in N, N-dimethyl formamide (Dielectric constant = 37, FWHM = 110 nm), which indicates the charged nature and the self-organization ability of Ag_n clusters in the medium. These clusters are dispersed in organic solvents such as toluene and methanol. This intrinsic physical property of the metal nanoclusters arises due to their unique structure, in which the hydrophilic part of the capping agent (carboxylic acid, primary and secondary amine or thiols) is attached to the metal atoms while hydrophobic part is protruded in the solvent. These structural features are prominently reflected in the Infra-Red (IR) and nuclear magnetic resonance (NMR) analysis.

6A.3.5 Fourier Transform Infrared spectroscopy results:

To understand the adsorption mechanism of benzoic acid on the surface of silver nanoparticles, FTIR measurements were carried out on pure benzoic acid and benzoic acid coated silver nanoparticles (Ag_n). Accordingly, Figure 6A.5(A) shows a typical IR spectrum of benzoic acid.

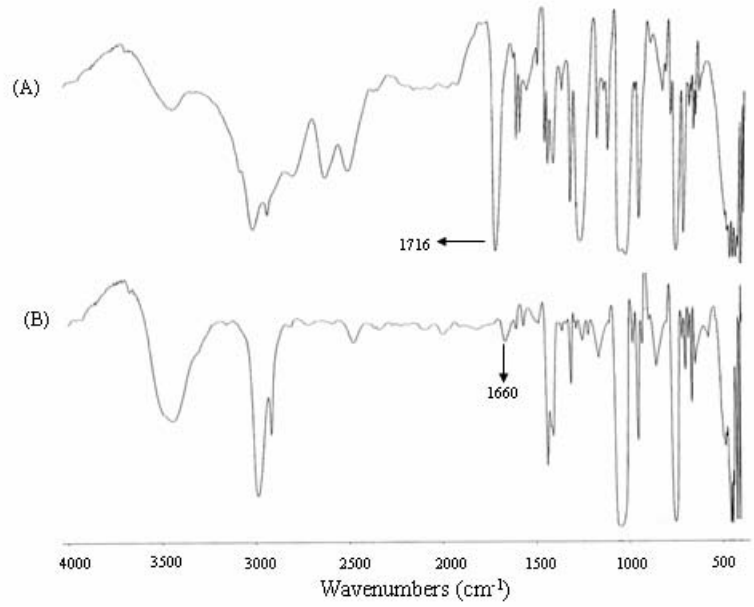

Figure 6A.5 *FTIR spectra of benzoic acid (A), and Ag_n-OCOPh (B)*

The broad band at 3500 cm^{-1} is undoubtedly due to the O-H stretch of the carboxylic acid. The intense peak at 1716 cm^{-1} is derived from the existence of the C=O stretch and the O-H in plane and out of plane bands appear at 1435 and 951 cm^{-1} respectively. IR spectrum of benzoic acid coated Ag_n clusters (Figure 6A.5 (B) shows a strong band centered around 3440 cm^{-1} corresponding to Ag_n-O vibrations due to the attachment of carboxylic acid group to silver atoms. It is worth noting that the characteristic C=O band shifted bathochromically around 1660 cm^{-1} as compared to the sharp carbonyl absorption at 1716 cm^{-1} for benzoic acid indicating that the surfactants surrounding the Ag nanoparticles are closely packed and also the intensity of the peak decreases dramatically. This reveals that the benzoic is chemisorbed as carboxylate onto the Ag nanoparticles.

6A.3.6 Nuclear Magnetic resonance spectroscopy:

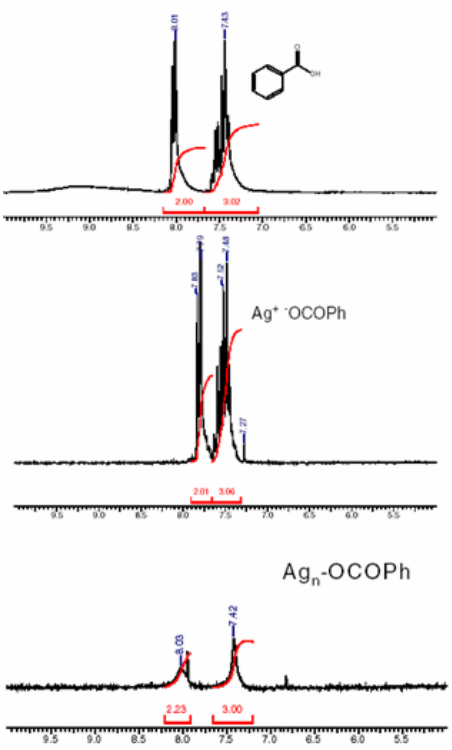

Figure 6A.6 *Proton magnetic resonance spectra of benzoic acid, Ag^+ $^-$OCOPh, and Ag_n-OCOPh. Spectra were obtained in $CDCl_3$ + DMSO-d_6 solvent system using tetramethylsilane internal standard.*

In order to confirm the formation of benzoic acid capped Ag_n in the Newman' silver reagent, clusters were separated from the organic solvent and redispersed in $CDCl_3$ + DMSO-d_6 for ^{1}H NMR spectroscopic measurements. Figure 6A.6 shows the ^{1}H NMR spectra recorded from pure benzoic acid, AgOOCPh, and benzoic acid capped silver nanoparticles (Ag_n) in $CDCl_3$ + DMSO-d_6 using trimethylsilane internal standard. The NMR spectra of both benzoic acid and AgOOCPh show a fine splitting pattern of five contiguous protons. However this significant pattern of aromatic protons collapses in ^{1}H NMR spectrum of Ag_n to give two broad resonances around δ= 7.42 and δ= 8.03 respectively, indicative of the paramagnetic nature of Ag_n. Above results further confirm the ability of benzoic acid to bind the Ag ions and the formation of Ag_n clusters.

Table 6A.1 illustrates the features of silver nanoclusters (Ag_n) prepared under different conditions of catalysis using various combinations of silver (I) compound and co-reagents and yield of the Wolff rearranged product.

Table-6A.1 Features of the silver-nanoclusters (Ag_n) formed under various conditions of silver (I)-catalysis of the α-diazoketone **1**.

	Silver (I) compounds	Co-reagents	Silver nanoclusters (Ag_n) UV-Visible λ_{max} (nm)	Particle size (nm)	Yield of **3**[*] (%)
(i)	AgOCOPh	Et_3N	308	0.5-15	91
(ii)	$AgNO_3$	NH_3	304	1-10	86[#]
(iii)	Ag_2O	Et_3N	433	250	87
(iv)	Ag_2O	$Na_2S_2O_3$	436	258	92
(v)	Ag_2O	---------	347	1-5	68
(vi)	AgOCOPh	---------	308, 440	1-14	76

Chromatographically isolated yield of an amide of the carboxylic acid **3**.

*General procedure: the silver-catalyst (5% by weight of the α-diazoketone), either silver-nanoclusters (Ag_n) prepared following the appropriate literature procedure excluding the α-diazoketone at room temperature (for cases i to iv) or the silver(I) compound (for the cases v and vi) is added in small portions at the regular interval of 20 min to the aqueous 1,4-dioxan solution of 2-hexanone-1-diazo-6-phenyl **1** (0.1 M) at 60°C till the complete decomposition of **1** (0.5 h to 1 h). A usual solvent extractive work-up followed by purification furnished the Wolff-rearranged product 3, matching with the reported physical and spectral characteristics.

Ag_n-catalysis of the α-diazoketone **1** in aqueous dioxane furnishes the 6-phenylhexanoic acid **3** in 91 % yield (Table-6A.1). The TEM image obtained after completion of the reaction shows the presence of relatively larger and polydispersed nanoclusters ranging from 10-80 nm. This phenomenon of cluster formation can be attributed to the unique ability of Et_3N to function simultaneously as an electron donor and cluster-stabilizing agent during the transition from atom to cluster.

$$nAg^+ + ne \longrightarrow Ag_n \qquad \text{eqn 1}$$

6A.3.7 Scanning electron microscopy and X-ray analysis:

Aqueous sodium thiosulfate can function as an electron donor leading to the reduction of silver(I) oxide (equation-2) [47]. Interestingly, the resulting bare silver

clusters self- assemble on the silver oxide surface giving rise to porous 3D secondary network with diffused boundaries composed of uniform sized (250 nm) grains as judged from scanning electron micrographs (SEM, Figure 6A.7).

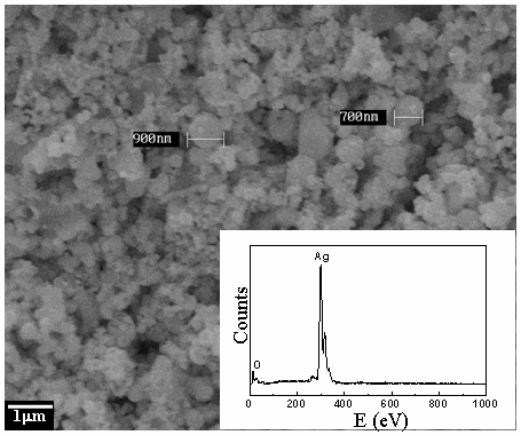

Figure 6A.7 *Scanning electron micrographs of the silver-agglomerate formed during the reaction between sodium thiosulfate and silver(I) oxide in aqu. Dioxane; an inset shows elemental analysis using energy dispersive X-analysis.*

The composition analysis by energy dispersive X- analysis (EDAX) confirms the sole presence of silver on the surface in contrast to the presence of silver and oxygen atoms in the silver (I) oxide. These drastic changes in surface composition and morphology are responsible for the reproducible and enhanced catalytic activity.

These structural changes were further confirmed by the powder X-ray diffraction (Figure 6A.8) pattern which shows the presence of both Ag_n [(111), (311), (220), (200)] and silver (I) oxide [(111) (100) (110) (113)].

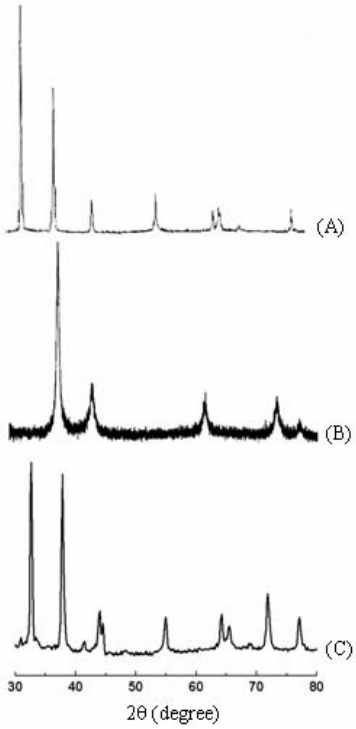

Figure 6A.8 *Powder X-ray diffraction pattern for Ag-agglomerate formed following an electron transfer between Ag_2O and $Na_2S_2O_3$.*

Similar results are obtained using triethyl amine (TEA) with silver(I) oxide (Table-6A.1). These silver particles also efficiently catalysize the Wolff-rearrangement of the α-diazoketone **1**.

$$Ag_2O + H_2O + 2e \longrightarrow 2\,Ag^0 + 2\,OH^-,\ E^0=0.342V \text{ Vs NHE} \quad \text{eqn 2}$$

Reactions of α-diazocarbonyl compounds catalysed by either silver(I) oxide or AgOCOPh alone has relatively large induction period till the copious evolution of nitrogen begins. UV-visible follow-up and the TEM-images recorded during the course of the reaction between silver(I) oxide and α-diazoketone **1**, shows that the reaction proceeds rapidly after the formation of polydispersed Ag_n ranging from 1 to 5 nm in diameter, due to an electron removal from α-diazoketone by silver(I) oxide [48]. Similarly AgOCOPh accepts an electron from the a-diazoketone **1** to yield polydispersed benzoic acid capped Ag_n (Figure 6A.8C), as encountered earlier (vide supra). Ensuing results are summarized in Table-6A.1.

6A.4 Conclusions

In conclusion, our results show that silver(I) compounds accept an electron either from various co-reagents or α-diazoketone to form silver atoms, which spontaneously grow to silver-nanoclusters which efficiently catalyze α-diazoketones in Wolff rearrangement. It has indeed been unknowingly used as a catalyst since long time in the Wolff-rearrangement of α-diazoketones. Our spectroscopic and electron microscopy results give the preliminary indication of formation of clusters and further analysis using different combinations of starting material and co-reagents suggest the role of silver clusters in the organic reaction. Their optical, physical and catalytic properties vary strongly as a function of size which in turn is governed by the starting silver(I) compound and the reaction conditions. The possibility of varying particle size and composition through nanoparticles preparation conditions makes nanoclusters uniquely suited to exploring and understanding the relative importance of these effects on catalytic reactions. We believe that this study gives a significant achievement in the understanding the role of silver compounds and co-reagents in Wolff rearrangement.

References

[1] (a) Henglein, A. *J. Phys. Chem.* **1993**, *97*, 5457. (b) Michaelis, M.; Henleign, A. *J. Phys. Chem.* **1994**, *98*, 6212. (c) Linnert, T.; Mulvaney, P.; Henleign, A. *J. Phys. Chem.* **1993**, *97*, 679. (d) Henglein, A. *Chem.Rev.* **1989**, *89*, 1861.

[2] (a) Mostafavi, M.; Marignier, J. L.; Amblard, J.; Belloni, J. *Radiat. Phys. Chem.* **1989**, *34*, 605. (b) Huang, Z.-Y.; Mill, G.; Hajek, B. *J. Phys.Chem.* **1993**, *97*, 11542.

[3] (a) Mallin, M. P.; Murphy, C. J. *Nano Lett.* **2002**, *2*, 1235. (b) Me´traux, G. S.; Cao, Y. C.; Jin, R.; Mirkin, C. A. *Nano Lett.* **2003**, *3*, 519.

[4] Ung, T.; Liz-Marza´n, L. M.; Mulvaney, P. *J. Phys. Chem. B* **1999**, *103*, 6770.

[5](a) Pastoriza,-Santos, I.; Liz-Marza´n, L. M. *Nano Lett.* **2002**, *2*, 903. (b) Jin, R. C.; Cao, Y. W.; Mirkin, C. A.; Kelley, K. L.; Schatz, G. C.; Zheng, J. G. *Science* **2001**, *294*, 1901. (c) Kreibig, U.; Vollmer, M. *Optical Properties of Metal Clusters*, Springer-Verlag: Berlin, **1995.**

[6] Ung, T.; Liz-Marza´n, L. M.; Mulvaney, P. *J. Phys. Chem. B* **2001**, *105*, 3441.

[7] (a) Adams, R. D.; Captain, B.; Zhu, L. *J. Am. Chem. Soc.* **2004**, *126*, 3042. (b) Schmid, G. *Clusters & Colloidal: From Theory to Application*; VCH: Weinheim, **1994**.

[8] (a) Whetten, R. L.; Shafigullin, M. N.; Khoury, J. T.; Schaaf, T.G.; Vezmar, I.; Alvarez, M. M.; Wilkinson, A. *Acc. Chem. Res*. **1999**, *32*, 397. (b) Templeton, A. C.; Wuelfing, M. P.; Murray, R. W. *Acc. Chem. Res*. **2000**, *33*, 27.

[9] Toshima, N.; Nakata, K.; Kitoh, H. *Inorg. Chim. Acta* **1997**, *265*,149.

[10] Schmidt, T. J.; Noeske, M.; Gasteiger, H. A.; Behm, R. J. *J.Electrochem. Soc*. **1998**, *145*, 25.

[11] Greenwood, N. N.; Earnshaw, A. *Chemistry of Elements*, 2nd ed.;Butterworth-Heinemann: Oxford, **1997**.

[12] Chen, C.-W.; Serizawa, T.; Akashi, M. *Chem. Mater.* **1999**, *11*, 1381.

[13] Zaera, F.; Gellman, A. J.; Somarajai, G. A. *Acc. Chem. Res*. **1986**, *19*, 24.

[14] Bonds, G. C. *Acc. Chem. Res*. **1993**, *26*, 490.

[15] (a) Pal, T.; Sau, T. K.; Jana, N. R. *J. Colloid Interface Sci.* **1998**, *202*, 30. (b) Pal, T.; Sau, T. K.; Jana, N. R. *Lamgmuir* **1997**, *13*,1481.

[16] Fendler, J. H. *Chem. Rev*. **1987**, *87*, 877.

[17] Ahmadi, T.; Wang, Z. L.; Green, T. C.; Henglein, A.; El-sayed, M. A. *Science* **1996**, *272*, 1924.

[18] Hercules, D. M.; Proctor, A.; Houalla, M. *Acc. Chem. Res.* **1994**, *27*, 387.

[19] Jackson, S. D.; McLellan, G. D.; Webb, G.; Conyers, L.; Keegan, M. B. T.; Mather, S.; Simpson, S.; Wells, P. B.; Whan, D. A.; Whyman, R. *J. Catal*. **1996**, *162*, 10.

[20] Jacobs, G.; Ghadiali, F.; Pisanu, A.; Borgna, A.; Alvarez, W. E.; Resasco, D. E. *Appl. Catal. A* **1999**, *188*, 79.

[21] Englisch, M.; Jentys, A.; Lercher, J. A. *J. Catal*. **1997**, *166*, 25.

[22] Cocco, G.; Campostrini, R.; Cabras, M. A.; Carturan, G. *J. Mol.Catal*. **1994**, *94*, 299.

[23] Longenberger, L.; Mills, G. *J. Phys. Chem.* **1995**, *99*, 475.

[24] Schmid, G. *Chem. Rev.* **1992**, *92*, 1709.

[25] Lewis, L. N. *Chem. Rev.* **1993**, *93*, 2693.

[26] Jiang, Z. J. Liu, C. Y., Sun, L.W. *J. Phys. Chem. B*. **2005**, 109, 1730

[27] Doyle, M. P.; Mckervey, M. A.; Ye, T. *Modern Catalytic Methodsfor Organic Synthesis with Diazocompounds*; Wiley: New York, **1998.**

[28] Gill, G. B. In *Comprehensive Organic Synthesis*; Trost, B. M., Fleming, I., Eds.; John Wiley: New York, **1991**; Vol. 3, pp 887-909.

[29] Ye, T.; Mckervey, M. A. *Chem. Re*v. **1994**, *94*, 1091.

[30] Meier, H.; Zeller, K. P. *Angew. Chem., Int. Ed. Engl.* **1975**, *14*, 32.

[31] Bachmann, W. E.; Struve, W. S. *Org. React.* **1946**, *1*, 38.

[32] Zhu, Z.; Bally, T.; Stracener, L. L.; Mcmahon, R. J. *J. Am. Chem.Soc.* **1997**, *121*, 2863.

[33] Likhotvorik, I.; Zhu, Z.; Tae, E. L.; Tippmann, E.; Hill, B. T.; Platz, M. S. *J. Am. Chem. Soc.* **2001**, *123*, 6061.

[34] Scott, A. P.; Platz, M. S.; Radom, L. *J. Am. Chem. Soc.* **2001**, *123*, 6069.

[35] Mueller, A.; Vogt, C.; Sewald, N. *Synthesis* **1998**, 837.

[36] Lindler, M. R.; Podlech, J. *Org. Lett.* **2002**, *3*, 1849.

[37] Sudrik, S. G.; Chavan, S. P.; Chandrakumar, K. R. S.; Pal, S.; Date, S. K.; Chavan, S. P.; Sonawane, H. R. *J. Org. Chem.* **2002**, *67*, 1574.

[38] Yuhawa, Y.; Tsuno, Y.; Ibata, T. *Bull. Chem. Soc. Jpn.* **1967**, *40*, 2613.

[39] Yuhawa, Y.; Tsuno, Y.; Ibata, T. *Bull. Chem. Soc. Jpn.* **1967**, *40*, 2618.

[40] Furniss, B. S.; Tatchell, A. R. *Vogel's Textbook of Practical OrganicChemistry*, 4th ed.; ELBS-Longmann: London, **1978**; p 485.

[41] Newman, M. S.; Beal, P. F. *J. Am. Chem. Soc.* **1950**, *72*, 3.

[42] Lee, V.; Newman, M. S. *Org. Synth*. **1970**, *50*, 77.

[43] Aiken, J. D., III; Aiken, R. G. *J. Mol. Catal. A.: Chem.* **1999**, *145*, 1.

[44] Mulvaney, P. In *Semiconductors Nanoclusters-Physical, Chemical, and Catalytic Aspects*; Kamat, P. V., Meisel, D., Eds.; Elsevier: Amsterdam, **1987**, pp 99-124.

[45] Templeton, A. C.; Pietron, J. J.; Murray, R. W.; Mulvaney, P. *J. Phys. Chem. B* **2000**, *104*, 564.

[46] Hostetler, M. J.; Wingate, J. E.; Zhong, C.-J.; Harris, J. E.; Vachet, R. W.; Clark, M. R.; Londono, J. D.; Green, S. J.; Stokes, J. J.; Wignall, G. D.; Glish, G. L.; Porter, M. D.; Evans, N. D.; Murray, R. W. *Langmuir* **1998**, *14*, 17.

[47] Bard, A. J.; Faulkner, L. R. *Electrochemical Methods, Fundamentals and Applications*; Wiley: New York, **2001**.

[48] Parker, K. A.; Su, D. In *Encyclopedia of Reagents for Organic Synthesis*; Paquette, L. A., Ed.; John Wiley: England, **1995**, 6, 4465.

CHAPTER VI-B

Application of Self-assembled molecular nanocathodes for rechargeable energy storage modules

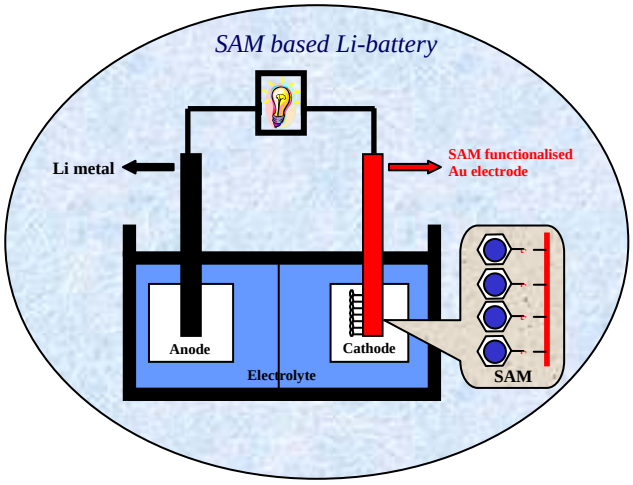

This chapter describes the proof-of-concept of using self-assembled molecular nanocathodes of aromatic thiol molecules such as diphenyl disulfide (DDS) as active elements for rechargeable Li batteries.

A part of the work reported in this chapter has been published in ***Chem. Phys. Lett.,*** *2004, 396, 277. and another part in* ***J. Pow. Sources****, 2003, 124, 133.*

University of Pune

6B.1 Introduction

Rechargeable lithium batteries are attractive power sources because of their high specific energy/power and long operational life compared with other rechargeable batteries [1,2]. Consequently, lithium batteries are used routinely in several electronic devices that include laptop computers, cellular phones, electronic watches, calculators, cameras, oxide semiconductor memories, electric vehicles, and inplantable devices. In these applications, lightweight and the small size are the crucial aspects for optimizing the device performance [1-4]. Although different types of rechargeable lithium cathodes such as transition metal oxides [5–7], organic compounds [8], chalcogenides [9], and complex metal oxides [10] are presently commercially available, their performance does not meet all the goals required for the development of batteries with efficient high specific powers [11]. The anodes usually comprise of Li distributed in an amorphous transition metal oxide matrix in a polymer electrolyte. Batteries with these electrode combinations, however, provide ~30–40% lower power density and inferior efficiency at high charge–discharge rates due to extremely slow Li diffusion in transition metal oxides as compared to anode active materials such as lithium metal (3861 mA h g^{-1}) and lithium intercalation (372 mA h g^{-1}) compounds [12,13]. Conventional cathode materials [14-16] also exhibit several drawbacks, such as: (i) a low capacity at moderate current density, surface degradation and grain growth during both cycling and in open-circuit stand; (ii) a high rate of self-discharge due to parasitic corrosion reactions; (iii) a large Ohmic drop due to the formation of insulating phases [11,17]. Further, problems like mechanical strength, poor utilization efficiency, relatively slow transfer of Li^+ ions and large Ohmic drop arise due to the use of external additives such as graphite or acetylene black and also polymeric binders during the cathode fabrication. Recently, conducting polymer-based cathode materials, which include several organo-inorganic nanocomposites, have been found to be promising to alleviate some of these difficulties so that high specific energy and improved cycle-life can be obtained. For example, Sotomura and co-workers [2] have shown the potential use of 2,5-dimercapto-1,3,4- thiadiazole (DMcT) as a part of composite cathode material for rechargeable lithium batteries, where thiol/disulfide redox processes facilitate the transfer of lithium ions. Most of such materials still, however, show capacity failure during continuous cycling and, more significantly, poor Li^+ transport

limits their high-rate capability [18]. Therefore, the development of cheaper, environmentally benign and lightweight rechargeable cathodes, which have high specific energy/power and long life, still remains a challenge.

Self-assembled monolayers (SAMs) are close-packed arrays of amphiphilic molecules like long-chain thiols and disulfides where the high coverage (10^{12} to 10^{13} molecules/cm^2) and monomolecular thickness can be used to design optimum energy/weight or energy/volume parameters. SAM molecules have great freedom and flexibility in their dynamic nature that causes dynamic re-organization. Easy preparation, reproducible film quality, good stability and control of the chain length to obtain the desired wetting and adhesion properties are the main advantages of the SAM. Due to these reasons, SAMs find tremendous applications in various areas such as corrosion protection [19], wetting [20], friction [21], adhesion [22], microelectronics and molecular electronics [23], optics [24], and chemical sensors [25].

SAMs consist of short-chained organic molecules of the type Y–(CH_2)n–X, where X and Y are either organic or inorganic moieties or functional groups such as –SH, –CH_3, aromatic ring(s) and NH_2. These molecules assemble in highly oriented configurations on surfaces by spontaneous adsorption from solution, often forming monolayers. For example, thiol-terminated SAMs on noble metal substrates such as Au have been widely studied because of the ease of monolayer formation with controllable pinhole radii ca. 0.1–10 μm and pinhole separations of 1–100 μm [26]. These SAMs typically consist of molecules canted at a 35–40^o angle with respect to the surface normal. These densely packed monolayers with ~94–96% surface coverage exhibit a low tendency for multilayer formation. Such attributes make SAMs attractive for use as nanoporous membranes that could allow faster and selective Li^+ diffusion through pinholes in exclusion to other elemental and molecular species, thereby promoting efficient charge–discharge cycles. Also, the ease of formation of SAMs could open up the possibility of extending battery life through facile electrode repair by SAM replenishment and reassembly [27]. The insulating nature of SAMs and their lack of redox activity necessary to sustain electrochemical reactions are potential hurdles for their use as electrodes.

In this chapter, we demonstrate a new approach of using self-assembled molecular layers (SAMs) of diphenyl disulfide (DDS) as high-efficiency cathodes. This strategy of using layered mesoassemblies of molecular nanostructures could open up new possibilities of creating lightweight and miniaturized rechargeable energy generation and storage modules with extended lifetimes that can be integrated with logic and memory devices.

We obviate the drawbacks by using SAMs of DDS as the cathode for a cell with a lithium anode. The presence of phenyl rings in a conjugate configuration in DDS provides a higher electrical conductivity than SAMs of thiol-terminated alkane chains. The spacing between individual molecules allows ion transfer pathways to the metallic substrate, similar to that reported in microarray electrodes [28]. We also envision that the flexibility of phenyl rings would allow readjustment of molecular orientation in the SAMs, thereby facilitating Li+ ion transport across the SAMs during the charge–discharge operations. Further, DDS SAMs have very high coverage, are relatively easy to form, and have been well characterized [29]. Furthermore, this type of a monolayer-based electrode materials can overcome several limitations that arise due to the use of external additives, e.g. graphite, acetylene black and Teflon binder, during cathode fabrication where the uniformity of mixing, method of electrode fabrication, wetting by electrolyte, etc. play important roles.

6B.2 Experimental Aspects

6B.2.1 Materials:

Diphenyl disulfide, lithium perchlorate ($LiClO_4$), and lithium (each 99.9%) were purchased from Aldrich chemicals and were used as received. The gold substrates were prepared by the thermal evaporation of 200 nm gold (purity 99.9%) on a Cr-buffer layer (20 nm), which was first deposited on to conventionally clean glass plates [30]. The gold coated glass slides cut to required size (1.1 cm^2) for use as electrodes. Au substrates were precleaned in baths of sulfochromic acid and 3% HF for a few seconds and thoroughly rinsed with deionised water. The copper foils (1 cm^2 area, purchased from Aldrich chemicals) were polished by SiC abrasive paper followed by etching using

phosphoric acid/sulfuric acid solution (130 ml 85% H_3PO_4, 20ml 97% H_2SO_4, 60ml H_2O) for removal of oxide impurities present on the surface [31].

6B.2.2 Formation of SAM and characterization:

The substrates (Au and Cu) were rinsed extensively with acetonitrile and dried prior to monolayer formation by immersion in a 1mM solution of DDS [32] to obtain a well-organized monomolecular film [23]. The substrates were removed from the DDS solution, washed repeatedly with the solvent, and then dried in a stream of argon. The film thickness was estimated to be 0.7 nm by ellipsometry measurements and calculations from a one-layer model were performed using an application written in Mathcad.

These SAM functionalized copper/gold electrodes as cathodes were coupled with a large-area lithium-metal anodes using 0.1M $LiClO_4$ in tetrahydrofuran (THF) as an electrolyte to fabricate cells. Electrochemical charge–discharge measurements were conducted for the initial few cycles using a constant current density of 0.03 $mAcm^{-2}$ that was controlled with the help of a computerized data-acquisition system. All procedures for handling and fabricating the cells were performed in a argon-filled glove box. The water content in the electrolyte was ensured to be less than 50 ppm by Karl–Fisher titrations. The DDS SAM electrodes were characterized both before and after charge–discharge measurements using CV, FTIR and XPS techniques in order to examine for monolayer destruction after electrochemical cycling. Cyclic voltammetry and impedance was performed in an oxygen-free atmosphere using a three-electrode cell, which comprised the monolayer, protected Au/Cu as the working electrode, a large-area platinum flag counter electrode, and a Ag/Ag^+ (non-aqueous) reference electrode.

6B.3 Results and discussion

6B.3.1 Charge-discharge measurements:

The charge–discharge profiles of a typical lithium cell fabricated using DDS SAM cathodes, measured at a current density of 0.03 $mAcm^{-2}$ at 30 ^0C for the first (A) and fifth cycles (B) are shown in Figure 6B.1. The open-circuit voltage of the freshly prepared cell is in the range 2.85–2.98 V, which is lower than the theoretical OCP of 3.20 V for the

$Li^+ + e^- \rightarrow Li$ electrochemical reaction. This difference is most likely due to contributions from competing electrochemical pathways and a lower Li^+ ion concentration on the SAM surface than in the bulk of the SAM and this value is found to be invariant with respect to cycling.

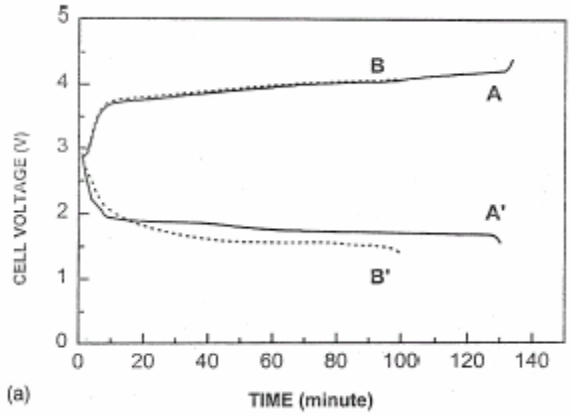

Figure 6B.1: *Charge and discharge profiles for (A, A') first cycle and (B, B') fifth cycle of Li-cell consisting of DDS SAM modified Cu as cathode, at rate of 0.03 mAcm^{-2} at 30^{0}C; electrolyte used is 0.1M $LiClO_4$ in THF.*

During discharge, the voltage first drops rapidly to 2.4 V and then decreases slowly to sustain the Faradaic reaction proceeding at a nominal voltage of about 1.4 V. Although the mass-transport limited region in both charging and discharging plots is found to decrease due to cycling, the nature of the plots is similar. For example, step-like features are clearly present in all the discharge plots. These are attributed to re-organization of SAM during Li^+ ion insertion. Similar staging can be seen even if substantially higher current densities (5–10 times more) are used. Since the cathode is a quasi two-dimensional system with pinholes and other defects, bulk phase changes (like staging for amorphous carbonaceous electrodes during lithium ion insertion) are not possible. In order to evaluate the features obtained for the DDS SAM on copper, charge–discharge measurements were carried out on a gold substrate. Representative charge–discharge characteristics of such a cell for the first few cycles are shown in Figure 6B.2. The maximum cell voltage of the charged battery remains essentially unchanged at ~4.3 V and is independent of repeated charging and discharging, suggesting that the SAM nanoelectrode is resilient to the influx and outflux of Li^+ ions.

In contrast, the discharge voltage decreases upon repeated charge–discharge cycles. This is seen from the monotonic decrease in discharge voltage from ~2 V for one cycle, to ~1.4 V after five recharging cycles, indicating degradation in discharge performance. While it takes a longer time to reach the saturation cell voltage during recharging, we note that the time taken to recharge the battery to full capacity actually decreases.

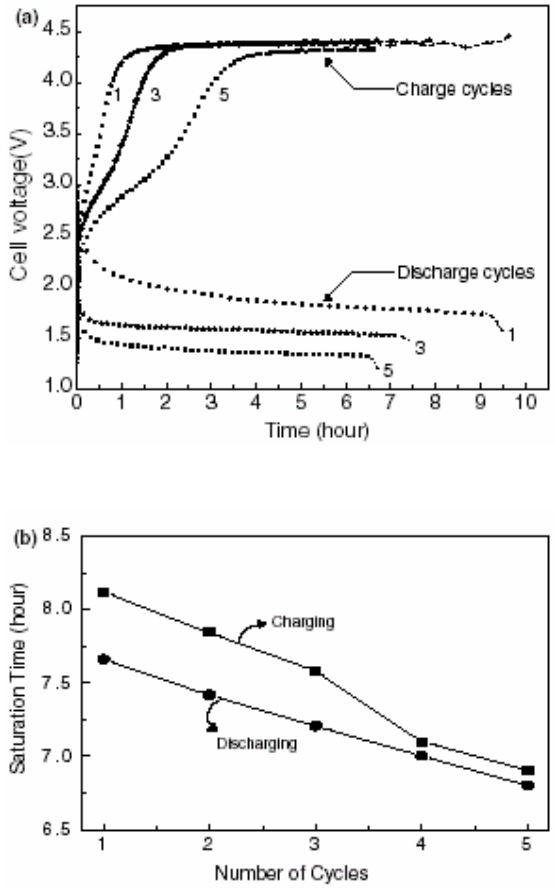

Figure 6B.2 *(a) Representative charge–discharge characteristics of DDS SAM recorded for the first, third and fifth cycle at a constant current density of 30 μA cm^{-2} (b) The time taken for the voltage to saturate as a function of the number of charge–discharge cycles.*

This is seen from the shorter time taken to attain the cell voltage for a battery being charged for the fifth time compared to that being charged for the first time (curve in Figure 6B.2a). The time to attain the operating voltage for discharge also decreases with

repeated charge–discharge cycles (see bottom curves in Figure 6B.1a). This behavior is summarized in Figure 6B.2b, which plots the time to attain the saturation cell voltage as a function of number of charging or discharging cycles.

Figure 6B.3 shows charge–discharge voltage profiles for different current densities between 0.04 and 125 μA cm^{-2}. The discharge voltage is ~0.5 V lower for >0.1 mA cm^{-2}, when compared with ~1.5 V obtained for lower current densities. As the current density becomes higher, the increased ohmic drop leads to a lower discharge voltage. The decreases in charging time, battery lifetime and the time taken to reach the discharge voltage, can be understood as follows. The insufficient Li^+ ions release due to entrapment by sulfur atoms and the steric confinement by the aromatic rings during recharging decreases the battery capacity. As a consequence, the Li^+ ions during subsequent recharging are screened from further entrapment by existing S–Li interactions, thereby resulting in faster insertion or release.

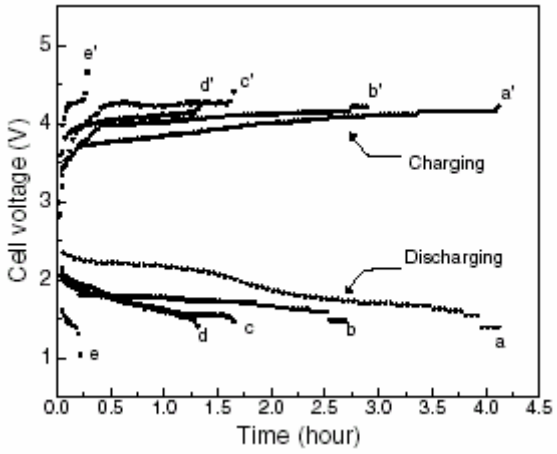

Figure 6B.3 *Discharging characteristics of DDS SAM recorded at different current densities of (a) 44 (b) 69 (c) 82 (d) 100 and (e) 125 μA cm^{-2}. Primed legends indicate the corresponding characteristics during charging.*

This explanation is supported by the surface electrochemical characteristics measured by cyclic voltammetry, and chemical changes in the SAM-electrodes during charging and discharging, revealed by FTIR and XPS. These results are presented below.

6B.3.2 Electrochemical analysis:

While SAMs are well known to block many electrode processes, pinholes due to imperfect adsorption can provide active sites for electrochemical reactions. We carried out cyclic voltammetry measurements to demonstrate the redox activity of these monolayers in presence of Li^+.

6B.3.2a Cyclic voltammetry:

Superimposed cyclic voltammograms of bare Cu and DDS SAM on copper in 0.1 M $LiClO_4$/THF at a scan rate of 500 mVs^{-1} are shown in Figure 6B.4(a) and (b), respectively. The drastic reduction in the non-faradaic current in the case of the voltammogram for the DDS modified copper as compared with that for the bare copper electrode clearly suggests the formation of a compact SAM.

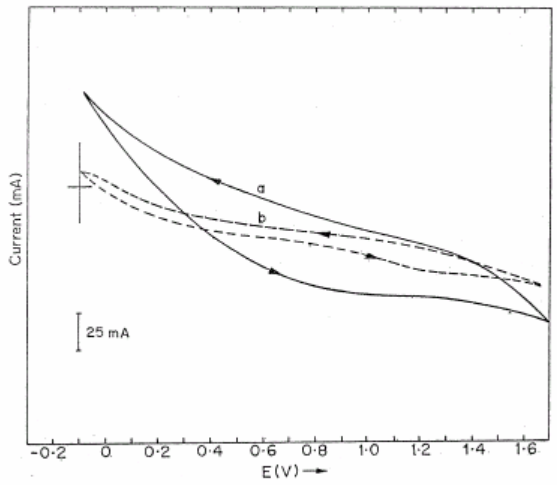

Figure 6B.4 *Superimposed cyclic voltammograms of (a) bare Cu (b) DDS SAM in acetonitrile with 0.1M $LiClO_4$ as supporting electrolyte and platinum flag as counter electrode at scan rate of 500mVs^{-1}; vs. Ag/Ag^+ reference electrode.*

In both the cases, no clear redox response is observed, although the raising cathodic current is much larger for the bare copper electrodes. Voltammograms taken for several cycles display identical behaviour. These observations ensure the formation

of a well-ordered monolayer on the copper surface, which slows down the electron-transfer kinetics by passivating the surface of copper [32].

The cycle-dependent voltammograms of DDS SAMs after discharging and charging cathodes are given in Figure 6B.5(a) and (b), respectively, for the same cycle number in a similar environment. In the discharged sample, a prominent oxidation peak is observed at 1.15 V. Although the peak potential is independent of cycle number, the peak current is seen to diminish considerably with cycling. Since the voltammogram for DDS SAM in the presence of Li^+ ions in the electrolyte (Figure 6B.4(b)) is electrochemically inert, the above irreversible peak is attributed to the insertion of Li ions, which are formed from the lithium-metal anode during the discharge process (Fig. 6B.5(a)).

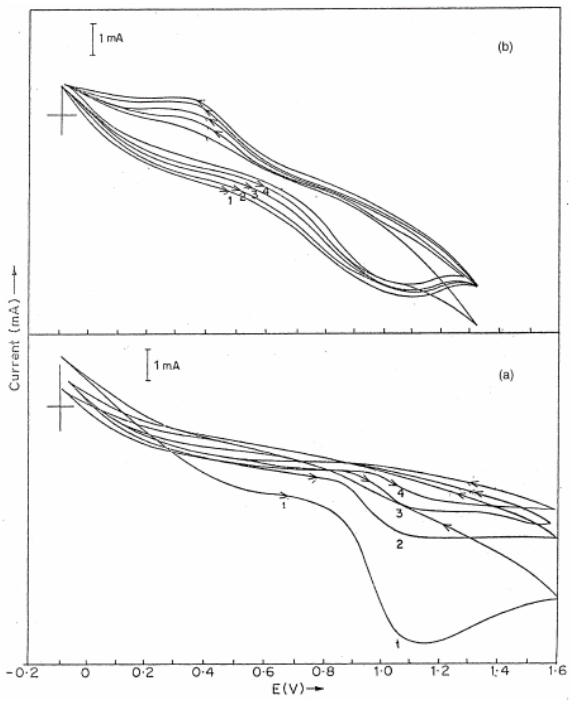

Figure 6B.5 *Cycle dependent voltammograms of (a) discharged DDS SAM and (b) charged DDS SAM at scan rate of 500 mVs^{-1}.*

In sharp contrast, the voltammogram for the charged sample gives a quasi-reversible couple with anodic and cathodic peaks at 1.1 and 0.35 V, respectively. This

cathodic peak may be attributed to the de-insertion of the Li^+ species present in the charged sample. The oxidation peak (1.1 V) with reduced current indicates the presence of some amount of Li^+ species. This clearly suggests that all the Li ions inserted are not removed by the reverse process and hence accounts the difference in the voltammograms. The capacity fading observed for different cycles can also be explained by this partial irreversible nature of lithium-ion de-insertion in the monolayer after each cycle.

Figure 6B.6 shows superimposed cyclic voltammograms obtained from discharged and charged samples. The nonfaradaic current is drastically suppressed by DDS-SAM-covered electrode (~20-fold) compared to that for blank gold electrodes (see inset of Figure. 6B.6), indicating the SAM has good coverage, and slows down the electron-transfer kinetics by passivating the gold surface [33].

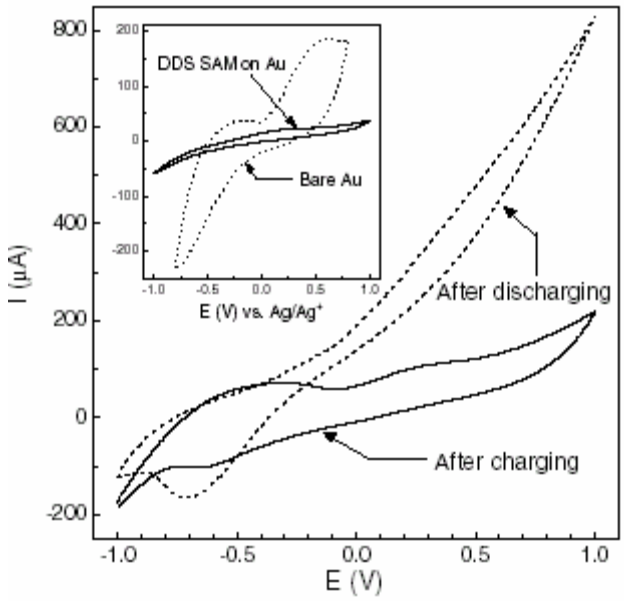

Figure 6B.6 *Cyclic voltammograms from discharged and charged DDS SAMs on gold, acquired at a scan rate 500 mVs^{-1}. Lithium was the counter electrode, Ag/Ag^+ the reference electrode, and 0.1M$LiClO_4$ the supporting electrolyte. Inset compares a reference voltammogram from bare gold with that obtained from the DDS SAMs on Au.*

In the discharged sample oxidation peak appears at -0.668 V due to Li^+-ion intercalation between SAMs while the voltammograms for the charged sample shows

quasi-reversible characteristics with cathodic and anodic peaks at -0.526 and -0.614 V, due to Li^+ de-insertion and insertion, respectively. The decreased anodic peak currents for the charged samples suggest the presence of few Li^+ ions in the charged samples, which may account for the fading capacity due to irreversible lithium ion deinsertion in the monolayer after several charge–discharge cycles.

6B.3.2b Impedance analysis:

A comparison of the impedance plots obtained from bare gold and DDS SAM-coated gold electrodes in Figure 6B.7a shows the effect of the adsorbed DDS monolayer and Li^+ ion diffusion on the ac response of gold electrodes. The bare gold electrodes show a semicircular $Z_{imaginary}$_Z_{real} characteristics for frequencies >0.1 Hz typical of electron transfer between a redox active species and the electrode surface. This is followed by a linear region at lower frequencies due to Li ion diffusion.

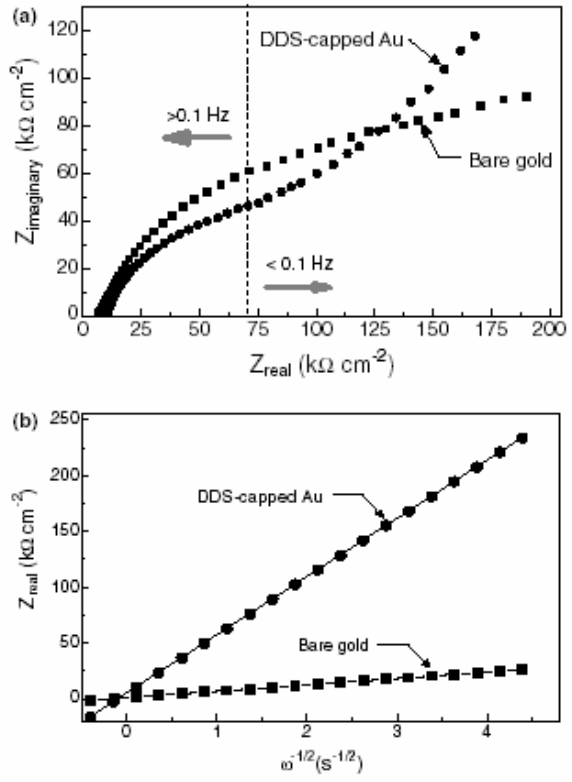

Figure 6B.7 *(a) Complex impedance plots for bare gold electrode, gold electrode derivatized with a DDS monolayer. The frequency range used is 100 kHz–10 mHz with a 10 mV rms. (b) Real part of faradaic impedance vs.* $\omega^{-1/2}$ *for bare gold and DDS-capped gold surfaces.*

The DDS coated gold electrodes also exhibit similar high frequency behavior. For <0.1 Hz, however, a larger imaginary component is seen for the SAM-coated electrodes due to Li^+ ion transport through pinholes in the SAM, similar to the behavior observed in electrodes coated with long-chain thiols [26,34]. The higher slope in the Z_{real} vs. $\omega^{-1/2}$ plot for SAM-coated electrodes compared to that of bare electrodes (see Figure 6B.7b), indicates faster Li ion transport at the SAM-coated electrode [33].

6B.3.3 FTIR characterization:

A comparison of the IR spectra of DDS powder and the DDS monolayer is given in Figure 6B.8(a) and (b), respectively. The spectrum for DDS powder was taken in order to confirm its purity and also for obtaining loss of distinct vibrational features after SAM formation. All the characteristic bands observed for DDS powder, such as C–H stretching (2850–2900 cm^{-1}), overtones or combinations (1600–2000 cm^{-1}), C–C ring stretching (1400–1600 cm^{-1}), out of plane C–C bending (688.5, and 736.8 cm^{-1}), C–S stretching (677 cm^{-1}) and S–S stretching (400–500 cm^{-1}) are in good agreement with the standard spectrum for pure DDS powder [36]. By comparison, Figure 6B.8(b) shows the absence of the S–S stretching band (400–500 cm^{-1}) after SAM formation. This indicates that the disulfide linkage has been cleaved, a conclusion that is in excellent agreement with QCM and scanning tunnelling microscopy (STM) investigations of DDS SAMs, where the facile S–S cleavage of DDS is inferred as one of the main reasons for the enhanced stability [29, 33]. Further, the vibrational band seen as a shoulder around 677 cm^{-1} in the bulk DDS spectrum is shifted slightly to 678.9 cm^{-1} in the monolayer. This band can be attributed to the C–S stretching vibration and the shift suggests Cu–S bond formation [36]. Also, the bands between 350 and 450 cm^{-1} can be attributed to the stretching mode of Cu–S bond, which is formed subsequent to the disulfide cleavage during monolayer development [36].

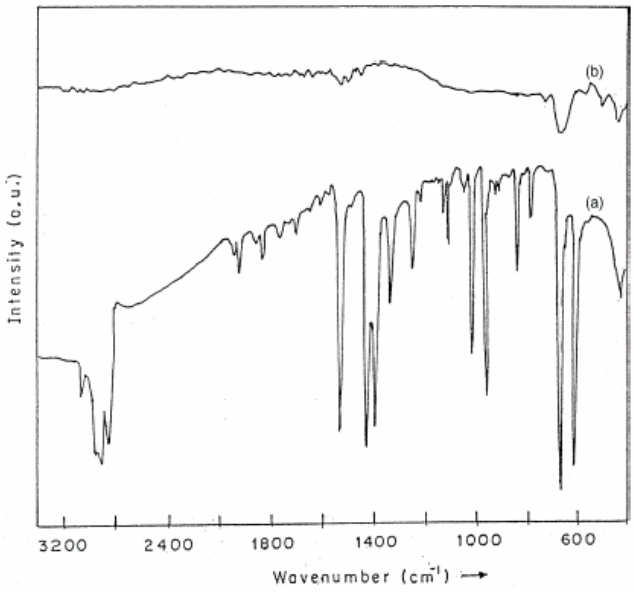

Figure 6B.8 *FTIR spectra of (a) DDS powder and (b) DDS monolayer on Cu substrate; monolayer formed by immersing substrate in 1mM DDS solution.*

Further, as the orientation of the aromatic ring changes after monolayer formation, the organization and tilt of molecules on a copper substrate, as well as the van-der-Waals interaction between adjacent molecules, may weaken the overtones and combination bands which correspond to the bezenethio group while all the remaining vibrational bands may become suppressed.

A comparison of the IR spectrum of discharged and charged samples is given in Figure 6B.9. Drastic changes can be seen in the spectral bands after charging and discharging as compared with the spectrum for the DDS SAM. For example in a discharged sample, the bands due to the overtones of the phenyl rings in the region 1600–2000 cm^{-1} are absent, while a pronounced new band appears at 1633.6 cm^{-1} (Figure 6B.9(a)). It is tentatively suggested that the appearance of this band (in both Figure 6B.9(a) and (b)) is due to π-cation interaction [37]. While, there is no direct evidence for the change in the relative orientation of phenyl rings with respect to each other in the SAM after lithium ion insertion/de-insertion, the disappearance of the aromatic overtone and combination bands suggests a change in the packing geometry of the phenyl ring planes. Also, the sharp peak appearing around 1087 cm^{-1} can be

attributed to the stretching vibrations of the lithium salts, which are characterized by a broad continuum [38] at around 1250–1500 cm^{-1}. Similar variations are also observed in the IR spectrum of the charged sample (Figure 6B.9(b)). Along with the dominant band at 1099 cm^{-1}, overtone bands are seen to reappear with a slight shift to higher frequency.

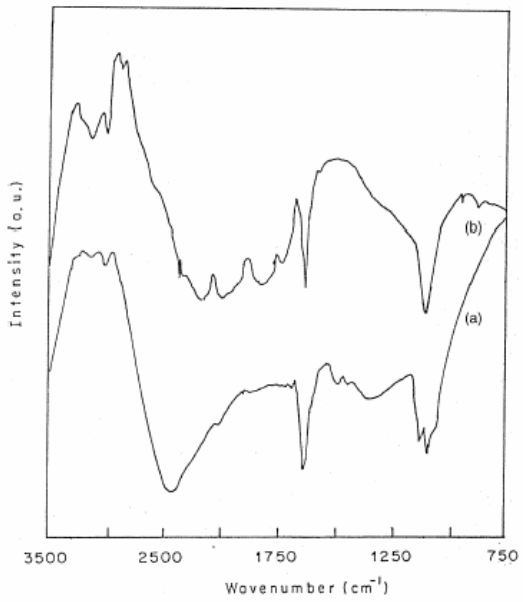

Figure 6B.9 *FTIR spectra of (a) discharged DDS SAM and (b) charged DDS SAM; spectra recorded after removing samples from cell followed by thorough washing.*

This can be attributed to de-intercalation of lithium ions concomitant with rearrangement of the phenyl rings. A pronounced band at 1099 cm^{-1} for lithium salts still remains, however, with a shift to higher frequency giving support for quasi-irreversible Li^+ de-insertion, which can also explain the capacity degradation after a few cycles. These results are in good agreement with the cyclic voltammetry results for the charged sample, which show both oxidation and reduction peaks (Figure 6B.5(b)) and where the appearance of the oxidation peak is attributed to partial irreversible de-intercalation of lithium ions.

Figure 6B.10 shows FTIR spectra from SAMs after recharging and discharging. Reference spectra from pristine SAMs are essentially featureless except for low-intensity aromatic ring stretching modes in the 1000–2000 cm^{-1} range. Discharged samples

exhibit a strong broad peak in the 1350–1800 cm^{-1} range. This arises from interactions between the Li^+ ions intercalated between the DDS molecules in the SAM during discharging and pi-electrons in DDS [37]. This is consistent with recharged samples showing a dramatically decreased peak width and intensity in this frequency regime, due to Li^+ de-intercalation.

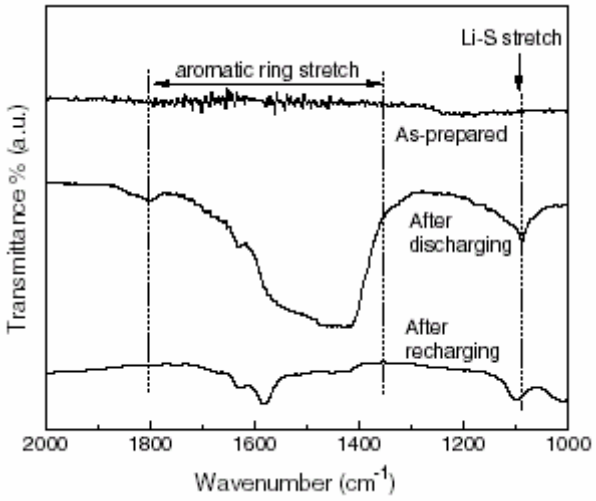

Figure 6B.10 *FTIR spectra of as-prepared DDS SAM on Au, after discharging, and after recharging.*

Both discharged and recharged samples show a peak at ~1087 cm^{-1} which corresponds to Li–S stretching modes [38] indicating that residual Li^+ ions not extracted during recharging are bound to sulfur in the SAM.

6B.3.4 X-ray photoelectron spectroscopy:

XPS was used to monitor the changes that occur on the copper substrate and in the SAM before and after cycling. This analytical tool is used mainly because it can provide elemental composition (mainly lithium, sulfur and copper, gold) and oxidation states of the elements present in the SAM. For all the samples, viz. DDS SAM, discharged SAM and charged SAM, the C 1s peak is symmetrical and can be Gaussian fitted with a single component. The binding energy values for Cu in SAM and discharged and charged samples are given in table 6B.1. In all the cases, a shift in the binding energy of the Cu $2p_{3/2}$ and Cu $2p_{1/2}$ peaks to higher values (Table 6B.1) along with

pronounced shake-up features around 940 eV [39], which are characteristic of the Cu(II) oxidation state, is observed. This suggests partial oxidation of the copper substrate. A shift to higher values of the BE of Cu irrespective of charging or discharging indicates changes on the substrate due to oxide formation during cycling.

Table 6B.1 Binding energies of O 1s, Cu $2p_{3/2}$, Cu $2p_{1/2}$, S $2p_{1/2}$, Li 1s for DDS SAM, charged monolayer and discharged monolayer.

B. E energy (eV)	O 1s	Cu $2p_{3/2}$	Cu $2p_{1/2}$	S $2p_{1/2}$	Li 1s
DDS SAM modified copper	532.9	934.4	954.6	162.4	-
Charged Sample	533.4	936B.4	956B.4	162.2	52.4
Discharged Sample	532.4	935.2	955.6	163.4	51.4

After background correction spectra have been fitted to Guassian curve.

This is expected since the insertion/de-insertion of Li^+ occurs primarily through interaction with the DDS monolayer. In comparison with the above results, the BE of sulfur should show interesting changes with respect to the charge–discharge process. For example, the S 2p XP signal, when fitted to the doublets of S $2p_{3/2}$ and S $2p_{1/2}$ at 162.4 and 163.6 eV, shows decreasing and increasing BE values upon lithium ion insertion and de-insertion, respectively, compared with that for pristine SAM (162.4 eV). More specifically, the XP spectrum of the discharged sample gives S 2p at 163.4 eV (S $2p_{3/2}$), which differs, from 164.04 eV (for standard S 2p). This shift corresponds to the adsorption of negative-charge bearing S on Cu metal. In a charged sample, the peak position shifts to a slightly to higher BE (164.2 eV). Clearly, these shifts are due neither to disulfonates nor oxidation products whose expected BE values are greater than 164.5 eV. Thus, the shifts can be indirectly co-related to the insertion and de-insertion of Li^+ ions on the monolayer. The additional peak at higher BE (168 eV) for all the samples is attributed to damage caused by the (sulfonate moiety) beam [39]. Also, the Li 1s peak obtained for the charged sample is shifted to a lower BE value (i.e. 55–51.4 eV) while a corresponding shift to a higher BE (52.78 eV) is observed for the discharged sample. This BE value for the charged sample can be explained by speculating that all the Li^+ ions are not de-intercalated during the charging process. This explanation is in agreement with the changes observed in the CV patterns presented in Fig.6B.5. Lastly,

the enhanced intensity of the oxygen and lithium peaks for both charged and discharged samples indicates the formation of lithium compounds during cycling [40].

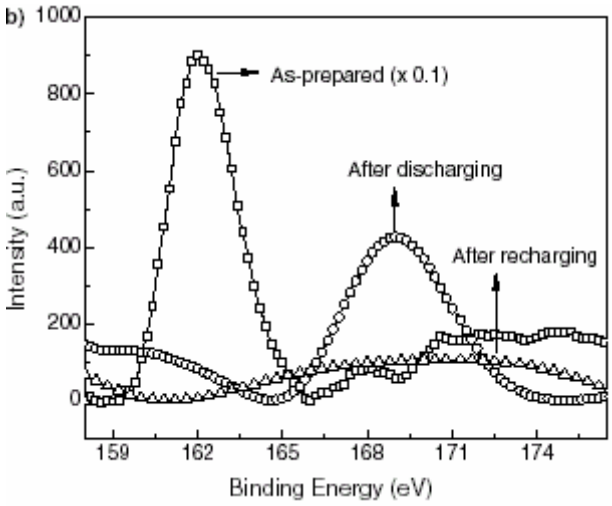

Figure 6B.11 *XPS spectra in the vicinity of the S 2p core level band obtained from the pristine DDS SAM on Au, after discharging, and recharging cycles.*

Li^+ ion trapping due to $Li^{+-}S$ interactions is corroborated by our XPS measurements of as-prepared, discharged and recharged samples. Figure 6B.11 shows that the S 2p core-level band at ~162 eV from the DDS SAM decreases in intensity upon recharging and discharging, and a broad band emerges at ~169 eV, which is attributed to lithium salt (e.g., LiS_2) formation [39]. The latter peak is unlikely to be due to X-ray beam-induced sulfate/ sulfonate formation [33] since all the samples were exposed to the same X-ray dose. The shape and position of the zero-valent Au 4f (84 eV) and C 1s (86B.6 eV) core level bands (not shown) are essentially identical for the pristine, discharged, and recharged, surfaces, indicating that the Au–SAM interface chemistry is unaltered during electrochemical recharge–discharge cycles.

6B.4 Mechanism of Li^+ ion insertion on DDS monolayers

To date, the nature of Li^+ ion interaction with SAM has not been sufficiently understood to elucidate a definite mechanism. On the basis of above experimental data, however, molecular models are proposed for the interactions of Li^+ (intercalation/de-

intercalation) with the DDS monolayer. The first model is based on the simple assumption of lithium-ion interaction with the pi- cloud of the benzene ring where the π-cation interaction is primarily responsible for Li^+ association (Scheme 6B.1(a)).

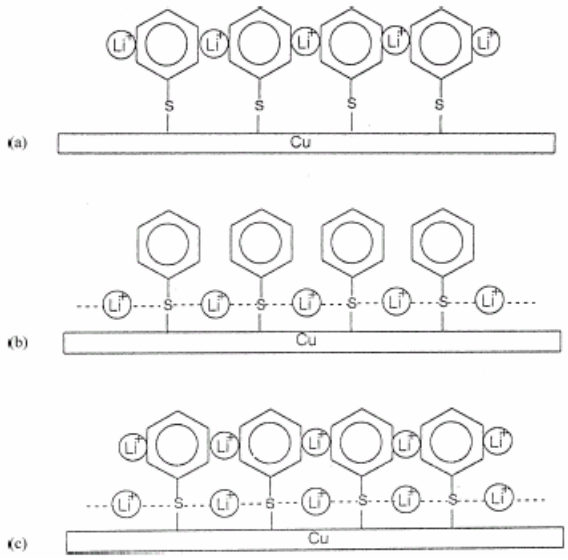

Scheme 6B.1 *Possible mechanism of Li^+ ion insertion on DDS monolayers based on: (a) π-cation interaction; (b) thiolate-lithium ion interaction; (c) combination of the both interactions, π-cation and thiolate–lithium.*

This can be supported from the IR spectrum of the discharged sample, where the overtones and combinations due to the benzene rings present in the pristine monolayer are missing. More interestingly, these bands do reappear in the spectrum for the charged sample where lithium-ion de-intercalation has taken place during charging. Thus, the reversible π-cation interaction is considered to be responsible for lithium-ion intercalation and cause orientational changes in the neighbouring benzene rings. An alternate model based on the interaction of Li ions with the thiolate linkage can also be visualized (Scheme 6B.1(b)) on the basis of the voltammetric results. Since the nature of the voltammogram obtained for both charged (quasi-reversible) and discharged (irreversible) electrodes is different, all the lithium ions intercalated are not able to de-intercalate and will thus result in the accumulation of some lithium ions in the monolayer. These Li ions are presumed to be irreversibly hooked up in the vicinity of Cu–S linkage and hence the thiolate bond is responsible for Li-ion association ($Li^{+\delta}$–$S^{-\delta}$). This is further

supported by the fact that even bulk copper sulfide is a well-known cathode for non-aqueous lithium batteries [41]. Hence, multiple factors appear to contribute to Li^+ ion intercalation/de-intercalation on DDS SAM. It is also possible to consider a model, which consists of both π-cation (responsible for the reversible behaviour) and thiolate-lithium ion (leading to irreversible nature) interactions, as shown in Scheme 6B.1(c). Since the exact mechanism of the lithium-ion interaction with a monolayer cathode is not clear at the present, further studies using different substrates and thiol molecules are in progress.

6B.5 Conclusions

The above results provide the first direct experimental evidence for the possibility of using self-assembled aromatic dithiol monolayers as cathode materials for rechargeable lithium batteries. This new class of nanostructured materials can electrochemically insert/de-insert lithium ions and facilitate high utilization. An especially striking feature is the high coulombic capacity in the initial cycles due to the quasi two-dimensional nature of the DDS monolayer. Infrared and electrochemical measurements suggest orientational changes during the charge–discharge processes as a consequence of lithium-ion insertion. The findings clearly suggests a significant potential for SAMs as cathode materials for lithium batteries of high specific energy, provided capacity fading in the initial cycles can be alleviated by more robust SAM-forming molecules. SAMs comprised of molecules with conjugate moieties (e.g., DDS), hold promise for use as nanocathodes in rechargeable lithium batteries. Potential advantages of such nanoelectrodes include high-surface area, facile fabrication and scalability, conducive for creating batteries with high power–weight ratios. The mechanism of recharging and discharging involves Li^+ ion release and capture, respectively, via the nanocrevices between DDS molecules in the molecular assembly. Entrapment of Li^+ ions due to interaction with the p-electrons and sulfur in the SAM decreases the battery lifetime upon repeated charging and discharging. Such challenges could be addressed by electrode revitalization through SAM desorption and molecular replenishment. For example, if the rate of discharge is slower than monolayer formation, unprecedented energy densities can be obtained using soluble organic cathode materials such as disulfides and thiols.

However, further investigations are needed before the properties of this new material will be fully understood and practical application be realized.

References

[1] Scrosati, B. *Nature* **1995,** 373, 556B.

[2] Oyama, N.; Tatsuma,. T.; Sato, T.; Sotomura, T. *Nature* **1995**, *373*, 598.

[3] Pistoia, G. *Lithium Batteries*, Elsevier, Amersterdam, **1994.**

[4] Desilvestro, J.; Bass, J. *Electrochem. Soc.* **1990,** *137*, 50.

[5] Ohsuku, T.; Ueda, A. *J. Electrochem. Soc.* **1994,** *141*, 2972.

[6] Yu, A.; Kumagai, N.; Liu, Z.; Lee, J. Y. *J. Power Sources* **1998,** *74*, 116B.

[7] Spahr, M. E.; Stoshitzki-Bitterli, P.; Nesper, R.; Haas, O.; Novak, P. *J. Electrochem. Soc*. **1999,** *46,* 2780.

[8] Ceder, G.; Chiang, Y. M.; Sadoway, D. R.; Aydinol, M. K.; Jang, Y. I.; Huang, B. *Nature* **1998,** *392*, 694.

[9] Brodhead, J.; Trumbora, F. A.; Basu, S. *J. Electroanal. Chem*. **1981,** *118,* 241.

[10] Kim, J.; Manthiram, A. *Nature* **1997,** *390*, 265.

[11] Winter, M.; Besenhard, J. O.; Spahr, M. E.; Novak, P. *Adv. Mater*. **1998,** *10*, 725.

[12] Naoi, K.; Kawase, K.; Mori, M.; Komiyama, M. *J. Electrochem. Soc*. **1997**, *144*, L173.

[13] Megahed, S.; Barnett, B. M.; Xie, L. (Eds.), *Rechargeable Lithium and Lithium Ion Batteries,* Electrochemical Society Proceedings Series PV 94-28 (and reference therein), Electrochemical Society, New Jersey, **1995.**

[14] Mizushima, K.; Jones, P. C.; Wiseman, P. J.; Goodenough, J. B. *Mater. Res. Bull.* **1980,** *15*, 783.

[15] Ohzuku, T.; Ueda, A.; Hirai, T. *Chem. Exp*. **1992,** *7*, 193.

[16] Manev, V.; Momchilov, A.; Kozawa, A. *J. Power Sources* **1993,** *43–44*, 551.

[17] (a) Peled, E.; Golodnitsky, D.; Ardel, G. *J. Electrochem. Soc*. **1997** *144* L208; (b) Winter, M.; Novak, P.; Monnier, A. *J. Electrochem. Soc*. **1998,** *145,* 428.

[18] (a) Krawiec, W.; Scanlon L. G.; Fellner, Jr., J. P.; Vaia, R. A.; Vasudevan, S.; Giannelis, E. P. *J. Power Sources* **1995,** *54,* 310; (b) Leroux, F.; Koene, B. E.; Nazar, L. F. *J. Electrochim. Soc.* **1996,** *143*, L181. (c) Goward, G. R.; Leroux, F.; Nazar*,* L. F. *Electrochem. Acta*. **1998**, *43,* 1306B.

[19] Strattmann, M. *Adv. Mater.* **1990,** *5,* 191.

[20] Nuzzo, R. C.; Dubois, L. H.; Allara, D. L. *J. Am. Chem. Soc*. **1990,** *112*, 558.

[21] Depalma, V.; Tiliman, N. *Langmuir* **1989,** *5,* 868.

[22] Ferguson, G. S.; Chaudhury, M. K.; Sigal, G. B.; Whitesides, G. M.; *Science* **1991,** *253*, 776.

[23] Chen, J.; Reed, M. A.; Tour, J. M. *Science* **1990,** *286*, 1550.

[24] Katz, H. E.; Wilson, W. L. Scheller*,* G. *J. Am. Chem. Soc*. **1994,***116*, 6636.

[25] Hickman, J. J.; Ofer, D.; Laibinis, D. E.; Whitesides, G. M. *Science* **1991,** *252,* 688.

[26] Finklea, H. O.; Snider, D. A.; Fedyk, J. *Langmuir* **1993**, *9*, 3660.

[27] Peng, Z.; Dong, S. *Langmuir* **2001**, *17 (16),* 4904.

[29] Bandyopadhyay, K.; Vijayamohanan, K.; Shekhawat, G. S.; Gupta, R. P. *J. Electroanal. Chem.* **1998,** *447,* 11.

[29] Aslam, M.; Bandyopadhyay, K.; Vijayamohanan, K.; Laskshminarayanan, V. *J. Colloid Interface Sci.* **2001,** *234,* 410.

[30] Bandopadhyay, K.; Sastry, M.; Paul, V.; Vijayamohanan, K. *Langmuir* **1997,** *13,* 866.

[31] Li, W. H.; Nichols, R. J.; *J. Electroanal. Chem*. **1998,** *456,* 153.

[32] Bandopadhyay, K.; Vijaymohanan, K.; *Langmuir* **1998**, *15 (16),* 5314.

[33] Bandyopadhyay, K.; Vijayamohanan, K.; Venkataramanan, M.; Pradeep, T.; *Langmuir* **1999**, *15*, 5314.

[34] Bandyopadhyay, V.; Sastry, M.; Vijayamohanan, K. *Langmuir* **1998,** *14,* 3808.

[35] Pouchert, C.J. The Aldrich Library of Infra-Red Spectra, third ed., Aldrich Chemical Co. Inc., **1981.**

[36] (a) Sandroff, C. J.; Herschbach, D.R. *J. Phys. Chem*. **1982,** *86,* 3277; (b) Raymond, L.; Sobocinski, M. A.; Jeanne, B.; Pemberton, E. *J. Am. Chem. Soc.* **1990,** *112*, 6176B.

[37] Kumpf, R. A.; Dennis, A.; Dougherty, S. *Science* **1990,** *250*, 1558.

[38] Aurbach, D.; Weissman, I. *Eectrochem. Commun*. **1999,** *1,* 324.

[39] Laibinis, P.E.; Whitesides, M.G. *J. Am. Chem. Soc*. **1992,** *114,* 9022.

[40] Colvin, V. L.; Goldstein, A. N.; Alivisatos, A.V. *J. Am. Chem. Soc.* **1992,** *114*, 5221.

[41] Fxnar, I.; Hep, J. *J. Power Sources* **1993,** *44*, 701.

CHAPTER VII

Summary

The salient features of the work detailed in the thesis and possible avenues for future work are briefly discussed.

Summary of work

This thesis addresses the important issues of nanomaterials related to their synthesis and experimental tools for their analysis and their applications. One of the main objectives of this thesis is to develop new versatile synthetic protocols for the generation of nanomaterials especially 1D structures and studying their properties. It also aims to demonstrate applications of self-assembled monolayers and monolayer protected nanoclusters. The thesis starts with an introduction to nanotechnology followed by a critical review of synthesis, characterization, properties and various strategies for the organization of self-assembled monolayers, monolayer protected metallic nanoparticles and 1D nanostructures. The impact of these materials on nanotechnology for diverse applications has been briefly discussed. Importantly, the thesis is divided into three main parts.

The first part presents the various synthesis protocols for the formation of nanomaterials, especially nanowires. In brief, three different methods of synthesis of nanowires are shown.

(a) First, a simple, room-temperature strategy for assembling gold nanowire networks through the coalescence of nanoparticles by agitation of gold hydrosol-toluene mixtures is shown. Such template-less, low-temperature assembly of mesostructures from nanoscale blocks would open up new possibilities of using liquid mixtures to create a variety of architectures for applications such as self-supporting nanocatalyst networks, nanowires for device interconnection, novel fluid heat-transfer agents and porous high-strength nanofillers for composites.

(b) Second, new approach towards the formation of custom designed silver nanowires by supramolecular self-assembly of nanoparticles in the presence of organometallic chiral molecules is presented. These molecules can serve as good candidates to offer a high degree of organization of nanoparticles, ease of chemical modification, and naturally occurring self-assembly motifs inherent in these systems, which is of interest for the preparation of novel nanomaterials. These types of structures are expected to be useful in future for fabricating various nanoelectronic devices such as integrated-circuit interconnects, quantum computing devices, transistors, and sensors.

(c) And third, one step room temperature synthesis of *water-dispersible* nanostructures such as nanoparticles and nanowires of silver and gold using triethyl amine by adjusting the ratio of metal ions to ligand has been shown. This method offers the exclusive use of water as solvent and the requirement of mild temperature conditions and the low cost precursors makes this method suitable candidate for large-scale manufacturing of low cost water-dispersible nanomaterials. These materials find potential applications in biological systems such as biolabeling, molecular markers, biosensors based on nanoparticles with receptors or sites and materials in the field of biolistics.

Though, several methods have been proposed in this work to synthesize nanostructures, each method has its own limitations. For example, the Template-less nanowire synthesis limits their use in different solvents and often yields nanoparticles or partially grown nanowires in other solvents while the *water dispersible* nanowire synthesis suffers with low thermal stability and purity. Despite these limitations, these methods offer an elegant one step, template-less route to synthesize metal nanoparticles and nanowires in moderate quantities and with well-controlled dimensions under favorable conditions. Besides, the applications indicated in the thesis, such approaches are likely to find use in several future nano electronic devices. Further the protocols for synthesizing silver and gold nanostructures can be extended to obtain nanostructures of other metals thus providing a simple general route for the synthesis of anisotropic nanostructures.

In the second part, the materials synthesized using different protocols were scrutinized using different characterization techniques and the effects of different parameters on their properties have been studied to reach better fundamental understanding of the mechanism of formation of these structures. The investigation of electron transfer properties of these nanomaterials provide the deep understanding of electrochemical behaviour of the nanoparticles and nanowires as well as demonstrates the fundamental difference in the electron transfer dynamics of these nanostructures due to the change in the shape. Also a significant medium effect on electron transfer behaviour of metal nanoclusters has been reported. This study suggests that electron transfer properties of metal nanoclusters are governed by judicious control of

electrostatic interactions between solvent molecules and an electrical double layer of clusters and can be advantageously used to control selectivity of reactions catalyzed by metal clusters.

The third part demonstrates applications of nanomaterials. We investigate the role of in-situ generated metal nanoparticles as a catalyst in organic reactions especially Wolff rearrangements of diazoketones. We believe that this study gives a significant achievement in the understanding the role of silver compounds and co-reagents in Wolff rearrangement and these results may prove germane to the understanding of the catalysis of several organic reactions by metal-nanoclusters. Further we have shown a new approach of using self-assembled molecular layers (SAMs) of aromatic molecules as high-efficiency cathodes, which may give birth to new generation of batteries. These nanocathodes justify the costs, weight, longevity, and safety. This strategy of using layered mesoassemblies of molecular nanostructures could open up new possibilities of creating lightweight and miniaturized rechargeable energy generation and storage modules with extended lifetimes that can be integrated with logic and memory devices

While many applications of nanomaterials can be envisioned, this field of research is clearly still in its early stages of development. Though quantum well based devices are maturing towards commercial applications, devices based on one dimensional nanoscale materials are still in their early development stage. The full promise of one dimensional nanostructures, especially metallic nanowires must await advances in device. The understanding of nanodevices based on nanowires is not complete, nor is their development, which is certain to continue. Further in-depth investigation integrating chemistry and nanotechnology will be required to fully achieve these important goals; knowing how to translate the rules of tailoring molecular-level functions into large-scale complex systems will be crucial to the fabrication of nanoparticle-based functional devices.

The major concern of nanotechnology today is not only limited to the development of versatile protocols for synthesis of nanomaterials and their rational assembly into working devices but also related to its potential hazardous consequences on human health and the environment. An inevitable consequence of this rapid growth is the eventual exposure of humans and other environmental receptors to nanoscale

materials. Little is currently known about the fate, transport, and transformation of nanosized materials once they enter the environment, although there is an increasing amount of research on the toxicology of nanomaterials. As the production of manufactured nanomaterials increases and as products containing nanomaterials are disposed of, unintended and deleterious repercussions from these activities may result. These potentially harmful effects may be attributable to the nature or behavior of the nanoparticles themselves, the characteristics of the products made from them, or aspects of the manufacturing process. The large surface area, crystalline structure, and enhanced reactivity may cause certain engineered materials to be considered a new class of toxins. However, the nanotechnology bullet train has left the station with the power to take us to some magical places we've barely even dreamed of. Although public distrust of the technology could potentially derail the train, many passengers are hoping that increased understanding of both its potential benefits and dangers will keep it on track and allow the journey toward discovery to continue.

LIST OF SELECTED PUBLICATIONS

1) "Wet-chemical templateless assembly of metal nanowires from nanoparticles"

   Maddanimath, **T.;** Kumar, A.; D'Arcy-Gall, J.; Ganesan, P. G.; Vijayamohanan, K.; Ramanath. G. *Chem. Comm*. 2005, *11*, 1435.

2) "Self-assembled molecular nanocathodes for rechargeable energy storage modules"

   Maddanimath, **T.** Ramanath G. Vijayamohanan. K. *Chem. Phys. Lett*. 2004, *396*, 277.

3) "Templateless Room-Temperature Assembly of Nanowire Networks from Nanoparticles"

   Ramanath, G.; D'Arcy-Gall, J.; **Maddanimath**, **T.;** Ellis, A. V.; Ganesan, P. G.; Goswami, R.; Kumar, A.; Vijayamohanan, K. *Langmuir*, 2004, *20(13)*, 5583.

4) "Evidence for the Involvement of Silver Nanoclusters during the Wolff Rearrangement of –Diazoketones"

   Sudrik, S. G.; **Maddanimath**, **T.;** Chaki, N. K.; Chavan, S. P.; Chavan, S. P.; Sonawane, H. R.; Vijayamohanan, K. *Org. Lett*. 2003, 5(13), 2355.

5) "Self-assembled monolayers of diphenyl disulphide: a novel cathode material for rechargeable lithium batteries"

   Maddanimath, **T.;** Khollam, Y. B.; Aslam, M.; Mulla I. S.; Vijayamohanan, K. *J. Pow. Sources*, 2003, *124*, 133.

6) "Hierarchical architectures of silver nanoparticles: use of chiral molecules as a precursor"

   Maddanimath, **T.;** Sudrik, S. G.; Chavan, S. P.; Ramanath, G.; Vijaymohanan. K. *J. Am. Chem. Soc*. (Communicated), 2006.

7) "One step synthesis of water-dispersible silver nanostructures and their shape-dependent electrochemistry"

   Maddanimath, **T.;** Vijaymohanan. K. *J. Mat. Chem*. (Communicated), 2006.

8) "Effect of chain length on the tunneling conductance of gold quantum dots at room temperature"

Chaki, N. K.; Gopakumar, T. G.; **Maddanimath**, **T.;** Aslam, M.; Vijayamohanan, K. *J. Appl. Phys*. 2003, *94(11*), 7379.

9) "Solvent mediated electron transfer behavior of silver nanoclusters"

Maddanimath, **T.** Sudrik, S. Vijaymohanan, K. *J. Phys. Chem. B.* (Communicated), 2006.

10) "Humidity sensing properties of surface functionalized polyethylene and polypropylene films"

Maddanimath, **T.;** Mulla, I. S. Sainkar, S. R.. Vijayamohanan, K Shaikh, K. I. Patil A. S.; Vernekar. S. P. *Sensors and Actuators B: Chemical*, 2002, *81*, 141.

PATENTS

1) "An improved process for preparation of cathode materials for high energy density rechargeable lithium batteries"

US patent No. 20030186123

2) "Proton Transport at Polymer Surfaces"

US patent, Filed (NF-289/2001)

3) "An Improved Humidity Sensing Instrument"

US patent, Filed (NF-280/2001)